MECHANICAL PROPERTIES AND ELECTROCHEMICAL DURABILITY OF SOLID OXIDE FUEL CELLS

Ke An

Dissertation submitted to the faculty of the
Virginia Polytechnic Institute and State University
in partial fulfillment of the requirements for the degree of

Doctor of Philosophy
in
Engineering Mechanics

Kenneth L. Reifsnider, Chairman
Carl L. Prather
Scott L. Hendricks
John J. Lesko
Scott W. Case

December 19, 2003
Blacksburg, Virginia, USA

Keywords: SOFC, Composite Cathode, Impedance, Durability, Aging, Mechanical Properties, Fracture Strength, Hardness

Mechanical Properties and Electrochemical Durability of Solid Oxide Fuel Cells

Ke An

(ABSTRACT)

The mechanical properties of unaged and aged constituent materials for solid oxide fuel cells were evaluated using microindentation, plate tensile, four-point bend, ball on ring and pressure on ring tests. The Vickers hardness of the anode, interconnect and electrolyte was determined before and after 1000 hours aging at 1000 ^{o}C in air. The fracture toughness K_{IC} was found for the electrolyte materials. Finite element analysis (FEA) was validated and used to calculate the stress distribution and peak stress for the biaxial strength test. A Weibull analysis was carried out on the test/FEA-predicted peak stresses, and Weibull strength, modulus and material scale parameters were found for each test methodology. The methodologies were evaluated based on the results of the Weibull analysis and the pressure on ring test is preferred one for brittle thin film fracture strength testing.

Half cell SOFCs with composite cathode $(Pr_{0.7}Sr_{0.3})MnO_{3\pm\delta}$ /8YSZ on the 8YSZ electrolyte were aged 1000 hours at 1000 ^{o}C in air with/without polarization and investigated using Electrochemical Impedance Spectroscopy (EIS), Scanning Electron Microscopy (SEM), Brunauer-Emmett-Teller (B.E.T.) method and X-ray Diffraction (XRD). The performance of the half cell SOFCs degraded after aging with/without polarization compared to the initial state, which was ascribed to the decrease of the electrolyte conductivity. The current load was shown to have impact on the performance by slowing down the decreasing rate of the polarization resistance of the SOFCs. After aging, the microstructural properties - pore size and pore volume changed, and growth of grains was found

on the $(Pr_{0.7}Sr_{0.3})MnO_{3\pm\delta}$ phases, which may have contributed to the decrease of the activation polarization by decreasing the capacitance and increasing the number of active sites. After aging the high frequency EIS arcs/peaks shifted to a lower frequency range, and the low frequency arcs/peaks became unapparent compared to before aging.

A 3-D multiphysics finite element model was used to simulate the performance of the half cell SOFC. The effective exchange current density and the effective ionic conductivity of the cathodes showed much influence on the performance of the SOFC. Predicted and observed performance was compared.

Suggestions were given for the further experiments on the composite cathode.

Acknowledgements

First of all, I would like to show my great appreciation to **Dr. Kenneth L. Reifsnider**, my committee chair, academic advisor, mentor and friend during my study at Virginia Tech. It has been a great pleasure working with **Dr. Reifsnider** over the last three years. Without his extraordinary guidance, frequent encouragement and deep help, I could not finish the program in such a short time. Whenever I had trouble with my research or personal issues, **Dr. Reifsnider** was always here helping me.

I am grateful to **Dr. Carl L. Prather**, **Dr. Scott L. Hendricks**, **Dr. John J. Lesko** and **Dr. Scott W. Case**, my committee members, for their knowledge, enthusiasm, encouragement and time. Their helps and suggestions are invaluable to my research work.

I want to thank **Dr. Howard G. Halverson**, a nice and gentle MRGer, for his face-to-face instructions on my research. His help deserved being named the sixth committee member of mine.

Mr. Marshal " Mac" McCord, the smartest lab technician in ESM, is the one who made my experiment possible. His intelligence and patience impressed me. Thank you Mac.

Ms. Shelia Collins, **Ms. Beverly Williams**, **Ms. Loretta Tickle** and **Ms. Joyce Smith**, the staff of the Materials Response Group and the ESM department, have offered invaluable assistances during my study at Virginia Tech.

Dr. Shuangyan Xu, **Dr. Xinyu Huang**, **Ms. Vasanthi Vinjamo**, **Dr. Michael Hays**, **Mr. John Bausano**, **Mr. James Fazio**, **Dr. Rob H. Carter**, **Ms. V. Binetti**, **Ms. Tara Vinton** and other former and current members of MRG, showed their friendships and helps during my stay at MRG.

Mr. Yahong Gu and his wife **Qingying**, **Mr. Yuqing Wang** and his wife **Jing**, **Dr. Aixi Zhou** (MRGer) and his wife **Wei**, **Mr. Zhongfu Ge**, and other lovely people, gave me a fantastic memory for the life at Blacksburg.

My M.S. advisor **Dr. Xu Chen**, my old friend **Mr. Xiaomin Zhang** and his family, and others are the strong supporters of my study far away from China.

People working in the Connecticut Global Fuel Cell Center gave me the maxi convenience and help on the experimental work there.

Finally, I want to thank my wife **Carrie** (**Yang**), my family and relatives in China for their continuous support, encouragement and help. I would especially like to thank my mother and my father for their steadfast and unselfish love and encouragement. Thank you for everything you have done for me. I would like to thank my lovely wife, without your love, the dissertation was undoable.

Dedication

To my mother,

my father,

my brothers,

and my wife,

whose love

I cherish

TABLE OF CONTENTS

LIST OF FIGURES

LIST OF TABLES

CHAPTER 1
INTRODUCTION AND LITERATURE REVIEW

1.1 Overview

1.1.1 Fuel cells

Over the last three decades, fuel cell development has attracted more and more research interest (Kostogloudis *et al*. 1997). A fuel cell is an electrochemical "device" that continuously converts chemical energy into electric energy (and some heat) for as long as fuel and oxidant are supplied (Hoogers 2003). Figure 1.1 shows a schematic of a single fuel cell.

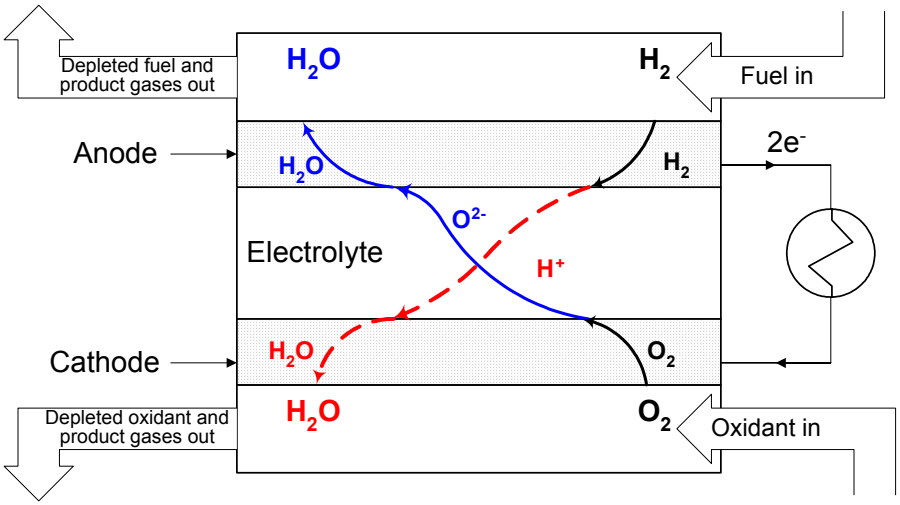

Figure 1.1. Schematic of a single fuel cell (oxygen ion conductor - solid line, proton conductor - dashed line).

The electrolyte works as an ion conductor to separate the fuel and oxidant allowing only ionized fuel or oxidant to pass through, which diffuses and is catalyzed through the porous anode or cathode, respectively.

Compared to traditional energy conversion systems, fuel cell systems have many advantages. Traditionally, gas turbine, steam turbine and reciprocating engines, which afford conversion to electrical energy, are limited thermodynamically by the Carnot efficiency. Fuel cell systems generate electricity at high efficiencies (Table 1.1). Hybrid SOFC-gas turbine power systems are expected to reach efficiencies approaching 70% (Singhal 2000). With heat recovery, system efficiencies may reach as high as 90% (Badwal 2001). It is a clean, pollution-free technology. When H_2 is used as fuel, the exhaust product is only water, which means the system has no noxious emissions.

Many types of fuel cells have been developed, from alkaline fuel cells (AFC), one of the oldest, to current widely studied proton exchange membrane fuel cells (PEMFC), molten carbonate fuel cells (MCFC) and solid oxide fuel cells (SOFC) *etc*. A summery of characteristics of major fuel cells is listed in Table 1.1. Low and medium temperature fuel cells (AFC, PEMFC and PAFC) have lower electrical efficiency, compared to high temperature fuel cells (MCFC and SOFC), but they are suited to automotive and portable electrical systems (Hoogers, 2003) because they can be started quickly. High temperature fuel cells have relatively good ion conductivity at elevated temperature and are generally developed for continuous electricity production.

Table 1.1. Summary of major differences of the fuel cell types.

	PEFC (PEMFC)	PAFC	MCFC	SOFC
Electrolyte[1]	Ion Exchange Membrane	Immobilized Liquid Phosphoric Acid	Immobilized Liquid Molten Carbonate	Ceramic
Operating Temperature[1]	80°C	205°C	650°C	800-1000°C, now 600-1000°C
Charge carrier	H^+	H^+	CO_3^{2-}	O^{2-}
External Reformer for CH_4[1]	Yes	Yes	No	No
Prime Cell Components[1]	Carbon-based	Graphite-based	Stainless Steel	Ceramic
Catalyst[1]	Pt	Pt	Ni	Perovskites
Efficiency[2]	35-45%	40%	>50%	>50%
Power Range[2]	5-250kW	200kW	200Kw-MW	2kW-MW
Product Water Management[1]	Evaporative	Evaporative	Gaseous Product	Gaseous Product
Product Heat Management[1]	Process Gas + Independent Cooling Medium	Process Gas + Independent Cooling Medium	Internal Reforming + Process Gas	Internal Reforming + Process Gas

[1](Herschenhofer *et al*. 1998), [2](Hoogers 2003)

1.1.2 Solid Oxide Fuel Cells (SOFCs)

SOFCs typically use ceramic oxides as electrolytes, which have excellent oxygen ion conductivity at elevated temperature (800-1000 °C). These fuel cell systems provide more reliability, better fuel adaptability and lower levels of NO_x and SO_x emissions (Singhal 2000). They are quiet solid-state devices that have vibration-free operation. Generally, since SOFCs operate at elevated temperature (800-1000 °C), it is possible to have natural gas fuel reformed within the cell / stack saving expenditure on other external reformer systems (Singhal 2000). Also, the exhaust heat can be used for process heat in industry or other heating services (Badwal 2001).

1.2 SOFCs design

Currently, several kinds of SOFC stacks geometry have been developed.

A planar SOFC design has a low physical component volume profile and short current path between single cells, which is perpendicular to the cell plane. Relatively low ohmic losses in the whole stack can be reached. However, the whole stack typically operates at a temperature around 800-1000^{o}C, which makes it tougher to seal the cell edges on both electrodes to avoid direct gas mixing.

A tubular SOFC has the advantage of simpler seal configuration with its cylindrical and closed end design. With air flow inside and fuel flow outside, gases are separated from inlets point to outlet zone. This design allows the inlets and outlets of gases to be far from the high temperature zone, which makes traditional seals possible. However, this tubular design has relative small interconnection between serial cells in a stack, which in turn results in large external ohmic losses. There is no short path for the current (Singhal 2000), so in this case the internal ohmic resistance will increase in proportion to the length of the current path. Compared to planar SOFCs, tubular SOFCs are complicated to fabricate (Orui *et al*. 2002).

To reduce the physical size and cost of an SOFC generator, an alternate geometry of cell is suggested. This new tubular style design is called a high power density solid oxide fuel cell, which keeps the advantages of tubular SOFCs, while providing higher power output. The current paths are shorted by the incorporated ribs; meanwhile, the airside electrode can be thinner with the existence of those ribs, which reduces the concentration polarization. The bottom and top are flattened, making a larger contact area between single cells. These innovations reduce the in-plane ohmic losses and electrode potential.

In the laboratory, button cells are designed for research study, which are low cost and easy to make. With round profiles, button cell test equipment is easy to machine.

1.3 Materials for SOFCs

State of the art materials currently used in most SOFC systems are yttria stabilized zirconia (YSZ) as the electrolyte, strontium doped lanthanum manganites (LSM) or LSM/YSZ composite as the cathode and Ni/YSZ cermets as the anode (Ivers-Tiffee *et al*. 2001). Electronic or mixed conducting (ionic and electronic) electrodes have to be porous with a large number of active triple phase boundary (TPB) sites to which the electrochemical reactions are restricted (Mizusaki *et al*. 1991; Steele 1997; van Berkel *et al*. 1994). With a higher TPB length per area, better electrochemical performance can be achieved (Brant *et al*. 2001). The electrolyte has to be gas tight and a purely ionic conductor with good conductivity (Ivers-Tiffee *et al*. 2001). Much research has been done on the materials, and the interface between the electrode/electrolyte and the reaction mechanisms of SOFC system.

1.3.1 Interconnects

An interconnect not only provides electrical connection between the anode of one cell unit and the cathode of a neighboring one, but also works as a physical barrier to keep the air and fuel on the air side and fuel electrodes, respectively, which it connects, separated from each other. Its stringent requirements in the rigorous environment of SOFCs have been reported (Zhu and Deevi 2003). An interconnect needs to exhibit excellent electrical conductivity, chemical stability, thermal expansion compatibility, good thermal conductivity, low permeability for oxygen and hydrogen, good high temperature strength and creep resistance, and to be easy to fabricate. Given these requirements, doped lanthanum chromite oxide

($LaCrO_3$) ceramic is currently the most common candidate material for SOFCs and in $LaCrO_3$ based solid solutions, Sr, Ca, Mg, Ni, or other elements are doped (Zhu and Deevi 2003).

1.3.2 Electrolytes

The electrolyte in SOFCs has to meet the following requirements in addition to a high ionic conductivity (Yamamoto 2000): low electronic conductivity, stability under oxidizing and reducing atmospheres, easy to make dense thin films, and good mechanical and thermal properties at operating temperatures.

Yttria stabilized zirconia (YSZ) is a state of the art electrolyte material for SOFCs. A conventional SOFC with 200 μm thick 8YSZ (ZrO_2 doped with 8mol% Y_2O_3) electrolyte works well at 850 - 1000 ^oC as at lower temperatures the ionic conductivity will decrease (Ivers-Tiffee *et al*. 2001). In one study, after 5000 minutes (83.3 hour) at 1000 ^oC, the ion conductivity of 8YSZ decreased about 11.8% from 15.6 to 13.75 Sm^{-1} (Gibson *et al*. 1998). However, the drop of the ion conductivity of 8.5YSZ was found to be less than that of 8YSZ, which was only 2.4% from 14.9 to 14.5 Sm^{-1}. The 8.5YSZ is a promising alternative to the currently used 8YSZ, although at the beginning of the aging its ion conductivity is larger than the later.

Some types of solid electrolytes have relatively high ionic conductivity at intermediate temperatures. Ce based oxide ionic conductors, such as Gd doped CeO_2, have a significantly higher ionic conductivity than most zirconia-based electrolytes and are a suitable basis material for intermediate temperature (500-600 ^oC) operation of SOFCs (Sahibzada *et al.* 1999; Sahibzada *et al.* 1997), but they need a protective coating of a stable electrolyte on the fuel side because under anode environment they may become ionic/electronic mixed conductors (Badwal 2001; Ivers-Tiffee *et al*. 2001). It was reported (Ishihara *et al*. 1994) that

the perovskite type $La_{0.9}Sr_{0.1}Ga_{0.8}Mg_{0.2}O_{2.85}$ (LSGM) exhibited an even higher ionic conductivity. The highest conductivity at 800 ^{o}C (0.17 S/cm) has been reported for the composition $La_{0.8}Sr_{0.2}Ga_{0.83}Mg_{0.17}O_{3-\alpha}$ (Huang *et al*. 1998). LSGM electrolytes have limited long-term and mechanical stability, and are also inhibited by the high cost of gallium which restricts their usage (Ivers-Tiffee *et al*. 2001). The $La_{0.9}Ba_{0.1}Ga_{0.8}Mg_{0.2}O_{3-\alpha}$ (LBGM) system, where Ba and Mg are substituted for the La and Ga site in a LSGM system has shown a good conductivity of 0.1 S/cm at 800^{o}C (Choi *et al*. 2000). The former showed a larger thermal expansion coefficient (Stevenson *et al*. 1997).

1.3.3 Electrodes

1.3.3.1 Anodes

Ni/Y_2O_3-ZrO_2 (Ni/YSZ) cermets have high electrochemical performance, good chemical stability and low cost and are widely used as fuel electrodes in SOFCs (Jiang and Badwal 1999). Many studies on this type of electrode have been carried out (Bieberle and Gauckler 2000, 2002; Jiang and Badwal 1997, 1999; Jiang and Ramprakash 1999; Lehnert *et al.* 2000; Matsuzaki and Yasuda 2000; Mizusaki *et al.* 1994).

In order to evaluate the reaction process and the TPB effect, instead of the general porous Ni-YSZ anode, a nickel strip pattern electrode prepared on the surface of YSZ has been used (Bieberle and Gauckler 2000; Fleig 2002; Mizusaki *et al*. 1994). The electrode activity for Ni anodes increases with the length of the three-phase boundary. The release of H_{ad} ('ad' denotes a component of an atom and a vacant adsorption site) may occur when (1) the produced H_{ad} itself moves away by diffusion or (2) the H_{ad} is attacked by another migrating H_{ad} to form H_2 and leaves the surface into the gas phase (Mizusaki *et al*. 1994). The rate limiting reaction occurs in a region close to the electrode/electrolyte interface; the reaction rate may be determined by the rate of removal of H or by the rate of attack of H_{ad}

to the H_{ad} produced by the decomposition of H_2O_{ad} or OH_{ad}. It was demonstrated (Jiang and Badwal 1997) that the hydrogen adsorption/diffusion process on the surface of Ni particles and the charge transfer process on zirconia electrolyte surface were rate-controlling ones. A study on porous nickel on the 3mol% YSZ (Y-TZP) showed (Jiang and Badwal 1999) that the Y-TZP in the Ni cermet electrodes had little effect on the reaction mechanism. It affected the electrode microstructure and kinetics of the fuel oxidation reaction.

To decrease the operation temperature of fuel cells below 800^{o}C is one of the main research interests in the field. At temperatures below 800^{o}C, the resistance of electrolytes can be quite large. An anode-supported fuel cell with a thin film of electrolyte (5-20 μm) can compensate the conductivity decrease caused by lower temperature (de Haart *et al*. 1998; Kek *et al*. 2001; Koh *et al*. 2002; Van herle *et al*. 2001; Yoon *et al*. 2002).

1.3.3.2 Cathodes

Cathode materials in solid oxide fuel cells have been intensively studied recently because the cathode overpotential makes a large contribution to the output losses in SOFCs (Horita *et al*. 2002; Svensson *et al*. 1996; Wen *et al*. 1999).

The properties required of a cathode material are (i) high electric and ionic conductivity, (ii) high catalytic activity for oxygen reduction, (iii) chemical and thermal compatibility with the electrolyte, and (iv) chemical stability in an oxidizing atmosphere (Endo *et al*. 2000). Noble metals such as gold and platinum can work as electrodes but they are not acceptable for practical application because of evaporation or activity related to electrochemical reactions at elevated temperature 900-1000^{o}C (Demin and Gulbis 2000; Lee 2003). Perovskite-type oxides can be a substitution for noble metal as cathode materials (Lee *et al*. 2003).

$LaMnO_3$ based perovskites are commonly used as cathodes. The strontium-doped lanthanum manganites (LSM) have high conductivity, relative

chemical stability, and a thermal expansion coefficient close to that of zirconia (Brant *et al*. 2001).

At the interface between the LSM cathode and ZrO_2 solid electrolyte, $La_2Zr_2O_7$ and/or $SrZrO_3$ may be formed (Clausen *et al*. 1994; van Roosmalen and Cordfunke 1992; Yokokawa *et al*. 1990), which degrades the long-term performance of SOFCs (Kuscer *et al*. 1995). At lower mole fractions of Sr^{2+}, $La_2Zr_2O_7$ is mainly formed (Mitterdorfer and Gauckler 1998; Yokokawa *et al*. 1990). It has been reported that the specific electrical resistivity of $La_2Zr_2O_7$ is at least three orders of magnitude higher than that of $LaMnO_3$ (van Roosmalen and Cordfunke 1992). At higher Sr^{2+} concentrations, the chance of formation of $SrZrO_3$ increases (Toshihiko Setoguchi *et al*. 1990; van Roosmalen and Cordfunke 1992). A study on the effect of the mole fraction of Sr^{2+} in $La_{1-x}Sr_x$-MnO_3 showed no $La_2Zr_2O_7$ created at 1400 ^oC for 5 hours when the substitution amount of Sr was 50% (Lee *et al*. 2003).

By creating a mixture of an ionic conductor and an electronic conductor increasing the total reaction zone of TPB, a composite electrode provides paths simultaneously for oxygen ions, electrons, and gaseous species and thus decreases the activation polarization (Virkar *et al*. 2000). An addition of 20 wt.% YSZ resulted in the best electrochemical performance in a study (Wang *et al*. 1998). An addition of up to 40 wt.% YSZ to the cathode improved its performance as a result of better adhesion to the base electrolyte and increased sites of TPB (Ostergard *et al*. 1995), and the minimum polarization resistance of the high-frequency arc was investigated (Kim *et al*. 2001). At 900 ^oC in air, an addition of 50 wt.% YSZ to an $La_{0.85}MnO_3$ decreased the specific polarization resistance from 0.77 to 0.16 ohm/cm^2 (Kenjo and Nishiya 1992). The process of charge transfer is expected to happen over some distance from the electrolyte/electrode interface into the electrode (Virkar *et al*. 2000). At low temperatures, a positive effect on the electrode performance was found in a range of thickness implying

the bulk of the LSM-YSZ composite cathode was active with respect to the oxygen reduction (Juhl *et al*. 1996).

Other advantages of a composite cathode were also reported (Choi *et al*. 2001). Fine-grained YSZ components can connect the gaps between LSM particles and the YSZ substrate, which does create a better adhesion between the electrode and electrolyte. Therefore, the sintering temperature of the interface of electrode/electrolyte can be lowered to decrease the possibility of formation of high resistive $La_2Zr_2O_7$ and/or $SrZrO_3$.

A complex interface of cathode and electrolyte has been developed (Herbstritt *et al*. 2001). Some individual 10YSZ particles were first screen printed onto a flat and dense 8YSZ substrate, and then an LSM layer was applied on the electrolyte. These particles increase the total surface of the interface cathode and electrolyte. Consequently, the TPB, the effective reaction location, has been increased. The impedance tests at non-operating and operating conditions showed a decrease of the polarization resistance and an increase of power output.

Other perovskite-type oxides have been studied (Adler 1998; Endo *et al*. 2000; Kostogloudis *et al*. 2000; Wen *et al*. 1999). Perovskite-type oxides with the general formula $La_{1-x}(Sr, Ca)_xMnO_3$ are the most widely investigated cathode materials, which have relatively better electronic conductivity and similar thermal expansion coefficients to the stabilized zirconia electrolyte (Wen *et al*. 1999). $La_{1-x}Sr_xCoO_{3-d}$ (LSC/LSCO) is a mixed conducting material which is reversibly reducible, has high rates of surface exchange and diffusion, and forms a clean well-characterized electrode system with little or no interfacial charge transfer resistance (Adler 1998). LSC is a promising material for making cathodes of SOFC under operation at 800 ^oC due to its high ion conductivity (Endo *et al*. 2000).

It has been reported (Ishihara *et al*. 1995) that among various Sr-doped rare earth manganites, those incorporating Pr^{3+} ion at the A-site exhibited the highest electrical conductivity and maintained the lowest overpotential values.

Some investigations have been done on $Pr_{1-x}Sr_xMnO_3$ cathodes. $Pr_{1-x}Sr_xMnO_3$ was synthesized with an orthorhombic structure in the range of $x<0.5$ and the electrical conductivity of this compound was one order of magnitude higher than $La_{1-x}Sr_xMnO_3$ at elevated temperature (Wen *et al*. 1999). The thermal expansion coefficient and chemical stability of this kind of cathode is compatible with the YSZ solid electrolyte. In Wen's study, after 100 hours at 1000 ^oC, the cathode film kept a porous structure and was coherent to the YSZ substrate. With different values of x, it was reported the thermal expansion was almost linear for compositions with $x \geq 0.15$ (Kostogloudis *et al*. 1997). The electrical conductivity increased with temperature for all compositions. When $x=0.5$, the $Pr_{1-x}Sr_xMnO_3$ showed the best characteristics, not only the best thermal compatibility with the electrolyte but also the best electrical conductivity. The characteristics of $Pr_{0.6-x}Sr_{0.4}MnO_3$ with different values of x were studied (Huang *et al*. 2000). The nonstoichiometric compound with $x>0$ exhibited higher conductivity and lower overpotential than the stoichiometric one and the usually used LSM cathode. When $x=0.05$, i.e. the nonstoichiometric $Pr_{0.55}Sr_{0.4}MnO_3$ had the lowest cathodic overpotential and exhibited the best conductivity. When using LSGM as an alternative electrolyte and $Pr_{0.8}Sr_{0.2}Mn_yCo_{1-y}O_3$ as a cathode, after 100 hours at 1300 ^oC, a distinct concentration of Co down to a depth of more than 100 μm was found (Naoumidis *et al*. 1999).

1.3.3.3 Oxygen reduction

The oxygen reduction mechanism on the cathode side is important because it is related to the cathode overpotential at the cathode/electrolyte interface which is the major resistance of SOFCs (Horita *et al*. 2002). Many oxygen reduction mechanisms have been reported (Adler 1998; Costamagna *et al.* 1998; Endo *et al.* 2000; Fleig 2002; Horita *et al.* 2002; Horita *et al.* 2001; Mitterdorfer and

Gauckler 1999a, 1999b; Mizusaki *et al.* 1991; Naito *et al.* 2000; Naoumidis *et al.* 1999; Ostergard and Mogensen 1993; Siebert *et al.* 1995; Svensson *et al.* 1996; Tsuneyoshi *et al.* 1989). Two major models for the reaction path of oxygen in the cathode are often discussed (Endo *et al*. 2000; Fleig 2002; Siebert *et al*. 1995; Svensson *et al*. 1996) as shown in Figure 1.2.

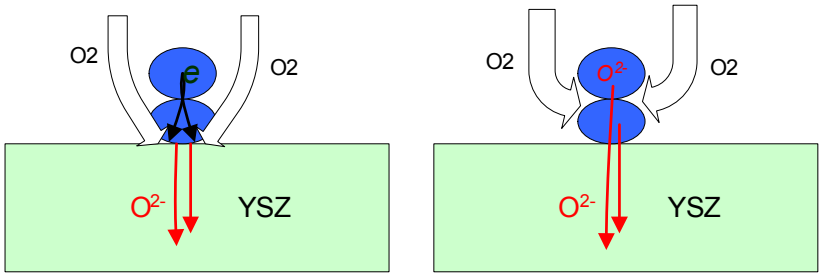

Figure 1.2. Configuration of oxygen reduction at cathode.

Under low cathodic overpotential, the reduction of oxygen in the cathode is believed to happen at the triple phase boundary where the oxygen atom is absorbed. This mechanism is a good fit with the experimental results for metal electrodes or perovskite cathodes treated as metal cathodes (Siebert *et al*. 1995). It has been reported (Mizusaki *et al*. 1991; Tsuneyoshi *et al*. 1989) that the oxygen reduction can only happen at the triple phase boundaries (TPB) of electrode/electrolyte/gas. In this case, the oxygen has to diffuse through the porous cathode to the reaction sites. If Pt is the electrode, the oxygen molecules are adsorbed disassociatively on the metal surface. The adsorbed atomic oxygen and the oxygen traveling through the pore network diffuse to the TPB, and the oxygen electrochemically changes into an oxygen ion at the TPB (Mitterdorfer and Gauckler 1999a). The diffusion rate of adsorbed oxygen will be limited by the

gradient of the chemical potential along the metal surface. It has been reported (Bieberle and Gauckler 2000; Mizusaki *et al*. 1991) that the total reaction rate was proportional to the TPB length per unit area.

Under higher cathodic overpotential, a steady state oxygen reduction reaction associated with oxygen transport through the electrode material is predominant, and even a poor mixed conducting electrode such as LSM shows evidence for involvement of bulk-transport (Endo *et al*. 1996; Lauret and Hammou 1996; Mizusaki *et al*. 1996; Siebert *et al*. 1995). The electrochemical reaction consists of vacancy exchange at the cathode electrolyte interface (Svensson *et al*. 1996). If there is the possibility that the oxygen molecules adsorb on the cathode surface, different paths could be possible (Ostergard and Mogensen 1993):

- Dissociation -> surface diffusion of oxygen atoms to the TPB -> electron transfer -> oxide ion transfer to the electrolyte.
- Dissociation -> electron transfer-diffusion of charged oxygen ions to the TPB -> oxide ion transfer to the electrolyte.
- Electron transfer -> dissociation-diffusion of charged oxygen ions to the TPB -> oxide ion transfer to the electrolyte.

Both the properties of the cathode material and the experimental conditions will have an effect on the mechanisms of the total reaction. It was determined that a steady state oxygen reduction reaction occurred (as in the first case) in an LSM-YSZ cathode (Siebert *et al*. 1995). From the study of the $La_{1-x}Sr_xCoO_{3-d}$/LSGM interface (Horita *et al*. 2001), it is imagined that the surface diffusion of oxygen atoms and the bulk diffusion of oxygen ions happen

simultaneously, and under the higher cathodic overpotential, oxygen ion diffusion in the bulk LSC is the dominant mechanism that controls the oxygen reduction rates at the interface. For a LSC/ceria/LSC fuel cell, the impedance analysis suggested that oxygen reduction on the cathode was limited primarily by surface chemical exchange and solid state diffusion (Adler 1998). However, the study on LSC/SDC (Endo *et al*. 1998) showed that oxygen absorption was the rate-determining step and the bulk diffusion of oxide ions in LSC did not control the resistance of cathodic reaction rates. It was recommended that a large surface area electrode could result in high performance. The roughness of the porous LSC electrode could enhance the surface reaction rates under cathodic polarization (Horita *et al*. 2001). The disassociative adsorption of O_2 and the transfer of oxygen ions to the YSZ electrolyte are comparably rate determining in an LSM electrode, while in LSM/YSZ, the addition of YSZ increases both steps by enlarging the TPB sites and the latter step is dominant (Wang *et al*. 1998). The relationship between overpotential and unit length of TPB under higher cathodic overpotential was investigated (Fukunaga *et al*. 1996), and it was shown that when the LSM-YSZ was used as a composite cathode, the overpotential was reduced suggesting a three dimensional distribution of TPB in the cathode. An effective charge transfer resistance defined by Virkar *et al*. (2000), can increase (low values of ion conductivity) or decrease (high values of ion conductivity) with an increasing cathode thickness and attain a limiting value.

1.4 Degradation of SOFCs

Due to the time consumed in conducting them, long-term performance investigations of SOFCs have been done less often than general tests.

The long-term performance degradation of button cells consisting of standard materials (LSM, YSZ and Ni/YSZ) has been studied (Hsiao and Selman 1997). Thermal cycling tests were conducted first between 312 and 649 hours,

and at 1321 hours a special potential-accelerated aging was applied to the cathode. After thermal cycling, the high frequency (HF) EIS region was enlarged. The DC polarization curves indicated that the potential-accelerated aging caused a large increase in polarization due to an increase of interfacial resistance. It was concluded from the AC impedance response that the microstructure of the cathode did not change but the interfacial resistance between the cathode and the electrolyte increased after electrically accelerated aging. A gap area was found between the anode and the electrolyte after the aging test.

A $LaMnO_3$/Pt/YSZ sandwich sample was made and aged at 1450 ^oC (Kuscer *et al*. 1995). After 100 hours of aging in air, compared to 2 hours, not only was a thicker LZ layer observed, but also the $LaMnO_3$ layer was separated along most of the interface with only a few sintered contacts, and increased porosity occurred at the $La_2Zr_2O_7/LaMnO_3$ boundary. The separation was a result of the diffusion of manganese oxides. A La silicate phase was found on the separated surface.

In the durability study on LSC/LSGM/Pt SOFC aged in air at 800 ^oC, the electrolyte resistance of LSGM decreased with an operation time under cathodic polarized condition, while the interface resistance increased. It was concluded that the applied voltage in a cathodic direction affected the LSC porous/LSGM interface nature (Horita *et al*. 2000).

A 150 W tubular solid oxide fuel cell stack was tested in a 3000 hours endurance run (Antonucci *et al*. 1998). From the X-ray peak profiles of the anode (Pt-CeO_2), after aging the particle size of the Pt and CeO_2 in the alloy changed relatively little. However, a formation of Pt-Ce alloy was found which led to depletion of CeO_2, resulting in a considerable change of reaction path and the creation of oxidation products.

A study on anode-supported fuel cells (de Haart *et al*. 1998) showed a performance degradation of 5% in 1000 hours of working under a relative dry (1-

3% H_2O) and low fuel utilization (<10%) conditions at 800 ^oC. The influence of water vapor concentration on the fuel cell was shown after 800 hours of operation with a comparable rate to the dry condition (1-3% H_2O). Another anode-supported fuel cell system (Charpentier *et al*. 2000) with 2000 μm Ni/YSZ, 20 μm YSZ and 5 μm LSM was evaluated for more than 100 hours under H_2 with a current of 100 mA/cm^2 and the average deterioration rate of 3.8% over 100 hours occurred due to an increase of the interfacial resistance between the cathode and electrolyte seen with EIS impedance measurements.

LSM ($(La_{0.85}Sr_{0.15})_{0.9}MnO_{3\pm\delta}$) - YSZ (TZ-3YB) composite cathodes with and without current passing through at 1000 ^oC in air were considered (Jorgensen *et al*. 2000). After 2000 hours, the composite LSM/YSZ electrodes tested without current load showed little or no degradation. For electrodes tested galvanostatically at –300 mAcm^{-2}, an increase in overvoltage exceeding 100% of the initial value was found after 2000 hours of testing. The subsequent SEM examination showed that there were a large amount of submicron pores formed close to the interfaces of the composite cathode layer for electrodes tested galvanostatically, but no changes occurred for the unloaded endurance tests.

A commercial level investigation has also been carried out (Elangovan *et al*. 1998). A single, stacked (5 cells) and tall stacked (62 cells) planar SOFC unit was studied. A single cell operated at 1000 ^oC, had a performance degradation of less than 0.5% per 1000 hours. Working under 850-900 ^oC with low temperature electrodes, the stack performance showed negligible degradation over 10000 hours of operation. Using 180 μm YSZ, a typical stack performance was greater than 95% of single cell performance. The tall-stacked cells system integrated with a pipeline natural gas fuel processor and air preheater showed performance stability over 250 hours.

1.5 Mechanical properties

At elevated temperatures, the SOFC materials have to have good strength, toughness and thermal compatibility (Yamamoto 2000). Compared to the electrochemical properties and fabrication of the new SOFC materials, reports concerning mechanical and thermal properties are few.

Mechanical stability of perovskites based on $LaCrO_3$ has been reported (Hilpert *et al*. 2003; Paulik *et al*. 1998). $La_{0.80}Sr_{0.20}Cr_{0.97}V_{0.03}O_{3-\delta}$ (LSCV) and $LaCr_{0.79}Mg_{0.05}Al_{0.16}O_{3-\delta}$ (LCMA) were investigated (Hilpert *et al*. 2003). The LSCV beams were tested in a 4-point bending fixture and the thinner LCMA disks were tested using a ring on ring device. The stress-strain curves of LSCV and LCMA showed a pseudo-plastic deformation behavior. The stiffness and strength of both materials increased with decreasing oxygen partial pressure but the reason was unknown. It was reported (Paulik *et al*. 1998) that a significant decrease in bending strength occurred when testing $La_{0.85}Sr_{0.15}CrO_3$ and $La_{0.70}Sr_{0.30}CrO_3$ in hydrogen. The calcium-substituted chromites showed a significant reduction in strength with increasing temperature, while the strength of strontium-substituted chromites was essentially invariant with temperature (Paulik *et al*. 1998).

The widely used YSZ electrolyte is subjected to thermal and external stresses under operation, so that the enhancement of the mechanical properties is an important issue in planar SOFCs (Kwon *et al*. 2001; Yamamoto 2000). The thermal expansion coefficient of 8YSZ has been reported to be about $10\text{-}11 \times 10^{-8}$/K (Mizutani *et al*. 1994; Yamamoto 2000). The shrinkage of the electrolyte occurred at elevated temperatures above about 1100 ^{o}C (Kwon *et al*. 2001). 3YTZP (3 mol% Y_2O_3-ZrO_2) exhibited a higher bending strength and fracture toughness than general 8YSZ, but the ionic conductivity (0.056 S/cm) was not more than half of that (0.16 S/cm) of the latter at 1000 ^{o}C (Mizutani *et al*. 1994; Yamamoto 2000). Several groups of cubic YSZ mechanical properties studies

have been done using ring on ring biaxial flexure tests (Lowrie and Rawlings 2000). It was illustrated that the surface defects from the tape-casting process were the main source of the initialization of fracture at room temperature but not at elevated temperature. After aging at 950 ^{o}C for 1000 hours, there was no structural instability displayed by SEM micrographs. By finite element analysis, the strength determined by the biaxial test ranged from 290 to 350 MPa at room temperature. The flexural strength of 8YSZ was tested to obtain values of about 330 MPa, and the 8.5YSZ was about 305 MPa (Gibson *et al*. 1998). The strength decreased with increasing temperature (Lowrie and Rawlings 2000). Fracture toughness of tape-cast YSZ was measured (Atkinson and Selcuk 2000; Selcuk and Atkinson 2000) using Vickers indentation at room temperature and double torsion methods at both room temperature and 900 ^{o}C, and the fracture toughness was found to decrease from around 1.61 MPa $m^{1/2}$ at room temperature to nearly 1.02 MPa $m^{1/2}$ at 900 ^{o}C. Vickers indentation tests (Kwon *et al*. 2001; Mizutani *et al*. 1994) indicated that the hardness of the 8YSZ electrolyte was about 11.7 GPa and the fracture toughness (K_{IC}) was about 1.3 MPa $m^{1/2}$ (Kwon *et al*. 2001; Mizutani *et al*. 1994). The crack in the cubic YSZ propagates through the grains and a transgranular fracture mode was observed (Bhargava and Patterson 1997; Lowrie and Rawlings 2000).

In the case of the electrode, the thermal expansion has to be compatible with the electrolyte (Stevenson *et al*. 1995). This can be achieved by adjusting the composition of the cathode. The thermal expansion coefficient of $La_{1-x}Sr_xMnO_{3\pm\delta}$ increases with increasing x (Hammouche *et al*. 1989). An unusual plastic deformation was found for LSM (Meixner and Cutler 2002a, 2002b). After being subjected to bending stresses of 40 MPa or less at room temperature a range of LSM compositions exhibited plastic deformation, and the deformation increased with increasing load. Some flat plate samples of LSM were fractured by four-point bending or disk biaxial flexure (Meixner and Cutler 2002b). LSM with high strontium content exhibited low Young's modulus and fracture strength.

1.6 2D or 3D simulation analysis of SOFCs

Simulation analyses of SOFCs have been reported (Achenbach 1994; Achenbach 1995; Fleig and Maier 1996; Iwata *et al*. 2000; Milliken *et al*. 1999; Nagata *et al*. 2001; Recknagle *et al*. 2003; Shiratori and Yamazaki 2003; Tanner and Virkar 2003; Yakabe *et al*. 2000; Yakabe *et al*. 2001). For a single planar type fuel cell or a fuel cell stack, three flow cases are mostly studied; cross-flow, co-flow and counter-flow. Current density profiles are strongly dependent of temperature distributions (Iwata *et al*. 2000), so these two profiles are always presented together. From a mathematical model for the simulation of a planar type SOFC, the most uniform current density distribution is observed for co-flow, and counter-flow has the highest cell efficiency. The largest temperature gradients in the solid structure occur for cross-flow (Achenbach 1994), and the co-flow case has the most uniform temperature distribution and the smallest thermal gradients (Recknagle *et al*. 2003). Considering the stresses caused by the mismatch of the thermal expansion of the interconnects, electrodes and electrolyte, the co-flow pattern has more thermo-structural advantages than the other flow cases (Recknagle *et al*. 2003; Yakabe *et al*. 2001). By implementing the thermal distribution profile of a simplified single-unit model to ABAQUS, it was found the internal reforming of CH_4 would induce a steep drop of fuel temperature near the inlet, which resulted in large tensile stresses (several tens of MPa) in electrolytes (Yakabe *et al*. 2001). When there is a radiative heat boundary on the upper and lower surfaces of single SOFCs, the temperature profiles are almost flat for all of these three flow types (Iwata *et al*. 2000). Increasing the operation pressure is effective in suppressing the cell temperature increase due to the increasing cell power (Iwata *et al*. 2000). Calculations of stack efficiency for a ceria electrolyte SOFC showed a decreasing efficiency with temperature increase (Milliken *et al*. 1999).

Concentration simulation on an anode-supported methane-reformed gas system (Yakabe *et al*. 2000) showed that the concentration polarization increased

considerably along the fuel flow path at high fuel utilization and the shift reaction was effective in reducing the concentration polarization.

Transient behavior analysis of an SOFC caused by load changes (Achenbach 1994) showed at it takes several minutes for the cell to respond to a load change to establish new steady-state conditions. An undershoot of cell voltage occurred just after the change of load. The relaxation depends on the thermal properties, geometry size and other configuration of the cell.

The effects of interconnects were numerically studied (Tanner and Virkar 2003). For a one-dimensional symmetric interconnect, the area-specific resistance was enlarged by increasing the interconnect spacing for widely spaced interconnect contacts. The size of the interconnect contact area had a minor effect. For the two-dimensional case, the area-specific resistance was found to increase as a function of interconnect contact spacing for widely spaced interconnects, and to be singular at zero contact area. A design with closely spaced interconnect contacts and a one-dimensional symmetry is preferred.

1.7 Objectives

During severe complex (elevated temperature, pressurized and electrochemical) long-term operations, the mechanical properties of the constituent elements of SOFCs, in addition to the electrochemical properties, definitely have effects on the SOFCs' performance and durability. However less work on mechanical properties has been reported than on electrochemical properties. Constituent materials of SOFC including electrolytes, anodes and interconnects are to be studied evaluate their fracture strength, fracture toughness and aging behavior. The present research work will determine and develop proper test methods to evaluate those important mechanical properties and their mechanical degradations after long-term aging. Finite element analysis validation will be performed for stress analysis.

The interfaces of electrodes/electrolyte are believed to be major contributors to electrical losses, by which the performance of fuel cells is degraded, and changes (physical or chemical) in the microstructure may affect the electrochemical properties of the constituent materials and the interfaces and lead to the degradation of cells (Hsiao and Selman 1997; Jorgensen *et al*. 2000; Kuscer *et al*. 1995). An interface of cathode/electrolyte on a kind of half cell SOFC (without anode on) will be investigated in the present work. Its behavior and stability with respect to the morphological and chemical composition in a fuel cell operation environment at 1000 ^{o}C with or without current load during long-term aging will be inspected and correlated to the electrochemical performance of the half cell.

Modeling of the fuel cell system will aid in the cell and the stack design. Modeling tools based on finite element methods will be optimized and multiphysics modeling of electrical, chemical, and fluid dynamical behavior will be performed for the half cell SOFC system.

1.8 Dissertation layout

CHAPTER 2 contains a description of the experimental procedures and measurement techniques. In CHAPTER 3 and 4, the mechanical properties of the anodes, interconnects, and electrolytes before and after aging are discussed. Some finite element models were created for different methodologies and the stresses distributions are presented. In CHAPTER 5, the long-term durability of the half cell SOFCs is given under various aging conditions and the results are interpreted with EIS, SEM, XRD and B.E.T. methodologies. In CHAPTER 6 a multiphysics modeling work was carried out on the SOFC and the simulation results are given. Finally, in CHAPTER 7 the major achievements in this work are summarized.

CHAPTER 2
EXPERIMENTAL PROCEDURE

In this chapter, general descriptions of samples, measurement techniques and set-ups are given. Details about samples of constituent materials of SOFCs studied in this dissertation and associated test parameters will be stated in the succeeding chapters where appropriate.

Major measurements or studies conducted on the constituent materials of solid oxide fuel cells are mechanical tests, electrochemical characterization, micro-structural investigation and chemical analysis on normal and aged samples.

2.1 Constituent materials of SOFCs

For a unit fuel cell or fuel cell stack system, the constituent materials of SOFCs, including interconnects, anodes, electrolytes and half cell SOFCs without anodes, were provided by McDermott Technology Inc. Their basic descriptions are given as follows.

2.1.1 Interconnects

The interconnect beams for bend testing are listed in Figure 2.1 and Table 1.1. They were made up from 8 layers of green tape, each layer nominally 0.375 mm thick after firing. The specimens were cut from laminated sheets of green tape prior to firing. After firing most of the specimens could easily be separated between layers 3 and 4, thereby leaving two thinner specimens of 3 layers and 5 layers. A total 52 samples (50% 3 layers) were tested.

Table 2.1. Interconnect specifications.

Samples	Nominal thickness (mm)	Young's modulus (GPa)	Laminates
SL3LI	1.125	190	3 layers
SL5LI	1.875	190	5 layers

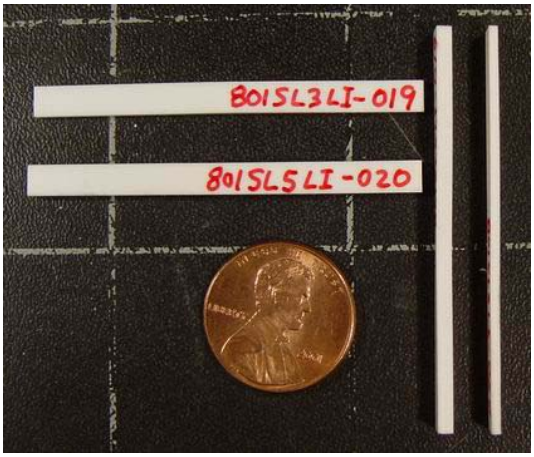

Figure 2.1. Interconnect samples.

2.1.2 Anodes

The anodes studied here to determine the hardness evolution using microindentation after long-term aging are composite materials. After they were fired, these beams were reduced in H_2 at elevated temperature. These black porous beams have approximately 45% porosity after reduction. Chemical analysis was performed on them using Electrochemical Impedance Spectroscopy (EIS).

2.1.3 Electrolytes

Several kinds of electrolyte materials were studied to determine different mechanical properties.

The YSZ electrolytes were in the shape of square plates, round disks and beams. Geometries and general mechanical properties are listed in Table 2.2. Tensile tests were performed on the square plates. Round disks of group 3 with a nominal diameter of 23 mm were cut from some broken electrolyte plates of group 1, which were not subjected to tension test. Biaxial flexural strengths for them were measured using a ball on ring test fixture. Some pieces from plates group 1 were placed into a furnace to be aged at 1000 ^{o}C in air and then indentation tests were performed on non-aged and aged ones. Single plates B, C and D were used to evaluate hardness and fracture toughness. Round disks of group 1 and 2 with a nominal diameter of 17 mm were used to perform biaxial flexural strengths measurement using a pressure on ring test system. Long-term aging effects on bend strength were evaluated on electrolyte beams, having a mixture of 35% 8YS, 35% 8Y and 30% 3Y-E sintered at 1350 ^{o}C for 6 hours.

Table 2.2. Electrolyte material specifications.

Samples	**Size (mm)**	**Nominal thickness (μm)**	**Young's modulus (GPa)**	**Memo**
Plates group 1	100×100	180	185	Tensile, indentation
Plate B	50×50	200	190.7	Indentation
Plate C	100×75	180	201.3	Indentation
Plate D	100×108	180	199.6	Indentation
Disks group 1	Nominal diameter 17	180	199.6	Pressure on ring
Disks group 2	Nominal diameter 17	180	199.6	Pressure on ring
Disks group 3	Nominal diameter 23	180	185	Ball on ring
Beams (35% 8YS, 35%8Y, 30%3Y-E.)	Nominal dimension 66×6.6×2.5	N/A	N/A	Bend before and after aging

2.1.4 Half cell SOFCs

The half cell SOFCs used in this study consist of a cathode and electrolyte, with a layer of cathode paste approximately 15~20 μm thick and 10 mm in diameter on the 180 μm thick electrolyte substrate as shown in Figure 2.2. Long-term aging effects on them with/without current were studied using electrochemical methods (EIS) during the process of aging. SEM/EDS/XRD analysis was conducted on the surface of the cathode and the interface between the cathode and electrolyte before and after aging.

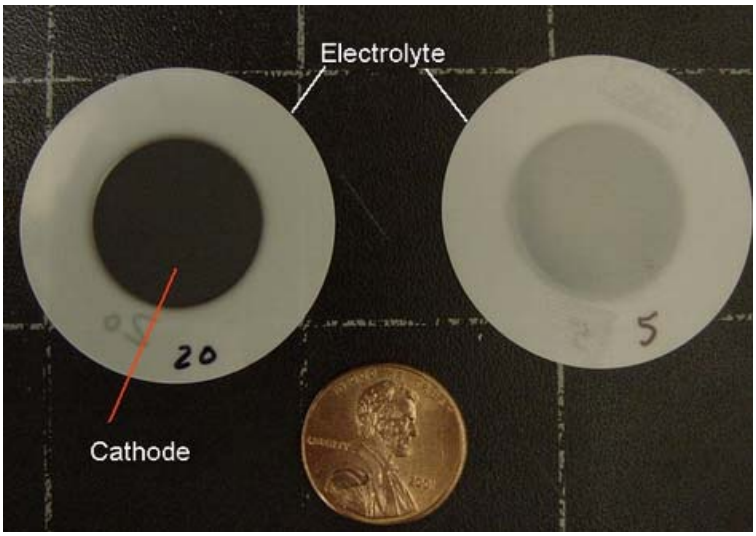

Figure 2.2. Half cell SOFC used in current study.

2.2 Aging set-up

Aging experiments were done in a digitally controlled furnace (Omega LMF-3550). The elevated temperature was up to 1000 ^{o}C. Heating up and cooling rates were controlled at 2 ^{o}C/min below 600 ^{o}C and 5 ^{o}C above 600 ^{o}C. The hold time at elevated temperature was up to 1000 hours. At the desired temperatures,

measurements were not performed until half an hour to achieve stabilization of the temperature.

For half cell SOFC aging work, a specific kind of alumina ceramic holder was designed and fabricated at Material Response Group, the Department of Engineering Science and Mechanics, Virginia Polytechnic Institute and State University. Its configuration is shown in Figure 2.3. Considering the shrinkage from casting the alumina ceramic and the different coefficients of thermal expansion between the half cell SOFCs and the alumina, a larger inner diameter of the holder was made. The internal supporting parts were designed with an air hole and a spider web surface to make sure the air flux was uninhibited.

The geometry of the holder was first machined from stainless steel, including the downside holder, upside holder, and internal supporters with a spider web surface. Then the assembly of the downside or upside holder with the internal supporter was separately dipped into silastic molding compound (T-2 base and curing agent from Essex Brownell Inc.) and left overnight to cure. These assemblies were then taken out of the silastic mold. Then we mixed precision castable alumina ceramic (RTC-60, Cotronics corp.) with water 100 to 8 parts by weight, then poured the ceramic mixture into the silastic mold and vibrated it to remove air bubbles. After curing overnight, the alumina parts of the holders were placed into the furnace to be held for 2 hours at 110 ^{o}C to remove excess water and then heated up to 1100 ^{o}C for 1 hour to get higher strength and possible maximum shrinkage.

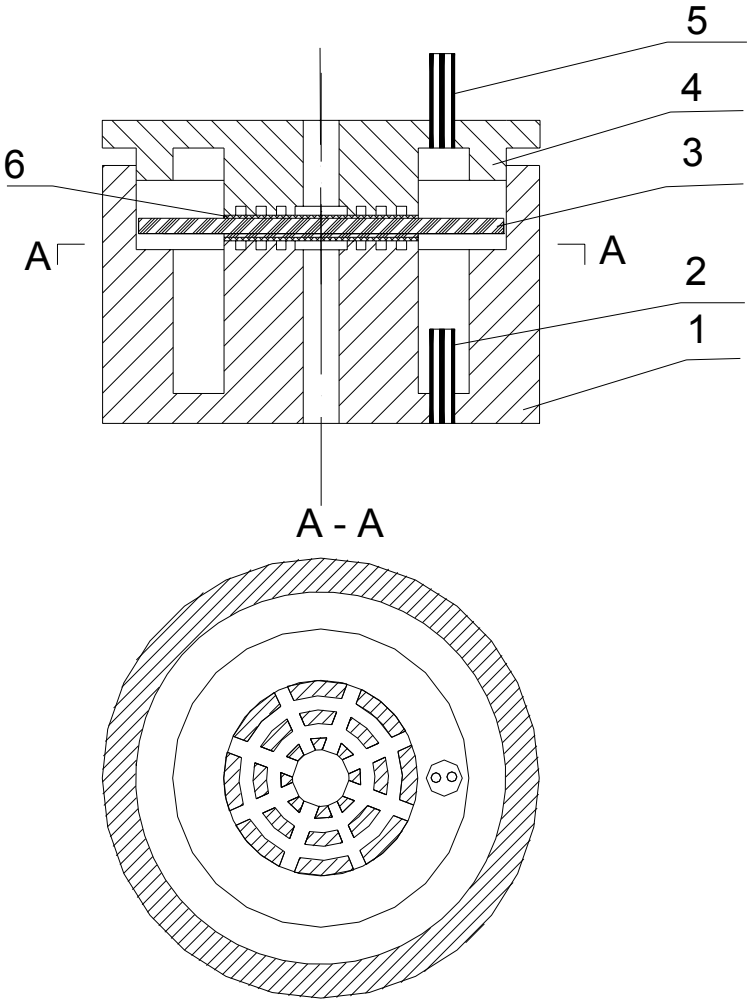

1) Downside holder, 2) two-hole ceramic tube, 3) half cell SOFC, 4) upside holder, 5) two-hole ceramic tube, 6) platinum paste and mesh

Figure 2.3. Half cell SOFC aging test holder.

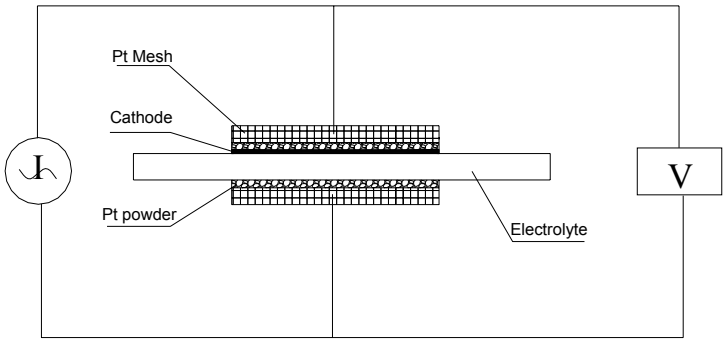

Figure 2.4. Half cell SOFC configuration.

The half cell SOFC was painted with platinum paste (lot#1070709, Structure Probe, Inc.) on both sides and covered by a set of platinum gauzes (100 mesh, 0.0762 mm diameter wire, 99.9%, Alfa Aesar) as current collectors. For DC sweep or AC impedance measurements, four-wire connections, as shown in Figure 2.4, were used to collect accurate readings. In the furnace, pure platinum wires of 0.381 mm (0.015 in) diameter were welded onto the platinum gauzes. The platinum leads coming out from the two-hole alumina ceramic tubes on the holders went together through 4-hole alumina ceramic tubes extending through the top of the furnace to lower the induction effect during high frequency impedance measurements. Outside the furnace, shielded wiring was used to decrease noise.

2.3 Mechanical properties measurements

2.3.1 Four-point bend test

Four-point bend tests were performed on the laminated interconnects and the electrolyte beams. An aluminum fixture as shown in Figure 2.5 that conforms

to ASTM C1161 specimen geometry B (40 mm support pin spacing, 20 mm load pin spacing) was fabricated at Material Response Group, the Department of Engineering Science and Mechanics, Virginia Polytechnic Institute and State University. The fixture was attached to platens in a screw-driven Instron test machine 4204 with a 1 kN load cell for all tests and the displacement rate was 1 mm/min for the interconnects and 0.2 mm/min for the electrolyte beams, respectively. Data acquisition (load and crosshead displacement) was computerized. Each kind of specimen was separated into two groups (in half) in order to evaluate the effect of long-term aging at 1000 ^{o}C on the material strength. The laminated interconnects and the electrolyte beams were aged at 1000 ^{o}C for 50 hours and 1000 hours, respectively. A total of 52 (50% 3-layer) interconnect beams and 14 electrolyte beams were tested.

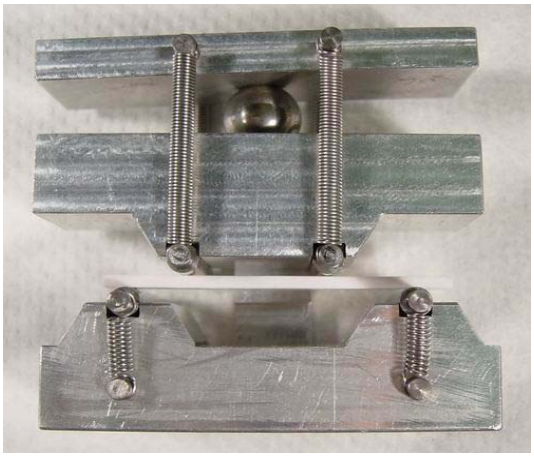

Figure 2.5. Four-point bend test fixture.

2.3.2 Ball/pressure on ring tests

2.3.2.1 Ball on ring test

The 23 mm diameter disks cut from damaged electrolyte plates, which were not tested in tension, were tested in a ball on ring test fixture as shown in Figure 2.6 (fabricated at Material Response Group, the Department of Engineering Science and Mechanics, Virginia Polytechnic Institute and State University). The support ring was 21 mm in diameter and the ball was 6.35 mm in diameter. The test fixture was attached to a tabletop mill. The load was applied through a hand crack with an attached digital displacement indicator and a 22 N (5 lbf) load cell with a peak detector was used to determine the peak (failure) load.

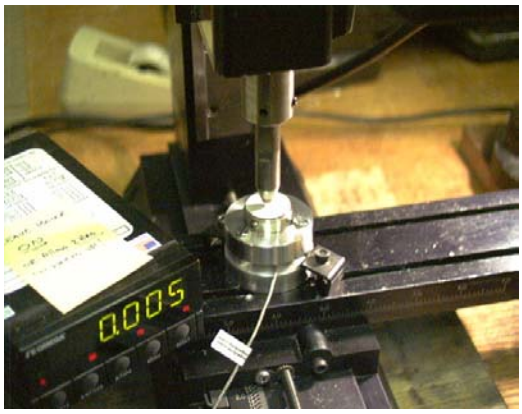

Figure 2.6. Ball on ring test fixture.

2.3.2.2 Pressure on ring test

The pressure on ring test of electrolyte disks was performed using a hydraulic tester as shown in Figure 2.7 and Figure 2.8 (fabricated at Material

Response Group, the Department of Engineering Science and Mechanics, Virginia Polytechnic Institute and State University).

An oil cylinder manually driven with a bolt was used to apply the hydraulic pressure on the disk, which was mounted on the support ring. An O-ring was placed between the pressurized surface of the disk and the oil chamber to make a seal. The O-ring was seated in the chamber with 1/3 of the diameter of the cross section top over the chamber. When the load was applied, the O-ring would deform and achieve a self-tight seal. Before it was seated on the support ring, the pressurized side of the electrolyte disk was covered by a piece of plastic tape to prevent contamination from the pressurizing oil and to keep the pieces together after testing. A linear variable differential transformer (LVDT, Omega LD400-1.5, ±1.5 mm stroke, 78 mV/V/mm sensitivity) was used to measure the displacement of the center of the disk. The load reading of the oil was from a pressure transducer (Omega PX792-200G5V, 200 psi range, 1-5 V output). The displacement and load were collected using a general data acquisition module in SOFCer (see 2.6).

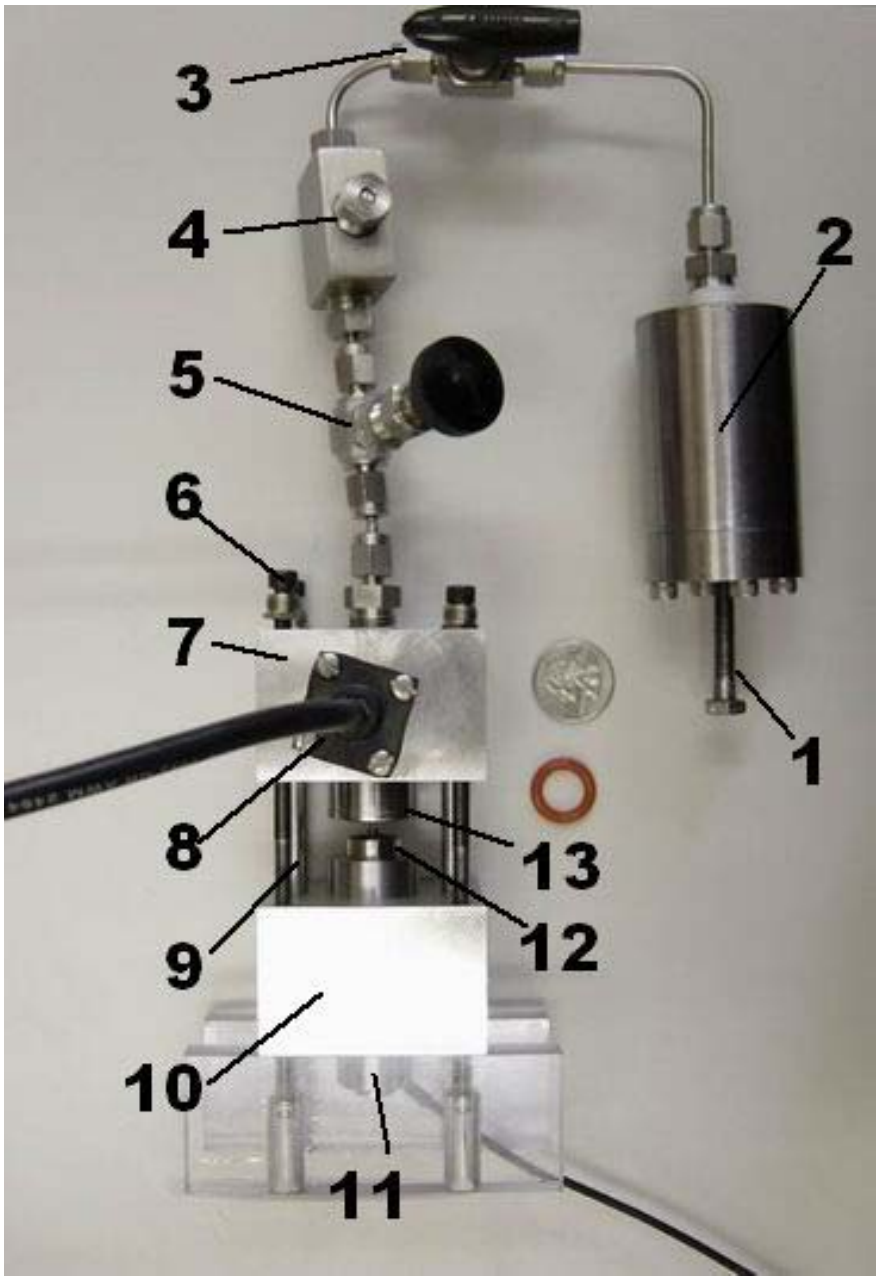

1) Pressure driving bolt, 2) oil cylinder, 3) ball valve, 4) pressure relief valve, 5) choke valve, 6) fasten bolts, 7) aluminum holder, 8) pressure transducer, 9) direction pins, 10) aluminum supporter, 11) LVDT, 12) support steel ring, 13) oil chamber.

Figure 2.7. Pressure on ring testing system.

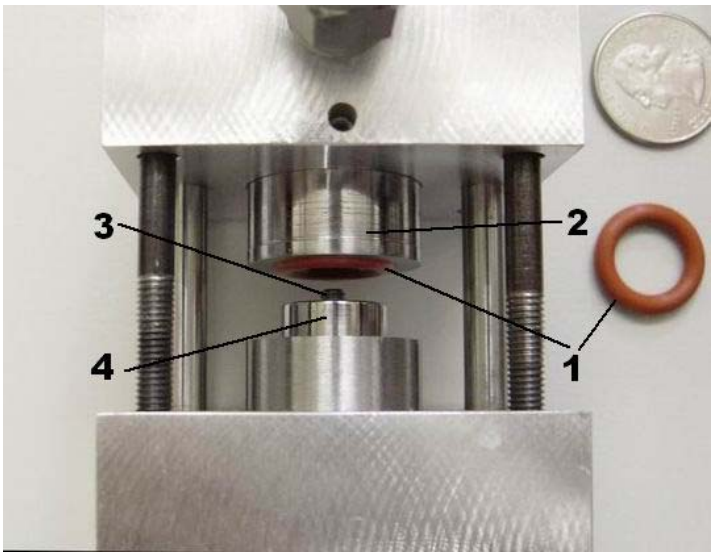

1) O-rings, 2) Oil chamber, 3) LVDT tip, 4) support steel ring.

Figure 2.8. Close view of the pressure on ring tester.

2.3.3 Plate tensile strength test

Due to the fact that the samples were about 200 μm thick, it was necessary to set up a special fixture to get the specimens mounted without creating large stress concentrations in the regions where the sample was fixed. The 100 mm square electrolyte plates were tested using the fixture designed by INEEL and manufactured by MTI. In the fixture, two rectangle adherents with 6.35 mm deep grooves were designed to hold the thin electrolyte in an Instron test machine. The thin film samples cleaned by acetone were bonded into the adherent grooves with Armstrong A-2 adhesive with activator. It took 12-16 hours to allow the epoxy to cure and after that the whole fixture with the brittle sample was mounted in the test frame of the Instron machine 4468 with the pin attachments. A crosshead displacement rate of 1.27 mm/min was used to perform the tensile tests. Both the displacement and the load were logged using a LabView monitoring program.

2.3.4 Microindentation test

A standard Vickers microindentation tester (Tukon 300, Instron Inc, Figure 2.9) was used to measure the hardness and the fracture toughness.

Figure 2.9. Vickers indentation tester, Tukon 300, Instron Inc.

Samples were mounted into a metallographic mount with epoxy and cured for at least 5-8 hours until the epoxy solidified. Then the surfaces of the specimens to be indented were polished successively by a Buehler grinder with 240, 400, 600 and 2400 grit grinding papers and lastly with 0.3 μm Al_2O_3 powder. During the polishing the surfaces were investigated under a microscope. Then the specimens were subjected to the indentation test using the standard Vickers microindentation tester whose Vickers diamond indenter has the angle between the opposite faces at the vertex of 136^o. Indentation load was applied with the

dwell time being 15 s. For each load, five indentation tests were made. The indents and the crack length measurements were conducted directly in the micro-hardness tester with the help of an optical instrument.

2.4 Electrochemical test

2.4.1 Chronoamperometry

Chronoamperometry is a type of DC method, where the source current or voltage is kept at constant level for a certain period of time and the voltage or current is measured as a function of time.

A SourceMeter, Keithley 2440 5A was used to conduct the chronoamperometry experiment. The SourceMeter can either source I and measure V or source V and measure I. In this study, in order to track changes of the half cell SOFCs over a long-term aging, source I and measure V was used for a period as long as 1000 hours at 1000 ^{o}C. During the aging process, the I-V curves were swept using the source meter from time to time.

Instrumental control and monitoring and data acquisition were automatically achieved using the SOFCer software, coded with Microsoft Visual Basic 6 programming language.

2.4.2 Electrochemical impedance spectroscopy

The kinetics of an electrochemical reaction is usually investigated using electrochemical impedance spectroscopy (EIS) (Bard and Faulkner 2001). The impedance Z is often plotted in a complex plane with minus the imaginary part along the ordinates and the real part along the axis of abscissas, called a Nyquist plot. In Figure 2.10, a Nyquist plot for a simple electrode is shown. Rs is the series resistance mainly ascribed to the electrolyte, Rp is the electrode

polarization resistance and C is the capacitance. If C is not a perfect capacitor a depressed arc will appear.

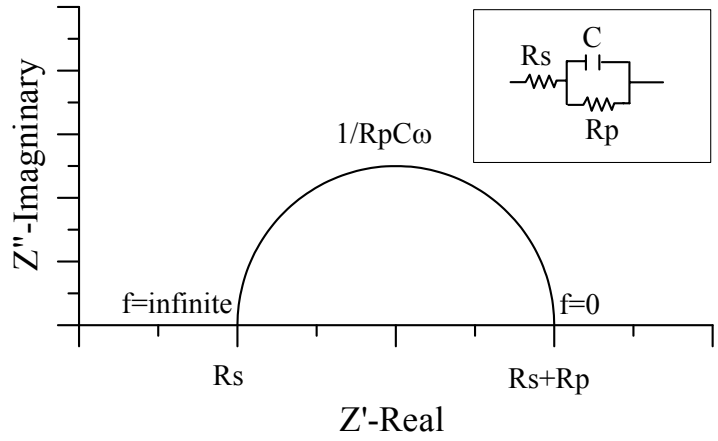

Figure 2.10. Nyquist plot for a simple RC circuit of an electrode.

A Solartron SI-1260 impedance gain-phase analyzer with a SI-1287 electrochemical interface and imbedded software Zplot was used to perform the impedance measurement for the half cell SOFC. Complex electrode reaction happened in the SOFC system from the absorption and diffusion of gases and charge transfer, and the specific equivalent circuit for this case will be discussed in the following chapter.

2.4.3 Experimental details

Two half cell SOFCs were aged in air without current at 1000 ^{o}C for 935 hours and 1000 hours, respectively. Another two half cell SOFCs were driven continually with 1 A constant current load for 1000 hours at 1000 ^{o}C. A third half cell SOFC was aged in air without current load for the first 500 hours and with 1

A current load for the next 500 hours at 1000 ^{o}C. Some of these SOFCs were performed with I-V sweep tests and EIS measurements from time to time.

2.5 Microstructural investigation and chemical analysis

Scanning electron microscopy (SEM) and energy dispersive X-ray spectrometry (EDS) were taken in a Leo 1400 instrument with an EDS integration. Brunauer-Emmett-Teller (B.E.T.) adsorption measurements using a Sorptomatic 1990 were performed to study the pore size and distribution of the porous cathode on the half cell SOFC before and after aging. X-ray diffraction (XRD) was used to detect chemical products on the cathode surface after aging.

2.6 Professional DAQ and control software

2.6.1 Introduction of SOFCer (version 2.6)

During long-term experiments, in order to monitor and acquire the experimental data and perform some necessary test actions automatically from time to time, such as an I-V curve sweep, it was necessary to program a proper instrumental control and data acquisition software. Using Microsoft Visual Basic 6.0 (Microsoft 1998), based on the NI Measurement Studio 6 (National-Instruments 2001) and IEEE-488.2 (GPIB 488.1) protocol, a fuel cell DAQ and control software named SOFCer was programmed. The screen shots are shown as in Figure 2.11 and Figure 2.12. The SOFCer v2.3 has been used successfully in a tubular solid oxide fuel cell durability test fed with H_2 as long as up to 440 hours at the Connecticut Global Fuel Cell Center (Du *et al*. 2003). The most recent version of the SOFCer software is 2.6.

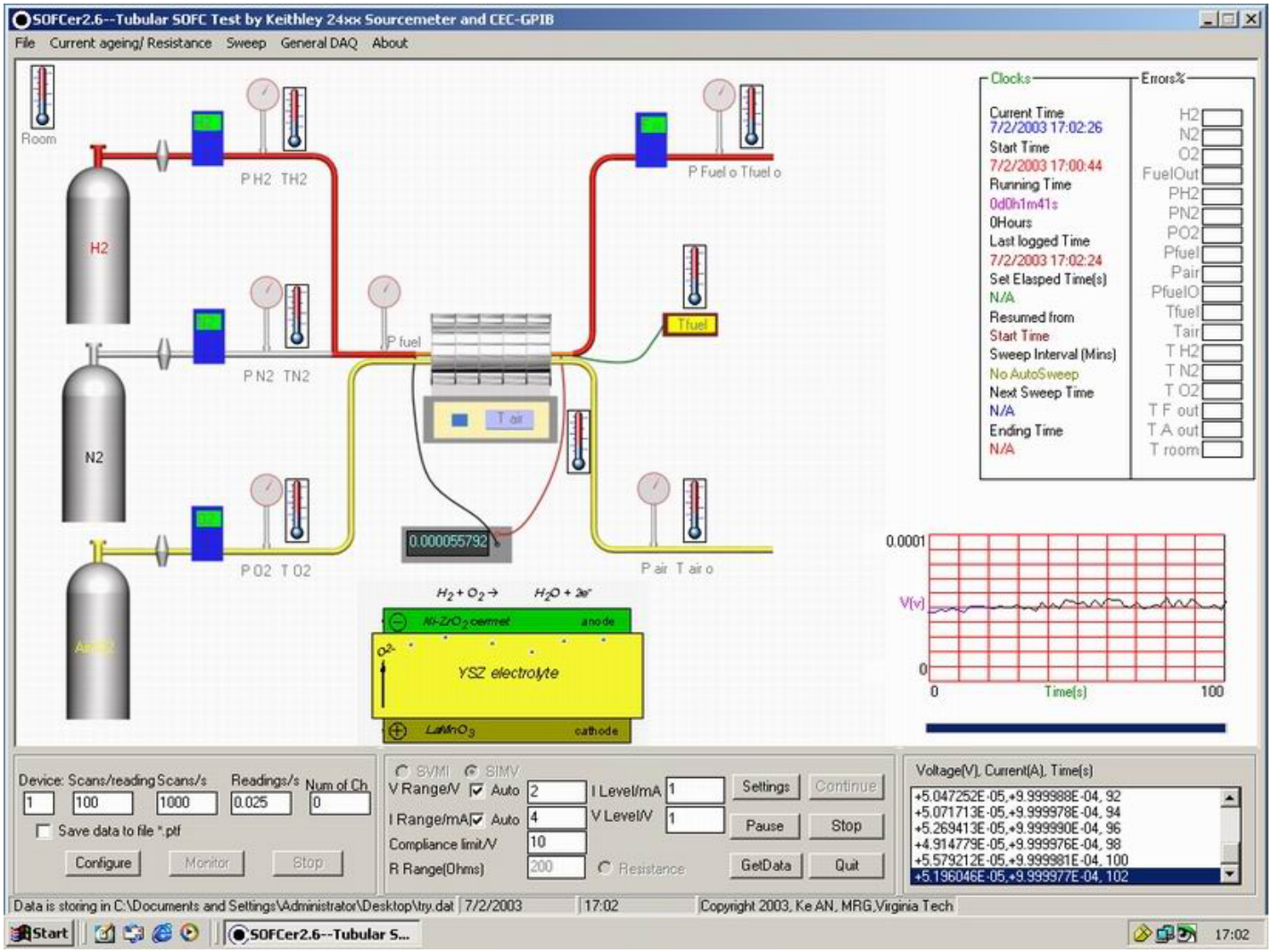

Figure 2.11. Screen Shot of the fuel cell DAQ and control software SOFCer.

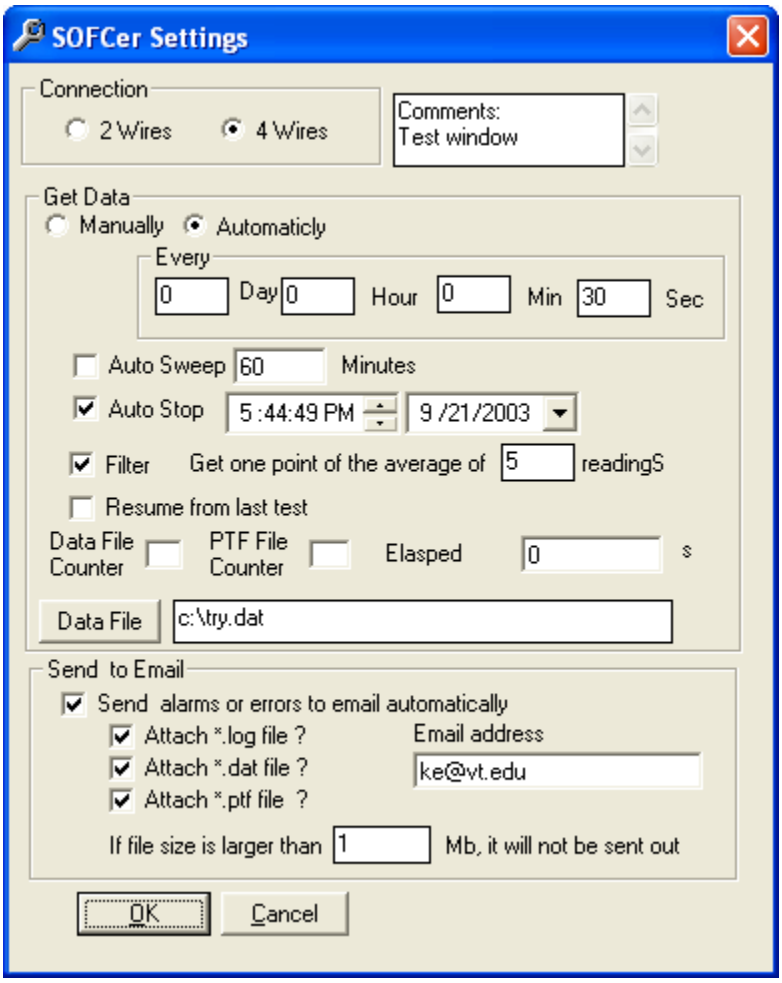

Figure 2.12. Settings dialog of SOFCer.

The key features of SOFCer 2.6 are listed below:

- Continually source I & measure V, source V & measure I and measure resistance.
- Analog or digital input or output.
- Automatically/manually data acquisition.
- Automatically/manually I-V sweep at specified time.
- Automatically start/stop and resume test as scheduled.
- Automatically create data series by size.
- Automatically send out data to specified email addresses.
- Temperature, flow rate, and pressure *etc*. experimental parameters monitor and alarm action.

- Weak signal acquisition.
- Operation log and errors report.
- Friendly and simulating operation interface.
- Remote controllable.
- Support NI/Keithley GPIB, NI DAQ interface and NI SCXI.
- General multi-channel DAQ

Most of the options can be set in the settings dialog window (Figure 2.12). The SOFCer software works not only for SOFC performance testing, but also for general fuel cell study. Programming of some features will be discussed below.

2.6.2 Programming languages

Microsoft Visual Basic 6.0 (VB6) is a kind of objected-oriented advanced programming language. Compared to other programming environments, VB6 has the advantages of easily creating Windows style interfaces and of being a fast programming environment. The interface of SOFCer was built up with standard controls, such as forms, text boxes, option buttons, labels and command buttons. Some special functions were programmed with ActiveX controls, for instance, Microsoft Common Dialog 6.0 and Microsoft MAPI controls 6.0 *etc*. Those controls can respond to Windows events individually, such as a mouse click and keyboard input. National Instruments (NI) Measurement Studio 6 has a set of DAQ ActiveX controls for VB6. With them the general DAQ function could be done. Through the GPIB interface, under GIPB or SCPI protocols and communicating with low-level dynamic link library (DLL) of the device drivers, the instrument operations were made.

2.6.3 Data acquisition programming

In a fuel cell performance experiment, many signals of experimental parameters need to be monitored or acquired, such as temperature, pressure and flux *etc*. This is done with DAQ devices, such as NI 16-MIO-XE DAQ with a BNC board, and low-level communication ActiveX controls used in the SOFCer.

Weak signals (thermo couple) from an SCXI module can be acquired through channel 0 of the device by hooking it up to the BNC board. In the VB6 development environment, the ActiveX DAQ control CWDAQ.OCX from NI Measurement Studio 6.0 must be added to the components panel. The sample code of analog input with CWDAQ.OCX is listed in List 2.1 (" ' " is the symbol of comment). CWAI* is the analog input module in CWDAQ.OCX.

List 2.1. DAQ sample code in the SOFCer.

```
==================================================

Private Sub Cmdmonitor_Click()

……

' Check the sampling rate to make sure it is compatible to the frequency
' range of the DAQ device
If GetData.AutoSweep = True Then
   If FrequencyNumEdit.Text < 0.016 Or FrequencyNumEdit.Text > 1
   Then
      MsgBox "0.016<frequency<1",  , "Wrong Number"
      Exit Sub
   End If
End If

' Set the number of channels to the device.
CWAI1.Device = DeviceNumEdit.Text
' Clear the channel strings of the device.
CWAI1.Channels.RemoveAll
' Add channel string to the device.
   For i = 0 To CheckItems.count - 1
         If CheckItems(i).value = 1 Then
                  CWAI1.Channels.Add ChannelStringTextBox(i).Text
         End If
   Next

CWAI1.StopCondition.Type = 0
' Set number of scans per reading
CWAI1.NScans = NScansNumEdit.Text
' Set scan rate
CWAI1.ScanClock.Frequency = TxtScanRate.Text
```

```
' Confirm the configures and start the device
CWAI1.Configure
CWAI1.Start
……

End Sub
```

==========

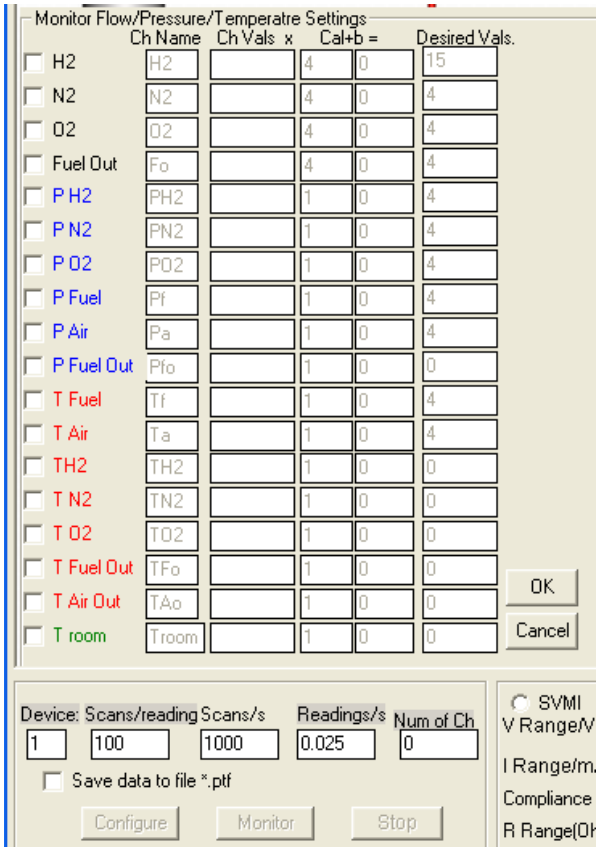

Figure 2.13. DAQ control panel of SOFCer.

Based on this kind of code the DAQ control panel is shown as running in Figure 2.13. The DAQ function can work with the virtual channels from LabView, by just inputting the virtual channel name into 'Ch name' boxes. After clicking the 'Monitor' button, this window will hide and the data acquired will be displayed where the device is virtually on the front panel. Data acquisition at a

specific time is activated and controlled by a public timer control. Other functions, such as analog output and digital input/output could be achieved with CWDAQ.OCX.

2.6.4 Instrument control programming

Instrument control to the 2440 SourceMeter is achieved with GPIB interface and IEEE-488.2/488.1 bus.

IEEE-488 bus is a communication system between 2 or more devices. A computer is always used in the system as a controller to supervise the communication of those devices. Each device has a unique address in this system. The 2440 SourceMeter can support two GPIB protocols, SCPI and IEEE-488.1. The latter has faster speed. When IEEE-488.1 is selected, the SCPI commands are still used to program the SourceMeter.

The SCPI command is written in terms of strings. For instance, ":CONFigure:<function>" means to configure the SourceMeter for measurements on specified function. The first 4 capital characters are necessary. In the SOFCer software, the subroutine MyGPIBSend/MyGPIBRead is used to call the low-level subroutine in the GPIB driver, which transfers the SCPI command to the listener of the SourceMeter. The SOFCer software supports two kinds of popular GPIB cards, NI-GPIB and Keithley-CEC. In the Visual Basic project of SOFCer, the modules, Ieeevb.bas and vbib-32.bas have to be added to declare the low-level subroutines in Ieee32m.dll and Gpib-32.dll GPIB hardware drivers for Keithley-CEC and NI-GPIB cards, respectively. List 2.2 shows a resistance measurement action sent to the SourceMeter and List 2.3 gives the proper action to the right GPIB card.

List 2.2. Sample code of control the SourceMeter.

```
==========================================================

Private Sub StartTestRes()
'Reset the SourceMeter
ComString = "*RST"
MyGPIBSend ComString, status%

'Configure to perform resistance measurement
MyGPIBSend ":TRAC:POIN 500", status%  'SET BUFFERSIZE
ComString = ":SENS:FUNC 'RES'"
MyGPIBSend ComString, status%
ComString = ":SENS:RES:RANG " + TxtResRange.Text
MyGPIBSend ComString, status%
ComString = ":SENS:RES:MODE AUTO"
MyGPIBSend ComString, status%
'Connection settings
If GetData.Con2or4wires = 2 Then
ComString = ":SYST:RSEN OFF"
MyGPIBSend ComString, status%
ElseIf GetData.Con2or4wires = 4 Then
ComString = ":SYST:RSEN ON"
MyGPIBSend ComString, status%
End If

'Turn on the SourceMeter
ComString = ":OUTP ON;SYST:TIME:RES"
MyGPIBSend ComString, status%
Call OutputLog("Output ON ", "Running...")
Call Fetchdata
End Sub

==========================================================
```

List 2.3. Code to call the proper GPIB card.

```
==========================================================

'Subroutine to send SCPI commands
Sub MyGPIBSend(cmd As String, status%)
If CardType = "NI" Then
        ibwrt DEV, cmd
```

```
ElseIf CardType = "CEC" Then
        sendKeithley GPIBCardAddress, cmd, status
Else
End If
End Sub

'Subroutine to acquire readings
Sub MyGPIBRead(data As String, status%)
If CardType = "NI" Then
        data$ = Space$(100)
        ibrd DEV, data$
ElseIf CardType = "CEC" Then
        enterKeithley data$, 300, Length%, GPIBCardAddress, status%
Else
End If
End Sub
```

==========

2.6.5 Emailing data programming

If the PC is connected to the Internet, for safety and other reasons, a short message or stored data files can be sent out through email. This would be useful for long-term operation. To achieve this feature, Microsoft MAPI controls 6.0 are used. If in the settings window (Figure 2.12), the send out email option is checked on, and the file option is on too, the selected file will be attached to the email message to be sent out automatically. The code is shown in List 2.4.

List 2.4. Code for Internet emailing.

==========

```
Private Sub sendemail (EmailAddress As String, Subject As String, _&
Message As String)
With GetData
On Error Resume Next
 MAPIS1.SignOn
 MAPIM1.SessionID = MAPIS1.SessionID
 MAPIM1.Compose
 MAPIM1.RecipAddress = EmailAddress
```

```
MAPIM1.MsgSubject = Subject
MAPIM1.MsgNoteText = Message

' Check file length and send out option
If FileLen(.TestLogName) < .emailFileSizeLimit * 1000000 And _&
.AttLogFile Then
MAPIM1.AttachmentIndex = 0
MAPIM1.AttachmentPathName = .TestLogName
End If
If FileLen(.TestFileName) < .emailFileSizeLimit * 1000000 And
.AttDatFile = 1 Then
MAPIM1.AttachmentIndex = MAPIM1.AttachmentIndex + 1
MAPIM1.AttachmentPathName = .TestFileName
End If
If .AttptfFile = 1 Then
If FileLen(.MonitorFileName) < .emailFileSizeLimit * 1000000 Then
MAPIM1.AttachmentIndex = MAPIM1.AttachmentIndex + 1
MAPIM1.AttachmentPathName = .MonitorFileName
End If
End If

MAPIM1.send
MAPIS1.SignOff
End With
End Sub
```

==========

2.7 Conclusions

The experimental test methodologies, including plate tensile, ball on ring, pressure on ring and microindentation are discussed. A pressure on ring tester for thin film material biaxial fracture strength was constructed.

The professional DAQ software SOFCer 2.6 for fuel cell long-term operation is utilized based on the Visual Basic 6.0 and the NI Development Studio. In addition to the basic DAQ functions, the SOFCer 2.6 has many other advantages such as simulation graphics, instrumental control, experiment task execution and internet remote communication, *etc*.

CHAPTER 3
ANODE AND INTERCONNECT

In this chapter, results are reported from aging tests performed on the anode and the interconnect materials. Microindentation tests were used to study long-term aging effects on the hardness of the anode and interconnect. Four-point bend tests were performed on the 3-layer and 5-layer laminated interconnect material before and after 1000 ^{o}C aging in air. Weibull analysis was conducted for the four-point bend results.

3.1 Experiments

3.1.1 Aging

The anode was aged at 1000 ^{o}C in air for 1000 hours. The ends of the anode beam were painted with platinum paste and then coiled with platinum wires. Its resistance was measured using the 2440 SourceMeter. After aging, one piece of the anode was reduced in H_2 for 2 hours at 800 ^{o}C.

Twenty-two of the total 52 (50% 3 layers) interconnect samples were aged for 50 hours at 1000 ^{o}C in air before bending. Several pieces of sample from 3LI-001 were aged for 1000 hours at 1000 ^{o}C in air.

3.1.2 Microindentation

The hardness of the materials was evaluated in the microindentation tester. SEMs were taken from the indented materials.

The hardness of the anode before and after aging was evaluated by indenting specific agglomerations in it. The hardness evolution of long-term aging of the interconnect material was investigated. After aging, the aged sample and unaged sample were polished at same time. The hardness of both samples was measured.

3.1.3 Four-point bend

Table 3.1. Dimensions and test results of the unaged interconnects.

Specimen	Thickness (mm)	Width (mm)	Failure Load (N)	Failure stress (MPa)	Delaminated
3LI-001	1.10	4.00	60.6	375.6	Y
3LI-002	1.09	3.96	119.3	760.7	
3LI-003	1.16	3.91	109.2	622.7	
3LI-004	1.15	3.90	59.8	347.8	
3LI-005	1.09	3.96	117.1	746.7	
3LI-006	1.11	3.98	106.3	650.3	
3LI-007	1.13	3.99	102.6	604.1	
3LI-008	1.17	3.95	130.6	724.6	
3LI-009	1.18	3.94	52.9	289.3	
3LI-010	1.17	3.94	113.2	629.7	
3LI-011	1.15	3.93	143.6	828.9	
3LI-012	1.17	3.94	106.6	592.9	
3LI-013	1.09	3.99	66.8	422.7	
3LI-014	1.09	4.01	138.3	870.9	
3LI-015	1.17	3.91	116.4	652.4	
5LI-001	1.88	3.95	145.5	312.7	
5LI-002	1.88	3.94	162.8	350.7	
5LI-003	1.88	3.98	149.4	318.6	
5LI-004	1.87	3.95	230.3	500.2	
5LI-005	1.86	3.92	163.9	362.6	
5LI-006	1.89	3.96	195.4	414.4	
5LI-007	1.89	3.95	297.3	632.1	
5LI-008	1.88	3.98	156.2	333.1	Y
5LI-009	1.91	4.02	264.6	541.3	
5LI-010	1.89	3.96	137.8	292.2	
5LI-011	1.90	3.97	227.5	476.2	
5LI-012	1.93	3.99	160.9	324.8	
5LI-013	1.90	3.92	70.3	149.0	Y
5LI-014	1.88	3.94	193.2	416.2	
5LI-015	1.91	3.93	185.2	387.5	

Total 52 samples (50% 3 layers) were tested in the ASTM standard four-point bend test fixture. SEM analysis was also done with some samples. The dimension of each specimen was measured and is listed in Table 3.1 and Table 3.2.

Table 3.2. Dimensions and test results of the aged interconnects.

Specimen	Thickness (mm)	Width (mm)	Failure Load (N)	Failure stress (MPa)	Delaminated
3LI-021	1.17	3.91	130.8	733.1	
3LI-022	1.14	3.96	93.7	546.2	
3LI-023	1.14	3.96	68.7	400.3	
3LI-024	1.17	3.92	113.7	635.7	
3LI-025	1.17	3.94	90.9	505.6	
3LI-026	1.13	3.95	68.0	404.5	
3LI-027	1.13	3.99	49.3	290.3	
3LI-028	1.20	3.91	116.7	621.8	
3LI-029	1.15	3.92	119.0	688.6	
3LI-030	1.10	3.96	124.7	780.7	
3LI-031	1.16	3.90	144.6	826.6	
5LI-021	1.92	3.96	158.7	326.1	Y
5LI-022	1.91	3.94	154.4	322.3	
5LI-023	1.91	3.94	149.6	3122	
5LI-024	1.91	3.96	130.2	270.4	
5LI-025	1.91	3.94	108.8	227.1	
5LI-026	1.90	3.89	148.8	317.9	Y
5LI-027	1.93	3.94	184.7	377.9	Y
5LI-028	1.92	3.98	84.3	172.4	
5LI-029	1.88	3.96	113.7	243.7	
5LI-030	1.87	3.92	123.5	270.3	
5LI-031	1.90	3.96	63.1	132.4	Y

3.2 Experiment results

3.2.1 SEM and Chemical analysis of anode

The anode beams were used to determine the hardness evolution during long-term aging. SEM photos in Figure 3.1 show the microstructure of the polished surface of the porous anode before aging. At 200 X, it is easy to see

some agglomerations in the porous anode. A close view at 10 kX on one of the agglomerations was taken. The scratches on the surface are due to the polish grinding. From the photo it is seen that the anode consists of two phases, dark and light ones, suggesting it is a composite electrode. The chemical elements were tested using EDS, and the EDS atomic concentration of the elements is shown in Figure 3.2. Due to the fact that the highest resolution of the EDS is around 1×1 μm, we cannot tell exactly what the atomic concentrations are in the phases. However, it is known that there are three kinds of atoms, Ni, Ce, and O, in the porous anode and that in the light grains the Ce is more abundant than in the dark grains. Ceria-based materials are used as electrolytes in intermediate temperature SOFCs (Milliken *et al*. 1999). The observed sample may be a Ni/ceria-based mix conducting composite anode.

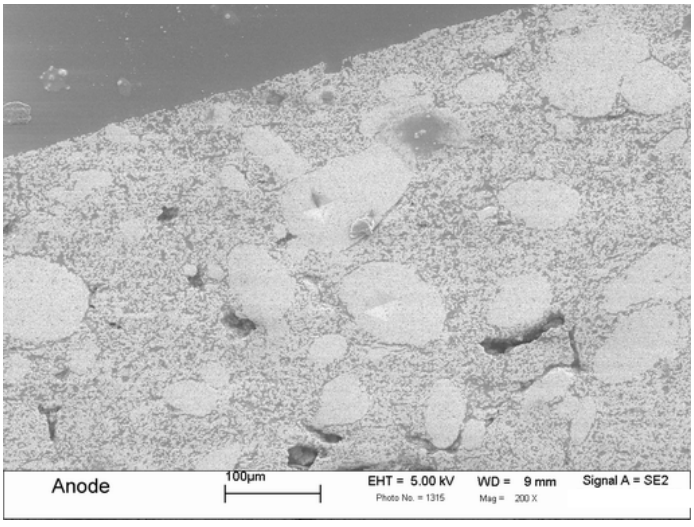

a) At 200X

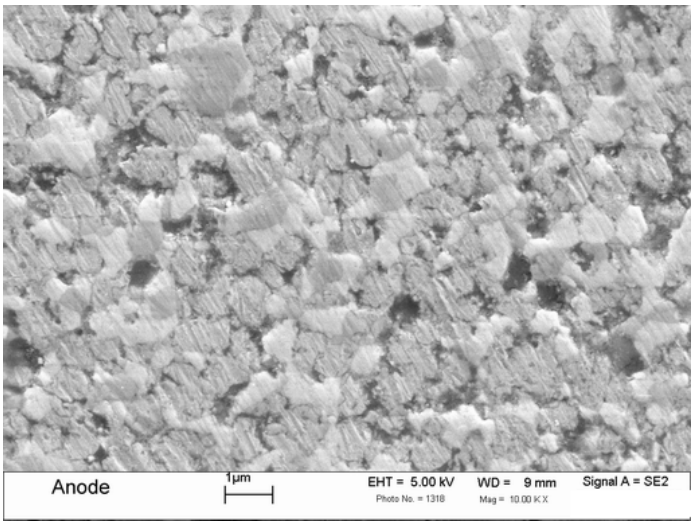

b) At 10kX

Figure 3.1. SEM of the anode at 200X and 10kX.

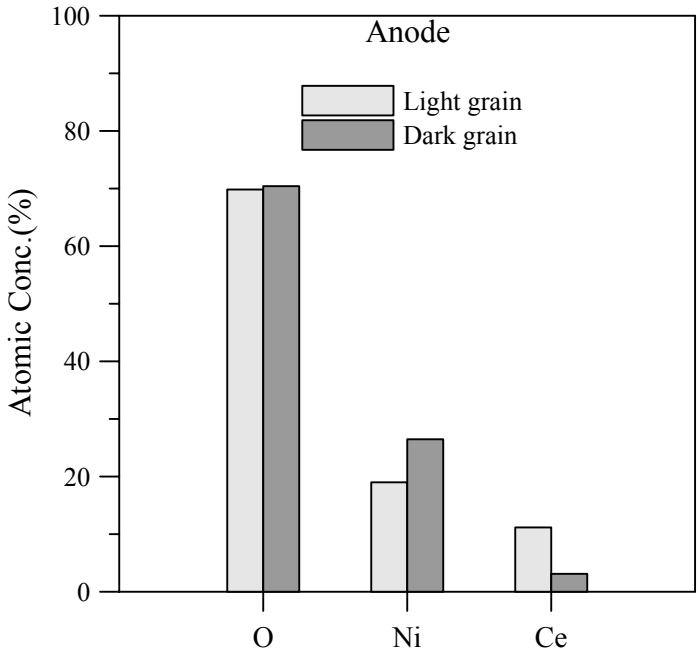

Figure 3.2. EDS spectrum and atomic concentration of anode elements.

3.2.2 Aging evolution of anode

The change of resistance with aging time is shown in Figure 3.3 and the resistance at different temperatures before and after aging is shown in Figure 3.4.

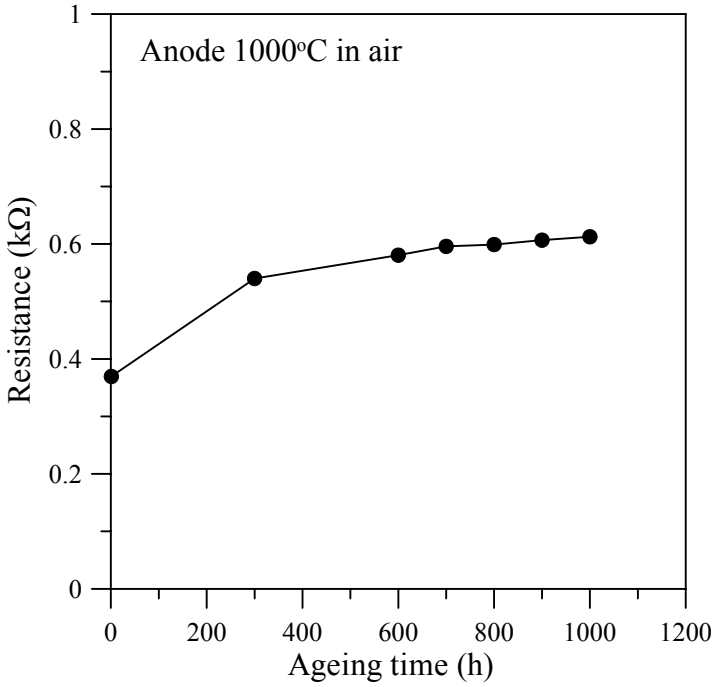

Figure 3.3. Resistance evolution of the anode in air.

From Figure 3.3, the resistance of the anode kept increasing along with the aging time but with a decreasing rate. In the initial 300 hours (maybe less, the refined data acquisition was not performed), the resistance increased 60% from 0.37 kΩ to 0.54 kΩ. When aging at 1000 ^{o}C, the Ni element in the reduced anode would be oxidized and the anode would lose some electronic conductivity. However the oxidation would be finished in a short time compared to the 1000 hours aging, which means the resistance change later was not the result of the oxidation. In Figure 3.4, when the temperature was increased, the resistance of the

aged Ce based anode decreased, which strictly follows the phenomenon of high temperature ionic conductors. However before aging, the resistance of the anode increased a little after the temperature was increased to 800 ^{o}C. This is because of the oxidation of Ni in the anode. It is easy to see that, after aging, the combination effect of the oxidation of Ni and the long-term aging leads to an increase of the resistance.

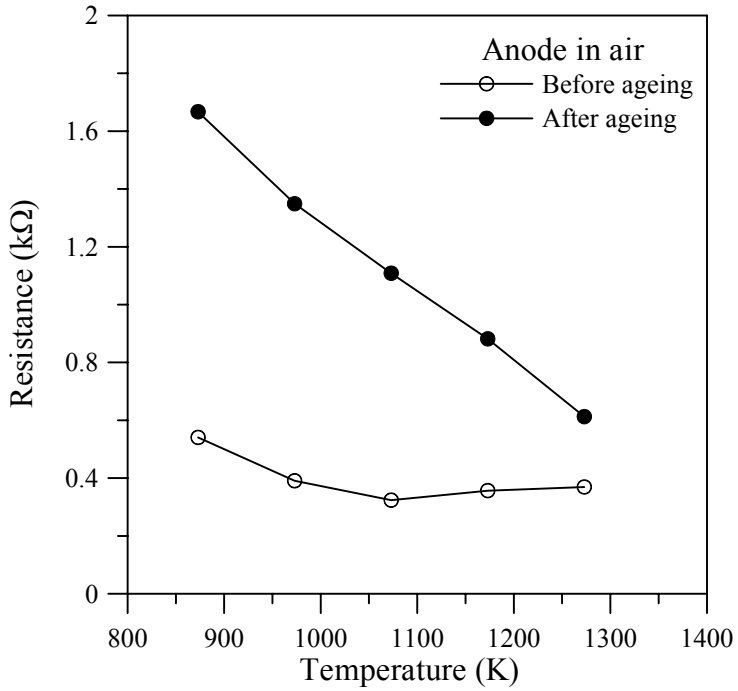

Figure 3.4. Resistance of the anode at different temperatures.

3.2.3 Microindentation test

3.2.3.1 Hardness of evolution of anode

Hardness measurements were performed on the area of those agglomerations mentioned earlier on each kind of anode. In Figure 3.5, the

indented areas are shown. After oxidation, the aged anode became denser and had less pores than the anode as received. The changes that happened were not reversible though the anode was reduced in H_2. It should be mentioned that at higher magnification the two phases are still viewable. The Vickers hardness of an indented material was found using the expression below,

$$HV=1.8544P/a^2 \tag{3.1}$$

where, P is the indentation load and a is diagonal length of the indent. The hardness results are given in Figure 3.6. Because of the dimension of the agglomerations, the maximum load was 200 g. The hardness of the aged anode had an average value of 5.70±0.88 GPa, higher than that of the anode as received, which had an average value of 2.91±0.51 GPa. However after it was reduced, the aged anode had a lower hardness with an average value of 1.76±0.26 GPa. The microstructural change from the oxidation of the Ni and long-term aging may be the reason for the observed hardness changes.

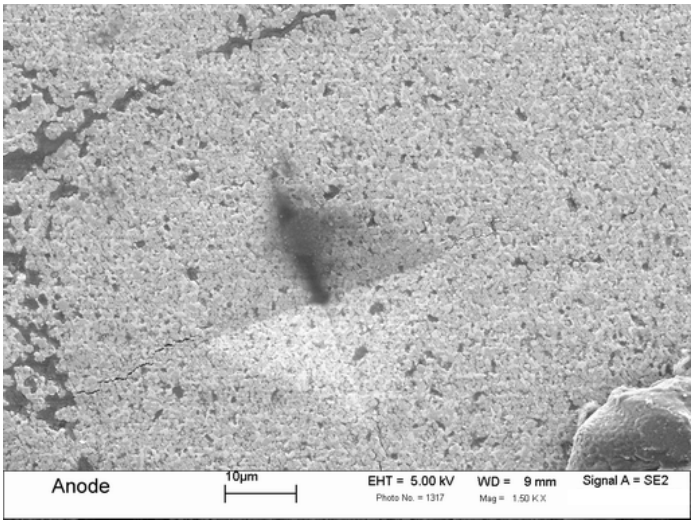

a) Anode as received

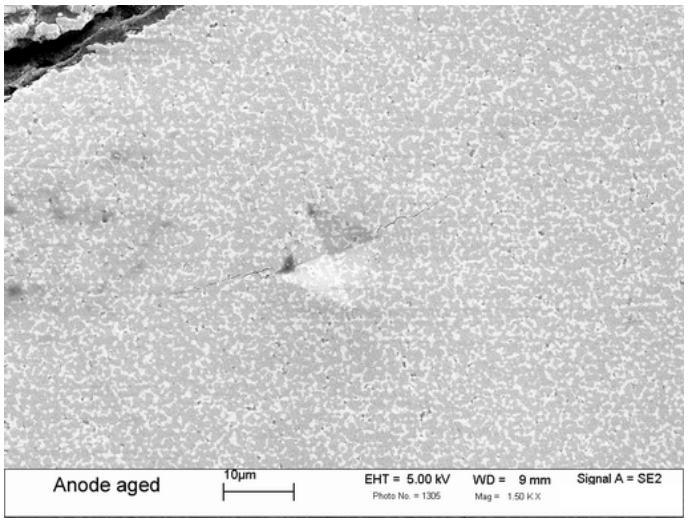

b) Anode aged

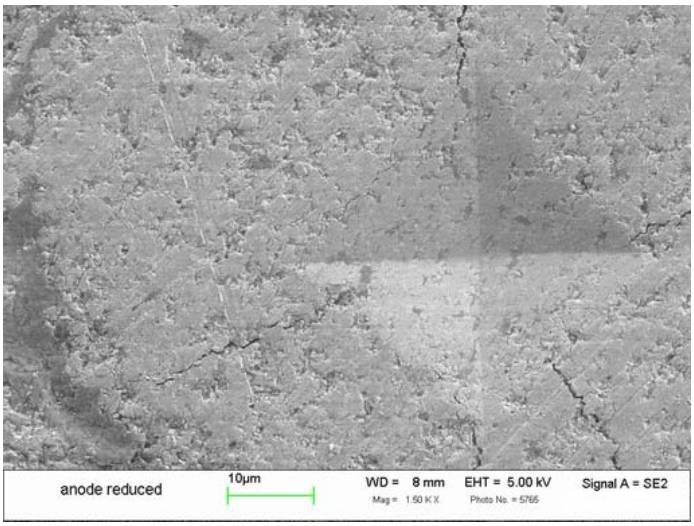

c) Anode reduced after aging

Figure 3.5. Microstructural evolution and hardness indents on the anodes

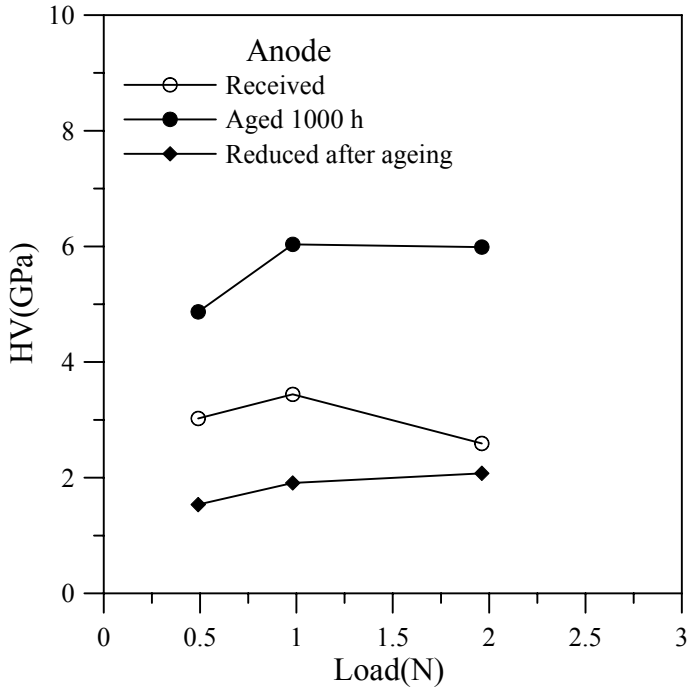

Figure 3.6. Vickers hardness changes of the anodes.

3.2.3.2 Hardness of interconnect

To evaluate the continuity of the laminated specimen, the cross section of the 3-layer section was polished and then was placed in the microindentation tester with the indentation surface rotated counterclockwise through a small angle. The specimen was moved forward slightly along a straight line after each indentation. In this way, under the load of 800 g, there was enough length for the indents along a line with a diagonal length of around 34 μm.

The indentation results are shown in Figure 3.7. A total of 120 indents were made. 116 of them were successful. There were about 4 unsuccessful indents due to the proximity of the boundaries. The thickness of the sample was about 1.1mm, so the distance between two indents' center points was about 1.1 mm/120=9.17 μm. Therefore the interfaces between each laminate should be covered by several indents. From the hardness results, there was not much

difference from edge to edge, even across the interface area. The average value of hardness was about 12.54±0.20 GPa. SEM photos in Figure 3.8 show the interface and the indents. There was discontinuous delamination at the interface found on the polished surface. Even when the indent was on the interface, corner cracks due to the interface were not visible.

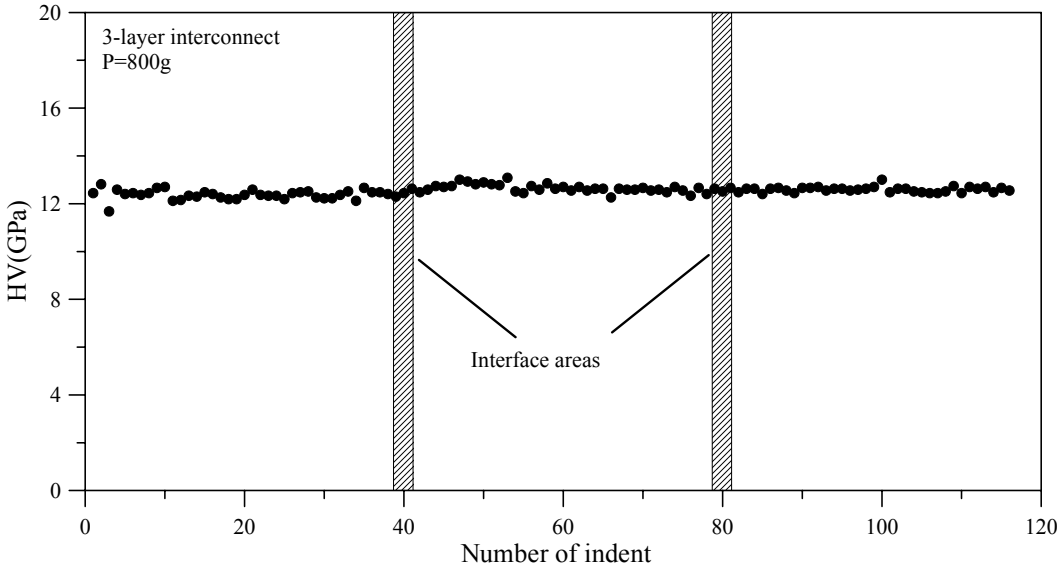

Figure 3.7. Microindentation on the cross section of the 3-layer interconnect.

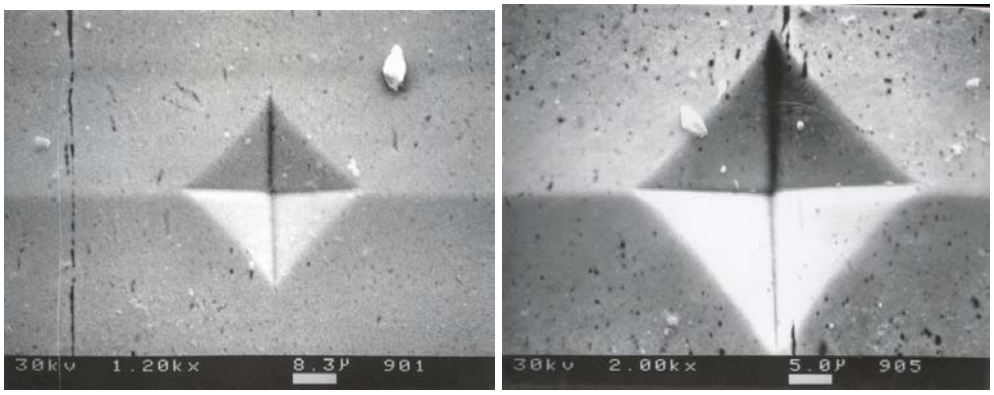

a) Indent close to the interface. b) Indent on the interface.

Figure 3.8. SEM of indentations around the interface of the 3-layer interconnect.

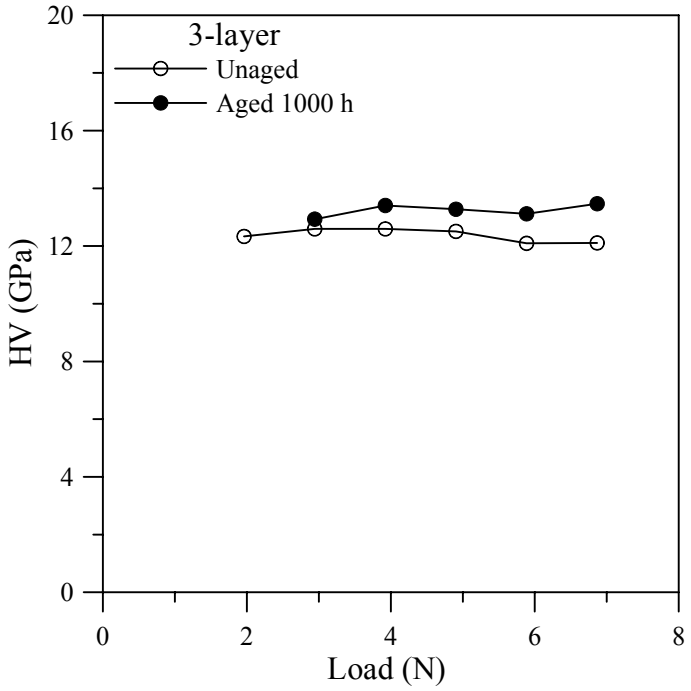

Figure 3.9. Hardness changes of the interconnect after long-term aging.

After 1000 hours ageing, the hardness evolution of the interconnect material is plotted in Figure 3.9. The long-term aging has some effect on the hardness with an average value of 12.37±0.23 GPa before aging, increasing to an average value of 13.24±0.22 GPa after aging, which is about a 7% change.

3.2.4 Four-point bend

In Figure 3.10, sample curves of the load vs. displacement data for these interconnect tests are given. The measured strengths and failure loads for these unaged and aged specimens are given in Table 3.1 and Table 3.2, respectively. Since the displacements at failure were less than the specimen thickness, linear stress analysis was used to determine the failure stresses. The stress can be found from the expression below.

$$\sigma_{\max} = \frac{My}{I} = \frac{\left(\frac{P}{2}\frac{L_0 - L_i}{2}\right)\frac{h}{2}}{\frac{bh^3}{12}} = \frac{3P\left(L_o - L_i\right)}{bh^2} \tag{3.2}$$

where L_o and L_i are the inner and outer spans of the bend fixture, P is the peak load, and b and h are the width and thickness of the specimen.

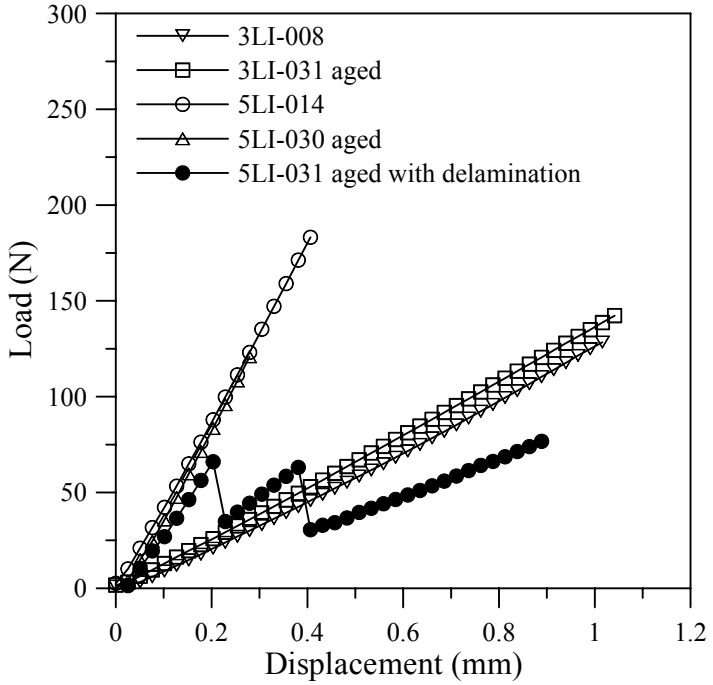

Figure 3.10. Load vs. crosshead displacement curves for interconnects testing.

SEM photos were taken for failure surfaces of unaged and aged interconnects and are shown in Figure 3.11 and Figure 3.12, respectively. In Figure 3.13, the interface on the polished edge is shown.

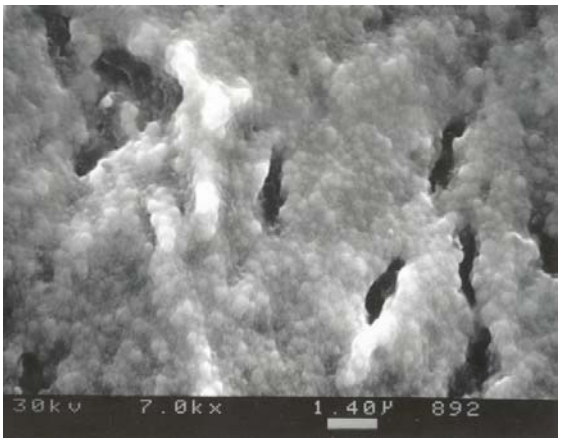

a) View of the edge

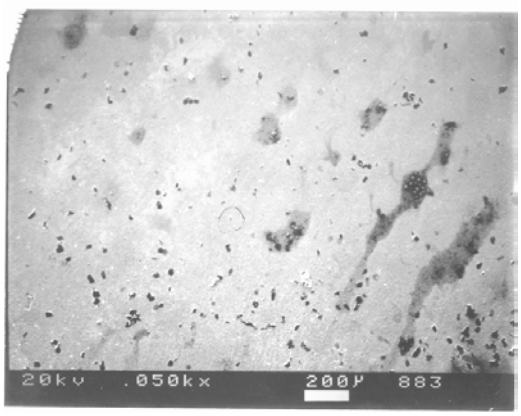

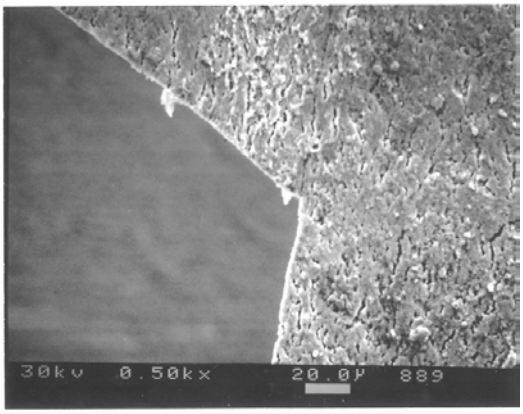

b) Delamination surface c) View of fracture surface edge.

Figure 3.11. Failure surfaces of the unaged interconnect.

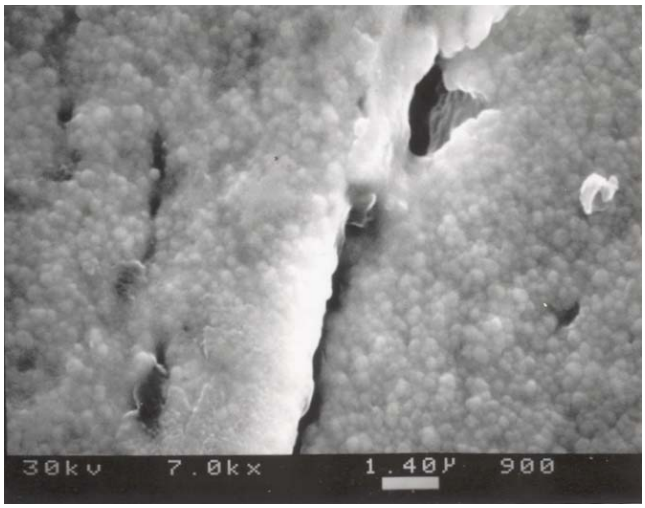

a) View of the edge

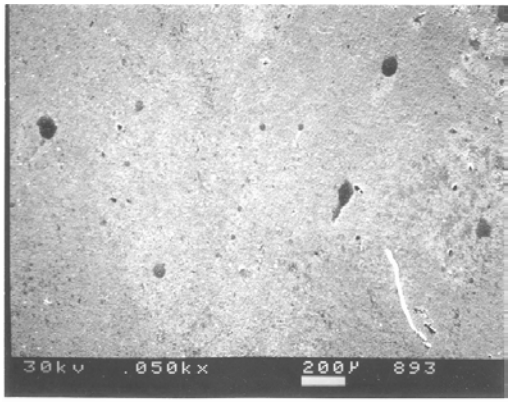

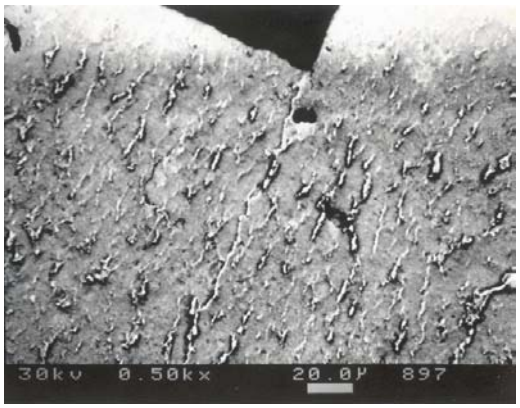

b) Delamination surface. c) View of fracture surface edge.

Figure 3.12. Failure surfaces of the aged interconnect.

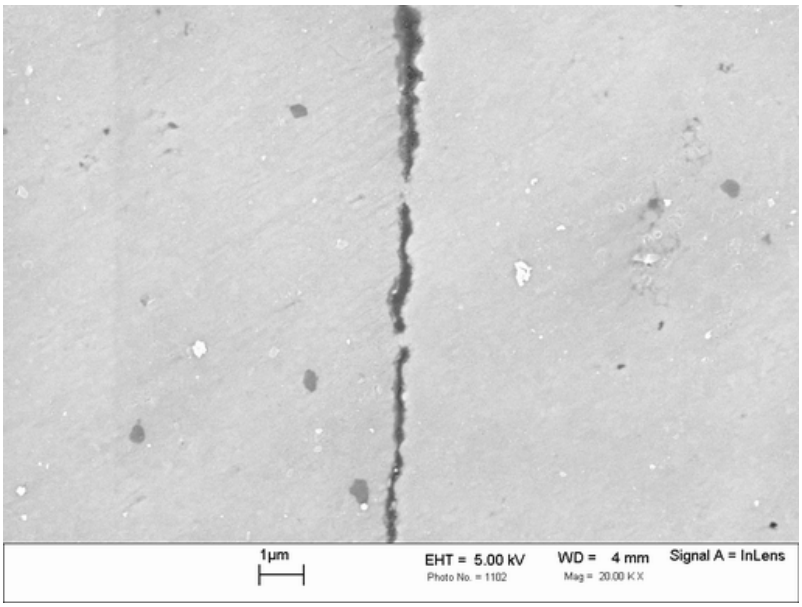

Figure 3.13. View of the interface on the polished edge of the unaged sample.

3.2.5 Weibull analysis

The statistical analysis of the strength of the interconnect materials was performed using a Weibull distribution following the practice of ASTM standard C1239.

The probability of failure is given by the cumulative distribution function as Equation 3.3.

$$P_f = 1 - \exp\left[-\left(\frac{\sigma}{\sigma_\theta}\right)^m\right], \sigma > 0$$
$$P_f = 0, \sigma \le 0 \tag{3.3}$$

Following the procedure set forth in ASTM C1239 (ASTM 2001), the estimated Weibull modulus, $\hat{m}$, and the estimated Weibull characteristic strength,

$\hat{\sigma}_\theta$, are found from the failure stresses using the maximum likelihood function. For a series of failure stresses, σ_i, $\hat{m}$ is calculated by solving the expression as Equation 3.4,

$$\frac{\sum_{i=1}^{N}(\sigma_i)^{\hat{m}}\ln(\sigma_i)}{\sum_{i=1}^{N}(\sigma_i)^{\hat{m}}} - \frac{1}{r}\sum_{i=1}^{r}\ln(\sigma_i) - \frac{1}{\hat{m}} = 0 \tag{3.4}$$

where, the failure stresses are separated into two groups. For $1 < i < r$, the specimens failed normally, while for $r < i < N$, the specimens delaminated. This follows the procedure for censored data as set forth in C1239.

Having found $\hat{m}$, $\hat{\sigma}_\theta$ is found from the expression as Equation 3.5,

$$\hat{\sigma}_\theta = \left[\left(\sum_{i=1}^{N}(\sigma_i)^{\hat{m}}\right)\frac{1}{r}\right]^{1/\hat{m}} \tag{3.5}$$

An alternative expression for the probability of failure is given by the following equation:

$$\begin{aligned} P_f &= 1 - \exp\left[-\int_V\left(\frac{\sigma}{\sigma_0}\right)^m dV\right], \sigma > 0 \\ P_f &= 0, \sigma \le 0 \end{aligned} \tag{3.6}$$

The four-point bend test has a well-defined stress state, resulting in a straightforward expression for the estimated Weibull material strength (ASTM 2001) (Weibull material scale parameter), $\hat{\sigma}_0$,

$$\hat{\sigma}_0 = \hat{\sigma}_\theta\left\{V\left[\frac{(L_i/L_0)\hat{m}+1}{2(\hat{m}+1)^2}\right]\right\}^{1/\hat{m}} \tag{3.7}$$

where, V is the gage section volume, L_i and L_0 are length of the inner load span and outer load span, respectively. This expression applies for volumetric flaws, assuming average values for V of each geometry.

The Weibull expression for $\sigma > 0$, Equation 3.3, is modified to the form

$$\ln\left(-\ln\left(1-P_f\right)\right) = m\ln\sigma - m\ln\sigma_\theta \tag{3.8}$$

which demonstrates a linear relationship between ln(-ln(1-P_f)) and ln(σ).

Stresses are ranked in ascending order and the probability of failure determined by rank according to the expression below,

$$P_f\left(\sigma_i\right) = \frac{i-5}{N} \tag{3.9}$$

where, $P_f(\sigma_i)$ is the probability of failure of the i^{th} specimen and N is the total number of specimens.

For unaged materials, in Equation 3.4, N was 15, and r was 14 and 13 for 3-layer and 5-layer interconnects, respectively. Since the amount of delaminated ones was small compared to the total number of specimens, different flaw population analysis was not done. In Table 3.3, the Weibull parameters for the unaged interconnect materials are given. The calculated value of $\hat{m}$ is 4.68 for the 3-layer and 4.40 for the 5-layer and the value of $\hat{\sigma}_\theta$ is 686.4 MPa for the 3-layer and 452.4 MPa for the 5-layer. $\hat{\sigma}_0$ was found to be 13.2 MPa $m^{3/m}$ for the 3-layer and 7.70 MPa $m^{3/m}$ for the 5-layer, assuming average values for V for each geometry. The relationship between ln(-ln(1-P_f)) and ln(σ) for each data set was plotted in Figure 3.14.

For the aged materials, no delamination was found for the 3-layer and N and r are 11. The calculated values of $\hat{m}$, $\hat{\sigma}_\theta$ and $\hat{\sigma}_0$ are 4.19, 645.7 MPa and

8.02 MPa $m^{3/m}$, respectively. However, 4 out of 11 5-layer specimens were found delaminated.

The 5-layer specimens had to be analyzed twice, once for material failure (r = 7) and once for delamination (r = 4). The calculated value of $\hat{m}$ was 4.47 for material failure and 5.27 for delamination and the value of $\hat{\sigma}_\theta$ was 326.1 MPa and 361.9 MPa, respectively. Weibull plots of $\ln(-\ln(1-P_{f\text{-material}}))$ and $\ln(-\ln(1-P_{f\text{-delamination}}))$ vs. $\ln(\sigma)$ are given in Figure 3.15. Both could not predict the distribution very well.

To generate a Weibull plot for the 5-layer aged material with the two flaw populations, the failure probability is defined as

$$P_f = 1-\left(1-P_{f-\text{material}}\right)\left(1-P_{f-\text{delamination}}\right) \tag{3.10}$$

The calculated value of $\ln(-\ln(1-P_f))$ by Equation 3.10 could fit the data. Weibull plots for aged materials are given in Figure 3.16.

Table 3.3. Weibull parameters for the interconnect material.

Sample	$\hat{m}$	$\hat{\sigma}_\theta$ **(MPa)**	$\hat{\sigma}_0$ **(MPa $m^{3/m}$)**
3-layer	4.68	686.4	13.2
5-layer	4.40	452.4	7.70
3-layer aged	4.19	645.7	8.02
5-layer aged material failure	4.47	326.1	5.90
5-layer aged delamination	5.27	361.9	11.68

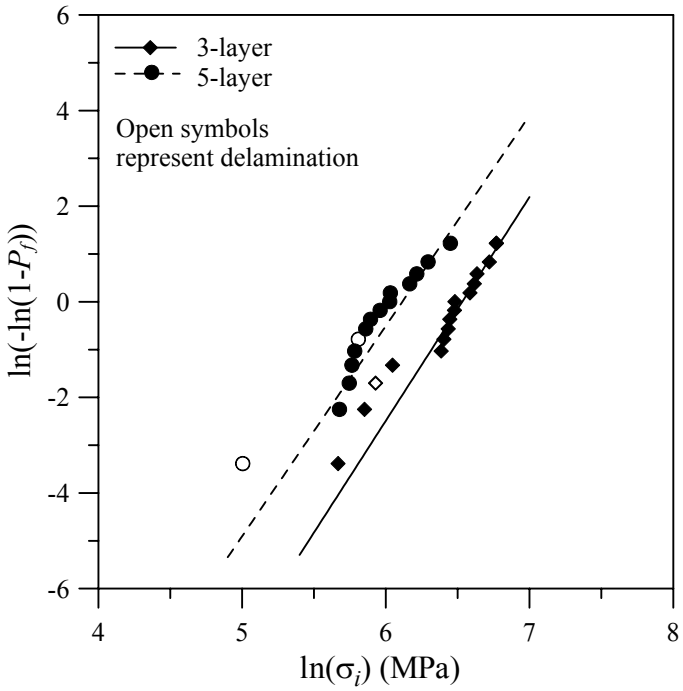

Figure 3.14. Weibull plot for the unaged interconnect bend tests.

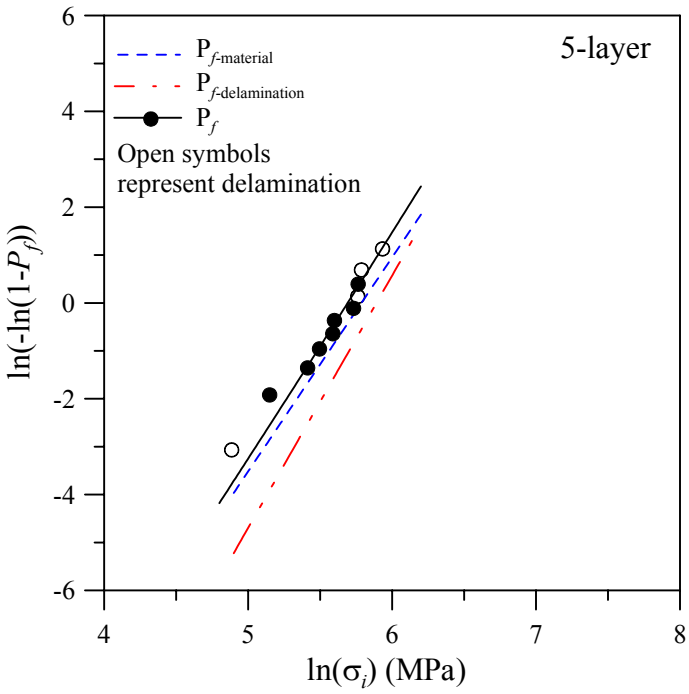

Figure 3.15. Weibull plot comparison for the 5-layer aged interconnect bend tests.

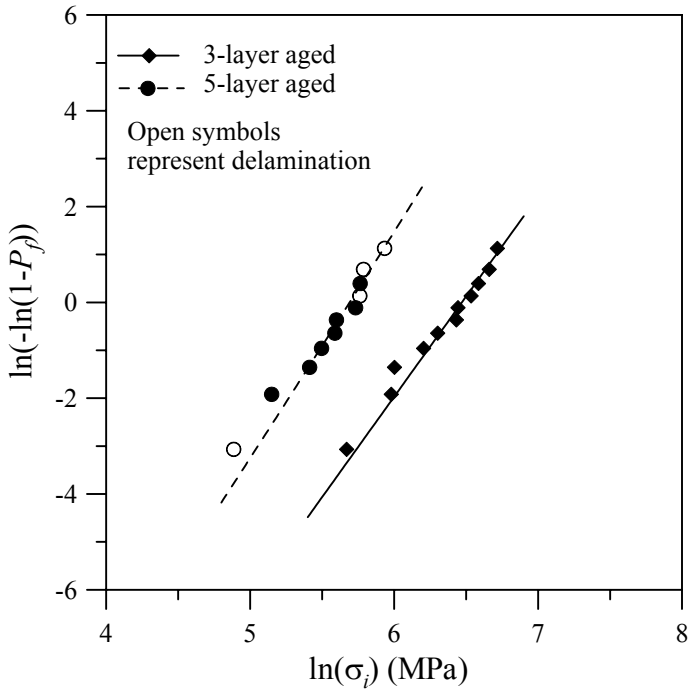

Figure 3.16. Weibull plot for the aged interconnect bend tests.

3.3 Discussion

The 3-layer and 5-layer interconnects were obtained from the same batch of matrix material but from different laminate groups. The geometry effect on the strength population was significant, no matter if the specimens were aged or not. From the fracture strength of the laminated specimens, the 3-layer interconnects showed higher value of peak stress as shown in Table 3.3. Lamination seems always to have an effect on the fracture pattern. As we see in Figure 3.8 and Figure 3.13, discontinuous delamination exists in these kinds of specimens. Fracture surfaces could not pass straight through the laminates, which illustrated a broken face of stair-step shape. In this kind of fracture, delamination occurred over the total specimen, but not exactly simultaneously when the fracture occurred. For the fully delaminated specimens, delamination initialized first, but without fracture, which did not occur until more displacement was applied.

5-layer interconnects showed more sensitivity to the aging effect than 3-layer ones did. After aging, the Weibull characteristic fracture strength of 3-layer interconnects changed slightly from 686.4 MPa to 645.7 MPa, but that of 5-layer decreased close to 30% from 452.4 MPa to 326.1 MPa for material failure and 361.9 MPa for delamination. Due to the existence of the interface, which could be incompletely sintered from layer to layer because of flatness and contaminations *etc*., the more layers the greater the possibility of the existence of a weak interface. The population of discontinuous delamination in aged 5-layer interconnects was more substantial. Also in the 5-layer interconnects, since they were laminated together from more layers, the residual stresses are more likely to exist at the interface. The weak interface would delaminate or become weaker at elevated temperature and would be worse if there were residual stresses.

From Figure 3.13, it is seen that the interface may have a partial delamination and its width is typically around one third of 1 μm. Under microindentation with the load of 800 g, the hardness continuity was not affected very much by the discontinuous delamination in the interface. The pushing force from the microindentation was negligible compared to the bond strength between the layers.

3.4 Conclusions

- As a function of aging time, the resistance of the anode increased continually but with a decreasing rate. At the initial aging of 300 hours, the resistance changed a lot. The hardness of the anodes before and after aging was measured by indenting on the micro-area of the agglomerations in the anodes. It was determined that the indentation hardness increased with aging time for the Ni-Ceria based anode materials tested in air. However, after reducing the

aged anode in H_2, the indentation hardness was smaller than that of the reduced anode before aging as received.

- Fracture strengths of the 3-layer and 5-layer interconnects were different statistical distributions.

- Aging had more effects on the 5-layer interconnects than on the 3-layer ones. After aging, the Weibull characteristic strength of the aged 5-layer interconnects decreased 30% from the unaged, and showed another failure population for delamination. The Weibull characteristic strength of the aged 3-layer interconnects changed slightly compared to that of the unaged. No delamination failure was found for the 3-layer after aging.

- The initial discontinuous delamination in the interface between each layer may contribute to the increasing delamination failure of the 5-layer after aging. Since more layers increases the possibility of weak layer interface existence, this is consistent with the data.

- The existence of the interface had little effect on the hardness continuity. The measured hardness changed little from layer to layer.

- After 1000 hours long-term aging, the hardness of the interconnect materials increased 7% from an average value of 12.37±0.23 GPa for unaged, to an average value of 13.24±0.22 GPa for aged.

CHAPTER 4
MECHANICAL PROPERTIES OF ELECTROLYTE

In this chapter, tensile, four-point bend, ball on ring, pressure on ring and microindentation data are reported from tests that have been done on zirconia based electrolyte materials. The aging effects on the materials will be discussed. Weibull analysis has been done with test results.

4.1 Experiments

4.1.1 Plate tensile strength test

The test preparation is described in section 2.3.3. A total of 20 pieces of the 100×100 mm plates were tested. Due to the difficulty in handling and mounting the fixtures and the brittle property of those ceramic electrolytes, the success rate of the tensile tests was just 50%.

4.1.2 Ball on ring

The 23 mm disks were cut from the larger plates, which were not used in tension tests. They were tested in the ball on ring test fixture, which was introduced in CHAPTER 2. The individual disk thicknesses were not measured, but assumed to be that of the plates from which they were cut. In Figure 4.1, the locations of disks cut from plates (E-7, E-8, E-18 and E-12) were outlined. The

grinding process used to cut the disk from the electrolyte plates was discussed in reference (Reifsnider *et al*. 2001).

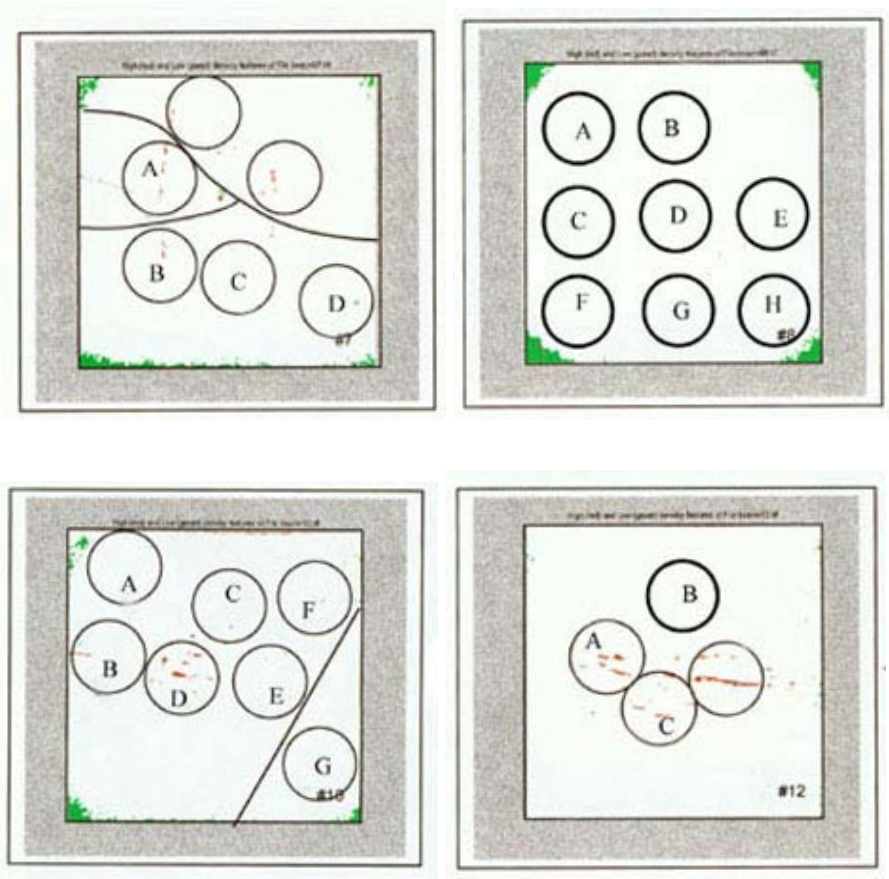

Figure 4.1. Locations of disks cut from electrolyte plates (E-7, E-8, E-18 and E-12).

4.1.3 Pressure on ring

A total of 43 pieces of 17 mm disks with a nominal thickness of 180 μm were tested in the pressure on ring system (see 2.3.2.2). Those disks were separated into two groups with the initial (3- and 4-) of the plate, from which they were cut. After test, the thickness of several fractured pieces were measured under a microscope to get the nominal thickness of each disk tested.

4.1.4 Aging effect on YSZ beam

Fourteen electrolyte beams with a nominal dimension of 66×6.6×2.5 mm were separated into two groups, unaged and aged. The aged samples were treated at 1000 ^{o}C up to 1000 hours in air. After aging, all of the specimens were tested in a flexural test in the four-point bend test fixture in an Instron test machine. During the bend test, each sample was pressed with the rough surface up.

4.1.5 Microindentation

Hardness and fracture toughness for the electrolyte films were measured in the microindentation tester. Some pieces of the electrolyte material were aged at 1000 ^{o}C in air for a total of 1000 hours. After each desired aging treatment time interval, the hardness evolution of the material was measured under a constant load of 500 g. Before and after aging, the hardness was measured under a series of loads from 200 to 900 g. The visible cracks at the corner of the indents were measured under the microscope. Five indents were averaged for each value.

4.2 Experimental results

4.2.1 Plate tensile test

The plate samples after test are shown in Figure 4.2 and a load-displacement plot for sample E1-4 is shown in Figure 4.3. After it was mounted in the Instron machine, initially the fixture was not exactly straight up. Therefore, the displacement of the crosshead is not recorded initially exactly from the very beginning of loading. The results of successful tests are listed in Table 4.1.

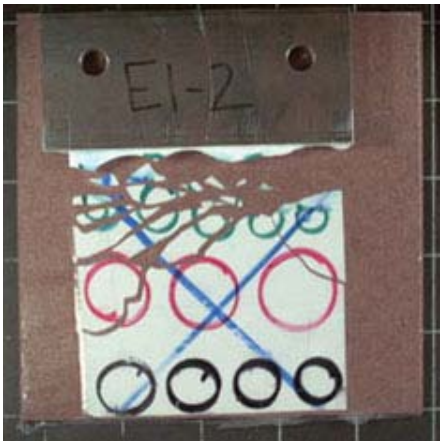

E1-2

E1-3

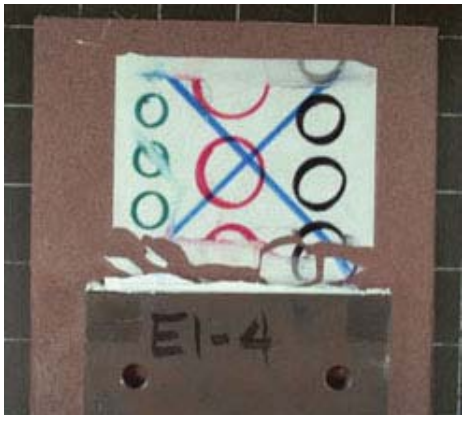

E1-4

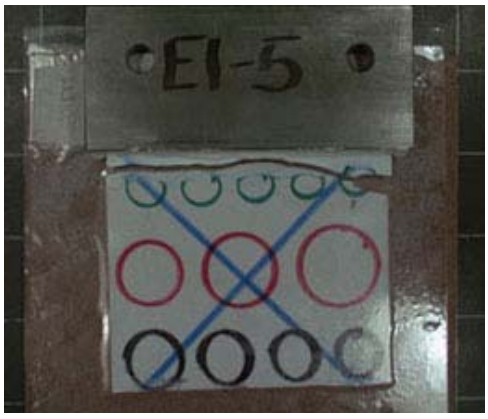

E1-5

E1-9

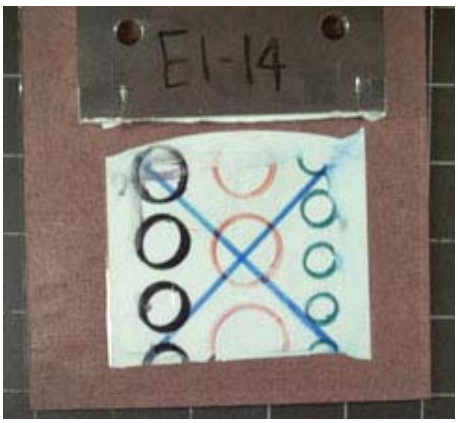

E1-14

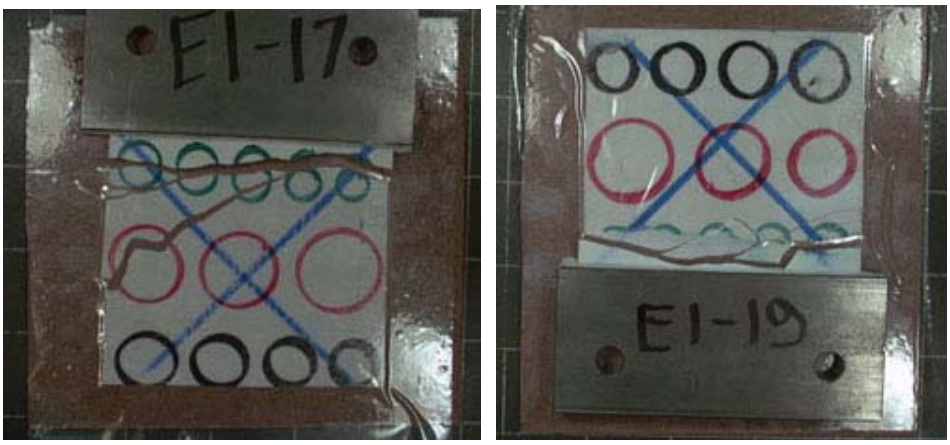

E1-17 E1-19

E1-21

Figure 4.2. Samples after tensile tests.

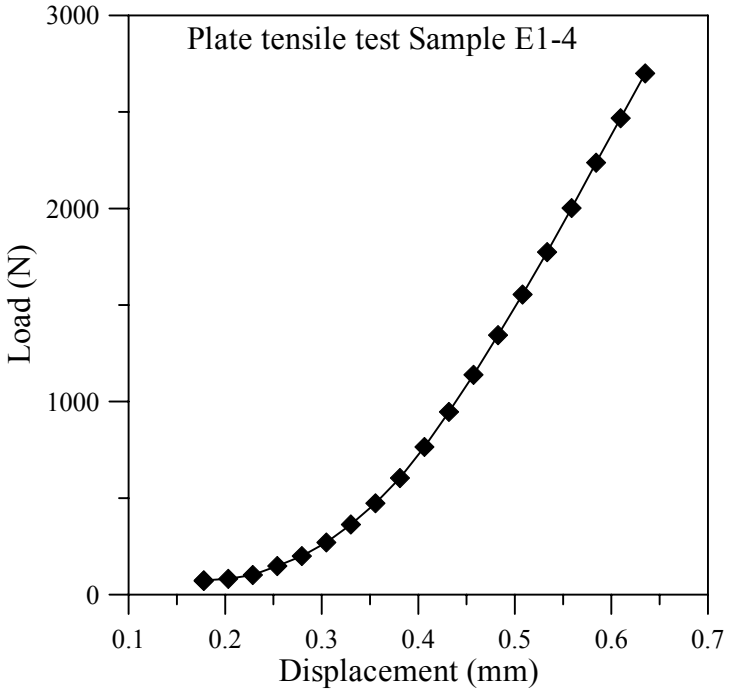

Figure 4.3. Load vs. crosshead displacement plot of the electrolyte tensile test.

Table 4.1. Tensile test results for the electrolyte plates.

Plate	Max. Load (N)	Thickness (μm)	Nominal Stress (MPa)
E1-2	2979	180	162.6
E1-3	2858	181	155.0
E1-4	2896	180	158.1
E1-5	1168	179	64.2
E1-6	2611	171	150.2
E1-9	1539	151	100.5
E1-14	2221	179	122.2
E1-16	2618	185	139.6
E1-17	1993	170	115.7
E1-19	1359	179	74.5
E1-21	911	173	51.9

4.2.2 Ball on ring test

The measured failure load, failure displacement and specimen thickness are given in Table 4.2. The broken disks are shown in Table 4.4. The disks were tested with the rough side in tension. The load-displacement data were not

acquired. The peak stresses were found from the FEA (see 4.3), and listed in the table.

Table 4.2. 23 mm disk tests cut from electrolyte plates.

Specimen	**Thickness (μm)**	**Failure Load (N)**	**Peak Stress (MPa)**	**Failure Displacement (μm)**
10A	172	8.00	833.6	229
10C	172	7.32	773.4	216
10D	172	7.29	770.7	320
10F	172	7.29	770.7	272
10G	172	5.46	601.8	234
12A	166	8.89	949.4	312
12B	166	10.47	1090.5	277
12C	166	6.82	758.6	262
12D	166	5.40	622.4	328
18A	203	9.86	762.1	246
18B	203	8.78	690.3	239
18C	203	10.24	786.6	262
18D	203	6.83	552.4	274
7A	172	8.65	890.1	391
7B	172	9.04	923.6	302
7C	172	8.74	897.9	340
7D	172	8.02	835.4	394
8A	172	9.47	960.4	290
8B	172	9.11	929.6	323
8C	172	9.20	937.2	318
8D	172	9.47	960.2	381
8E	172	9.86	993.0	325
8F	172	8.78	901.3	318
8G	172	10.24	1024.7	328
8H	172	6.83	729.2	320

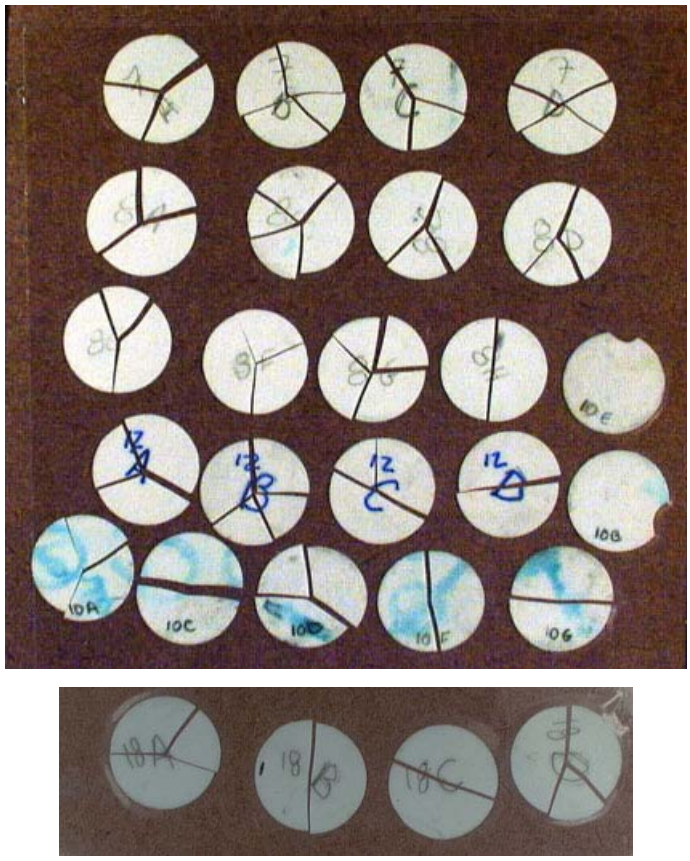

Figure 4.4. 23 mm disk test specimens.

4.2.3 Pressure on ring test

A total of forty-three 17 mm electrolyte disk tests were performed with the pressure on ring test. The two groups of electrolytes were treated the same as each other. The disks were tested with the rough side in tension. The load-displacement data was recorded for each test and a sample plot is shown in Figure 4.5. Their measured average thicknesses and the failure pressure loads are listed in Table 4.3. The FEA calculated peak stresses are listed in the table. The FEA on this kind of test methodology will be discussed in next section. In Figure 4.6, the failure patterns are shown. The cracks were dyed with paint. There were mainly two fracture patterns. Most of the samples failed in a spider-web pattern. Several disks failed close to the edge where the stainless steel ring supported them rather than

around the center where the theoretical maximum value of the stress distribution is located under a uniform pressure load. The higher the failure load, the more broken pieces the specimen fractured into.

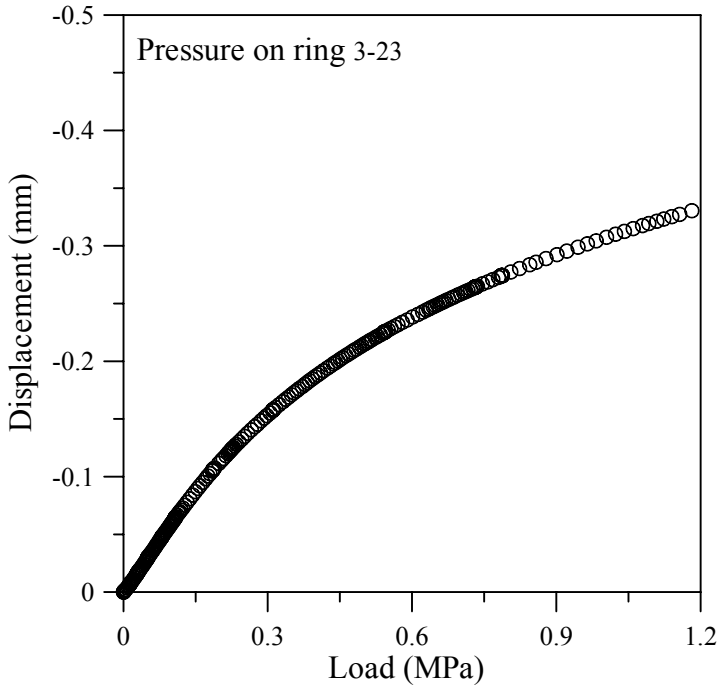

Figure 4.5. Sample 3-23 load-displacement of the pressure on ring test.

Table 4.3. Pressure on ring results for electrolyte disks.

Sample	**Average thickness (μm)**	**Failure load (MPa)**	**Peak stress (MPa)**
3-01	196.6	0.655	482.3*
3-02	190.0	0.441	388.4
3-03	190.3	0.703	503.4
3-04	185.0	0.600	465.1
3-05	195.2	0.517	423.2
3-06	193.9	0.676	492.5
3-07	196.1	0.786	531.7

3-08	196.3	0.607	463.0
3-09	195.7	0.593	457.0*
3-10	205.0	0.689	491.2
3-12	194.1	0.979	596.0
3-14	194.4	0.621	470.5
3-15	180.0	0.558	449.5
3-16	190.0	0.296	298.3*
3-17	194.6	0.531	429.9*
3-18	193.8	0.703	502.8
3-19	195.0	0.876	562.9
3-20	193.4	0.738	515.5
3-22	195.0	0.634	475.2
3-23	198.0	1.179	653.5
3-24	196.3	0.538	432.1
3-25	196.0	0.855	555.2*
3-26	197.0	0.276	274.6*
3-28	194.2	0.414	369.8*
4-01	194.8	0.586	454.9
4-03	195.0	0.469	398.9
4-04	193.6	0.476	403.6
4-05	192.0	0.496	415.3
4-06	194.0	0.641	478.7
4-07	193.0	0.462	396.9
4-08	193.0	0.421	374.5*
4-09	194.4	0.614	467.5
4-10	192.0	0.427	379.1*
4-12	195.0	0.503	416.3
4-13	194.3	0.476	403.6
4-14	195.0	0.386	352.0
4-15	192.0	0.869	561.1
4-16	192.0	0.476	405.2
4-19	192.8	0.586	455.8
4-20	192.5	0.407	366.5
4-22	194.4	0.510	420.7
4-23	189.7	0.310	308.2
4-24	193.0	0.993	599.7

*Failed close to edge.

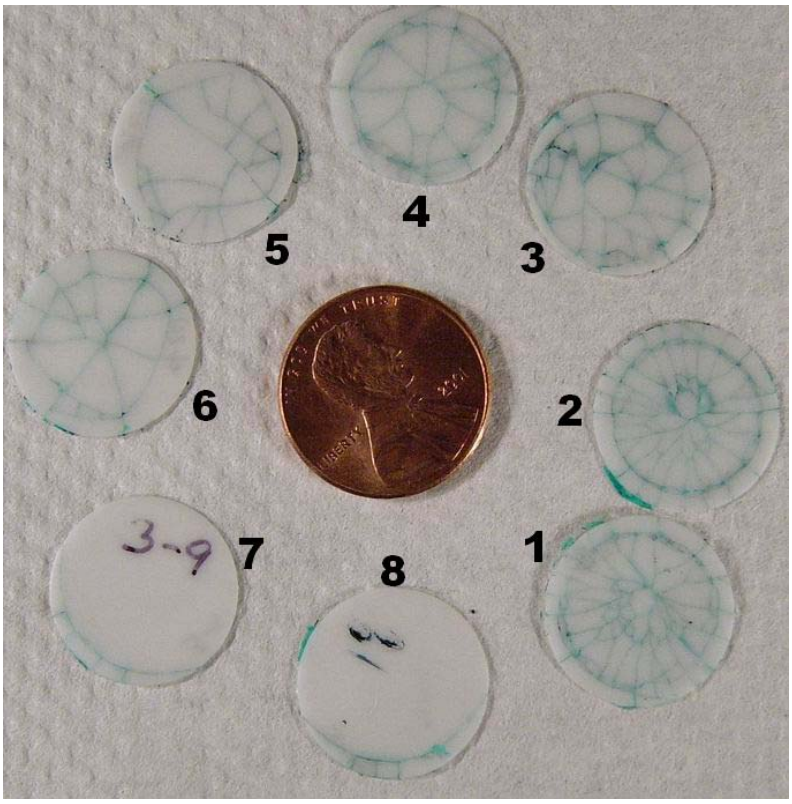

1) 3-2, 2) 3-4, 3) 4-12, 4) 4-18, 5) 3-24, 6) 4-20, 7) 3-9, 8) 3-8.

Figure 4.6. Fracture patterns of the pressure on ring test.

4.2.4 Aging effect on the electrolyte beam

Fourteen four-point bend tests were completed on the unaged and aged electrolyte beams. In Figure 4.7, some samples are given. The measured strengths and failure loads for the beams are given in Table 4.4. Since the displacements at failure are less than the specimen thickness, linear stress analysis was used to determine the failure stresses. The stress values can be determined from Equation 3.2 and the calculated failure peak stresses are listed in the same table.

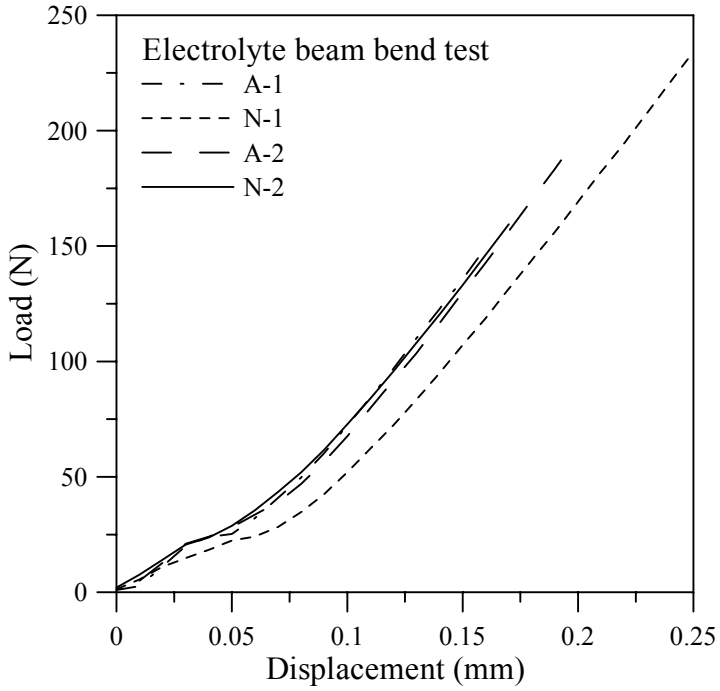

Figure 4.7. Load vs. crosshead displacement plot of electrolyte beam bend test.

Table 4.4. Four-point bend test results for the electrolyte beam.

Specimen	**Thickness (mm)**	**Width (mm)**	**Failure Load (N)**	**Failure Stress (MPa)**
YSZ-A1	2.517	6.647	162.4	116.7
YSZ-A2	2.487	6.677	202	146.8
YSZ-A3	2.373	6.553	175.6	142.7
YSZ-A4	2.495	6.605	155.1	113.2
YSZ-A5	2.498	6.623	167.9	121.8
YSZ-A6	2.493	6.597	170.8	124.9
YSZ-A7	2.497	6.590	179.8	131.3
YSZ-N1	2.427	6.590	236.2	182.6
YSZ-N2	2.473	6.627	162.1	120.0
YSZ-N3	2.397	6.630	206.6	162.8
YSZ-N4	2.407	6.660	206	160.2
YSZ-N5	2.453	6.640	230.2	172.8
YSZ-N6	2.463	6.640	209	155.6
YSZ-N7	2.453	6.553	171.1	130.1

4.2.5 Microindentation test

4.2.5.1 Hardness

The electrolyte film material was subjected to the hardness test. Figure 4.8 is an SEM photo for the indent on the electrolyte material in this study. There were cracks at the corners of the indent.

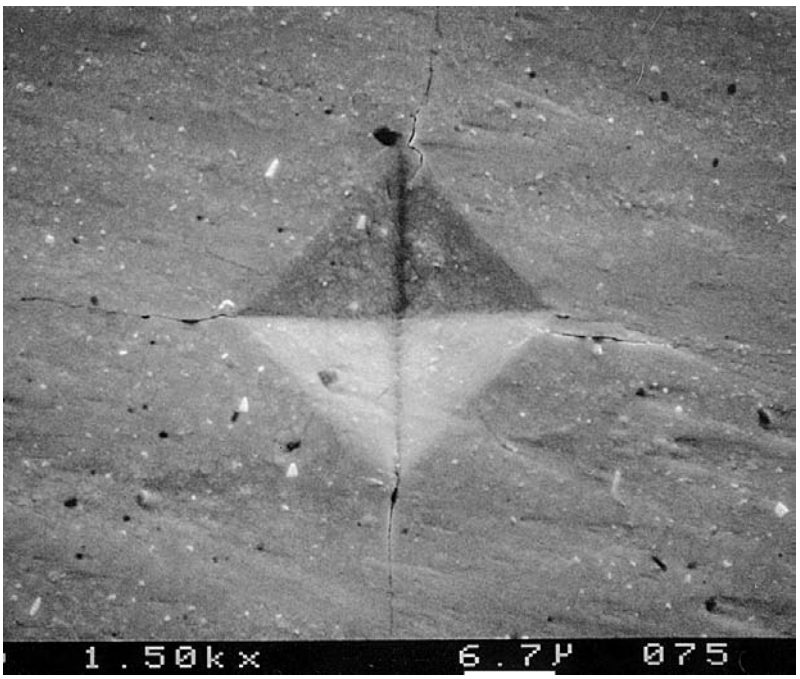

Figure 4.8. An indent with cracks on the electrolyte material.

On the electrolyte specimens from plate piece, microindentation tests were both performed on the surface and the 180 μm thick edge to evaluate the homogeneity through the internal of the material. Figure 4.9 shows the calculated Vickers hardness versus load for the electrolyte edge and surface. The hardness was fairly independent of both load and orientation.

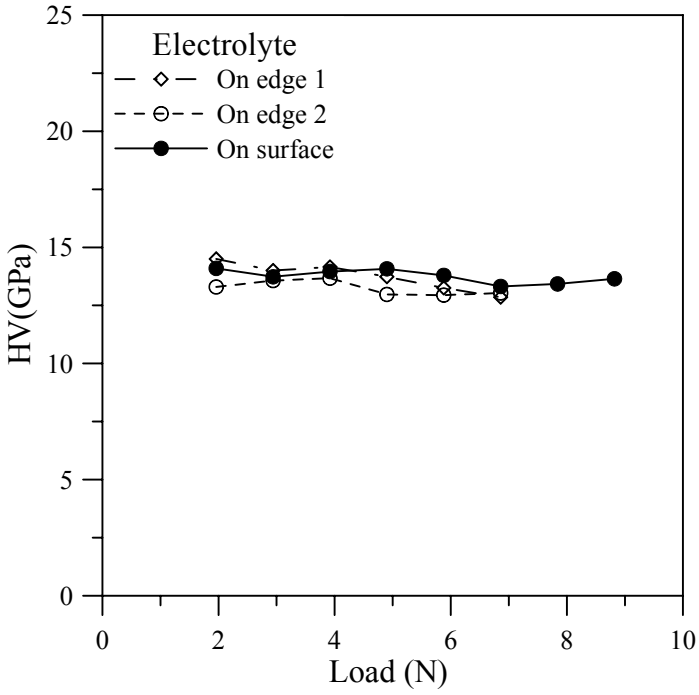

Figure 4.9. Hardness vs. load for the electrolyte material.

After the microindentation tests were conducted on the original electrolyte sample, aging tests were performed at 1000 ^{o}C as long as up to 1000 hours in air. Figure 4.10 and Figure 4.11 show the SEM photos for the unpolished surface of the original and aged electrolyte. There was not large change in the distribution of the grain size. The aging test was stopped from time to time and the electrolyte sample was picked out of the furnace and indented under a load of 500 g. The hardness evolution with the aging time is shown in Figure 4.12. Initially the hardness increased a little but did not appreciably change during the later aging. The mean value of the hardness during aging is 14.15 GPa with a standard deviation of 0.35 GPa. The hardness of the electrolyte aged 1000 hours was compared with that of the original one under a series of loads, and the result is shown in Figure 4.13. After aging the hardness of the electrolyte was slightly greater than before aging. The average hardness increased from 13.72±0.27 GPa to 14.56±0.35 GPa.

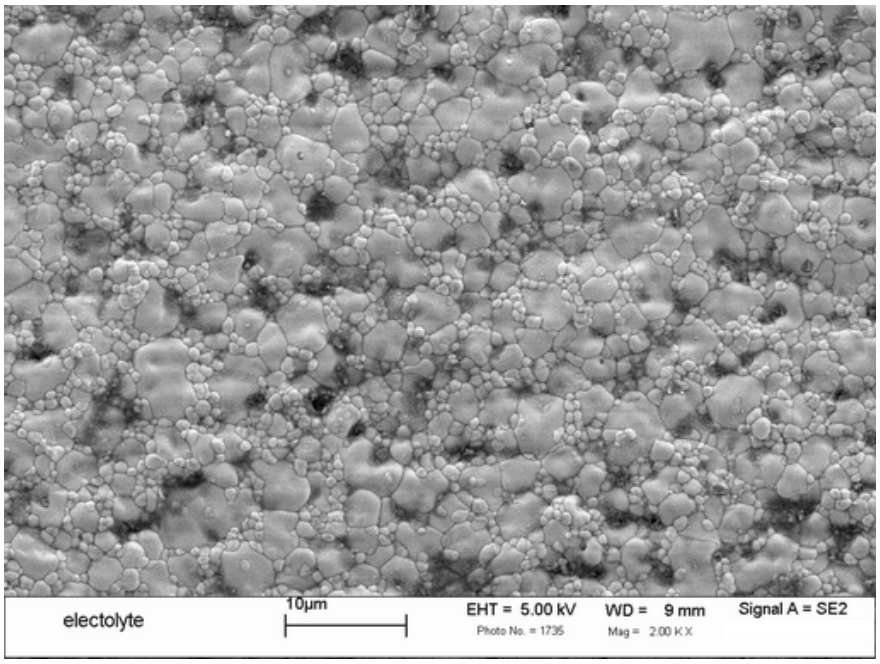

Figure 4.10. SEM of electrolyte surface as received.

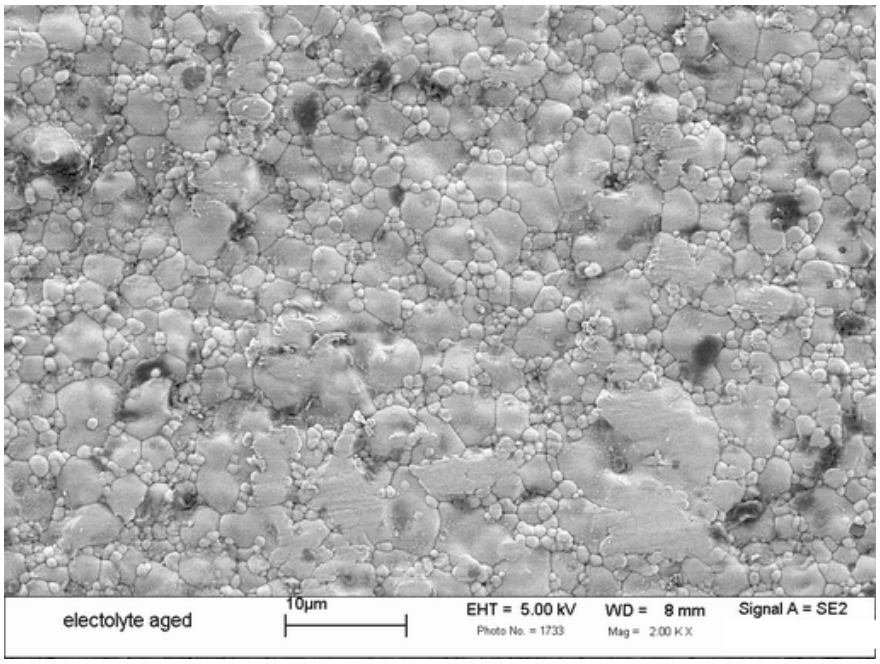

Figure 4.11. SEM of electrolyte surface aged at 1000 ^{o}C in air for 1000 hours.

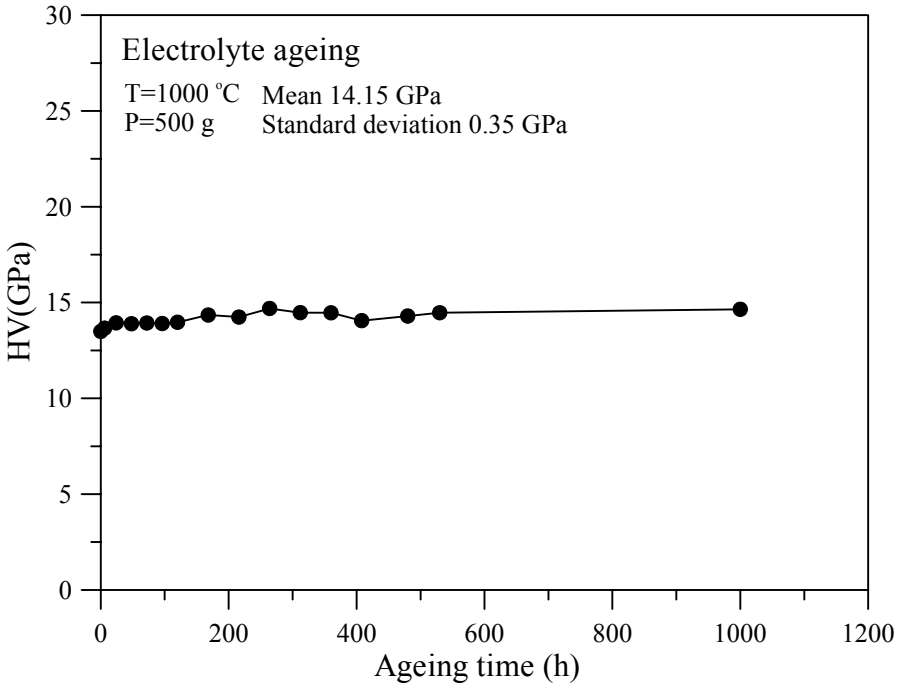

Figure 4.12. Hardness evolution of electrolyte material during aging.

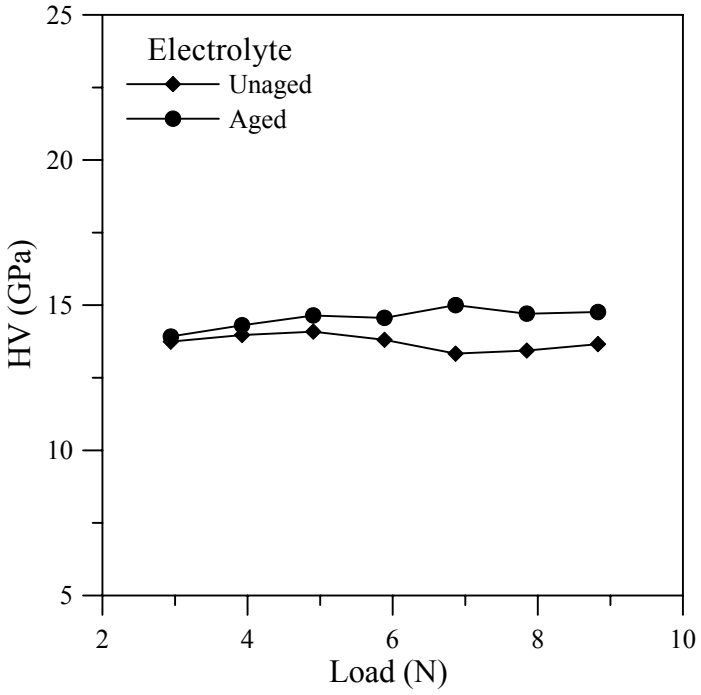

Figure 4.13. Hardness for the unaged and aged electrolytes.

4.2.5.2 Fracture toughness

Indentation cracks could be classified into two groups depending on the geometrical shape of the cracks beneath the indentations (Lankford 1982). One is the halfpenny shaped crack system (also called median or radial-median crack system) and the other is the Palmqvist crack system. If one polishes away the surface layers, the median cracks would remain connected to the corner of the diagonal while the Palmqvist cracks would become detached as shown in Figure 4.14.

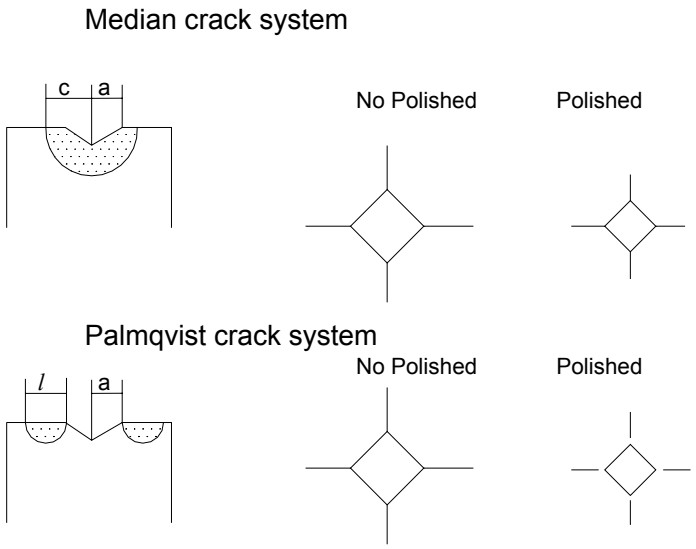

Figure 4.14. The cracks system induced by Vickers indentation.

A crack resistance W was defined (Exner 1969), based on the observed linear relationship between indentation load, P, and the average crack length, *l*, at the corner of the Vickers indent:

$$W=P/4l \quad (4.1)$$

On the other hand, the fracture mechanics analysis of the halfpenny cracks in soda-lime glass has been discussed and the following relation between the crack length, c, and the indentation load, P, was observed experimentally (Lawn and Fuller 1975)

$$c=KP^{2/3} \quad (4.2)$$

where, the constant K is a function of the Young's modulus, hardness, and fracture toughness of the ceramic and the geometry of the indenter.

The crack length *l* as a function of load P is given in Figure 4.15. In Figure 4.16, the crack length, c, as a function of load $P^{2/3}$ was also plotted to see how the plot fits to the halfpenny crack system. The second item of the linear relationship in Figure 4.16 was smaller than that in Figure 4.15, and R-squared value was larger. These two values indicate that the Exner model could not describe the relationship between the crack length, *l*, and load P of the electrolyte. The relationship between the crack length, c, and the indentation load, P, perfectly satisfied the condition for the median cracks system.

Figure 4.17 gives the relationship between the indent half diagonal, a, and the crack length, c. Generally, if the ratio, c/a, was found to be greater than 2.0, it suggested that the type of crack produced by the indentation was more than a median or half-penny type (Liang *et al*. 1990; Muchtar and Lim 1998). In this study, the average ratio of c/a was 2.61, and therefore we concluded that the electrolyte fell in the median cracks system.

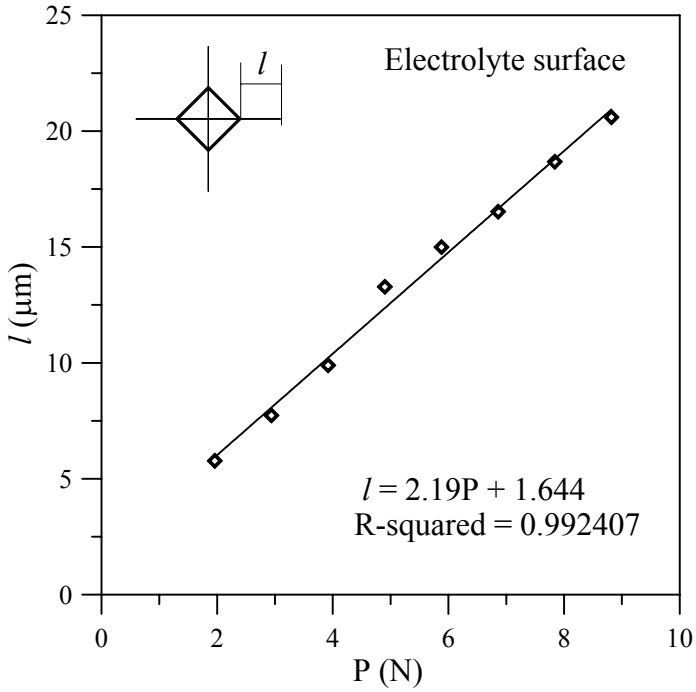

Figure 4.15. Linear dependence of crack length *l* on indentation load P.

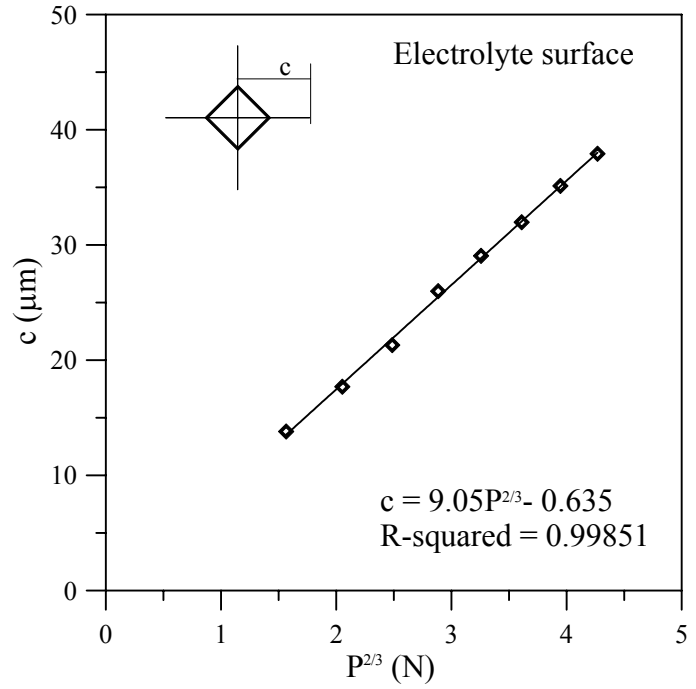

Figure 4.16. Linear dependence of crack length c on indentation load $P^{2/3}$.

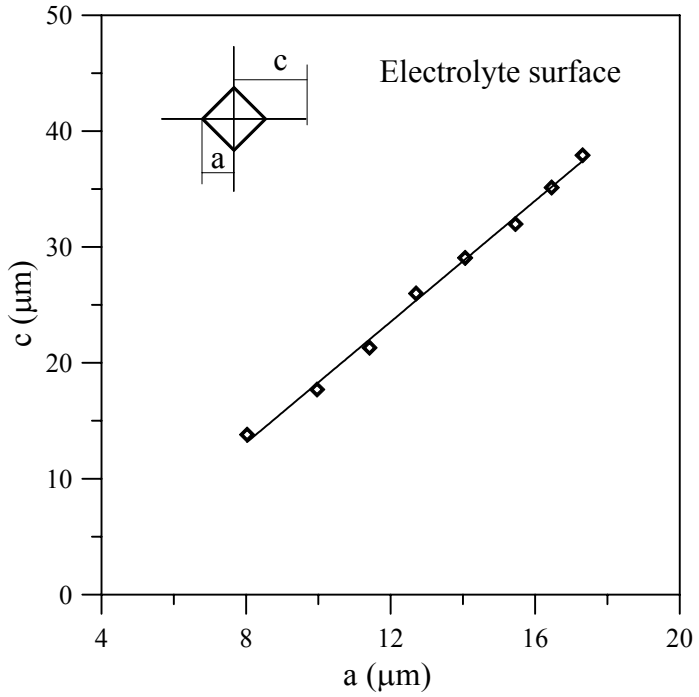

Figure 4.17. Relationship between half diagonal, a, and crack length, c.

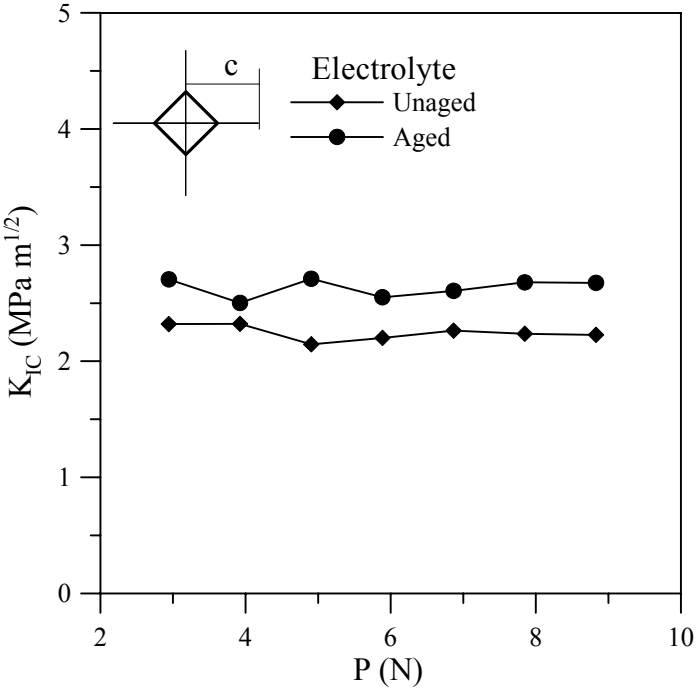

Figure 4.18. Fracture toughness K_{IC} of the unaged and aged electrolytes.

The method used to calculate the fracture toughness (K_{IC}) of a media cracks system was developed (Lawn *et al*. 1980):

$$K_{IC} = \alpha\left(\frac{E}{H}\right)^{1/2}\left(\frac{P}{c^{3/2}}\right) \tag{4.3}$$

where α is an empirical constant according to the geometry of the indenter; for Vickers indenter α is 0.016 (Lawn *et al*. 1980). In Equation 4.3, E is the elastic modulus, H is the hardness, c is the crack length as defined formerly and P is the indentation load. The calculated fracture toughness K_{IC} under each load for the unaged and aged electrolyte was plotted in Figure 4.18. The fracture toughness fluctuated in a very small range and was fairly load independent. The average value was 2.25 ±0.06 MPa $m^{1/2}$ and 2.63±0.08 MPa $m^{1/2}$ for the nonage and aged, respectively.

Microindentation results for other electrolyte pieces are summarized in Table 4.5. For the electrolyte B the cracks were short and hard to see so the cracks were not measurable using a microscope attached to the microindentation tester.

Table 4.5. Microindentation results on the electrolyte materials.

Sample	**Elastic modulus (GPa)**	**Average Hardness (GPa)**	**K_{IC} (MPa $m^{1/2}$)**
Plate piece	185	13.72±0.27	2.25±0.06
Plate piece aged 1000 h	Assume 185	14.56±0.35	2.63±0.08
Electrolyte B	190.7	13.18±0.16	N/A
Electrolyte C	201.3	14.18±0.44	1.88±0.03
Electrolyte D	199.6	13.73±0.21	1.91±0.10

4.3 Finite element analysis

4.3.1 Plate tensile test

A 3-D finite element analysis of the plate tensile test was conducted, using ANSYS (ANSYS 2002). Due to symmetry, only one-eighth of the plate was modeled. The exact geometry of the stainless steel tab was modeled together, which is not shown here. The 3-D ten node tetrahedral SOLID187 element (ANSYS 2002) was used to mesh the geometry. The electrolyte plate was assumed to be 180 μm thick with E = 185 GPa and $\nu = 0.31$. The depth and width of the groove were 6.35 mm.

The first principal stress was assumed to be the stress that caused material failure. A plot of the stress contours over one quadrant of the specimen for this geometry is shown in Figure 4.19. The applied force was 3040 N under which the nominal stress was 169 MPa. A stress concentration was found at the corner of the plate. The principal stress has been normalized by the nominal tensile stress. Figure 4.20 shows the first principal stress from the tab to the middle on the centerline of the plate. Out of the tab, the normalized stress changes from 0.83 to 1.05. Figure 4.21 gives the first principal stress from the edge to the center at the middle of the plate. The normalized stress changed from 0.83 to 1.05 similarly as in Figure 4.20. In Figure 4.22, the stress distribution along the edge of the plate is shown. The stress peaked near the specimen edge and declines toward the center of the specimen. From the photos of the failed specimens, it is apparently seen that the stress concentration has contributed to the possible failure location. Most of the specimens failed close to the tab where the stress concentration occurred.

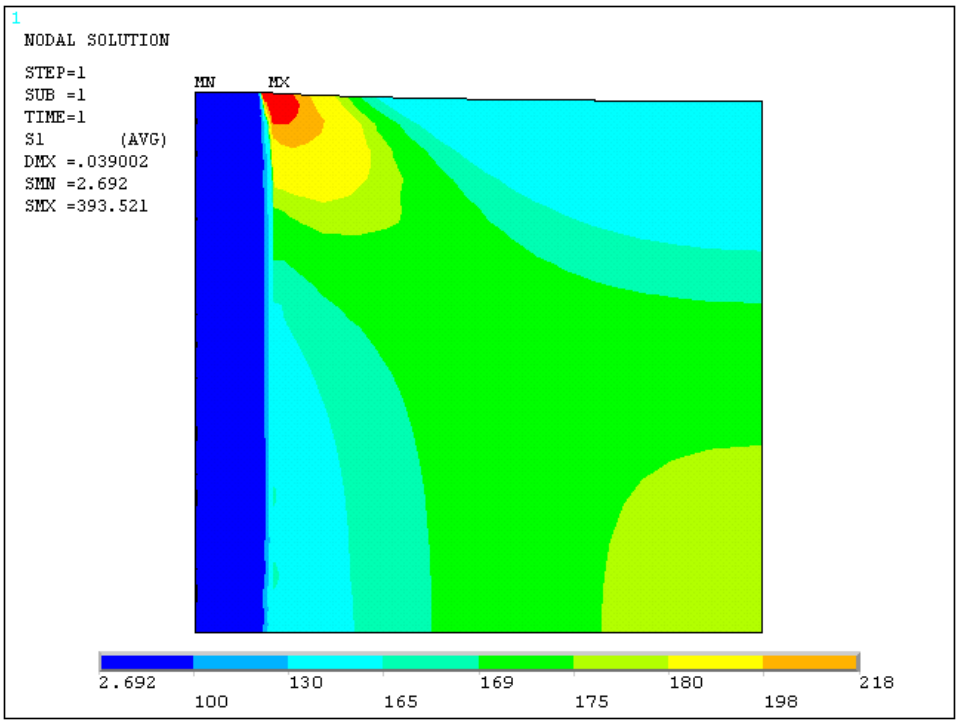

Figure 4.19. First principal stress profile in the upper right quadrant of plate test.

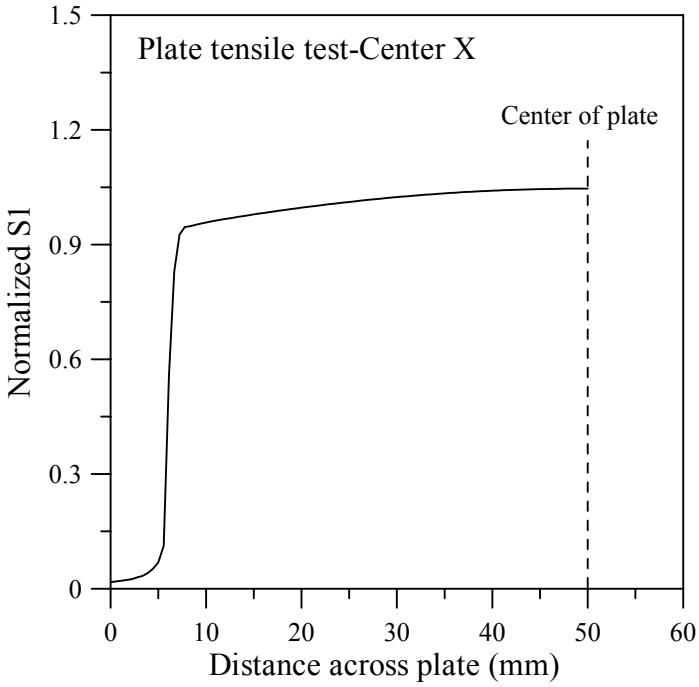

Figure 4.20. First principal stress along X direction at center of test specimen.

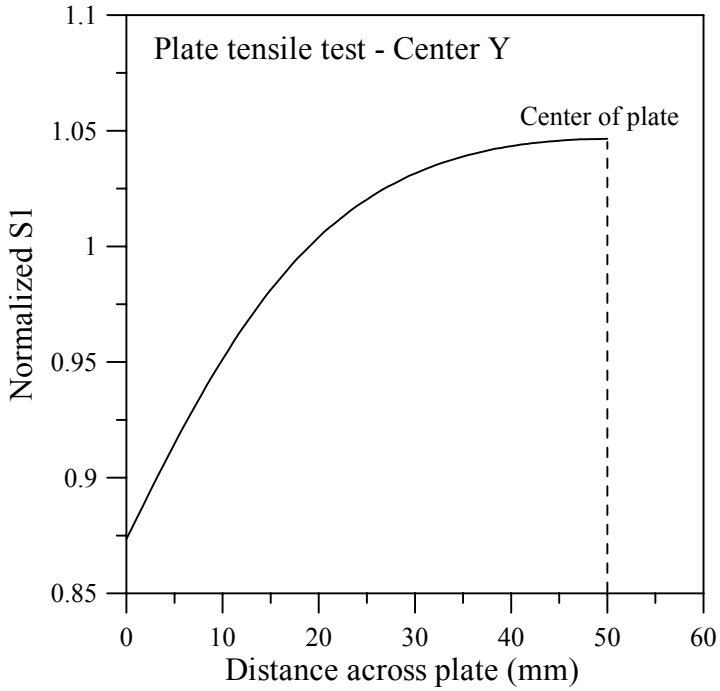

Figure 4.21. First principal stress along Y direction at middle of test specimen.

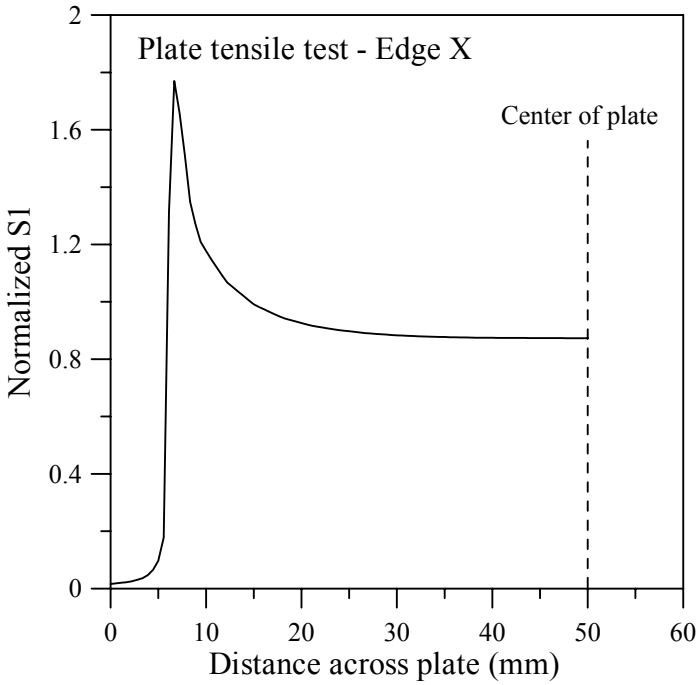

Figure 4.22. First principal stress along X direction on the edge of test specimen.

4.3.2 Ball on ring test

A 2-D axisymmetric finite element analysis of the ball-on-ring test was generated in ANSYS with the 2-D axisymmetric PLANE82 element. The loading ball had a diameter of 6.35 mm. The contact between the loading ball and the specimen was modeled using the 2-D 3-Node Surface-to-Surface contact element CANTA182 and the target element TARGE169, while the support ring was modeled as a rigid support. The electrolyte properties used to generate the curve were E = 185 GPa and $\nu = 0.31$ and a range of disk thicknesses were considered. The stainless steel ball and ring had E = 200 GPa and $\nu = 0.3$. A force load of a total of 15 substeps was applied at the center of the loading ball. As large deformations were expected during the mechanical tests, large-displacement strain formulations were used. The meshed geometry of the FEA model is given in Figure 4.23.

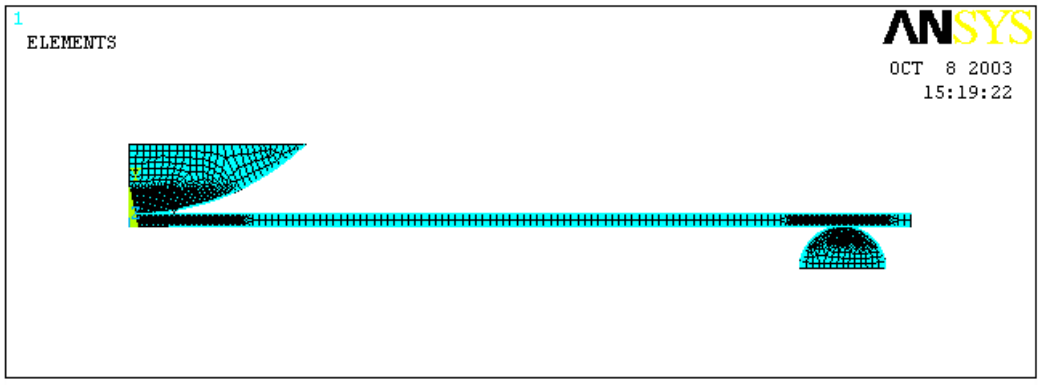

Figure 4.23. FEA model for the ball on ring test.

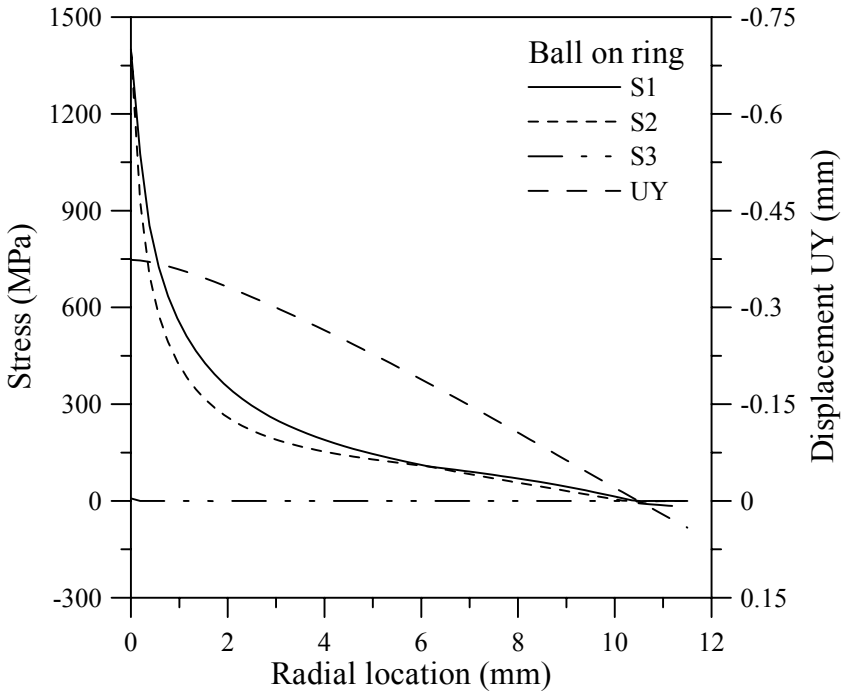

Figure 4.24. Stress and displacement distribution for 172 μm disks.

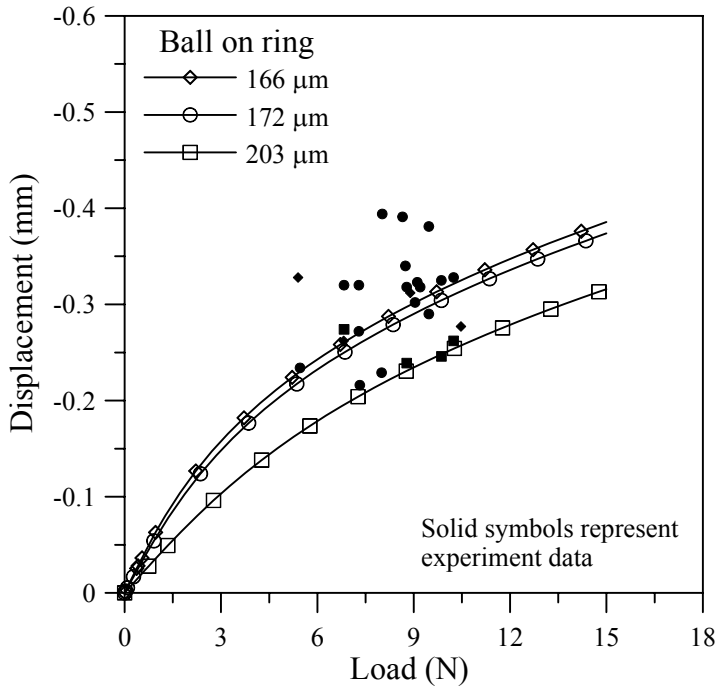

Figure 4.25. Load-displacement curves of ball on ring test.

The FEA stresses and displacement distribution at the tension surface along the radial location for an electrolyte 23 mm disk of 172 μm thickness under an applied load of 15 N are given in Figure 4.24. Stresses peaked at the center of the disk and declined sharply along radius.

The specimen deflection under the load point versus the applied load is shown in Figure 4.25. Also shown in this plot are the loads and deflections at failure measured during the mechanical testing. Experimental data are scattered even for disks with same thickness at similar load. There are several points falling away from the predicted relationship.

The FEA stress analysis was conducted to compare the stresses to ASTM F394, a ball-on-3-ball standard fixture for disk testing.

The standard has:

$$
\begin{aligned}
S &= \frac{3}{4\pi}\frac{P}{d^2}(X-Y) \\
X &= (1+\nu)\ln\left(\frac{B}{C}\right)^2 + \frac{(1-\nu)}{2}\left(\frac{B}{C}\right)^2 \\
Y &= (1+\nu)\left[1+\ln\left(\frac{A}{C}\right)^2\right] + (1-\nu)\left(\frac{A}{C}\right)^2
\end{aligned}
\tag{4.4}
$$

where:

S = maximum center tensile stress (MPa),
P = the applied load (N),
ν = 0.31, the Poisson's Ratio of the specimen,
A = 10.03, the radius of the support circle (mm),
B = 0.1, the radius of the loaded area (mm),
C = 11.5, the radius of specimen (mm), and
d = 0.175, the specimen thickness at fracture origin (mm).

It has been reported that the maximum center tensile stress for ball on ring test is almost independent of supports (Dewith and Wagemans 1989). Figure 4.26 shows the results of the FEA as compared to Equation 4.4. It shows that there is fairly good agreement between the two analyses under lower loads. The standard stipulates that the specimen thickness be such that no non-linearity is active during the test and under the low load the FEA has good linearity. In the range of the load from 5 to 11 N, in which most samples failed, the relative error between the FEA analysis and the ASTM F394 standard is 6.65% to 11.9% and the FEA results are smaller that the ASTM F394 predicted result. In the standard, the contact area is treated as a constant, while in FEA the contact surface will increase when the ball is pushed under increasing load. The larger the contact surface is the smaller the peak stress is from Equation 4.4.

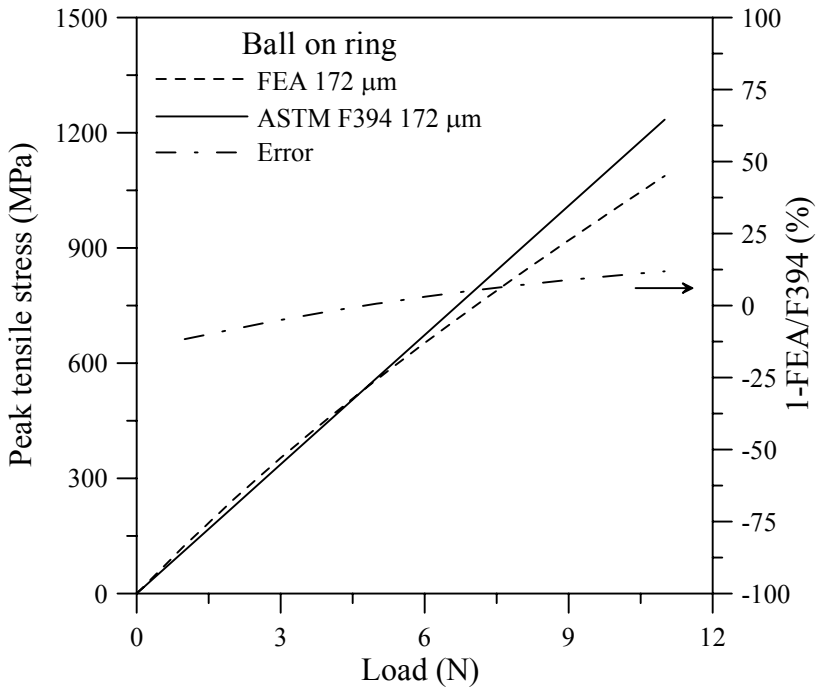

Figure 4.26. Comparison of peak stress as determined by FEA and ASTM F394.

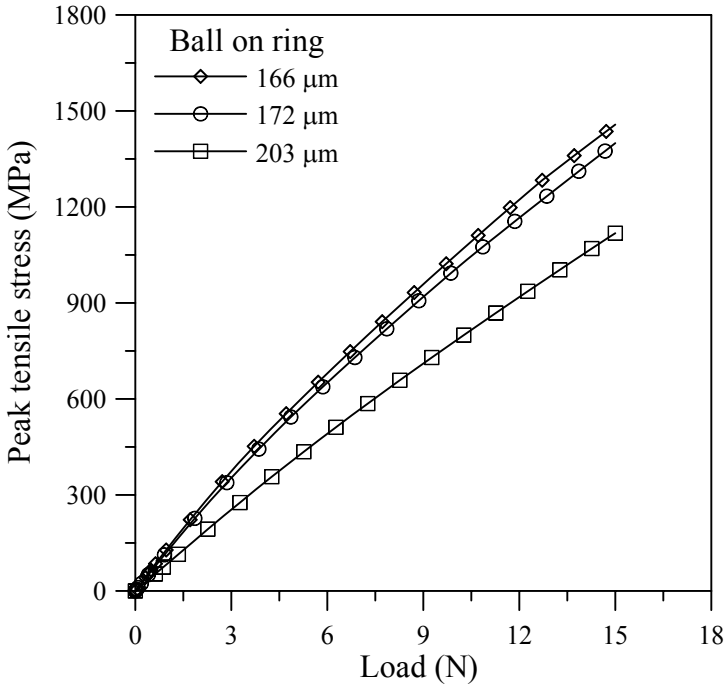

Figure 4.27. FEA Load-stress relationship for 23 mm disk ball on ring tests.

The relationship between load and peak stress is shown in Figure 4.27. The load-stress curves of different thickness were fitted with a 4th order polynomial equation below, and the values of these coefficients are listed in Table 4.6. The peak stress for each specimen was calculated and listed in Table 4.2.

$$S(MPa)=A_0+ A_1\times P(N) + A_2\times P(N)^2 + A_3\times P(N)^3 + A_4\times P(N)^4 \qquad (4.5)$$

Table 4.6. Polynomial fit parameters for the ball on ring FEA results.

	166 μm	**172 μm**	**203 μm**
A_0	-1.630	-0.4889	-1.358
A_1	142.9	130.4	88.49
A_2	-7.294	-4.793	-1.072
A_3	0.4859	0.2315	0.004672
A_4	-0.01349	-0.005099	-0.0009838

4.3.3 Pressure on ring test

An axisymmetric FEA modeling on the pressure on ring test was performed. The 2-D axisymmetric model was built up according to the real geometry as show in Figure 4.28. The diameter of the sample was 17 mm and the normalized thickness was 0.2 mm. The support stainless steel ring had an inner diameter of 12.5 mm and an outer diameter of 15 mm. The support ring was 5 mm high with a 0.625 mm round fillet. The depth of the oil chamber was 2.8 mm. On the pressurized side, a rubber O-ring seal was used to achieve the self-tighten seal function during the pressure load was applied. The O-ring had an inner diameter of 10 mm and an outer diameter of 17.5 mm, which was same as the inner diameter of the oil chamber.

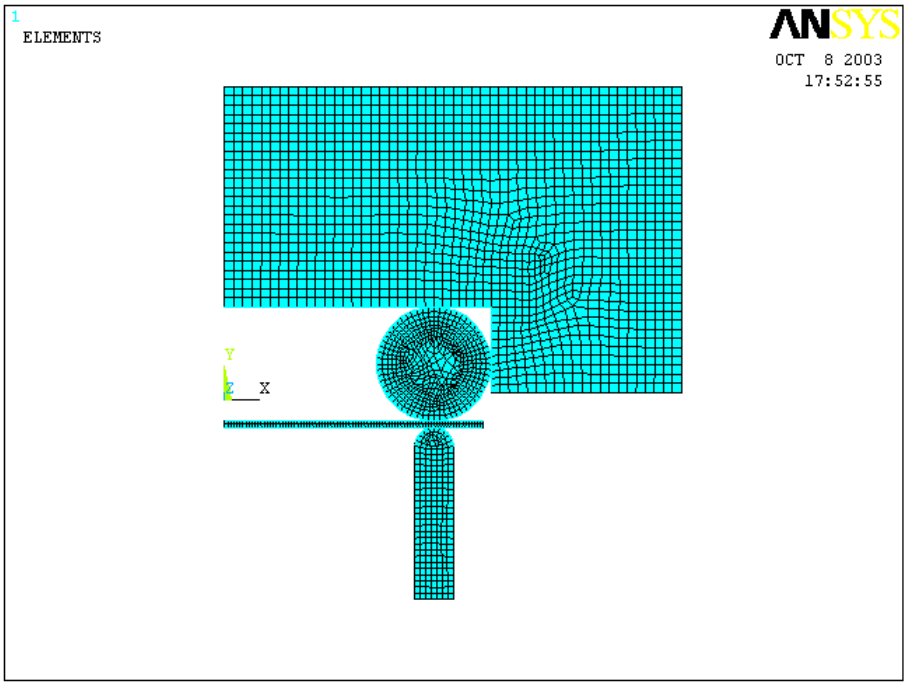

Figure 4.28. FEA model for the pressure on ring test.

An isotropic linear elastic material model was used here to describe the stainless steel fixture and the electrolyte disks. The Young's modulus and Poisson's ratio of the stainless steel were 200 GPa and 0.3, respectively. The elastic properties for the 17 mm electrolyte disk were E = 196 GPa and ν = 0.31, respectively. The sample disk had a thickness of 195 μm.

Since the rubber O-ring will generate large elastic deformation when compressed, it is necessary to consider using a hyperelastic model. The load was driven slowly by manually screwing the bolt on the oil cylinder so that the rubber O-ring could be considered isotropic and isothermal. The strain energy potential based hyperelastic constitutive model used here is the nonlinear three-term Ogden model embedded in ANSYS.

The strain energy potential is:

$$W = \sum_{p}^{N} \frac{\mu_p}{\alpha_p}\left(\bar{\lambda}_1^{-\alpha_p} + \bar{\lambda}_2^{-\alpha_p} + \bar{\lambda}_3^{-\alpha_p} - 3\right) + \sum_{p}^{N} \frac{1}{d_p}\left(J-1\right)^{2p} \tag{4.6}$$

where, W is the stain energy potential, $\bar{\lambda}_p (p = 1,2,3)$ are deviatoric principal stretches, defined as $\bar{\lambda}_p = J^{-\frac{1}{3}}\lambda_p$, λ_p are the principal stretches of the left Cauchy-Green tensor. J is the determinant of the elastic deformation gradient. N, μ_p, α_p and d_p are material constants. The initial bulk modulus K (10 MPa) is defined by:

$$K = 2/d_1 \tag{4.7}$$

A higher value of N can provide a better fit to the real solution. When N=3, the material parameters of μ_p, α_p and d_p are assigned values of μ_1=0.63 MPa, μ_2=0.0012 MPa, μ_3=0.01 MPa, α_1=1.3, α_2=5.0, α_3=2.0, d_1=0.2, d_2=0 and d_3=0 (the second and third incompressibility are zero).

In ANSYS, the 2-D axisymmetric 8-node PLANE82 element was used in meshing the linear elastic material and the 2-D axisymmetric 4-node PLANE182 used with the hyperelastic rubber O-ring. The O-ring was bounded by three contact surfaces, two with the oil chamber and one with the sample. Another contact pair was located where the stainless steel supported the samples. The 2-D 3-Node Surface-to-Surface contact element CANTA182 and the target element TARGE169 were used to create these contact pairs. The real constant contact normal stiffness FKN of the contact element was set as 1 at the O-ring contact surface and 0.02 at the support ring contact surface to get easier convergence. The meshed geometry was constructed as shown in Figure 4.28.

The bottom line of the support ring was constrained with a zero displacement boundary condition both in the X and Y directions. On the central axis of the geometry the nodes were not allowed to move in the X direction.

According to the experimental test procedure, two load steps were applied. First the chamber block was moved down by a distance of 0.6 mm to provide initial compression on the O-ring. Under the first step the solution easily converged. The deformation of the O-ring could afford enough seal to avoid oil leaking during loading. The deformed body is shown in Figure 4.29. After the first load step, the O-ring deformed great deal leading to a large contact surface with the specimen. In the experiments, when applying the first load step by fastening the four long neck bolts, several specimens were broken close to the edge. In Figure 4.30 and Figure 4.31, the stress distribution showed that there were peak stresses where the stainless steel ring supported the specimen. On the pressurized side due to the deformation of the O-ring there was a larger tensile stress. The value was not large (about but 20 MPa) but if the bolts were not tightened evenly, larger values of it would be possible and might break the brittle ceramic.

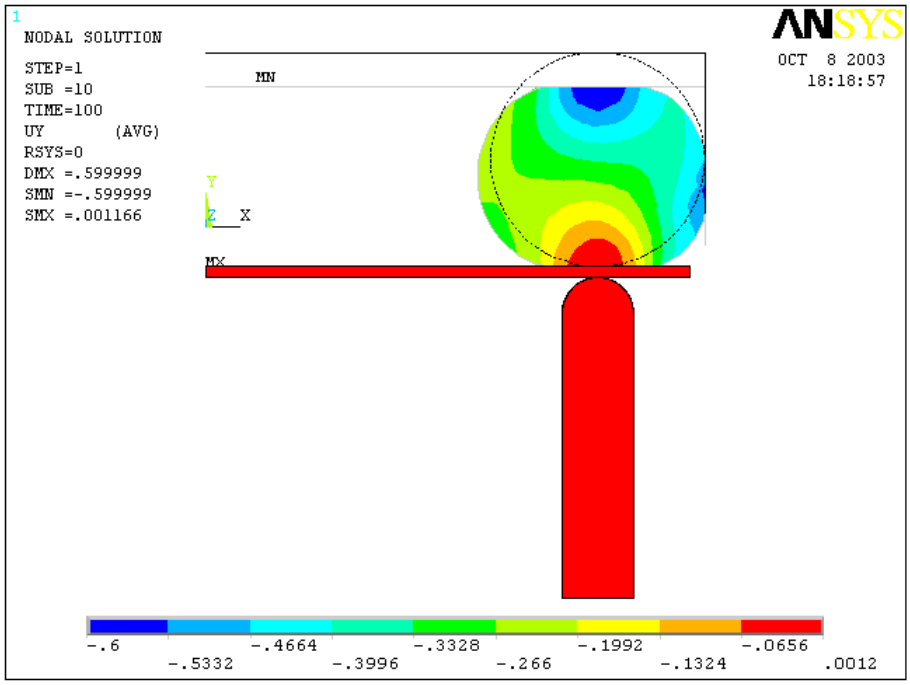

Figure 4.29. Deformation of the O-ring after load step 1.

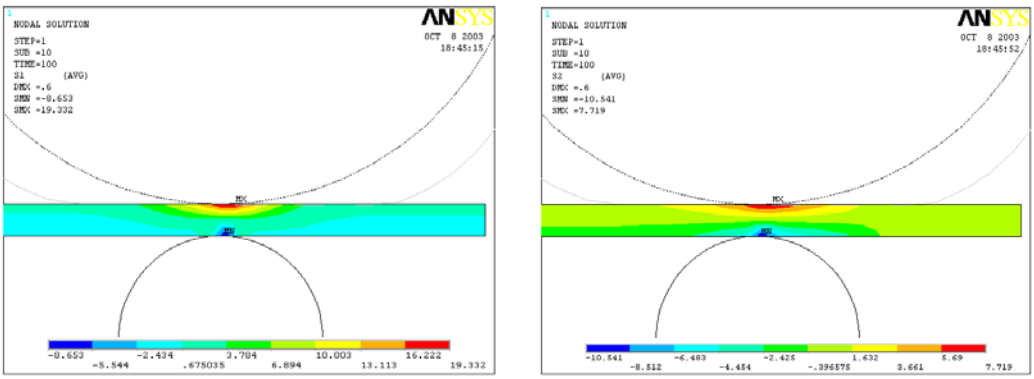

a) Principal stress S1. b) Principal stress S2.

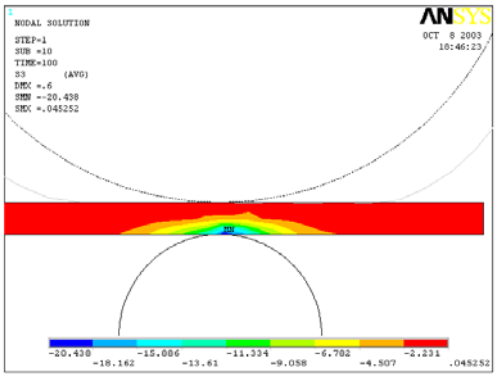

c) Principal stress S3.

Figure 4.30. Stress distribution after load step 1.

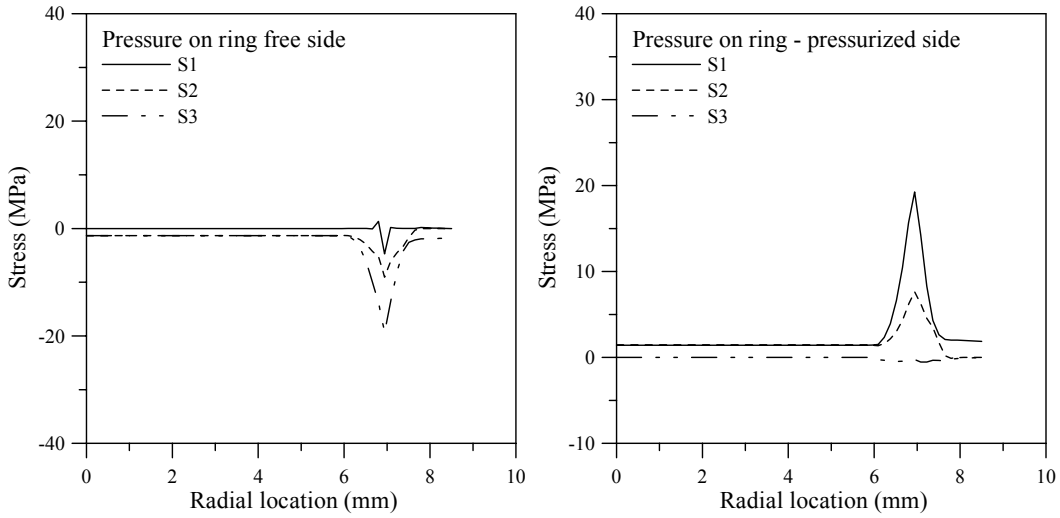

a) On the free side b) On the pressurized side.

Figure 4.31. Stress distribution along the radius after load step 1.

After the initial seal load, a (total) uniform pressure load of 1.2 MPa was applied in the chamber, compressing the O-ring and the specimen. To get an

easier convergent solution and material response under different values of pressure load the substep was set as 50. The deformed shape with O-ring is shown as in Figure 4.32 and the stress and strain distributions are shown as in Figure 4.33.

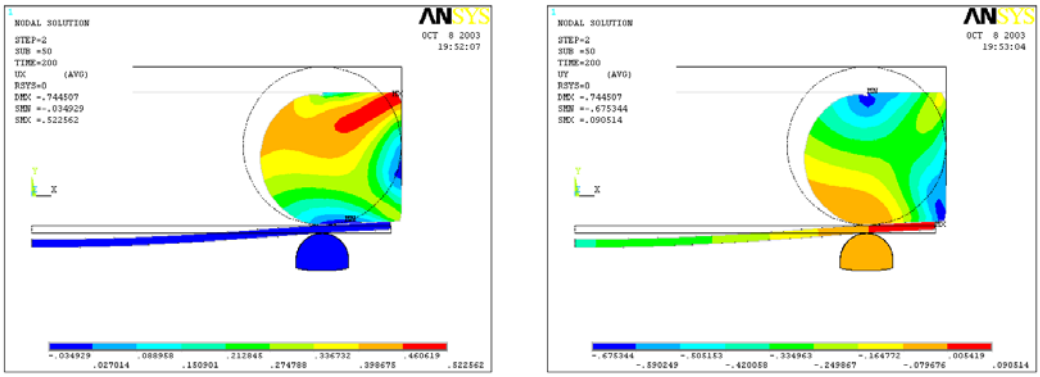

a) UX. b) UY.

Figure 4.32. Displacement distribution after the load step 2.

At the end of the load, the originally circular cross-section of the O-ring has filled the rectangular corner of the oil chamber while remaining circular on the left, where the pressure loading was applied. Meanwhile the ring edge of the specimen was fully compressed by the deformed O-ring, which caused a tensile stress concentration on the pressurized side close to the stainless steel ring. In Figure 4.34 to Figure 4.37 the stress and strain distributions along radius on the pressed and free sides are shown. Under the load value of 1.2 MPa, the calculated maximum first principal stress on the pressed side is about 366 MPa. This stress explains why some specimens failed close to the edge. During the test, on the free side, there were also stress concentrations where the stainless steel ring supported the disk. The dominant one is compression. On the free side, the tensile stress

dominated the stress distribution. In the whole disk, the maximum stress occurred at the center of the disk on the free side, which was about 659 MPa under the load of 1.2 MPa.

From Figure 4.24 and Figure 4.34, it is clearly seen that the stress distributions of the ball on ring and the pressure on ring have different profiles even though the shapes of the displacement UY are similar. Since the pressure is uniform, the change of the stress close to the peak stress under the pressure on ring test is not as sharp as that under the ball on ring test. The pressure on ring test is more approximate to the practical operation of the SOFC working under pressurizing gases. The most possible failure area of the pressure on ring test is larger than that of the ball on ring test. From the failed pictures of 23 mm and 17 mm disks, different fracture styles are found for the two different kinds of loading styles.

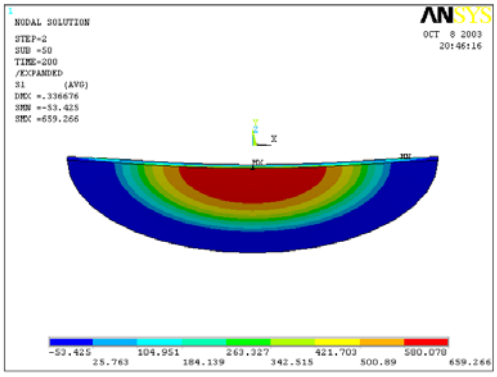

a) Principal stress S1 of free side.

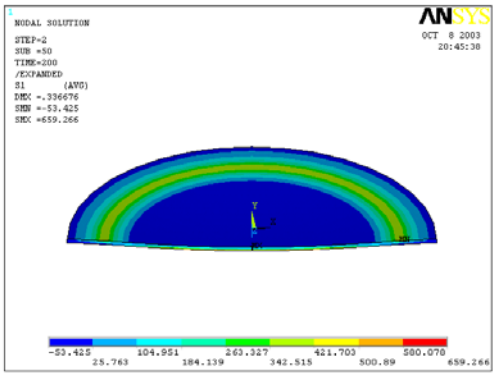

b) Principal stress S1 of pressurized side.

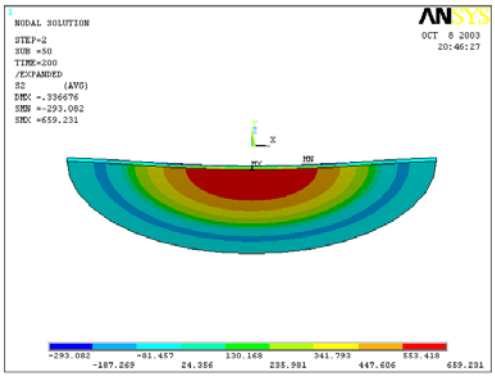

c) Principal stress S2 of free side.

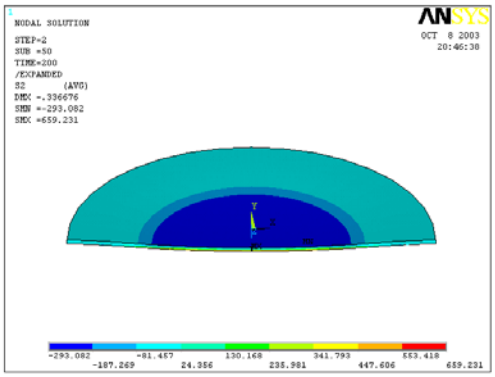

d) Principal stress S2 of pressurized side.

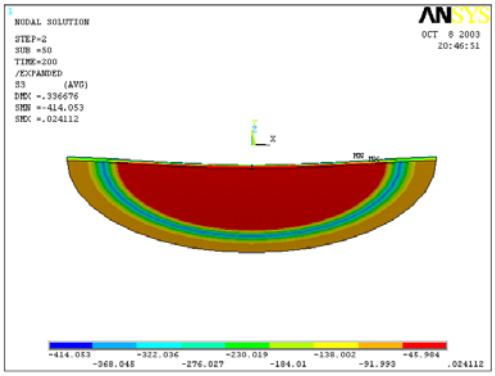

e) Principal stress S3 of free side.

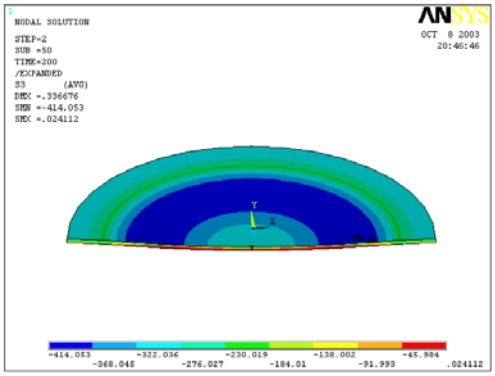

f) Principal stress S3 of pressurized side.

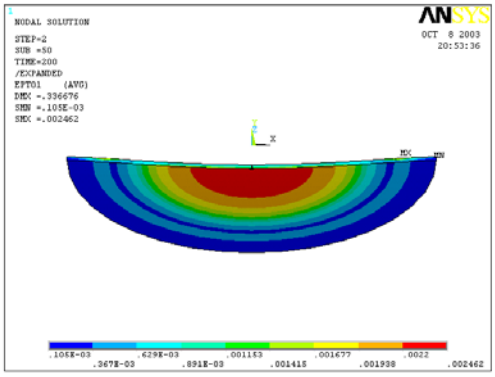

g) Principal strain E1 of free side.

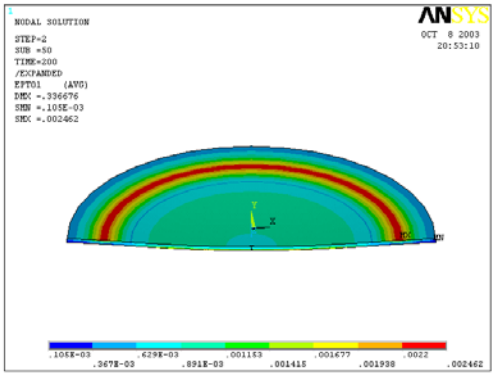

h) Principal strain E1 of pressurized side.

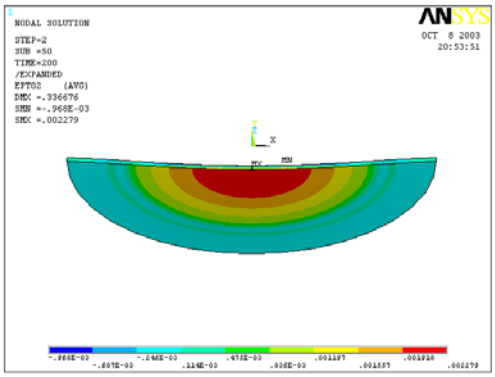

i) Principal strain E2 of free side.

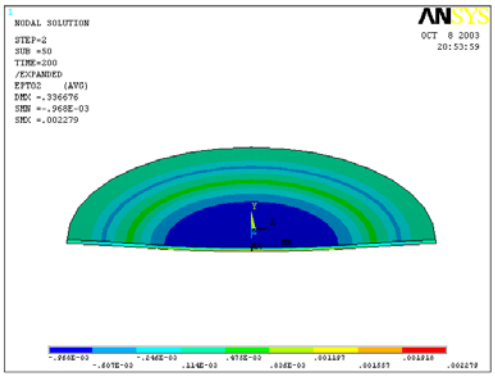

j) Principal strain E2 of pressurized side.

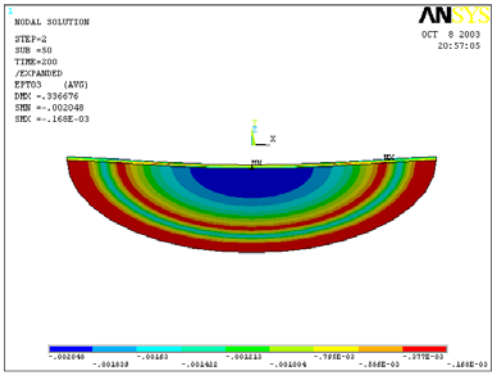

k) Principal strain E3 of free side.

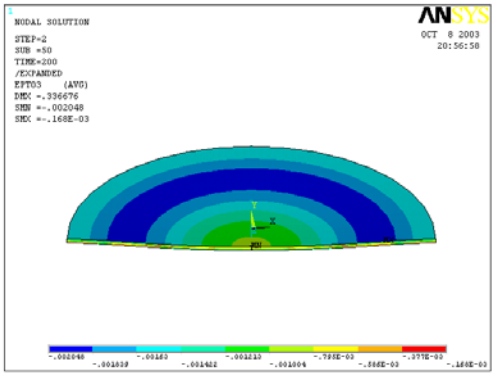

l) Principal strain E3 of pressurized side.

Figure 4.33. Stress and stain distributions of the pressure on ring test.

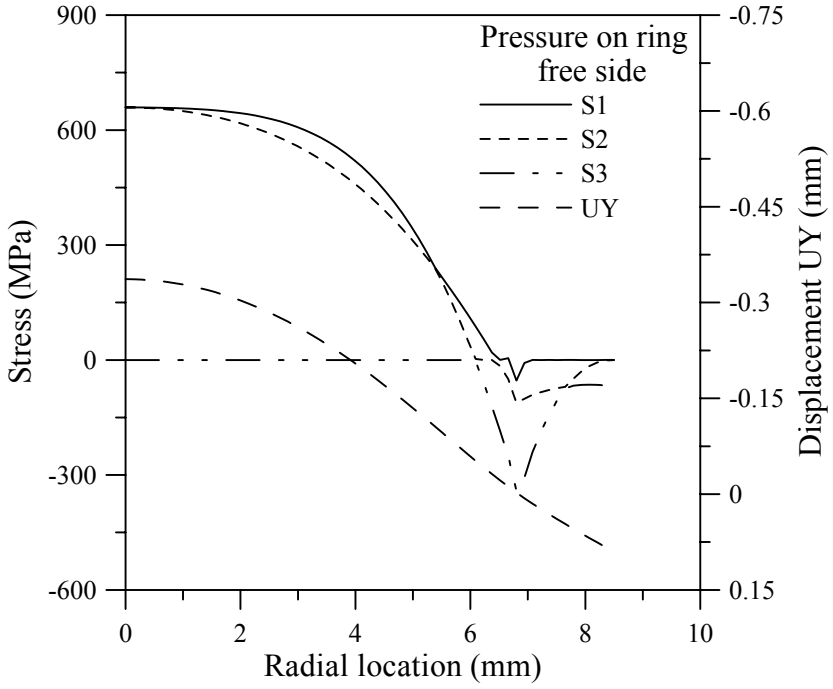

Figure 4.34. Principal stress and UY along radial direction of free side.

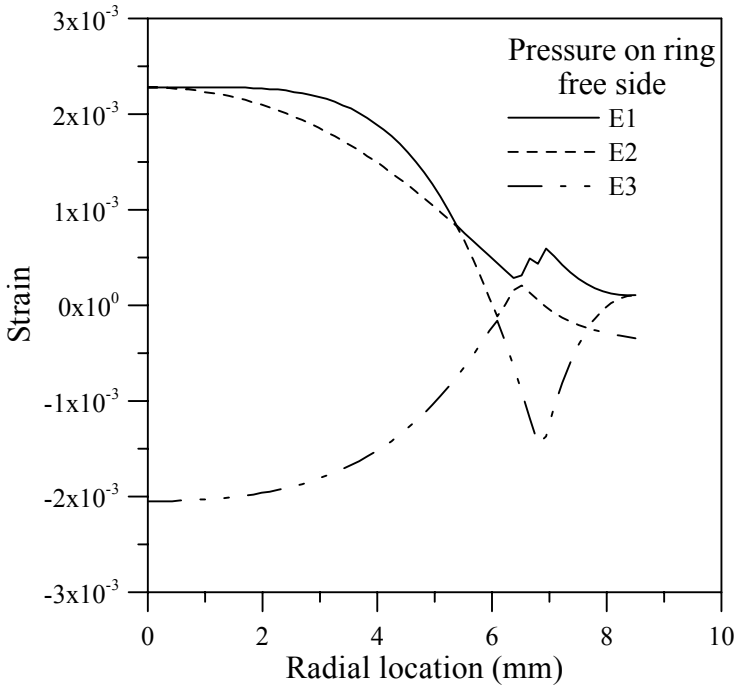

Figure 4.35. Principal strain along radial direction of free side.

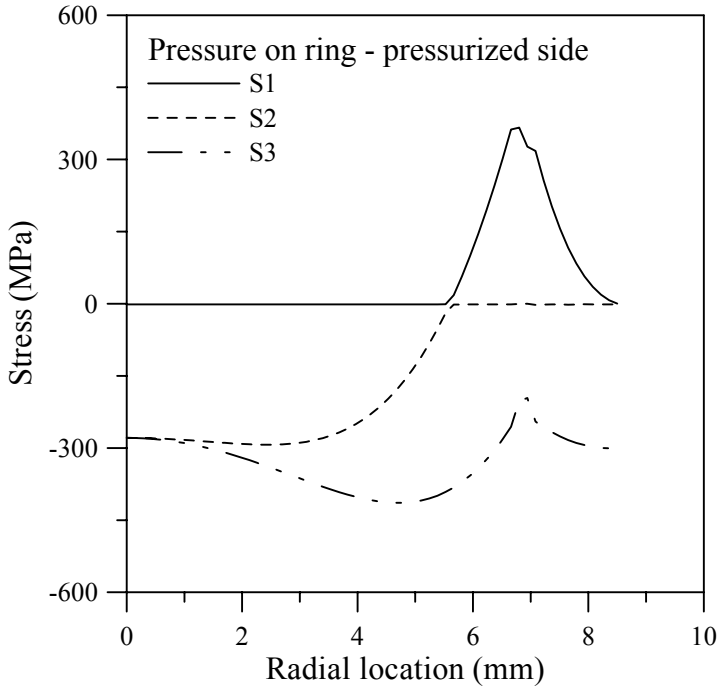

Figure 4.36. Principal stress along radial direction of pressurized side.

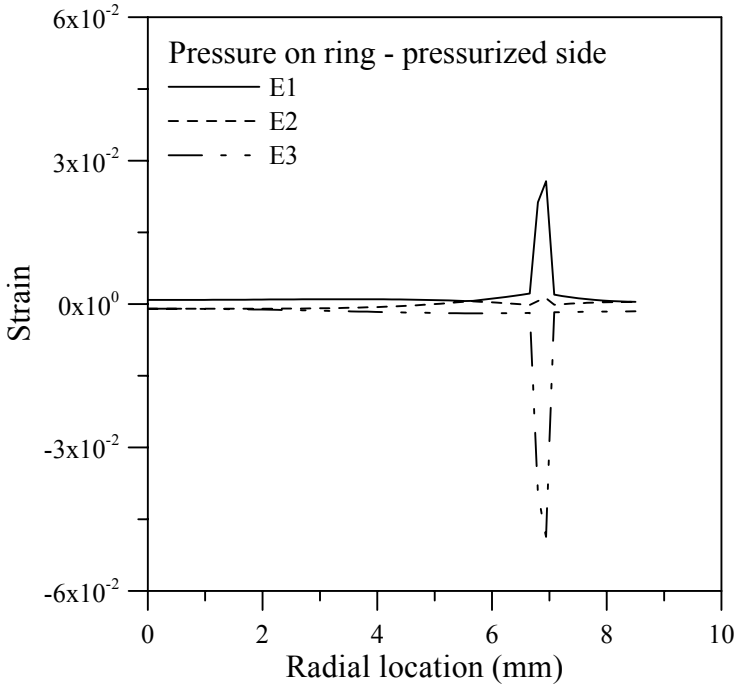

Figure 4.37. Principal strain along radial direction of pressurized side.

Experimental results with higher loads were used to validate the FEA simulation. The specimen 3-23 with thickness of 198 μm was failed under the peak load of 1.179 MPa and the specimen 4-15 with thickness of 192 μm was failed under the peak load of 0.869 MPa. The experimental data of the peak displacement at the center of the disks and the FEA simulated results for them were plotted in Figure 4.38 and Figure 4.39. The FEA results matched the experimental data very well. The calculated peak stresses for the two specimens are 653.48 MPa and 561.05 MPa, respectively. The failed peak displacement at the center and the applied load for other specimens were plotted in Figure 4.40 with FEA simulated curves for three different thicknesses 180 μm, 193 μm and 205 μm. The thinner the specimen, the larger the peak displacement is. Their calculated peak stress with applied load was plotted in Figure 4.41. It is shown from the FEA that the effect of the thickness was less when a higher load (not more than 1.2 MPa in this study) was applied.

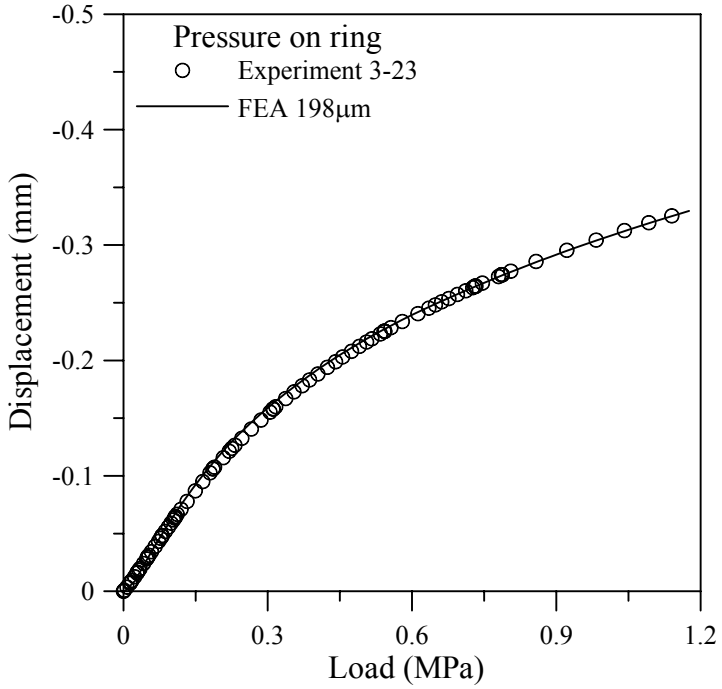

Figure 4.38. Validation of FEA simulation of sample 3-23.

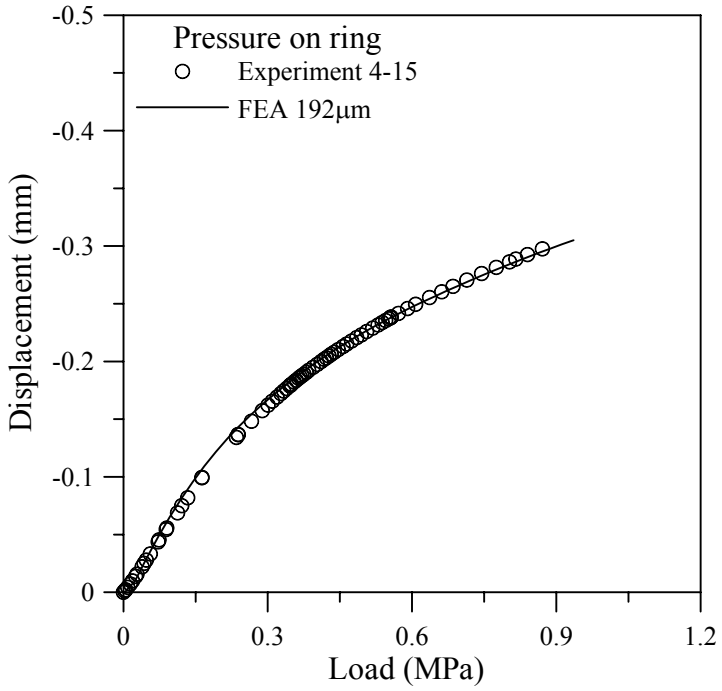

Figure 4.39. Validation of FEA simulation of sample 4-15.

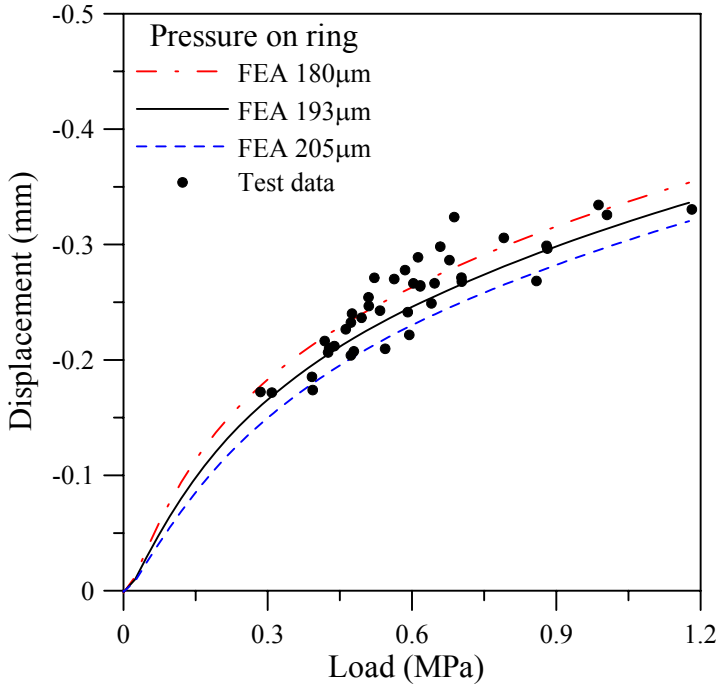

Figure 4.40. Load-displacement curves of the pressure on ring tests with all experimental data.

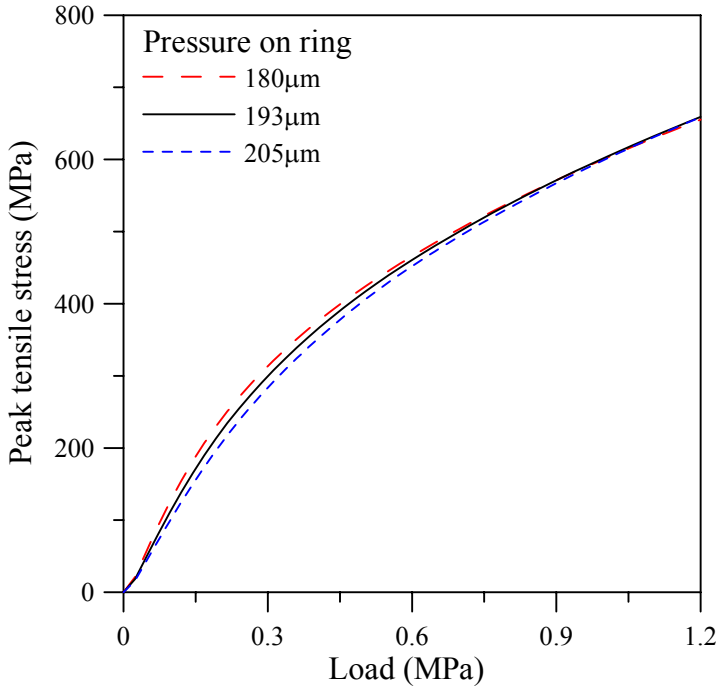

Figure 4.41. FEA Load-stress relationship for the 17 mm disk.

The load-stress curves of different thicknesses were fitted with a 4th order polynomial equation below, and the values of these coefficients are listed in Table 4.7. The peak stress for each specimen was calculated and listed in Table 4.3.

$$S(MPa)=A_0+ A_1\times P(MPa) + A_2\times P(MPa)^2 + A_3\times P(MPa)^3 + A_4\times P(MPa)^4 \quad (4.8)$$

Table 4.7. Polynomial fit parameters for the pressure on ring FEA results

	180 μm	**185 μm**	**190 μm**	**191 μm**	**192 μm**	**193 μm**	**194 μm**
A_0	-1.694	-1.945	-1.477	-2.154	-2.178	-2.201	-2.221
A_1	1509	1449	1382	1375	1363	1350	1338
A_2	-1936	-1736	-1523	-1499	-1459	-1420	-1381
A_3	1459	1240	1010	983.8	941.9	900.4	859.6
A_4	-428.7	-348.7	-265.6	-256.2	-241.2	-226.4	-211.9
	195 μm	**196 μm**	**197 μm**	**198 μm**	**199 μm**	**200 μm**	**205 μm**
A_0	-2.239	-2.254	-2.268	-2.277	-2.286	-2.293	-2.290
A_1	1325	1312	1300	1287	1275	1262	1199
A_2	-1342	-1304	-1267	-1229	-1191	-1154	-975
A_3	819.0	779.0	739.5	700.0	661.6	632.9	444.5
A_4	-197.5	-183.3	-169.3	-155.5	-142.0	-128.9	-67.29

4.4 Weibull analysis

According to ASTM C1239 (ASTM 2001), an alternative expression for the probability of failure is given as Equation 3.6:

$$P_f = 1 - \exp\left[-\int_V \left(\frac{\sigma}{\sigma_0} \right)^m dV \right], \sigma > 0$$
$$P_f = 0, \sigma \le 0 \tag{3.6}$$

The integration in the exponential is performed over all tensile regions of the specimen volume. The integration is sometime carried out over an effective section instead of over the total volume or area.

By replacing the uniaxial tensile stress in Equation 3.3, with the maximum tensile stress with in the test specimen of interest, thus

$$P_f = 1 - \exp\left[-\left(\frac{\sigma_{\max}}{\sigma_\theta} \right)^m \right], \sigma > 0 \tag{4.9}$$

also, performing the integration given in Equation 3.6 such that

$$P_f = 1 - \exp\left[kV \left(\frac{\sigma_{\max}}{\sigma_0} \right)^m \right] \tag{4.10}$$

where, k is a dimensionless constant that accounts for specimen geometry and stress gradients. The product kV is often referred to as the effective volume. The effective volume can be interpreted as the size of an equivalent uniaxial tensile specimen that has the same risk of rupture as the test specimen or component (ASTM C1239). By setting Equation 4.9 and Equation 4.10 equal to one another, one obtains the following expression for the estimated Weibull material scale parameter:

$$\hat{\sigma}_0 = (kV)^{1/\hat{m}} \hat{\sigma}_\theta \tag{4.11}$$

The stress distribution was obtained from the FEA analysis and used to calculate Weibull parameters.

4.4.1 Electrolyte plates

Figure 4.43 shows the Weibull plot of the failure stresses for the plate tests. This plot is based on the nominal plate stresses and the values of $\hat{m}$ and $\hat{\sigma}_\theta$ in Table 4.8.

One issue is that the stress profile in the plate is dependent on the plate thickness. This results in a different value of kV for each plate thickness, and therefore a different value of $\hat{\sigma}_0$. Table 4.8 shows the results of determining kV and $\hat{\sigma}_0$ for two plate thicknesses that approximately correspond to the thickest and the thinnest plates tested. Given that the variation in $\hat{\sigma}_0$ is small, the average, 3.65 MPa $m^{3/m}$ is suggested as an approximate value of $\hat{\sigma}_0$ for the electrolyte plates.

Table 4.8. Weibull parameters for plates of different thicknesses.

Thickness (microns)	kV **(m^3)**	$\hat{m}$	$\hat{\sigma}_\theta$ **(MPa)**	$\hat{\sigma}_0$ **(MPa $m^{3/m}$)**
152	1.04×10^{-6}	3.69	139	3.59
178	1.19×10^{-6}	3.69	139	3.72

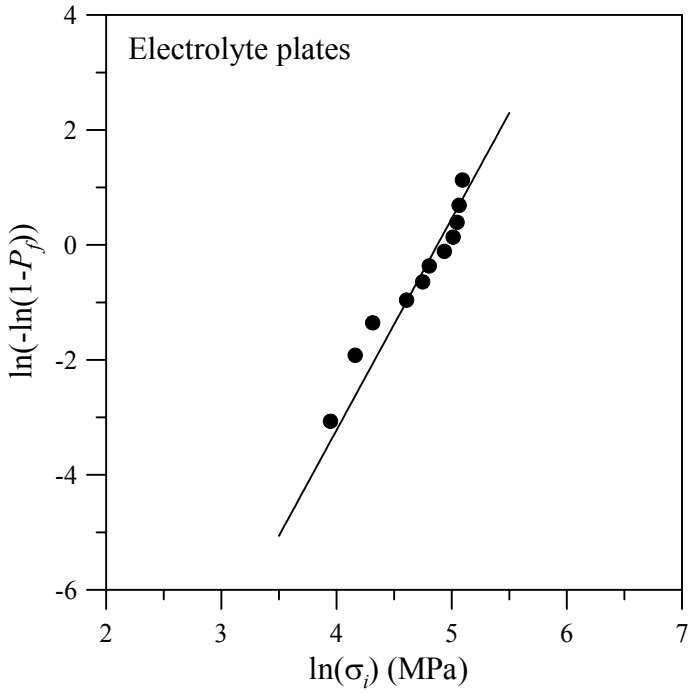

Figure 4.42. Weibull plot of the electrolyte plates.

4.4.2 Electrolyte disks

4.4.2.1 23 mm disks

The maximum tensile stress used to carry out Weibull analysis was from Equation 4.5 and the coefficient values in Table 4.6 for each thickness. The determination of $\hat{\sigma}_0$ and kV was made for the three kinds of thicknesses of the samples and summarized in Table 4.9. The integration value of Equation 3.6 for the 23 mm disk was carried out over a tensile area of 10.5 mm in radius on the tension side. Figure 4.43 shows the experimental probability data and the Weibull distribution curve. The Weibull modulus was found to be 7.35 and the Weibull characteristic strength was 893.8 MPa. A weighted average value of 28.5 MPa $m^{3/m}$ is suggested for the Weibull material scale parameter $\hat{\sigma}_0$ of 23 mm disks.

Table 4.9. Weibull parameters for the ball on test on 23 mm electrolyte disks.

Thickness (μm)	kV **(m^3)**	$\hat{m}$	$\hat{\sigma}_\theta$ **(MPa)**	$\hat{\sigma}_0$ **(MPa m$^{3/m}$)**
166	7.88x10^{-12}	7.35	893.8	27.6
172	9.04x10^{-12}	7.35	893.8	28.1
203	1.82x10^{-11}	7.35	893.8	30.9

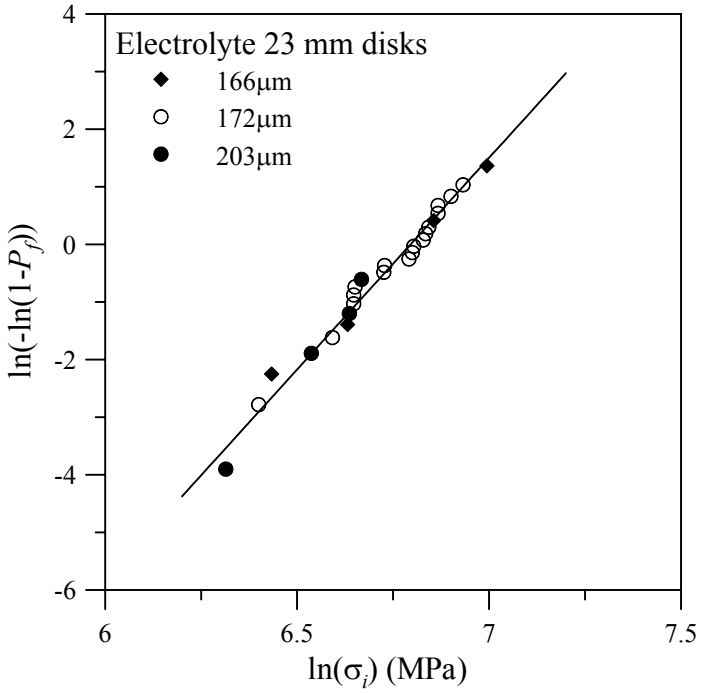

Figure 4.43. Weibull plot for 23 mm electrolyte disks.

4.4.2.2 17 mm disks

Similar to the 23 mm disks, the maximum tensile stress used to carry out Weibull analysis was from Equation 4.6 and the coefficient values in Table 4.7 for each thickness. The determination of $\hat{\sigma}_0$ and kV were made for a variety of thicknesses, the thinnest, the middle and the thickest of the 17 mm disks as summarized in Table 4.9. The integration value of Equation 3.6 for the 17 mm

disk was carried out over a tensile area of 6.5 mm in radius on the tension side. Figure 4.44 shows the experimental probability data and the Weibull distribution curve. The Weibull modulus was found to be 5.96 and the Weibull characteristic strength was 483.1 MPa. An average value of 20.7 MPa $m^{3/m}$ is suggested for the Weibull material scale parameter $\hat{\sigma}_0$ of 17 mm disks.

Table 4.10. Weibull parameters for the pressure on ring test on 17 mm disks.

Thickness (μm)	kV **(m^3)**	$\hat{m}$	$\hat{\sigma}_\theta$ **(MPa)**	$\hat{\sigma}_0$ **(MPa $m^{3/m}$)**
180	7.62×10^{-9}	5.96	483.1	21.0
195	7.00×10^{-9}	5.96	483.1	20.7
205	6.63×10^{-9}	5.96	483.1	20.5

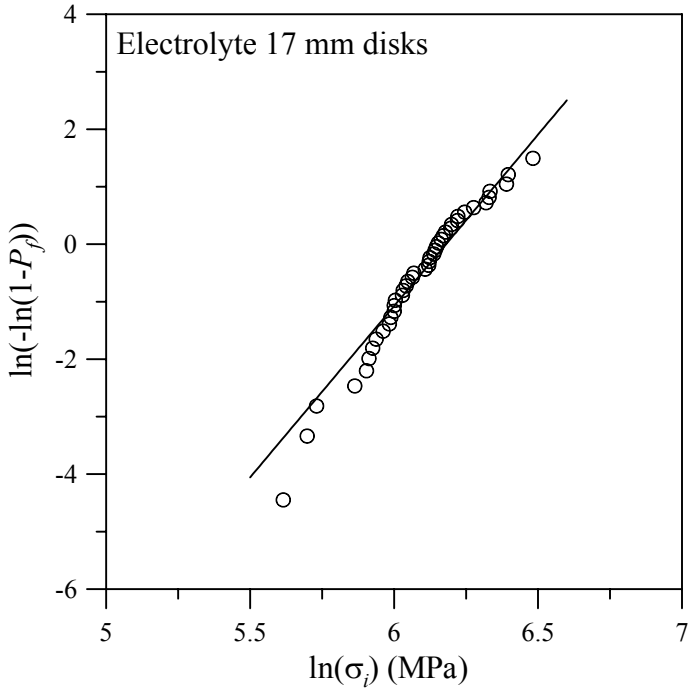

Figure 4.44. Weibull plot for 17 mm electrolyte disks.

4.4.3 Electrolyte beams

Weibull analysis was carried out for the unaged and aged electrolyte beam four-point bend test results. The result is summarized in Table 4.10 and the Weibull plot is shown in Figure 4.45.

Table 4.11. Weibull parameters for the YSZ beam.

Sample	$\hat{m}$	$\hat{\sigma}_\theta$ **(MPa)**	**Average** V **(m^3)**	$\hat{\sigma}_0$ **(MPa m$^{3/m}$)**
YSZ unaged	9.34	163.7	6.458×10^{-7}	24.1
YSZ aged	11.56	133.8	6.557×10^{-7}	28.0

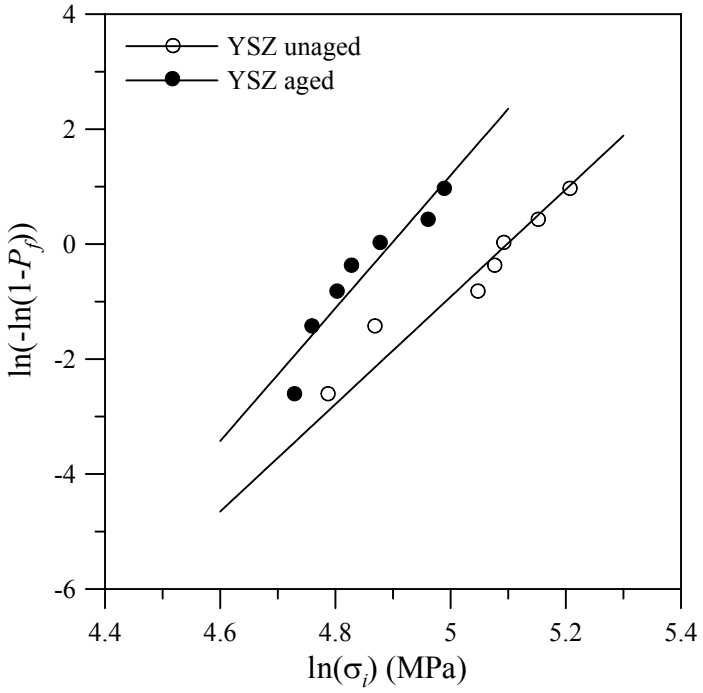

Figure 4.45. Weibull plot for YSZ electrolyte beam bend tests.

The unaged and aged specimens are distributed in different populations. The unaged electrolyte beams had 9.34 and 163.7 MPa for the Weibull modulus

and the Weibull characteristic strength, while the aged ones had 11.56 and 133.8 MPa, respectively. Therefore, the long-term aging affected the material Weibull characteristic strength with a relative degradation of about 18.3% from the normal samples. Considering the average volume for each group, the estimated Weibull material scale parameter was found to be 24.1 MPa $m^{3/9.34}$ and 28.0 MPa $m^{3/11.56}$ for the unaged and aged samples, respectively.

4.5 Discussion

From the hardness measurement of the electrolyte on the surface and the edges, the values of the hardness varied little. This implies that the thickness of 200 μm was proper for the measurement without possible effects from the stainless steel substrate, and that the hardness was independent of orientation. The aging effects on the hardness were not very apparent, since the average hardness increased from 13.72 GPa to 14.60 GPa. Also, from the SEM of the electrolytes before and after aging, not much difference in the grain size was detected, which would have had a microstructural effect on the hardness. Vickers indentation tests indicated that the hardness of the 8YSZ electrolyte was about 11.7 GPa (Kwon *et al*. 2001; Mizutani *et al*. 1994) and 9.4 GPa (Abraham and Gritzner 1993). This study indicated an average value of 13.70 GPa for all the tested electrolytes. The fracture toughness had an increasing value of 20% from 2.25 MPa $m^{1/2}$. The electrolyte C and D tested had value of 1.88 MPa $m^{1/2}$ and 1.91 MPa $m^{1/2}$. For 8mol% YSZ, other studies reported the fracture toughness of 2.4 MPa $m^{1/2}$ (Jue and Virkar 1990) or 1.3 MPa $m^{1/2}$ (Kwon *et al*. 2001; Mizutani *et al*. 1994). Since it is difficult to measure the exact crack length because the cracks may not be straight, a systematic bias would be involved in the measurements. A fracture toughness measured with double torsion method was reported as 1.61 MPa $m^{1/2}$ (Selcuk and Atkinson 2000). The values of K_{IC} may vary by a factor of more than 3 depending on the test method and the form of the material and it was thought

that the results for the double-torsion measurements are more reliable (Selcuk and Atkinson 2000).

From this study the test methodologies might have great influence on the failure parameters. The Weibull strengths are 139 MPa, 483.1 MPa and 893.8 MPa and the Weibull moduli are 3.69, 5.96, and 7.35 for the tensile, pressure on ring and ball on ring tests, respectively. The values would be different from materials not sintered at same time. 8YSZ disks with a diameter of 21 mm and a nominal thickness of 150 μm were tested in a ring-on-ring fixture (Selcuk and Atkinson 2000). The Weibull strength was 416 MPa with the Weibull modulus of 6.7, while 8YSZ disks from two supporters with a diameter of 22 mm had value of 332 MPa and 294 MPa for Weibull strength and 5.1 for Weibull modulus (Lowrie and Rawlings 2000). Another ring-on-ring bi-axial strength study on 8YSZ disks with a diameter of 23 mm and a nominal thickness of 200 μm reported the Weibull strength is 232 MPa with the Weibull modulus of 5.7 (Atkinson and Selcuk 2000). By the ring on ring test, the results from different references have a maximum different value of 184 MPa, while in this study the min difference of Weibull strength, was 344 MPa, which is ascribed to the different test methodologies.

The fracture strength of brittle ceramics is generally reduced by the defects such as flaws, cracks, or inclusions, existing in the sintered body (Mencik 1992), and even small flaws on the surface could remarkably decrease the fracture strength (Jeong *et al*. 2002). The fractography study of the 23 mm ball on ring electrolyte disks in this study indicated the existences of impurities, near-surface pores, pore clusters and large grains, *etc*., and the near-surface pores were often close to the fracture origin (Lessing 2002). It is believed that that these defects could not be avoid in other tested specimens. It is easy to see that the possibility of existence of defects will increase with the volume/area. From the FEA results, the distribution of the tensile stress, which mainly contributes to the fracture, varies according to the test methodology. The tensile plate test has more uniform

stress distribution than the others. The peak stress of the ball on ring test drops sharply from the center compared to that of the pressure on ring test as seen in Figure 4.24 and Figure 4.34. The more uniform the tensile stress distribution, the more volume/area fraction is subjected to possible fracture stress. For the tensile test, not only the surfaces but also the internal volume were subjected to uniform tensile stress, and the volume fraction subjected to the tensile stress was max compared to the others. This means that more defects, which existed in the specimen, would have contributions to lowering the fracture strength. Under the ball on ring test, only the surface very closely around the center has the highest failure possibility. About 10% of the radius away from the center of the disk, the tensile stress drops more than 50% from the peak stress. However, for the pressure on ring, it reduces to 50% of the peak stress at a distance from the center of about 70% of the radius.

Tensile stress concentrations also have some contribution to the position where the fracture occurs and lower the fracture strength. In the tensile test, most of the samples failed close to the adhesive tab, where the stress concentration were caused by the thickness changes between the specimen and the adhesion. For the pressure on ring test, on the pressurized side, since the O-ring would deform very much under pressure, there was a tensile stress peak located underneath the O-ring. The maximum was about 60% of the peak stress on the free side, which could induce failure near the location where the O-ring sealed.

The pressure on ring test method is a better one for brittle thin film fracture strength tests. It is low cost, convenient, and relatively easily done. For the pressure on ring test, compared to the peak stress, the stress concentration was not dominant. The tensile test was most affected by the distribution of deflects but would be a good test method to measure the fracture strength of the ceramic thin film if the stress concentrations could be eliminated. Ball on ring tests are easier to perform but it may yield higher fracture strength than the brittle material demonstrated under applications that involve uniform stress over large volumes.

4.6 Conclusions

In this chapter, different mechanical methodologies have been developed and used to characterize the electrolyte materials, and the some experiments were analyzed with FEA. From this study, several conclusions can be made and are listed below:

- The cracks of the microindentations were found to be median crack systems. The hardness and fracture toughness for the given electrolyte materials were found. The hardness evolution during aging did not change apparently with the aging time studied.

- The plates in tension failed mostly close to one of the tabs, which held them adhesively because there were stress concentrations close to the corners of the plate.

- The FEA result for the ball on ring test was verified with the ASTM F394 standard, and the nonlinear relationship of the load and peak stress from FEA analysis was used to predict the failure tensile stress for each sample.

- The experimental data for the pressure on ring test were well predicted by the FEA model, and the stress/strain distributions were determined for the pressurized disk. Using the FEA model, the maximum failure stress was reported for each test.

- Based on the experimental or FEA predicted results, the Weibull analysis was performed for the flexural tests and their Weibull moduli, Weibull characteristic strengths and Weibull material scale parameters were found.

- The aging had an effect on the Weibull characteristic strength for the electrolyte beam, with a degradation of about 18.3% compared to the unaged one.

- The test methodologies have in influence on the fracture strength; the pressure on ring test method is the preferred one for brittle thin film fracture strength testing.

CHAPTER 5
ELECTROCHEMICAL DURABILITY OF SOFCS

In this chapter, the electrochemical durability of the SOFC materials was studied. Some half cell SOFCs were aged at 1000 ^{o}C up to 1000 hours and DC and AC electrochemical test methodologies were used to measure the electrochemical properties. After aging the microstructure and chemical compositions were studied with SEM, EDS, B.E.T. and XRD.

5.1 Experiments

Half cell SOFCs with cathode on an electrolyte substrate were studied. Chemical analysis of the cathode and the electrolyte was performed using EDS before the aging test. The aging test was run at 1000 ^{o}C in air. I-V curves and impedance measurements were performed at different temperatures before and after durability testing. I-V curves were swept with the Keithley 2440 SourceMeter. The EIS measurements were carried out using a combination of instruments from Solartron (1260 Impedance Gain-Phase Analyzer + 1287 Electrochemical Interface). The maximum frequency used in the impedance was 10^6 Hz and the lowest was 0.1 Hz. After being painted with platinum paste and covered with the platinum mesh, the working area of the button SOFCs was about 3.14 cm^2. For button SOFCs aged with applied current, a constant current of 1 A or about 318 mA/cm^2 was applied using the Keithley 2440 Sourcemeter. The voltage evolution was measured from time to time. The I-V curves and impedance measurements were performed approximately every 100 hours. The half cell SOFC 1, 2 and 3 were all painted with platinum and aged together. The half cell SOFC 4 and 5 were half pieces from a single half cell SOFC and the half cell

SOFC 5 was aged in air 935 hours without any extra pre-processing. The half cell SOFC 6 was aged with a constant air flux of 15.0 ml/min pumped onto the cathode side. The length of the platinum leads and the thickness of the platinum paste were not exactly the same from cell to cell. The experimental details for the tested SOFCs are listed in Table 5.1.

Table 5.1. Aging test for the half cell SOFCs.

Name	**Half SOFC 1**	**Half SOFC 2**	**Half SOFC 3**	**Half SOFC 4***	**Half SOFC 5***	**Half SOFC 6**
Aging time (h)	1000	1000	1000	0	935	1000
Current load	1A	No	1A after 500 h	N/A	No	1A
V-Time curve	Yes	N/A	No	N/A	N/A	Yes
Sweep I-V	Yes	Yes	Yes	N/A	Yes	Yes
EIS	Yes	Yes	Yes	N/A	No	No

*Cell4 and cell5 were half pieces from a single half cell SOFC.

During the aging, the YSZ beam studied in CHAPTER 4 was monitored for the tendency of resistance change over time. The ionic conductivity of the electrolyte beam was measured using the 2440 SourceMeter. Both ends of the electrolyte beam were painted with platinum paste and rolled with platinum wires. The resistance of the platinum wires was negligible compared to that of the electrolyte beam. The effective dimension of the conductivity measurement was 61.6×2.5×6.59 mm. The changes of ionic conductivity before and after aging at different temperatures 600, 700, 800, 900 and 1000 ^{o}C were measured.

The samples were examined by scanning electron microscopy (SEM). X-ray element analysis was performed with EDS.

The XRD and B.E.T. tests were run on the samples of half cell SOFC 4 and 5. After broken into small pieces, the B.E.T. test for the samples was carried

out with a Sorptomatic 1990 and the data were analyzed using an Advanced Data Processing 4.0. For the XRD test, they were scanned from 20^o to 90^o with a step of 0.02^o, and after the test, the data was analyzed to investigate the possible chemical components.

5.2 Results and discussions

5.2.1 Chemical analysis

The half cell SOFCs used in this study consisted of a cathode and electrolyte, having a layer of cathode paste of around 15-20 μm thickness and 10 mm diameter on the 180 μm thick electrolyte. To see the interface of the button SOFCs, one of them was fractured manually. The SEM pictures of the surface of the cathode, the electrolyte and the interface between cathode and electrolyte are shown in Figure 5.1, Figure 5.3 and Figure 5.3, respectively. In the porous cathode, it is clearly seen that there are two different grain shapes, namely smooth grains and multifaceted grains, respectively. Few contaminations were found on the cathode. The EDS test results for the cathode surface, the smooth grain, and the multifaceted grain and the electrolyte are show in Table 5.2. The EDS results for the cathode surface suggest that the smooth grains are YSZ and the multifaceted ones are $(Pr_{1-x}Sr_x)MnO_{3\pm\delta}$, respectively. From the atomic concentration of Pr and Sr in smooth grains, the x has a value of about 0.3. The EDS tests as shown in Figure 5.4 were performed for the electrolyte material on the half cell SOFC surface and the fractured surface. The electrolyte material is the 8 mol% YSZ from the EDS result. On the edge, an intensity peak of Mn was found. No other elements were apparently found in this kind of SOFC.

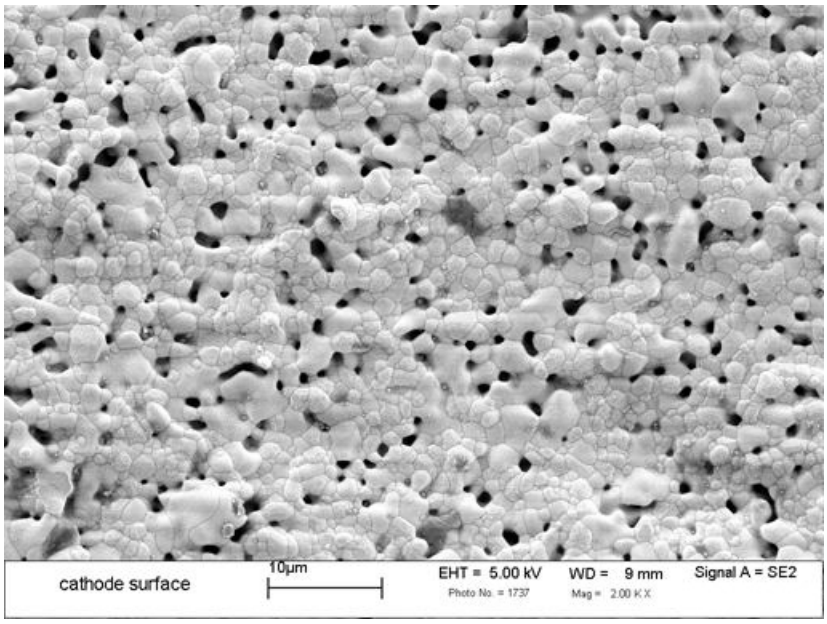

a) SEM of the cathode surface at 2 kX.

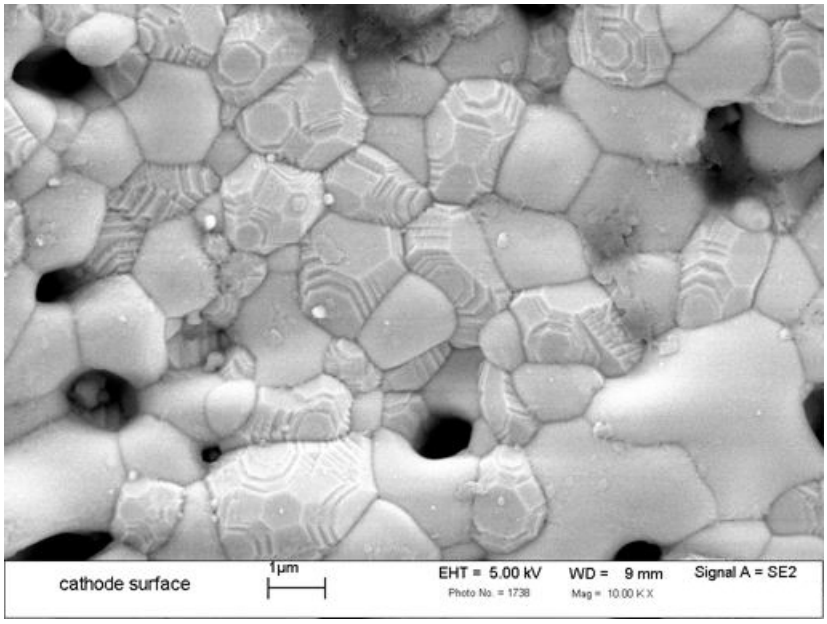

b) SEM of the cathode surface at 10 kX.

Figure 5.1. SEM of the cathode surface.

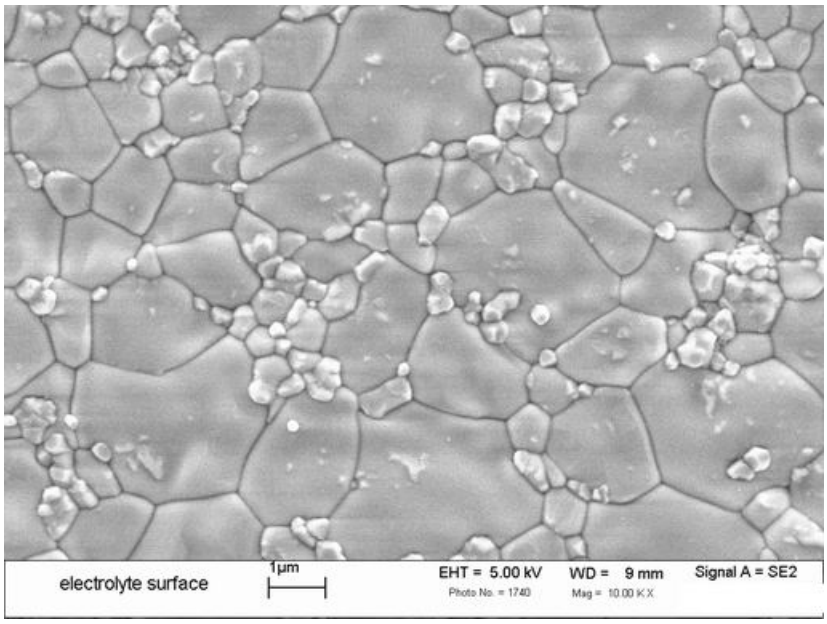

Figure 5.2. SEM of the electrolyte substrate surface at 10 kX.

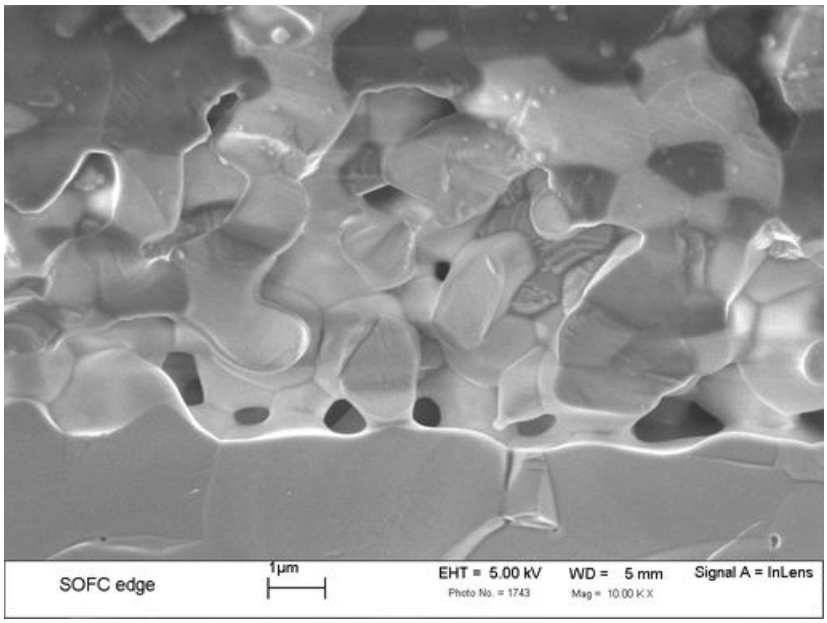

Figure 5.3. The interface of the cathode and electrolyte fractured manually.

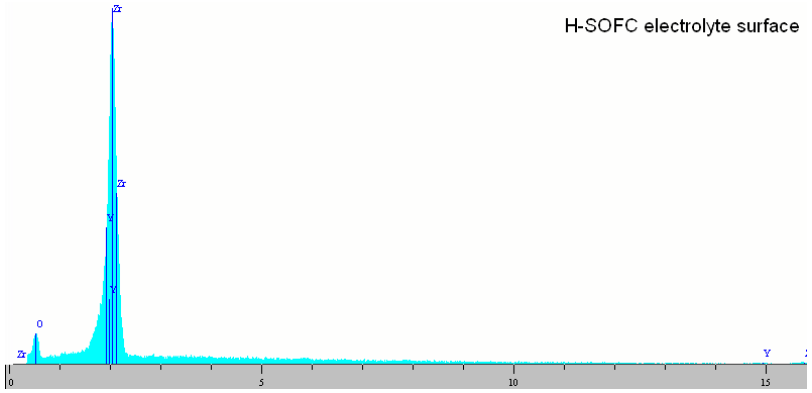

a) On the surface

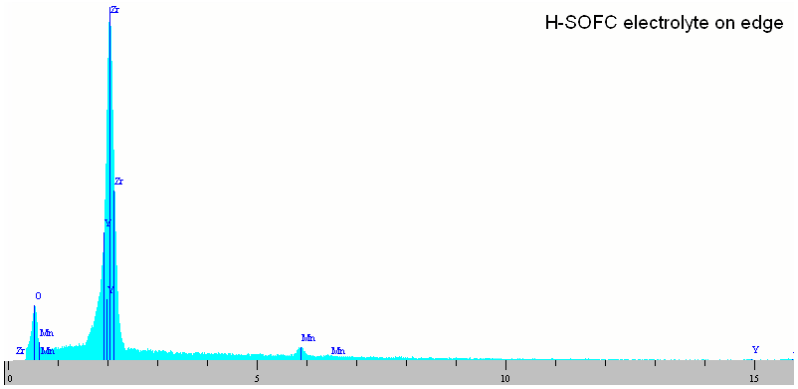

b) On the edge

Figure 5.4. EDS spectrum of the electrolyte of the half cell SOFC.

Table 5.2. Elements atomic concentration (%) in the half cell SOFCs.

	Pr	**Sr**	**Mn**	**Y**	**Zr**	**O**
Cathode surface	8.39	2.34	4.54	4.08	13.15	67.58
Smooth grain	4.01	1.73	1.06	5.82	18.33	69.06
Multifaceted grain	10.51	3.65	8.29	0.30	2.40	74.86
Electrolyte surface	N/A	N/A	N/A	7.97	21.90	70.14
Electrolyte edge	N/A	N/A	0.904	5.89	16.73	76.48

5.2.2 Durability test

5.2.2.1 Half cell SOFCs

Current-voltage (I-V) curves swept at 1000 ^{o}C for half cell SOFC 1, 3 and 6 before and after the durability test are shown in Figure 5.5. Half cell SOFC 1 and 6 were aged with 1 A current all the way, and after long-term aging, the ASR (Area Specific Resistance) of both SOFCs increased, which was mainly ascribed to changes in the electrolyte. Half cell SOFC 3 was aged in air only for the first 500 hours and after that it was polarized with current of 1 A. From the slope of half cell SOFC 3 in Figure 5.5(b), the resistance of half cell SOFC 3 increased after 500 hours aging in air. However, after the operation condition was changed to polarisation, there was not apparent changes of I-V found at the end of the test. The series resistance from the I-V curve is mainly from the electrolyte. The degradation of the conductivity of the electrolyte was reported to have an exponential decreasing rate with time (Muller *et al*. 2003).

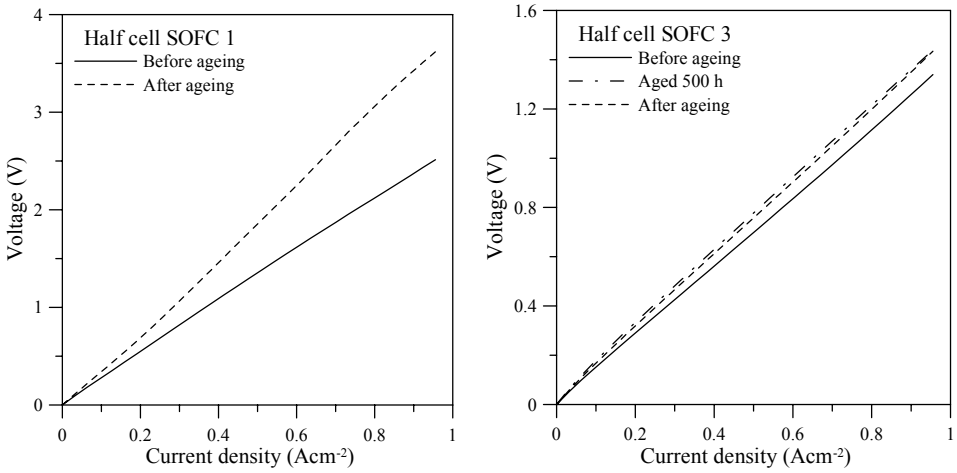

a) Half cell SOFC 1. b) Half cell SOFC 3.

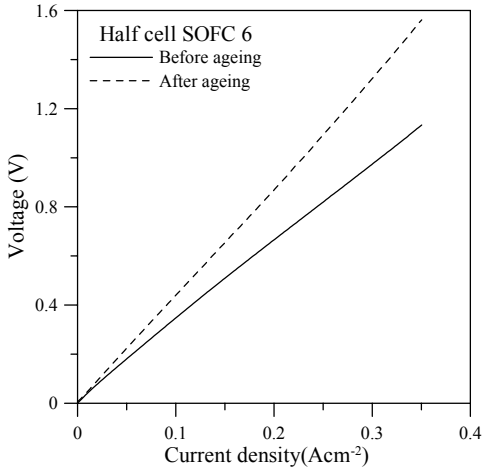

c) Half cell SOFC 6.

Figure 5.5. I-V curves for half cell SOFCs.

In Figure 5.6 and Figure 5.7, the voltage and series resistance evolutions with time for them are shown. The series resistances were measured at low overvoltage, when the current-voltage curves are assumed to be linear. During both tests, there were unexpected temperature drop due to power outage or other operations. This is the reason why there were unusual voltage peaks in those plots. Total voltage changes of 0.353 V and 0.419 V were found for half cell SOFC 1 and half cell SOFC 6 after the durability test.

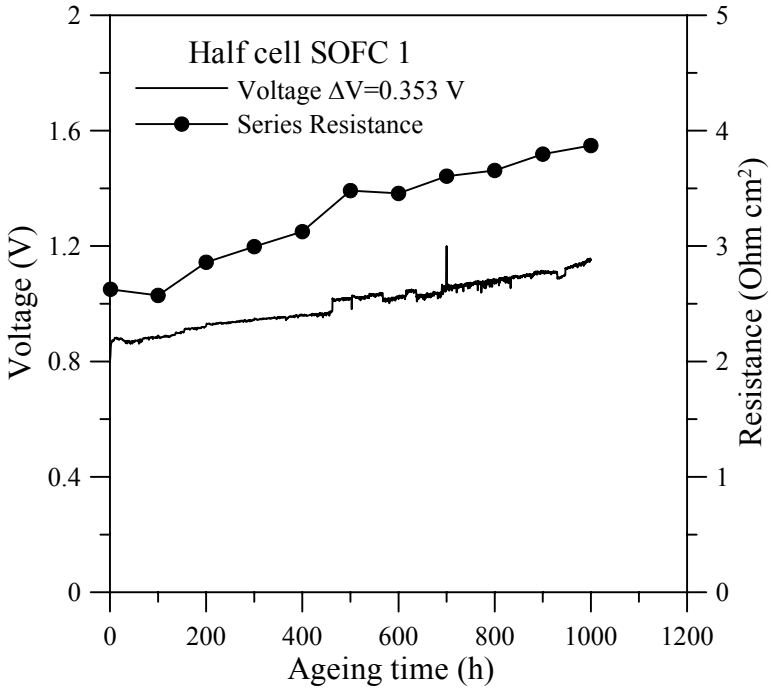

Figure 5.6. Voltage evolution during aging for half cell SOFC 1.

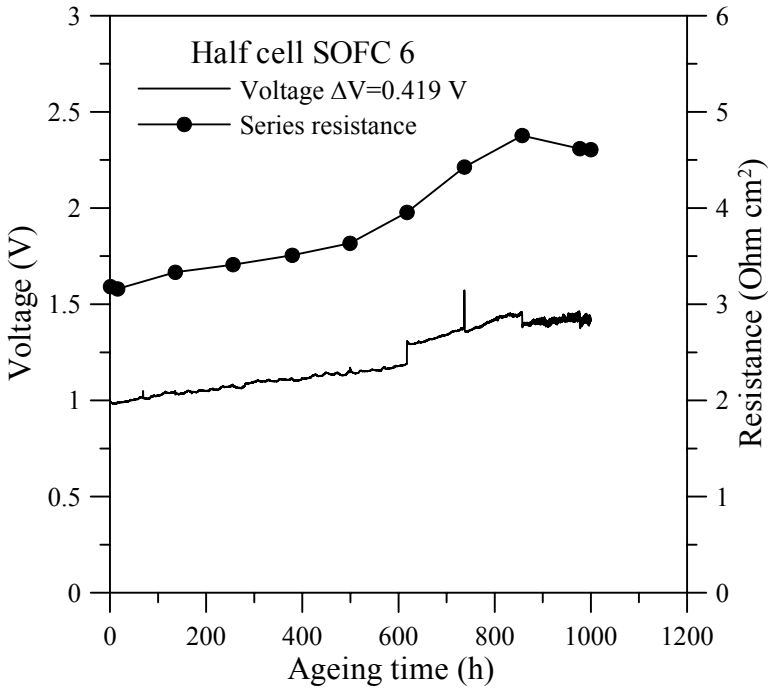

Figure 5.7. Voltage evolution during aging for half cell SOFC 6.

5.2.2.2 YSZ beam

The ionic conductivity was measured for the YSZ beam aged in air at 1000 ^{o}C from time to time. In Figure 5.8, the evolution of ionic conductivity vs. time is shown. The ionic conductivity dropped continually with time, while the degradation rate slowed down. There was an ionic conductivity drop from 15.98 to 8.42 S/m after 1000 hours aging in air, about 47.3% of the initial conductivity. The study on the degradation of the zirconia based electrolyte has been reported (Muller *et al*. 2003). When the 8YSZ sintered at 1350 ^{o}C was annealed at 950 ^{o}C, its ionic conductivity dropped from the initial value of 16.1 S/m to 12.4 S/m and 10.8 S/m after 500 hours and 1000 hours aging, respectively. The 3YSZ sintered at 1300 ^{o}C degraded from 4.9 S/m to 4.2 S/m and 4.0 S/m after the same aging duration above. After 1000 hours aging, the 8YSZ and 3YSZ showed a degradation rate of 33% and 18%, and the degradation rate decreased exponentially by time.

The ionic conductivity at different temperatures before and after the aging test is given in Figure 5.9. A series of electrolyte ionic conductivities at different temperatures have been reported (Weber *et al*. 2000). The ionic conductivity of the YSZ beam was between the reported ones of 8YSZ (about 16 S/m at 1000 ^{o}C) and 3YSZ (about 6 S/m at 1000 ^{o}C). After long-term aging, it was still higher than that of 3YSZ.

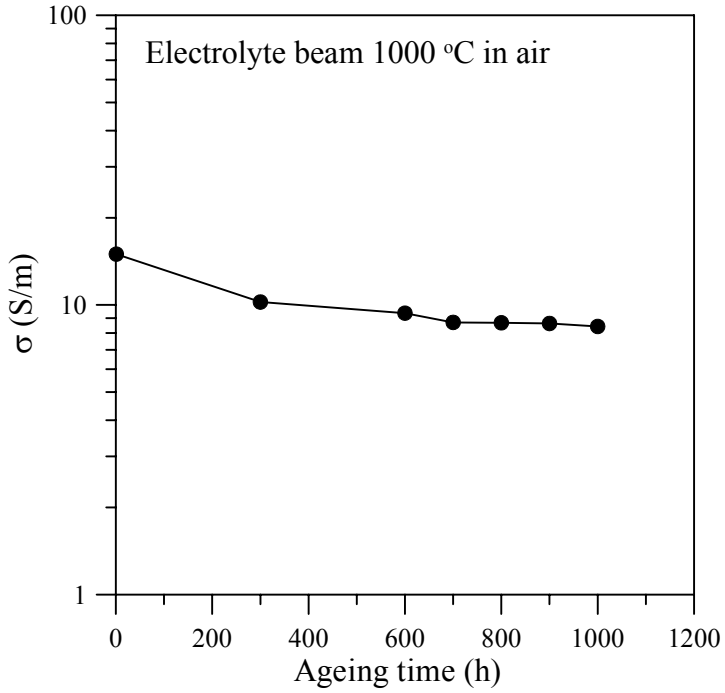

Figure 5.8. Ionic conductivity evolution of the electrolyte beam.

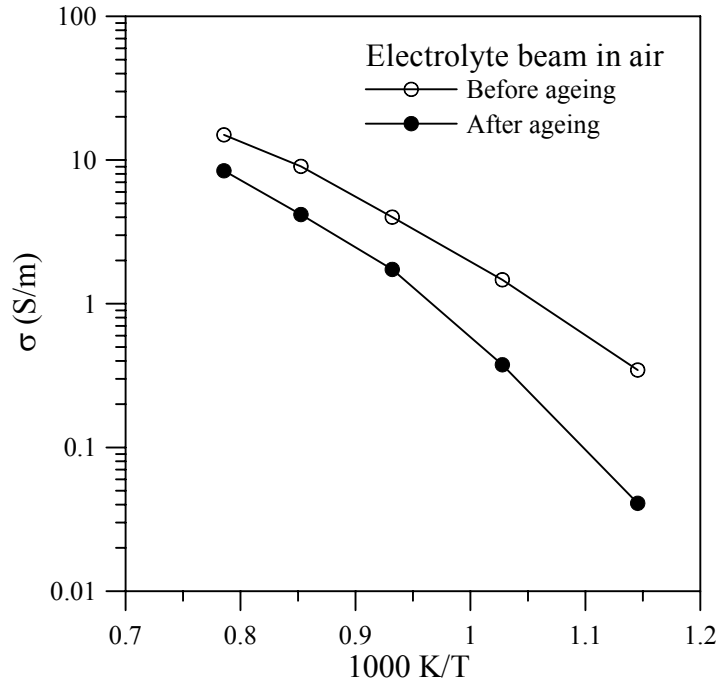

Figure 5.9. Aging effect on ionic conductivity of the electrolyte beam.

5.2.3 XRD and B.E.T.

5.2.3.1 XRD test

It is well known that it is undesirable for the cathode materials of SOFCs to react with electrolytes because the reactions will generally produce low- or non- conductive products. The XRD study on $Pr_{1-x}Sr_xMnO_3$ (Rim *et al*. 1998) sintered with YSZ at different temperatures for 100 hours, showed that when X=0.3, only $SrZrO_3$ was found at 1200 ^oC. In another study (Sakaki *et al*. 1999) on the mixture system at or over 1000 ^oC, when X<0.2, $Pr_2Zr_2O_7$ was found and when X>0.4, $SrZrO_3$ was found. No such chemical components were found when X=0.3. After long-term aging, the reactivity of $(Pr_{0.7}Sr_{0.3})MnO_{3\pm\delta}$ and 8YSZ was studied using the XRD test. The XRD results for the samples of half cell SOFC 4 and 5 were plotted in Figure 5.10. Tests were carried out on the surface of the composite cathodes. From the spectra of the XRD, there were no new chemical products found except the $(Pr_{0.7}Sr_{0.3})MnO_{3\pm\delta}$ and 8YSZ phases on the cathode surface for the SOFCs. After being aged at 1000 ^oC in air for up to 935 hours, any difference between the XRD spectra of half cell SOFC 5 and that of half cell SOFC 4 was not found.

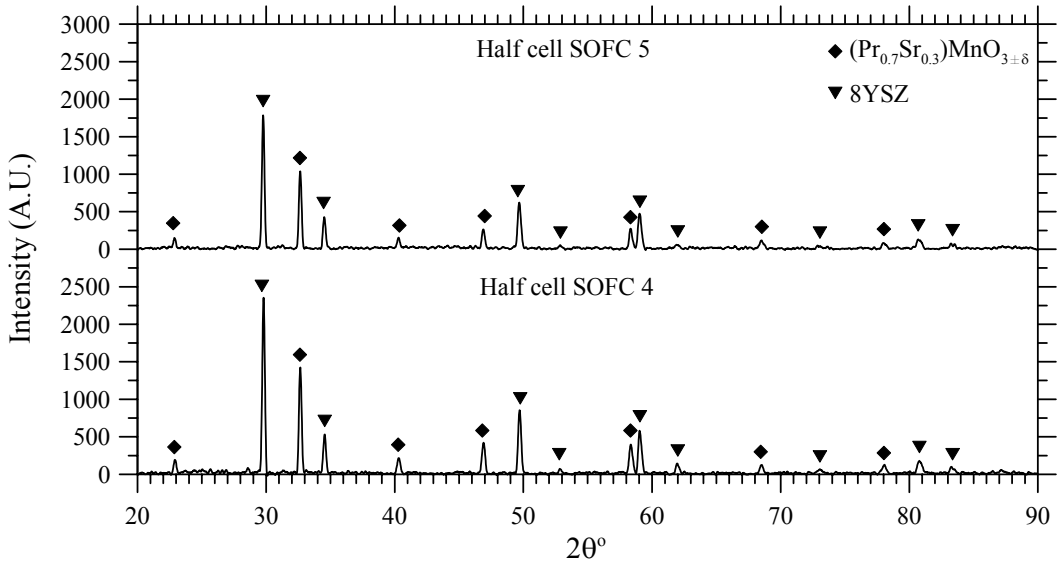

Figure 5.10. X-ray diffraction of the composite cathode.

5.2.3.2 B.E.T. test

The desorption curves and 3-parameter B.E.T. fit results of half cell SOFC 4 and 5 are shown in Figure 5.11. The calculated B.E.T. surface area is 0.46 m^2/g and 0.18 m^2/g for half cell SOFC 4 and 5, respectively. Pure $Pr_{0.7}Sr_{0.3}MnO_3$ has been reported to have a B.E.T. surface area of 2.0104 m^2/g with an average particle size of 3.365 μm (Rim *et al*. 1998). The mean pore widths predicted by the Cranston model were 225.5 nm and 292.3 nm, and the cumulative pore volumes were 0.2114 cm^3/g and 0.1653 cm^3/g for half cell SOFC 4 and 5, respectively. The predicted result illustrated that the volume percentage of a large amount of nano-scale pores was decreased after long-term aging test, which is reasonable for high temperature sintering of porous materials. This would decrease the capacitance of the cathode.

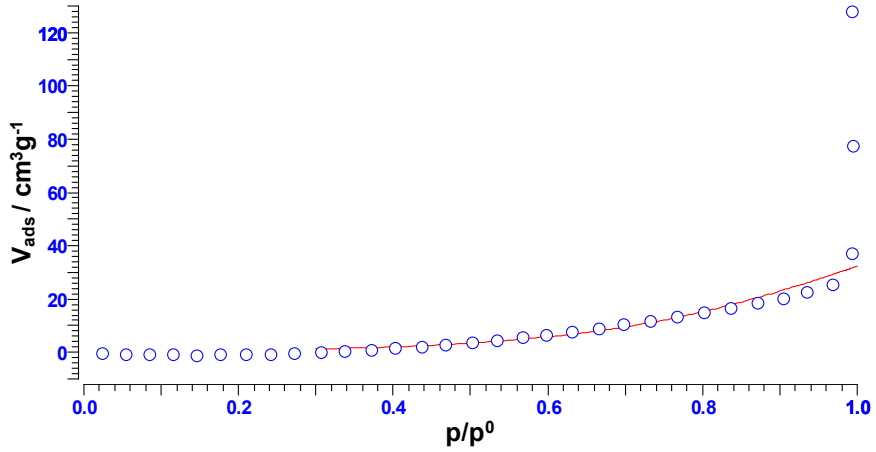

a) Half cell SOFC 4

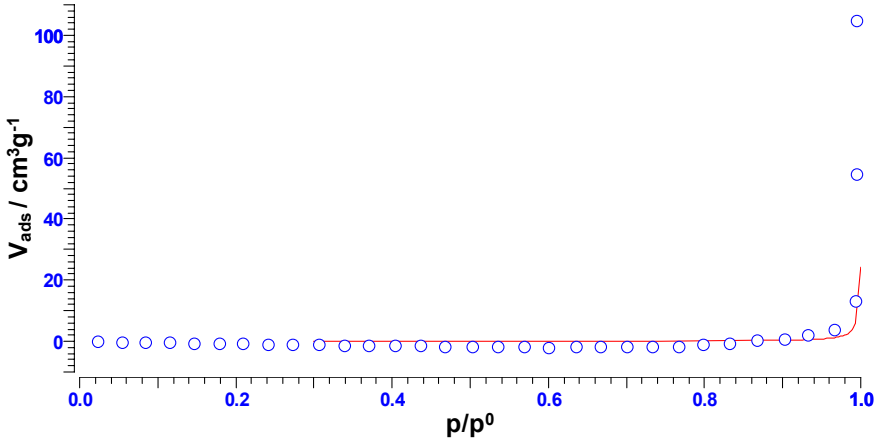

b) Half cell SOFC 5

Figure 5.11. Desorption curves and B.E.T. results.

5.2.4 SEM/EDS investigations

5.2.4.1 SEM

The SEM photos of the cathode surfaces are shown in Figure 5.12 to Figure 5.21 and the SEM photos of the fractured cross sections of the SOFCs are shown in Figure 5.22 to Figure 5.27. After the durability test, when half cell SOFC 1 and 3 were taken off from the holder, it was found that the some areas of the SOFCs cathodes were delaminated from the electrolyte substrate and left on

the platinum meshes as they were separated. The surfaces of the delaminated interface were also investigated. Figure 5.12 shows the area where the boundary of delamination occurred for half cell SOFC 1. Close views of the cathode surface and the electrolyte substrate with the cathode debris due to delamination are given in Figure 5.13 and Figure 5.14. From the SEM of the substrate, it is seen that on some delaminated area, where the grain boundaries of the 8YSZ are clear, the 8YSZ particles in the composite cathode were not sintered well with the 8YSZ electrolyte substrate. Similar results could be seen in the SEM picture in Figure 5.18 for the electrolyte substrate of half cell SOFC 3 after delamination. The coefficient of thermal expansion for $(Pr_{0.7}Sr_{0.3})MnO_{3\pm\delta}$ was found to be over $11.5\times10^{-6}/^{o}C$ (Sakaki *et al*. 1999) and in this study it was measured as $10.8\times10^{-6}/^{o}C$ for the electrolyte and an average value of $11.0\times10^{-6}/^{o}C$ for the composite cathode. If the cathode was not mixed completely or the 8YSZ particles in the composite were not sintered well with the electrolyte substrate, the thermal stresses might result in delamination during the durability test.

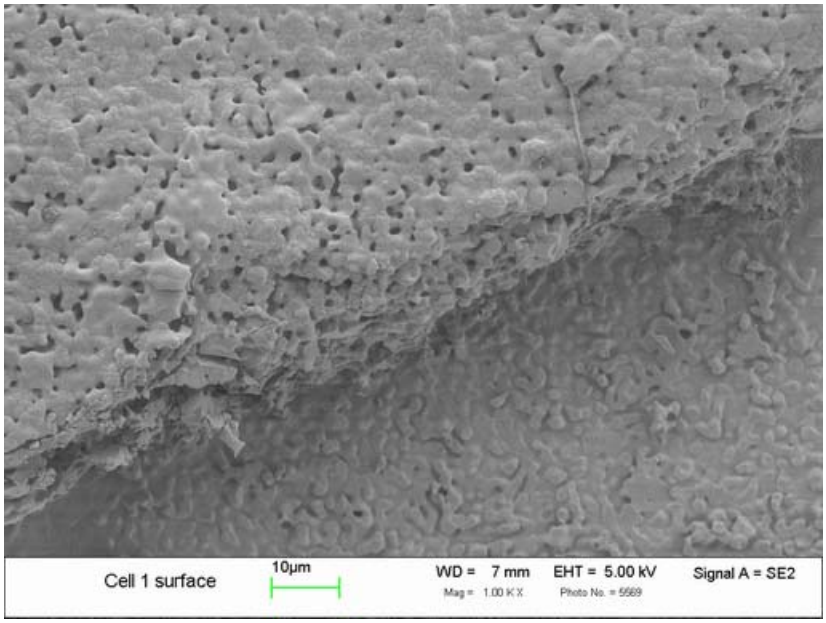

Figure 5.12. Surface of half cell SOFC 1 with delaminated interface.

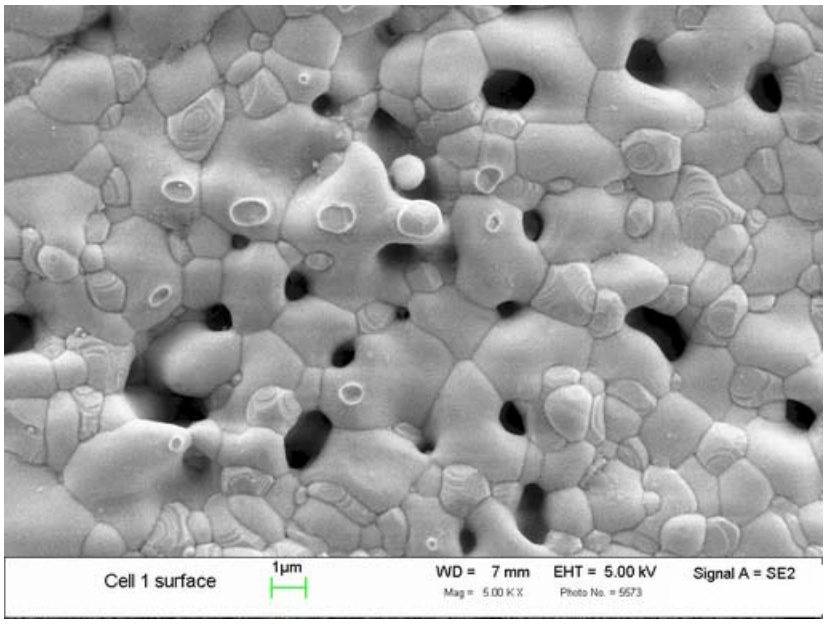

Figure 5.13. The cathode surface of half cell SOFC 1.

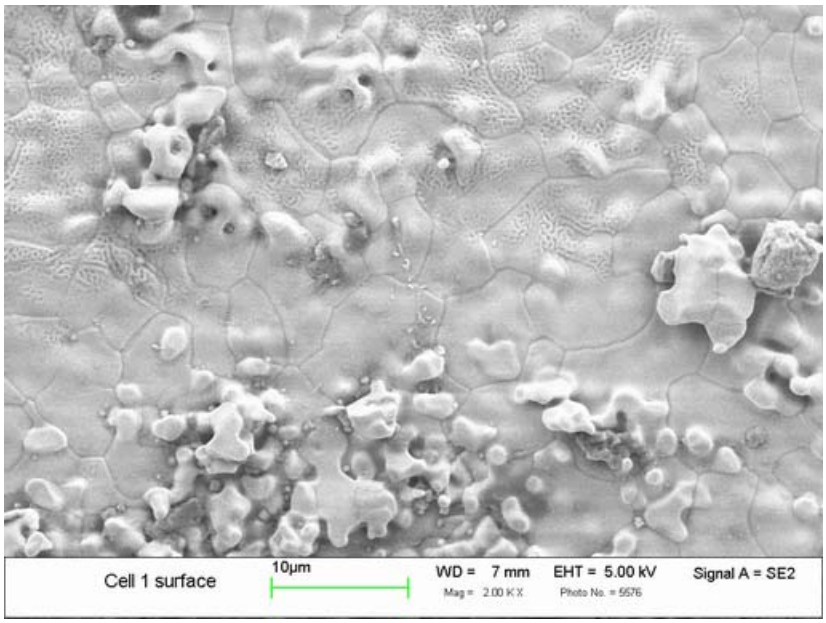

Figure 5.14. Electrolyte substrate of half cell SOFC 1 with cathode debris.

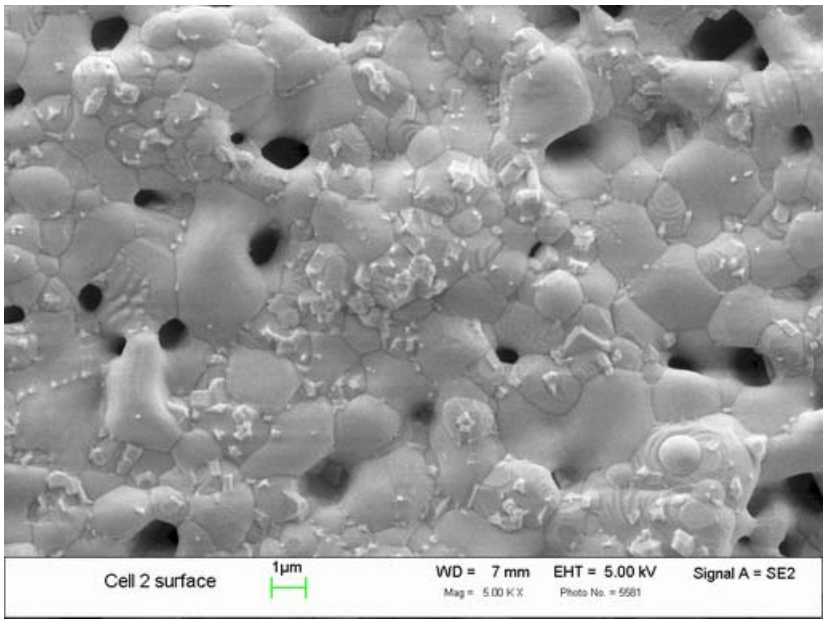

Figure 5.15. Cathode surface of half cell SOFC 2.

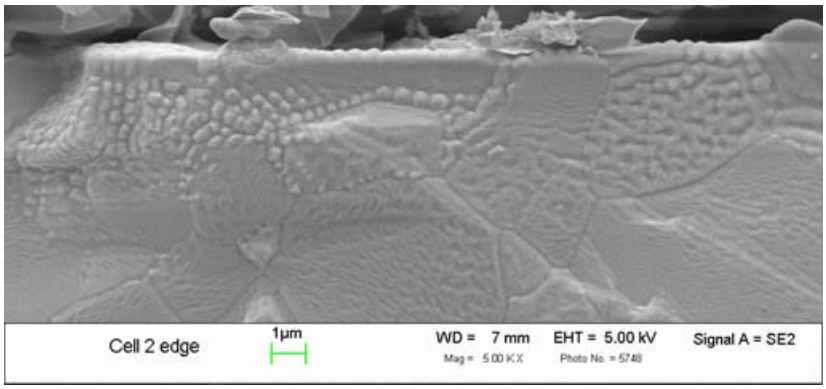

Figure 5.16 Electrolyte cross section of half cell SOFC 2.

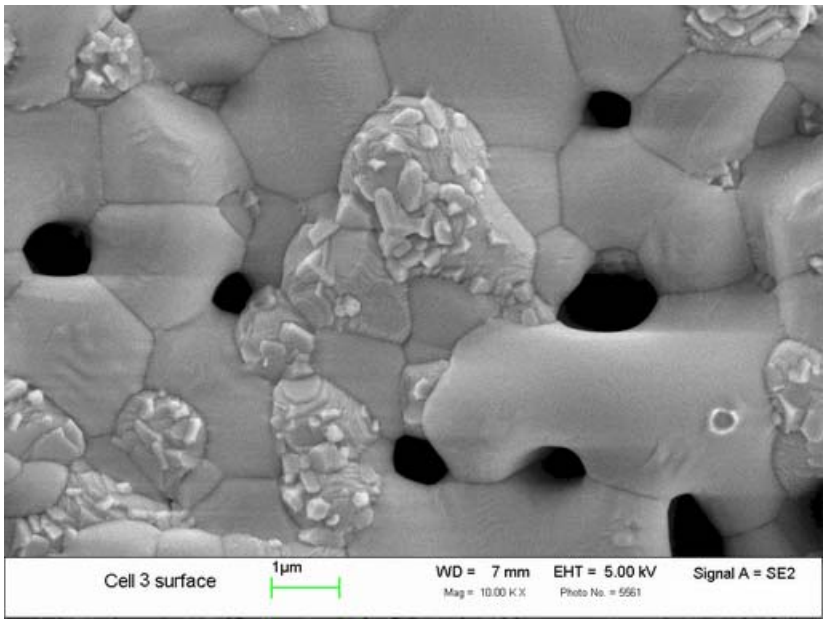

Figure 5.17. Cathode surface of half cell SOFC 3.

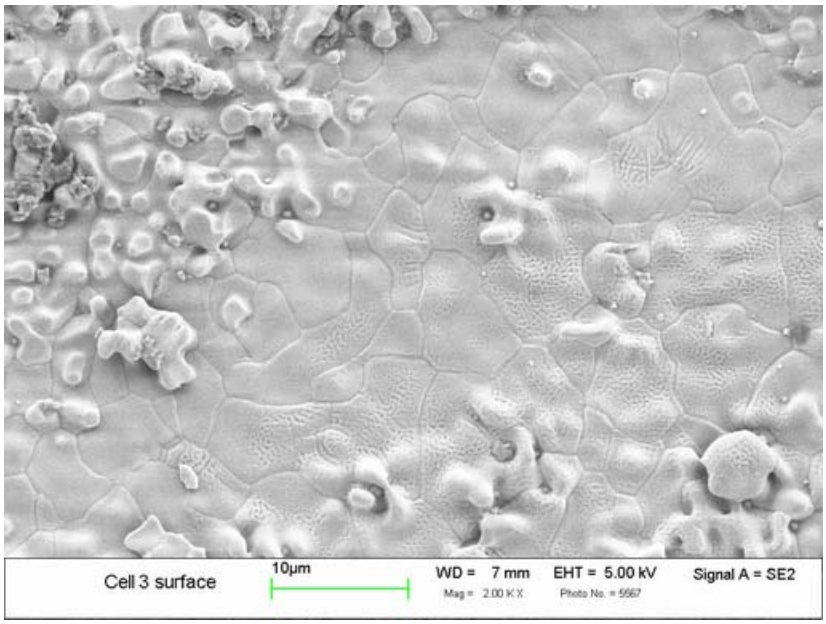

Figure 5.18. Delaminated electrolyte substrate of half cell SOFC 3.

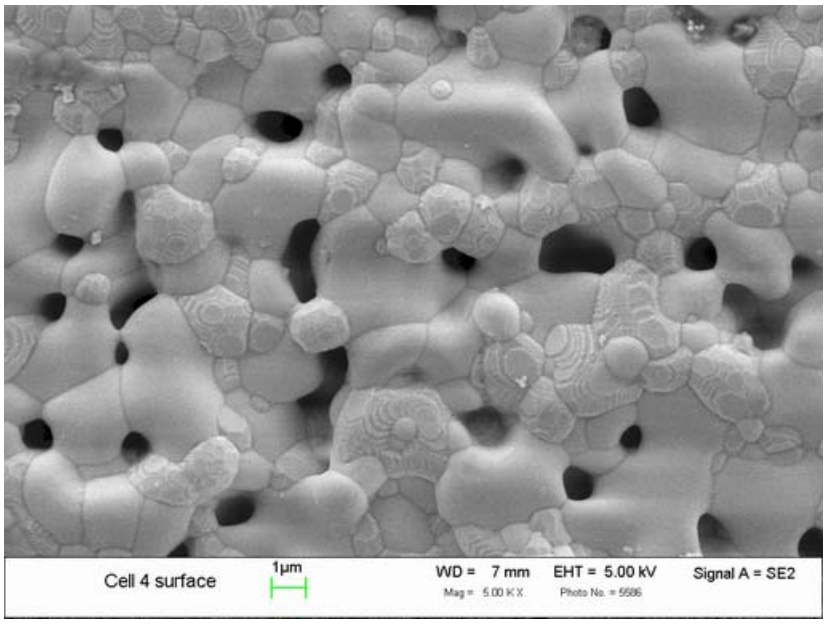

Figure 5.19. The cathode surface of half cell SOFC 4.

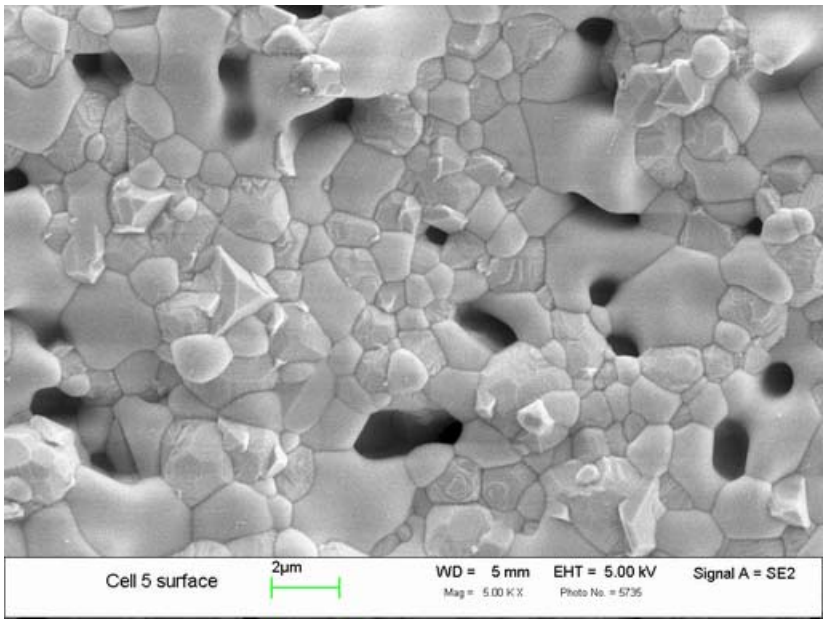

Figure 5.20. The cathode surface of half cell SOFC 5.

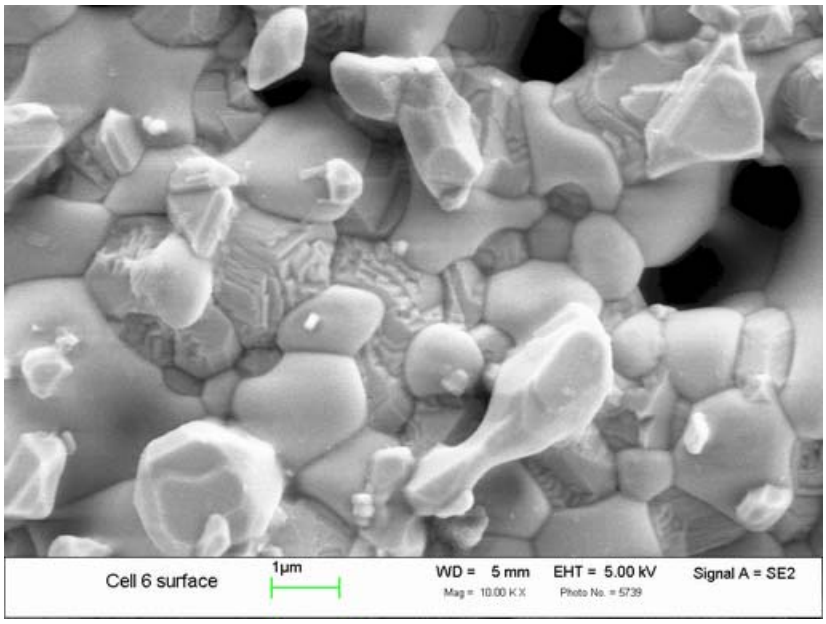

Figure 5.21. The cathode surface of half cell SOFC 6.

After aging, the shape of $(Pr_{0.7}Sr_{0.3})MnO_{3\pm\delta}$ grains on the aged half cell SOFC 2 and 3 was different from the unaged ones. Small grains grew on the multifaceted $(Pr_{0.7}Sr_{0.3})MnO_{3\pm\delta}$ grains. This situation is not that apparent on the surface of half cell SOFC 1, 5 and 6. Half cell SOFC 3 was aged in the same experimental condition as half cell SOFC 2 was for the first 500 hours aging. Half cell SOFC 5 was also aged in air without current, but it was not covered with Pt paste. EDS tests on the aged grains illustrated that not much difference was found from the unaged half cell SOFC and Pt was negligible on that kind of grain surface. The existence of the Pt paste may have catalytic function on the growth of the granular grains. However, the current load may be able to prohibit them from growing, since there were not many small grains growing on the surface of half cell SOFC 1 and 6.

For the electrolytes, on both the delaminated surfaces and the fractured cross sections, an amount of grains with non-smooth surface was found, as shown

in Figure 5.14, Figure 5.16, and Figure 5.18 *etc*. Similar structures have been reported at the Ni/YSZ interface and called hill and valley structure (Jensen *et al*. 2003). The structures were found where the electrolyte was covered with the cathode and occurred in or close to the interface. By decomposing into the hill and valley structure, the thermodynamically unstable surfaces attempt to reduce the surface free energy (Jensen *et al*. 2003). It suggests that the surfaces of the electrolyte without the cathode have the lowest surface energy, but the interfaces do not. From the SEM photos of delaminated electrolyte substrates, the hill and valley structures dominated where the YSZ powders left were sparse. There could be a gap area coming with the fuel cell or from the delamination as aging where the composite cathode powders were not sintered strongly onto the electrolyte. That the hill and valley structures occurred on the fractured cross section was possible after the electrolyte was fractured, since the cracked surfaces were not stable.

In Figure 5.22, a gap area of the interface with big blocks was found for half cell SOFC 1. In this area the pores in the cathode looked like they were blocked by some other materials. Gaps were also found for half cell SOFC 2 as shown in Figure 5.23. From other views of the interfaces of composite cathode and electrolyte, it is hard to tell the changes in pore distribution before and after aging.

The fractured cross sections of half cell SOFC 1, 3 and 6 show damaged sites close to the interface in the electrolyte. Compared to half cell SOFC 1 and 6, which were polarized during aging, the damage development of half cell SOFC 3 is not significant. It has been reported that under two hours polarization with a high current density of 4.5 A/cm^2 at 950 ^{o}C, the 500 μm thick 8YSZ disks (using Pt as electrodes) showed a similar damage development close to the anode side accompanying with grain boundary pore decoration and dislocation activity (Matus *et al*. 2003). A highly oxygen deficient material was found at the grain boundary fractures. At high current densities the oxygen interstitials, which might

result in dislocation decoration and pore formation, were swept to the anode. Matus *et al*. suggested that at low current densities the oxygen interstitial-vacancy pair would be almost immobile, and thus no consequence. In this study the current density was close to 0.3 A/cm^2, which was only 1/15 of the current density 4.5 A/cm^2, but the similar damage development was found. For half cell SOFC 3, which was aged 500 hours with current, the area where the damage developed was not pronounced compared with half cell SOFC 1 and 6. Until after two hours at the high current density value, a rapid rise of the resistance did not occurred (Matus *et al*. 2003). Therefore, the aging time with current would be another effective factor.

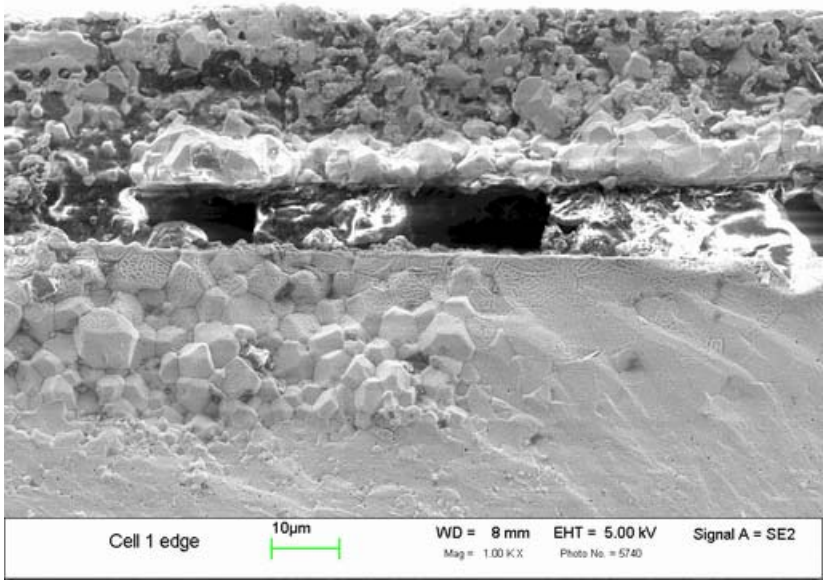

Figure 5.22. The edge of half cell SOFC 1.

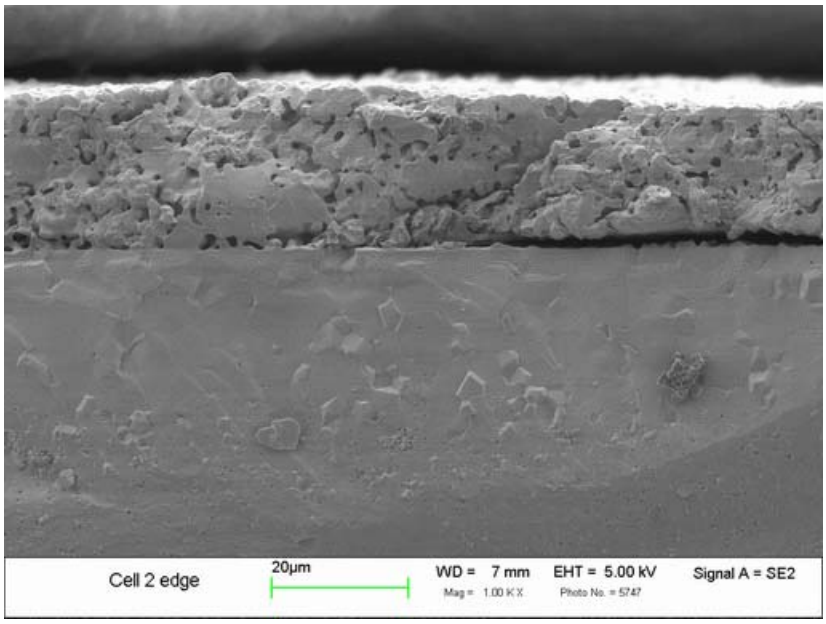

Figure 5.23. The edge of half cell SOFC 2.

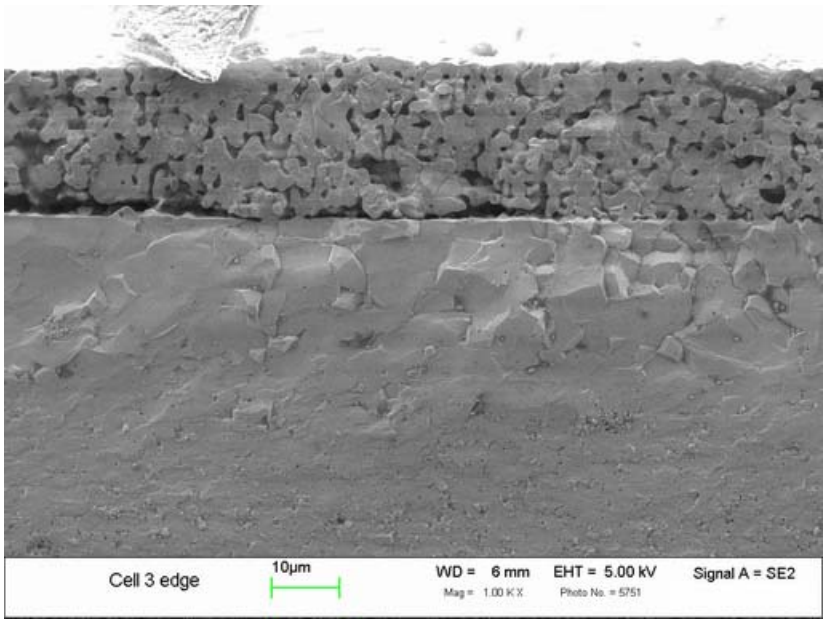

Figure 5.24. The edge of half cell SOFC 3.

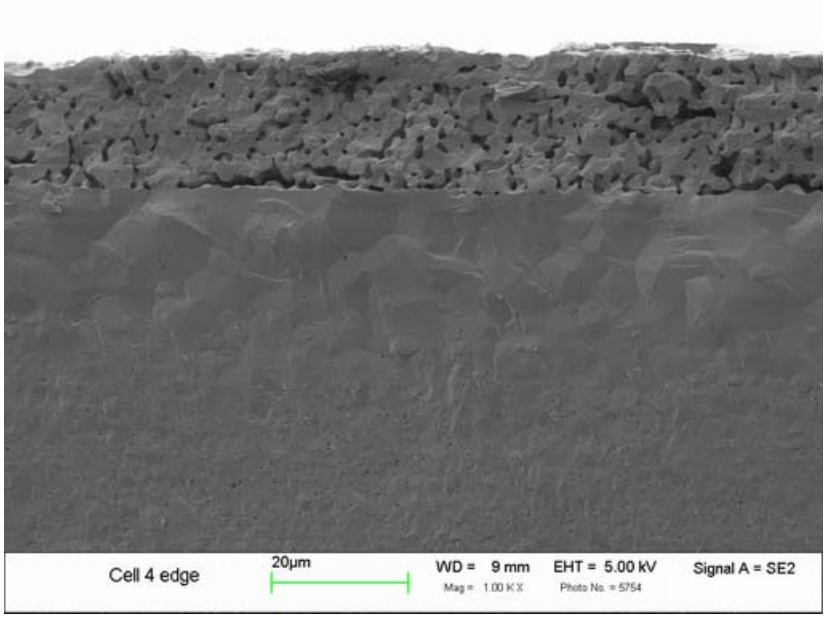

Figure 5.25. The edge of half cell SOFC 4.

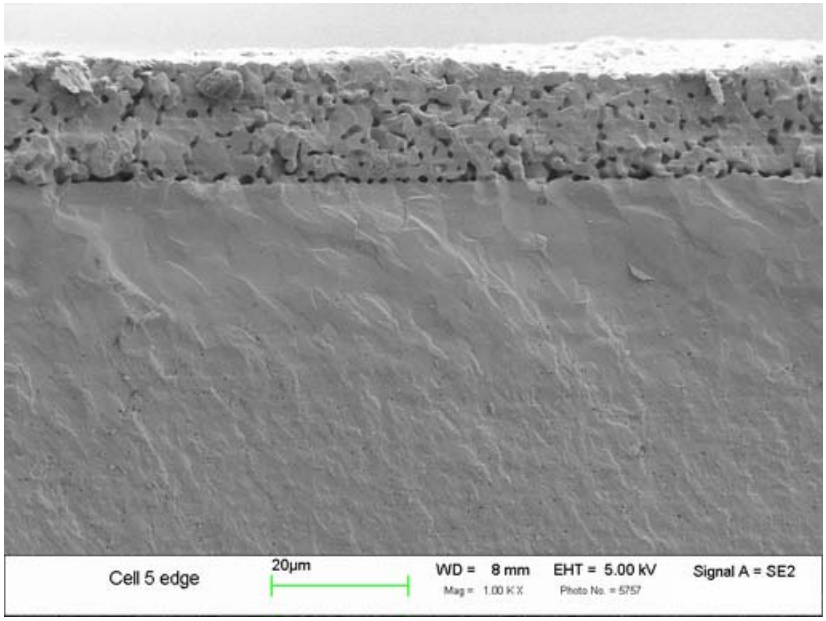

Figure 5.26. The edge of half cell SOFC 5.

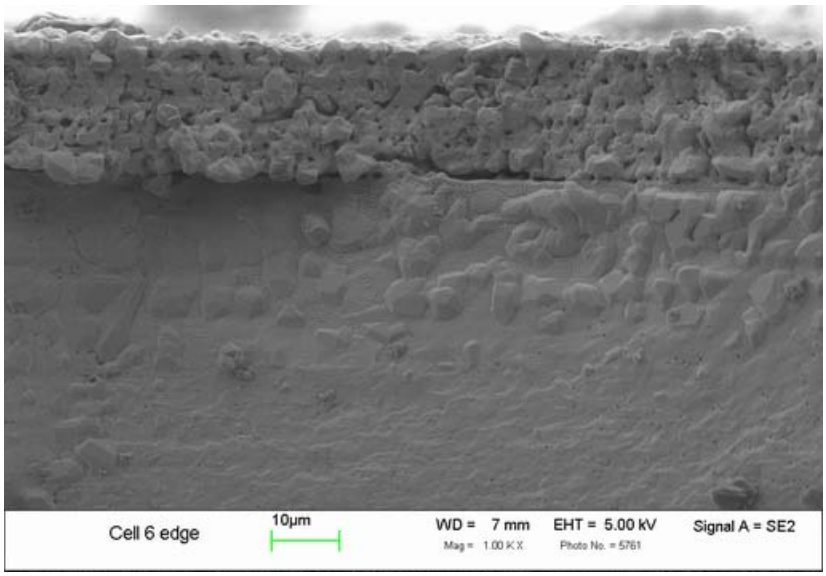

Figure 5.27. The edge of half cell SOFC 6.

5.2.4.2 EDS

On the edges of SOFC 1, 2, 3 and 4, EDS tests were performed on the electrolyte substrate with a series distance of 5 µm, 20 µm and 50 µm from the interface. The data with the distance of 0 µm was taken from the surface of the electrolyte substrate after delamination. Some elemental traces of Pr, Sr and Mn were found. The atomic concentrations of Pr, Sr and Mn are show in Figure 5.28, Figure 5.29 and Figure 5.30, respectively. The atomic concentrations of Pr and Mn were found to be higher close to the interface than inside the electrolyte for all of the samples tested with EDS. As deep as 50 µm into the electrolyte, the concentrations are almost 0. Where the distance is 5 µm, the data show that the Pr and Mn concentrations of half cell SOFC 2 is higher that those of other SOFCs. No other apparent difference in the concentrations was found for SOFCs tested with and without current load. This work shows that the concentration distribution of the cathode material in the electrolyte was not the result of long-term aging, but one from making the interface, since it was found in the unaged half cell SOFC 4. The atomic concentrations of Sr distributed randomly with distance from SOFC to SOFC.

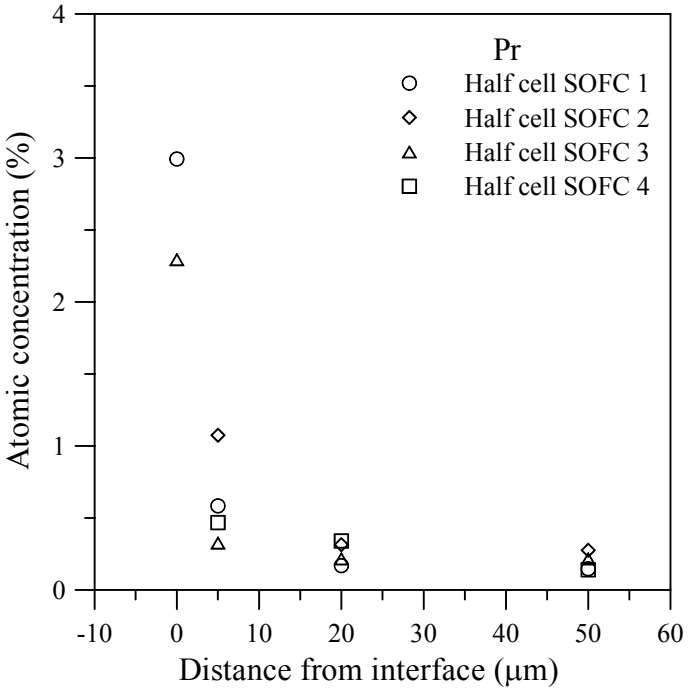

Figure 5.28. Pr atomic concentration.

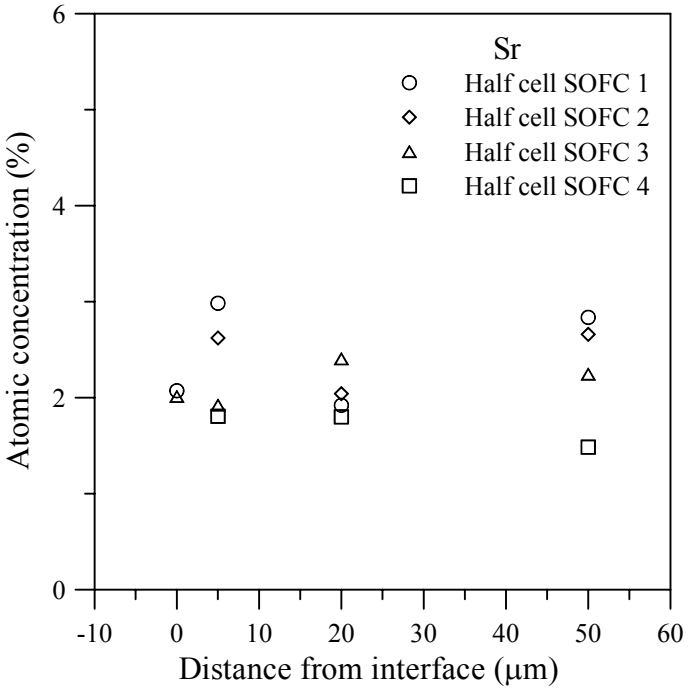

Figure 5.29. Sr atomic concentration.

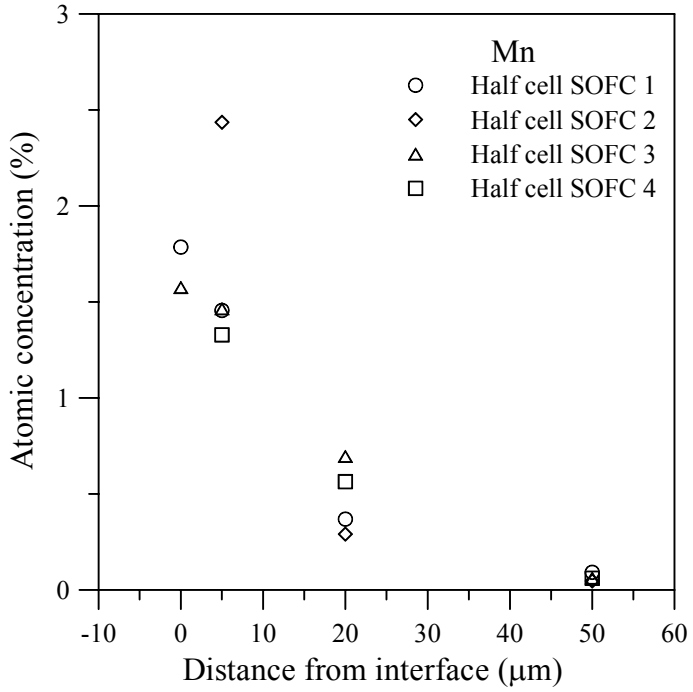

Figure 5.30. Mn atomic concentration.

5.2.4.3 Contaminations

For the Ni/YSZ interface it was reported that the polarization resistances for the impure electrodes are one order of magnitude higher than for the pure electrode and the impurities increased the hill and valley structure height (Jensen *et al*. 2003; Mogensen *et al*. 2002). Many contaminations or impurities were found from the cathode to the electrolyte. The dark particles were found on the delaminated interfaces as shown in Figure 5.31 to Figure 5.33. Inside the electrolyte substrate as shown in Figure 5.34, impurities were also detected. EDS results illustrated the existence of Na, K, Ca, Cl and O *etc*. in those dark particles. These contaminations may come from the additive solvents or raw materials involved in making the SOFCs. Their existence may lead to the degradation of performance of the SOFCs by blocking the pores, decreasing the total conductivity and increasing the possibility of delamination of the interface (Figure

5.22). They also could weaken the strength of the electrolyte by initializing cracks, *etc*.

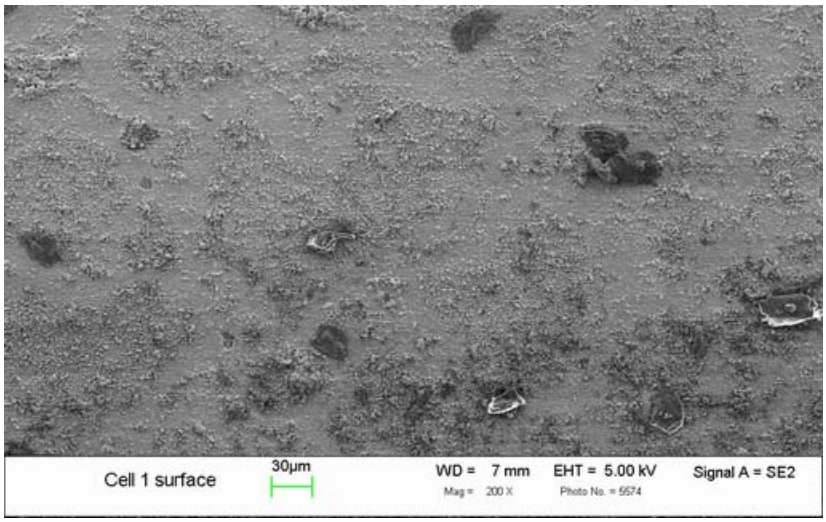

Figure 5.31. Contaminations on the delaminated interface of half cell SOFC 1 at 200 X.

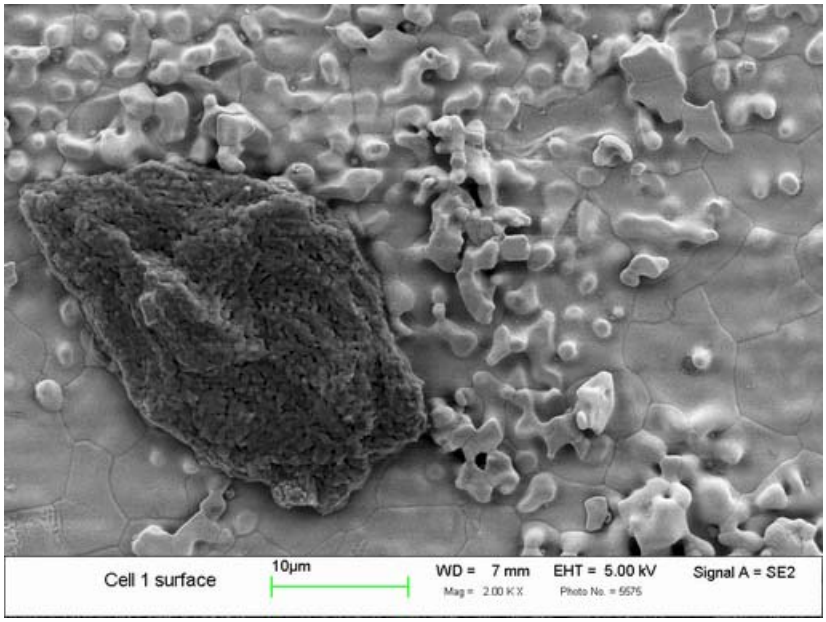

Figure 5.32. Contaminations on the delaminated interface of half cell SOFC 1 at 2 kX.

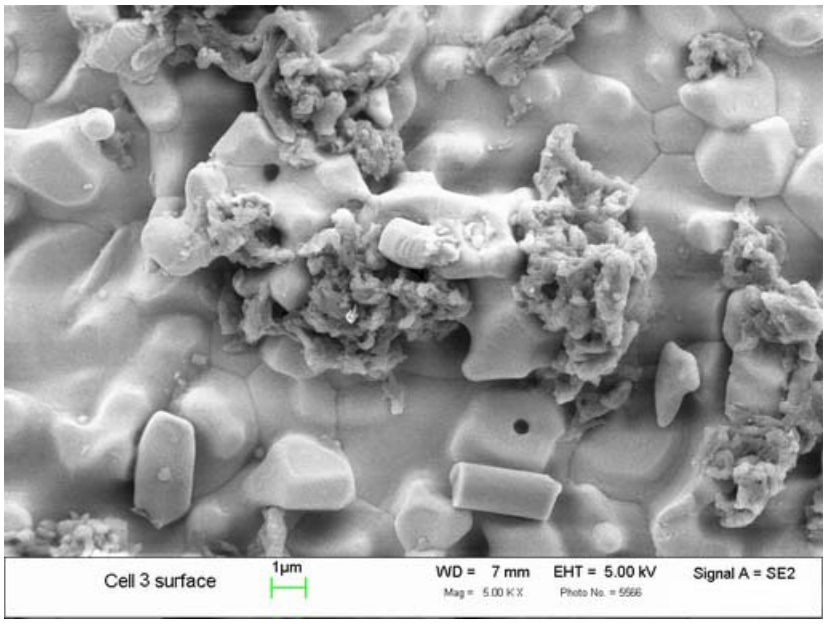

Figure 5.33. Contaminations on the delaminated interface of half cell SOFC 3 at 5 kX.

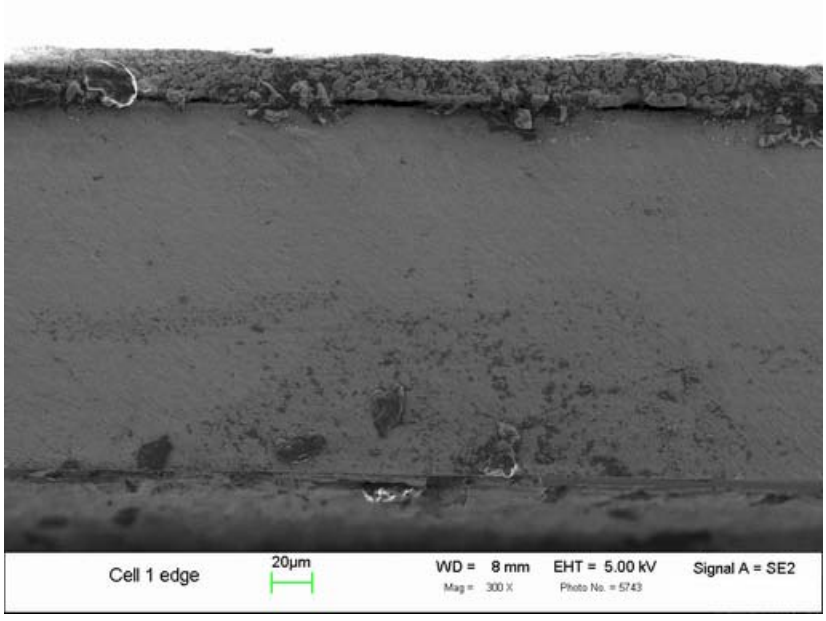

Figure 5.34. Contaminations on the edge of half cell SOFC 3.

5.2.5 Impedance test

Figure 5.35 gives a series of impedance sweeps on half cell SOFC 1 at 1000 ^{o}C. Before the impedance measurement, the polarization current was stopped and the SOFC stayed under the OCV condition for about 5 minutes. The frequency was from 0.1 Hz to 1 MHz and the controlled voltage amplitude was 10 mV. Between every two sweeps, the interval time was 5 seconds. Data whose imaginary part is more than zero are not shown.

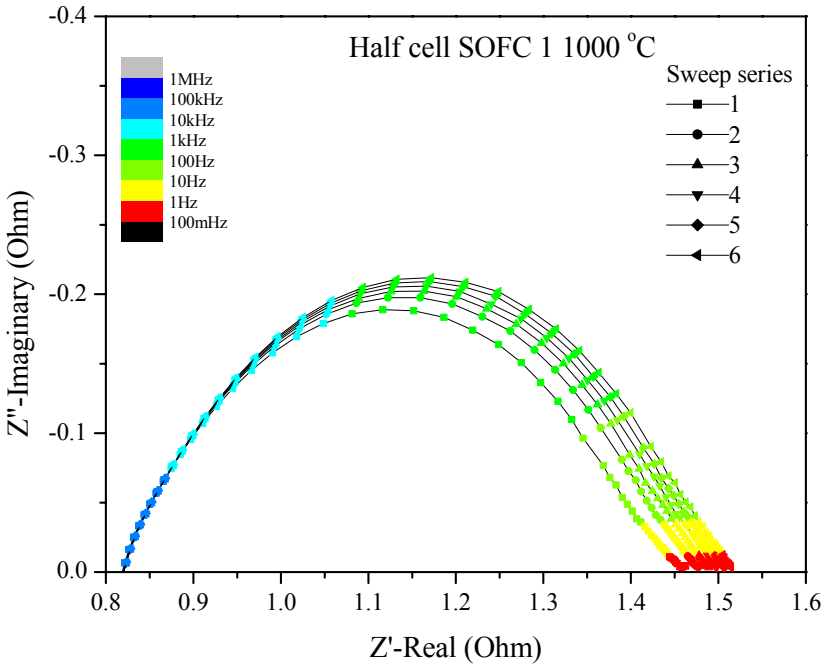

Figure 5.35. Polarization of the cathode.

After several sweeps, the polarization resistance was higher than before. This is due to the activation of cathodic current on the cathode. When an SOFC is driven with polarization current, the cathode will be activated compared to the OCV condition. After the polarization was stopped, the activation reversed as the

polarisation resistance increased with time after interruption of the current. Similar activation effects have been reported for LSM electrodes (Jiang *et al*. 1999; Jorgensen 2001; Lee *et al*. 1995; Leng *et al*. 2003; Odgaard and Skou 1996). It has been shown (Jiang and Love 2001; Jiang *et al*. 1999) that the activation effect of the cathodic current treatment is attributed to the breaking of the surface passive layer associated with Sr and/or Ln (La, Pr) segregated to the electrode surface and corresponding induced microstructural changes of the electrodes.

The equivalent circuit used for fitting the impedance data (Boukamp 1986) is shown in Figure 5.36. L is an inductor, R is a resistor and CPE is a constant phase element. The CPE is defined by two values, CPE-T and CPE-P. If CPE-P equals 1 than the equation is identical to that of a capacitor. Low and high refer to the frequency range.

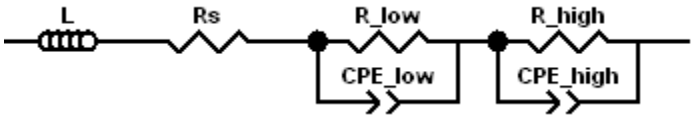

Figure 5.36. Equivalent circuit for the impedance measurement.

Impedance spectra measured at OCV before and after the galvanostatic durability test on half cell SOFC 1 and 3 are shown in Figure 5.37 and Figure 5.38, respectively. Both SOFCs have a larger polarization resistance after 1000 hours of aging. The arcs at lower frequency of the SOFCs were not seen when the polarization resistances were large after aging. If we ignore the process of aging, the polarization resistance of half cell SOFC 3 has apparently increased after polarized with 1 A current. The total change of ohmic resistance Rs, which is mainly ascribed to the electrolyte, was larger after durability test for half cell SOFC 1 than the initial value, while it was smaller for half cell SOFC 3.

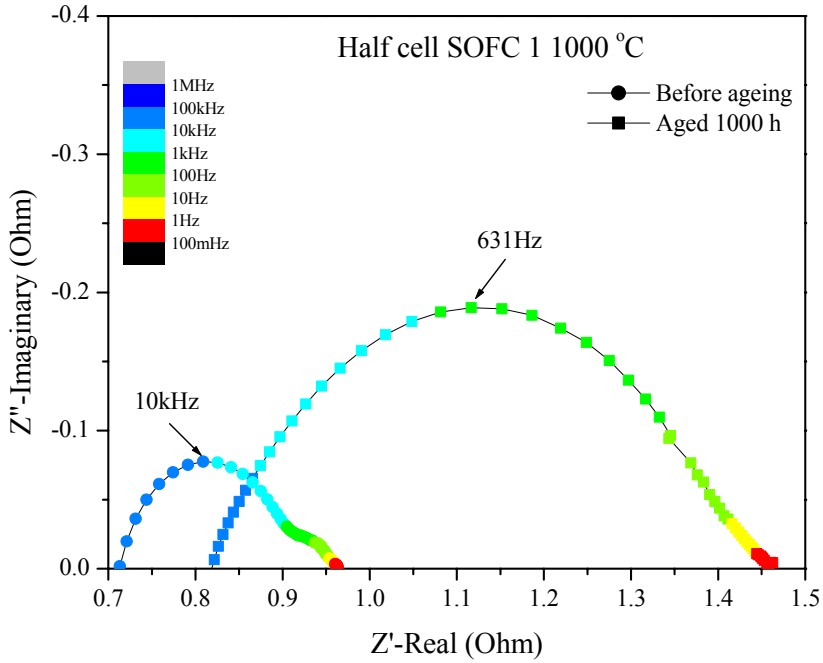

Figure 5.37. Impedance spectra for half cell SOFC 1 before and after aging.

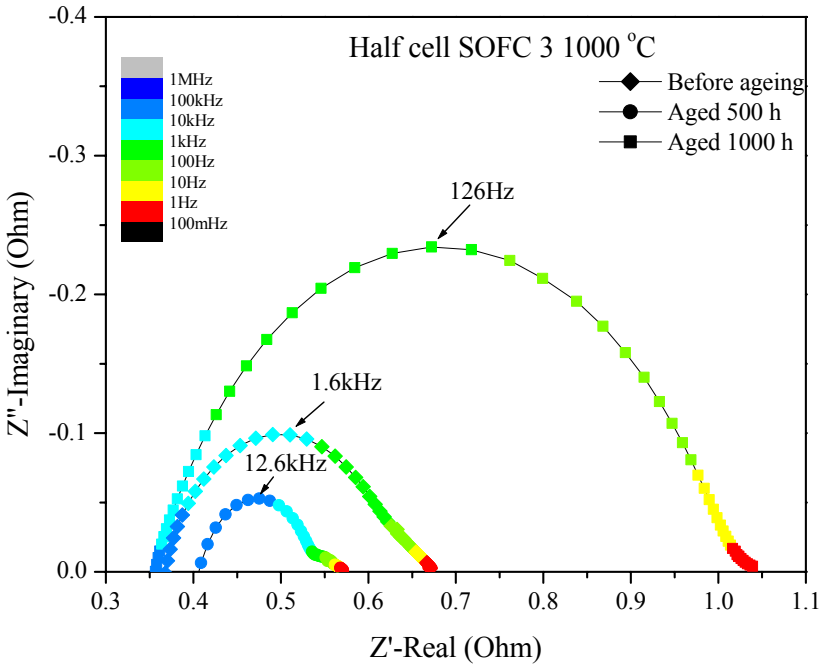

Figure 5.38. Impedance spectra for half cell SOFC 3 before and after aging.

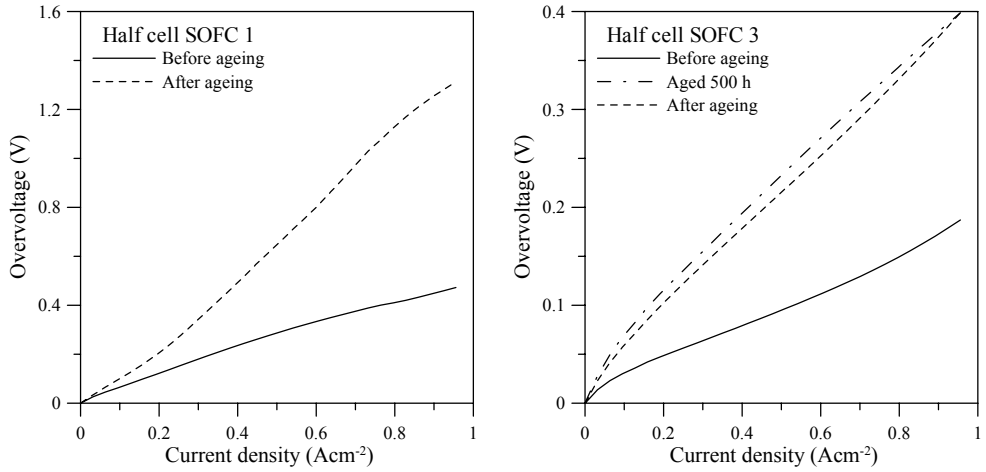

a) Half cell SOFC 1. b) Half cell SOFC 3.

Figure 5.39. Overvoltage vs. current for half cell SOFC 1 and 3.

After subtracting the voltage part for the ohmic resistance Rs from the measured voltages, the relationships of overvoltage and current density for half cell SOFC 1 and 3 were plotted in Figure 5.39. After aging, the degradation was large for the overvoltage. From the relationship between the overvoltage and current density for half cell SOFC 3, there was not much difference from aging for 500 hours and 1000 hours. However, significant difference was seen in the impedance spectra under a lower measuring voltage of 10 mV as shown in Figure 5.38. The relationship between overpotential and current density in the cathode was not linear. It has been reported (Rim *et al*. 1998) that at 900^{o}C the pure $Pr_{0.7}Sr_{0.3}MnO_3$ cathode indicated a cathodic overpotential of 0.079 V at 0.1 Acm^{-2} and 0.11 V at 250 Acm^{-2}, respectively.

The influence of the sintering temperature on the impedance for half cell SOFC 1 and half cell SOFC 3 before and after aging is illustrated in Figure 5.40 and Figure 5.41. The data are shown in Bode plots from 800 ^{o}C to 1000 ^{o}C with

intervals of 100 ^{o}C. Before aging, the Bode plots of both SOFCs were similar. At a lower temperature of 800 ^{o}C two peaks were visible in the Bode plot of phase, but only one impedance peak was visible at higher temperatures. The peaks shifted with the temperature. The effect from temperature was more pronounced at high frequency than that at low frequency. After aging, the peaks that at lower frequency and temperature were invisible. The peaks at higher frequency shifted to a lower frequency. The peaks for half cell SOFC 1 happened from 200 Hz to 700 Hz, while for half cell SOFC 3 they took place in the range from 50 Hz to 100 Hz. The mode of the impedance shifted up at that frequency range. Meanwhile, apart from the peaks, close to the lower or the higher frequency values, the phase was independent of temperature. The study on the (La, Sr) MnO_3 cathode (Jiang *et al*. 2003), showed apparently two impedance peaks or arcs measured from 700 ^{o}C to 850 ^{o}C. Similar impedance results were reported for the LSM/YSZ composite electrode and YSZ electrolyte SOFCs at temperatures from 800 ^{o}C to 1050 ^{o}C (Jorgensen 2001). That two peaks were visible suggested that the LSM/YSZ cathode had at least two limiting processes (Jiang *et al*. 2003; Jorgensen 2001). The high frequency arc/peak can be attributed to the migration and diffusion of oxygen species from the three-phase boundary region into the electrolyte and has some characteristics of electrolyte contribution. The low frequency arc/peak can be attributed to concentration impedance associated with dissociative adsorption and diffusion of oxygen on the cathode surface. Before aging the peaks happened at lower frequency and temperature were not influential at higher temperature because the concentration diffusion of oxygen was negligible as the diffusivity increases with the temperature increased. From the Bode plots, after aging, the reaction process had been affected. The impedance behavior of one peak was similar to that for the mixed ionic and electronic conducting electrodes such as $(LaSr)(CoFe)O_3$ (Jiang 2002) and $La_{1-x}Sr_xCoO_{3-d}$ (Endo *et al*. 2000; Horita *et al*. 2001)

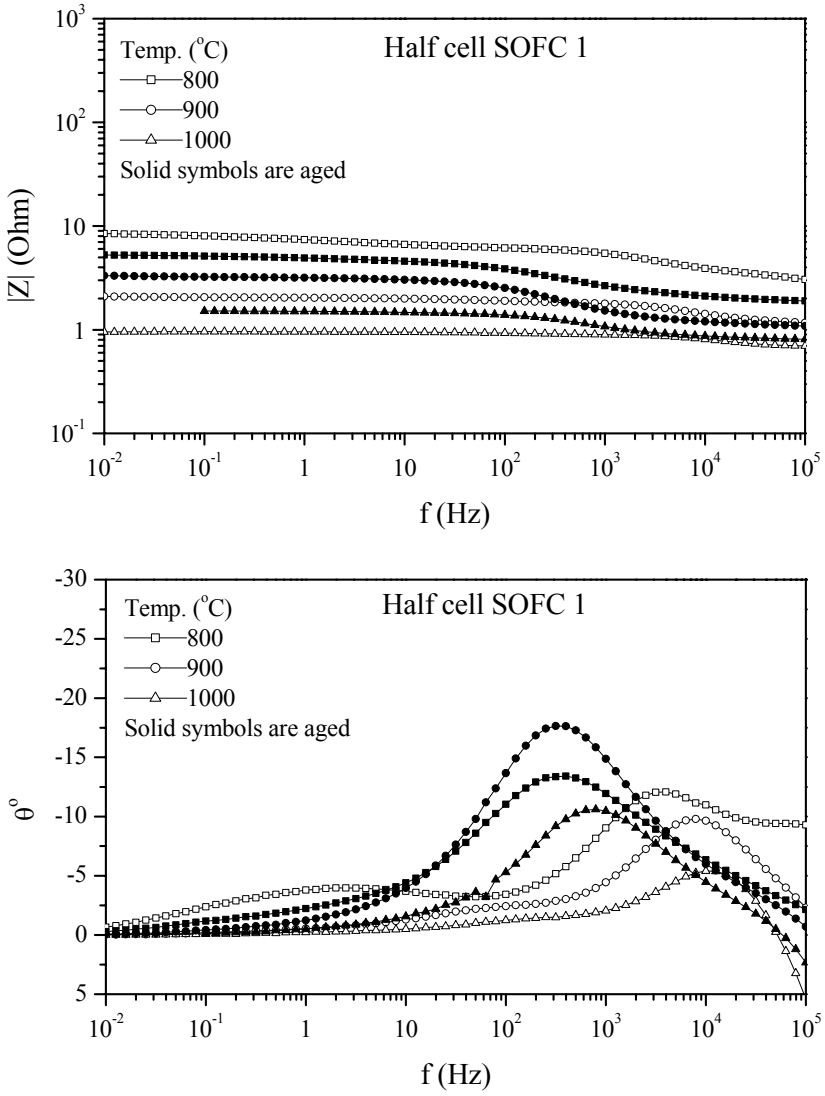

Figure 5.40. Bode plot of half cell SOFC 1 at different temperatures.

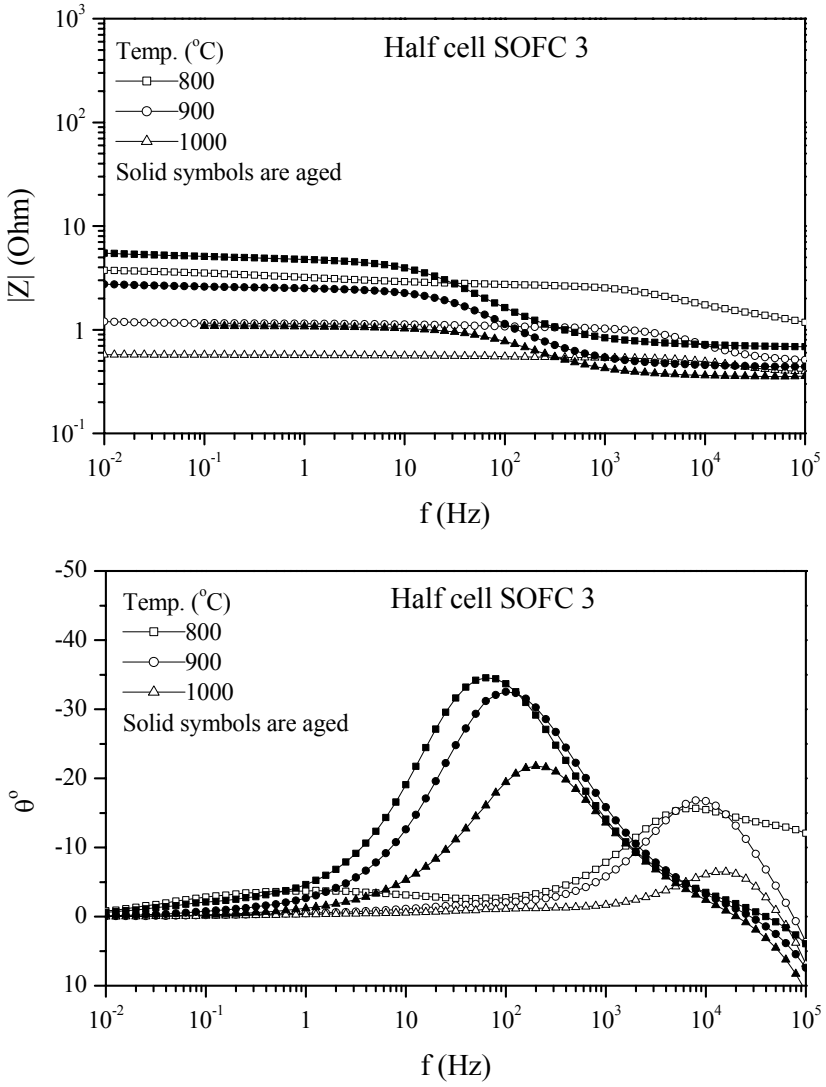

Figure 5.41. Bode plot of half cell SOFC 3 at different temperatures.

The impedance spectra evolutions with time measured for half cell SOFC 1 and 3 are shown in Figure 5.42 and Figure 5.43, respectively. The time dependence of the ohmic resistance Rs, which is mainly ascribed to the electrolyte, and the polarisation resistance Rp (Rp=R_low+R_high) were calculated from the impedance spectra using the equivalent circuit and were plotted in Figure 5.44 and Figure 5.45, respectively.

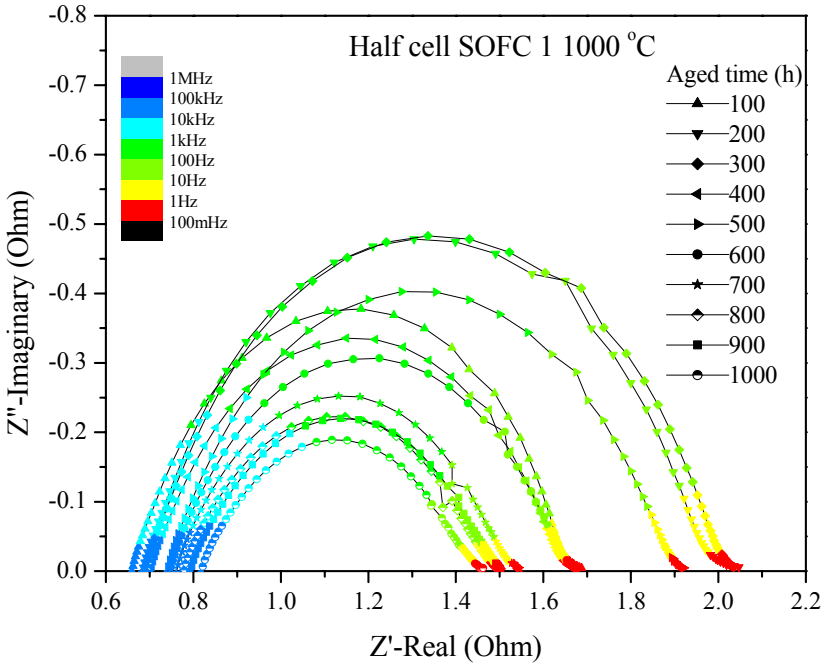

Figure 5.42. Impedance spectra evolution for half cell SOFC 1 during aging.

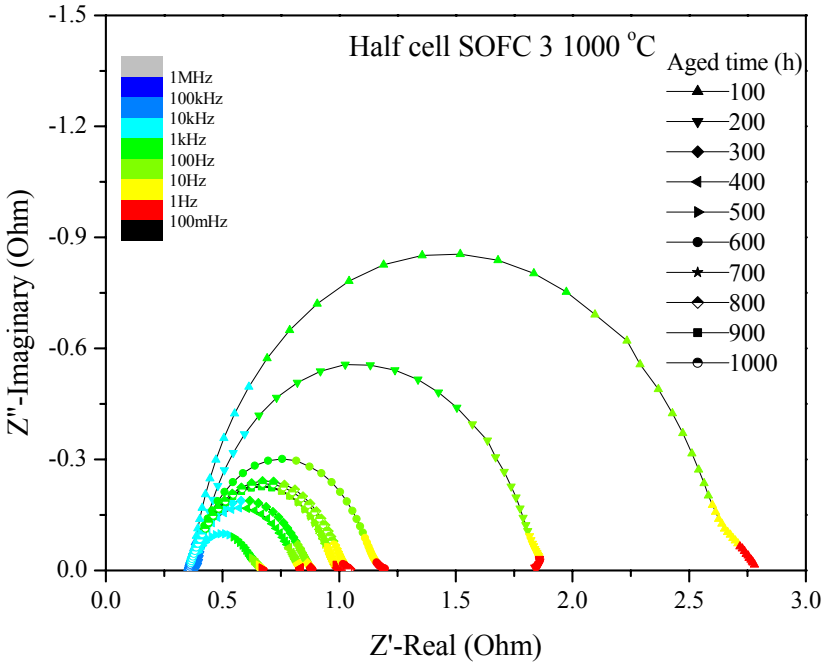

Figure 5.43. Impedance spectra evolution for half cell SOFC 3 during aging.

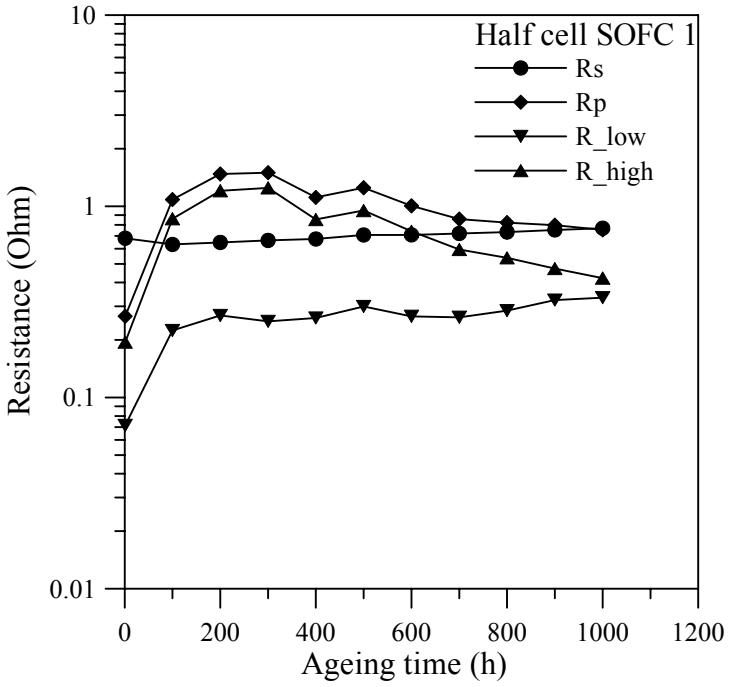

Figure 5.44. Rs and Rp resistance with time for half cell SOFC 1.

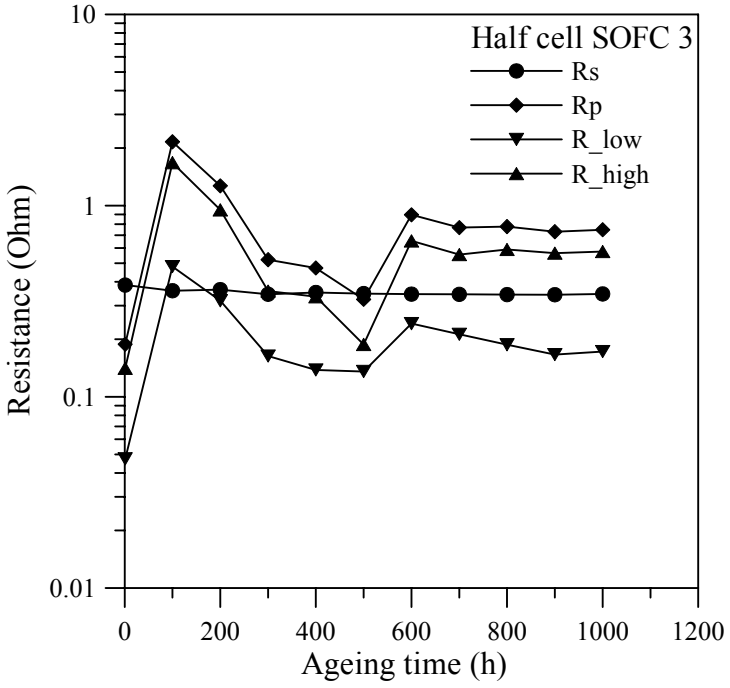

Figure 5.45. Rs and Rp resistance with time for half cell SOFC 3.

Compared to the polarisation resistance Rp, the ohmic resistance Rs changed less with time. The conductivity of the 8YSZ electrolyte exhibited severe degradation during long time exposure at high temperature (Muller *et al*. 2003; Nomura *et al*. 2000). This has significant importance for electrolyte supported single cells. As discussed above for the Bode plots, the high frequency arcs are apparent in the impedance spectra. The R_high part has more contribution to the value of Rp than the R_low part. Just after couples of hundred hours aging time, the polarisation resistance Rp increased a lot with a slight drop of Rs compared to that at the initial state of the SOFCs. Because this happened to both SOFCs, the current should not have an effect on this. The study of the interface between a single nickel wire and YSZ substrate indicated similar results for the interfacial region changes (Hansen and Mogensen 2003). These effects might come from the stabilization of platinum paste or migration of impurities to the interface and TPB sites and the increasing contact area between the platinum mesh and the SOFCs. Because there was no data during the first 100 hours, it is hard to say how the process was occurring.

With current load, the polarization resistance of half cell SOFC 1 decreased after hitting the peak at around 200 hours aging time and kept stable for about 100 hours with the low frequency part R_low increasing little with time. The B.E.T. study before indicated that the total volume of pores was reduced from 0.2114 cm^3/g to 0.1653 cm^3/g. This would effect the oxygen diffusion and concentration and increase the R_low part of the polarization resistance. For half cell SOFC 3, before the current was applied, the SOFC was activated increasingly with aging time. After it was loaded with the current, the value of polarisation resistance was increased for both the low and high frequency parts and the activated rate slowed down. The huge drop of the polarization for the first 500 hours aging of half cell SOFC 3 may be attributed to the growth of the granular grains on the $(Pr_{0.7}Sr_{0.3})MnO_3$ thereby increasing the total length of TPB and adsorption area of oxygen. Compared with the possible pore volume change, this increase had a larger contribution to the performance of the SOFC. The current

load of polarisation may have an impact on the stability of the non-loaded cell. Sudden changes of the operation had more of an impact on the cell performance than the activation of the cathodic current. From the calculated polarisation parts and the rate limiting processes (Jiang *et al*. 2002), the adsorption, diffusion and charge transfer performance were affected by the current load. However, after duration, the effect was compensated by the microstructure surface changes such as the growth of granular grains and the decrease of the nano-scale pores, but the Rp could not reach the initial state. As seen for both SOFCs, during the final part of 400 hours aging, the rate of decrease of the polarization resistance was reduced.

In the study on the long-term performance degradation of button cells consisting of standard materials (LSM, YSZ and Ni/YSZ) (Hsiao and Selman 1997), thermal cycling tests were conducted first between 312 and 649 hours and at 1321 hours a special potential-accelerated aging was applied to the cathode. After thermal cycling, the high frequency region was enlarged. The DC polarization curves indicated that the potential-accelerated aging caused a large increase in polarization due to an increase of interfacial resistance. In the LSM/YSZ composite durability measurement (Jorgensen *et al*. 2000), the polarized cells showed more degradation due to increased voids that were found in the composite layer.

5.3 Conclusions

From the study on the composite $(Pr_{0.7}Sr_{0.3})MnO_3$/YSZ cathode, several conclusions can be summarized as below.

- After aging in air, in the composite cathode, no reactivity was found between or in the grains, and the volume of pores was reduced due to the decrease of the amount of nano-scale pores.

Growth of granular grains was found on the $(Pr_{0.7}Sr_{0.3})MnO_{3\pm\delta}$ phases.

- Aging time with current had an effect on the damage development area in the electrolyte. Low current densities could also lead to the damage development if the aging time is long.

- A certain amount of impurities or contaminations was found in the interface and the electrolyte substrate. Some cathode chemical elements such as Pr and Mn were found in the electrolyte substrate after the SOFCs were sintered. No increasing atomic concentrations were found for them after long-term aging.

- During the aging tests, the EIS and DC aging curves were given. The SOFCs degraded after long-term aging, which was mainly ascribed to the resistance increase of the 8YSZ electrolyte substrate. The decreasing polarization resistance could not recover to the initial state of the SOFCs.

- Activation from cathodic current was confirmed for the composite cathode.

- The gradual decrease of the polarization after a couple of hundred hours aging time may be ascribed to the microstructural surface change thereby increasing the reaction sites of TPB through the cathode and the decrease of the amount of nano-scale pores thereby decreasing the capacitance of the cathode.

- The current load applied had an impact on the overpotential and slowed down the decreasing rate of the polarization resistance of the SOFCs.

- After aging the high frequency Bode arcs/peaks shifted to a lower frequency range, and the low frequency arcs/peaks became small compared to their values before aging.

CHAPTER 6
MULTIPHYSICS MODELING OF SOFCS

An SOFC system involves multiphysics phenomena, including the mass balance of diffusion and adsorption of the gases; the electronic/ionic current balance of the interconnects/current collectors, the electrodes and the electrolyte; the heat transfer and energy balance; and the electrochemical charge transfer reactions. Thermal stress will also be a critical issue for high temperature operation. In this chapter, modeling of SOFCs will be discussed and a proper FEA model framework for the half cell SOFC studied will be presented.

6.1 Basic models of SOFCs

6.1.1 Chemical reaction

If hydrogen is used as fuel in an SOFC system, then the reaction steps can be described as below.

At the triple phase boundary (TPB) of cathode/electrolyte/air, if that is where the incorporation of oxygen into the electrolyte occurs,

$$\frac{1}{2}O_2 + 2e = O^{2-} \tag{6.1}$$

After oxygen ions transfer from the cathode side to the anode side through the electrolyte, the following reaction occurs at the TPB of anode/electrolyte/fuel:

$$H_2 + O^{2-} = H_2O + 2e \tag{6.2}$$

and the total reaction can be written as

$$H_2 + \frac{1}{2}O_2 = H_2O \tag{6.3}$$

This is a simple representation of the total chemical reaction.

6.1.2 Nernst equation

From electrochemical theory, the Gibbs free energy change ΔG, which is defined as the reversible energy dissipated through an infinite load resistance in this system (Rubinstein 1995), equals the electrical work released (Song *et al*. 1993):

$$\Delta G = -nF\Delta E_r \tag{6.4}$$

where, n is the number of electrons, F is the Faraday constant and ΔE_r is the reversible electric potential or open cell voltage.

When the cell is operating under standard conditions and all the components are at unit activity, the relation can be written:

$$\Delta G^o = -nF\ \Delta E_r^o \tag{6.5}$$

$$\Delta G = \Delta G^o + \overline{R}T \ln \prod_B \left(\frac{p_B}{p_0} \right)^{v_B} \tag{6.6}$$

where, $\overline{R}$ is the gas constant, T is temperature, p_B is the partial pressure of specie B, p_0 is the standard pressure and v_B is the coefficient of reaction for specie B. Then the voltage of the cell is

$$\Delta E_r = \Delta E_r^o - \frac{\overline{R}T}{nF}\ln\prod_B\left(\frac{p_B}{p_0}\right)^{v_B} \tag{6.7}$$

This is the Nernst equation for a basic cell.

6.1.3 Electrochemical reaction heat

During the reversible discharge of the cell, the chemical reaction heat is from reversible heat Q_r and

$$Q_r = T\Delta S \tag{6.8}$$

where ΔS is entropy. Since $\Delta G = \Delta H - T\Delta S$, then (Chan *et al*. 2002)

$$\Delta S = -\left(\frac{\partial \Delta G}{\partial T}\right)_p = nF\left(\frac{\partial \Delta E_r}{\partial T}\right)_p = \left(S^o_{H_2O} - S^o_{H_2} - \frac{1}{2}S^o_{O_2}\right) + \overline{R}\ln\left(\frac{p_{H_2}p_{O_2}^{1/2}}{p_{H_2O}}\right) \tag{6.9}$$

so the reaction heat released from the cell is

$$Q_r = T\left(\left(S^o_{H_2O} - S^o_{H_2} - \frac{1}{2}S^o_{O_2}\right) + \overline{R}\ln\left(\frac{p_{H_2}p_{O_2}^{1/2}}{p_{H_2O}}\right)\right) \tag{6.10}$$

6.1.4 Cell voltage for an SOFC system with losses

For a fuel cell system, the circuit voltage is generally described as below:

$$E_i = E_{nernst} - \eta_{act} - \eta_{ohm} - \eta_{con} \tag{6.11}$$

where E_{nernst} is the Nernst potential, η_{act} is the activation overpotential in the electrodes, η_{ohm} is the ohmic loss by the system resistance and η_{con} is the concentration overpotential induced by the diffusion of gases in the porous electrodes. The losses depend on the level of current density (Herschenhofer *et al*. 1998).

For a hydrogen fuel cell system, the Nernst potential can be written in terms of partial pressures of water vapor, oxygen and hydrogen as below:

$$E_{nernst} = \frac{-\Delta G_{H_2O}(T)}{2F} - \frac{\overline{R}T}{4F} \ln\left[\frac{\left(p_{H_2O}\right)^2 p_0}{\left(p_{H_2}\right)^2 p_{O_2}}\right] \tag{6.12}$$

where $\Delta G_{H_2O}(T)$ is the standard Gibbs' free energy of formation of water at temperature T and p is partial pressure for each kind of gas.

6.1.5 Concentration Overpotential

Concentration polarization/overpotential is related to the transport of gaseous species through porous electrodes, and is related to the microstructure of the electrodes, such as the porosity, the pore size and the tortuosity factor (Virkar *et al*. 2000).

The effective gas diffusion coefficient for component i in the porous media can be expressed as a combination of the Knudsen diffusion and ordinary diffusion (Bird *et al*. 2002):

$$D_{ieff} = \frac{\varepsilon}{\tau}\left(\frac{1}{D_{i,m}} + \frac{1}{D_{iK}}\right)^{-1} \tag{6.13}$$

where, ε is the porosity and τ is the tortuosity of the porous material.

The Knudsen diffusion coefficient for the component *i* in the mixture gas is:

$$D_{iK} = \frac{2}{3}\left(\frac{8\bar{R}T}{\pi M_i}\right)^{1/2}\bar{r} \tag{6.14}$$

where, M_i is the molecular weight of the component *i*, and $\bar{r}$ is the average radius of the pore.

$$D_{i,m} = \frac{1-y_i}{\sum_{k\neq i}\frac{y_k}{D_{ik}}} \tag{6.15}$$

where, y_i is the molar fraction, D_{ik} is the binary diffusion coefficient in the system having components *i* and *k* which can be determined by Chapman-Enskog theory (Bird *et al*. 2002)

$$D_{ik} = 0.001858\frac{T^{3/2}}{p\sigma_{ik}^2\Omega_D\left(\frac{1}{M_i}+\frac{1}{M_k}\right)^{1/2}} \tag{6.16}$$

where, σ_{ik} is the characteristic length, and Ω_D is the collision integral.

Because the diffusion of gases in the pores exists, the partial pressure of gases in the active sites will be less than in the fuel or air channels, which results in a loss of total voltage. Normal concentration polarization does not increase excessive voltage losses until the current densities approach the limiting current (Chan *et al*. 2001).

6.1.6 Activation Overpotential

Activation polarization is related to charge transfer processes and depends on the nature of electrode-electrolyte interfaces (Virkar *et al*. 2000). Activation overpotential is normally expressed by the well-known Butler-Volmer equation (Bard and Faulkner 2001).

$$i = i_0 \left\{ \exp\left(-\beta \frac{n_e F \eta_{act}}{\overline{R} T} \right) - \exp\left[(1-\beta) \frac{n_e F \eta_{act}}{\overline{R} T} \right] \right\} \tag{6.17}$$

where, β is the transfer coefficient, n_e is the number of electrons transferred per reaction and i_0 is the exchange current density. The transfer coefficient is considered to be the fraction of the change in polarization that leads to a change in the reaction rate constant, and is usually taken as 0.5 for fuel cells.

A similar expression for activation potential is defined as (Sawata *et al*. 1990):

$$i = i_0 \left\{ \exp\left(\frac{2F \eta_{act}}{\overline{R} T} \right) - \exp\left[-\frac{\alpha F \eta_{act}}{\overline{R} T} \right] \right\} \tag{6.18}$$

where,

$$i_0 = \frac{\sigma_0 \overline{R} T}{(2+\alpha) F} \tag{6.19}$$

where, α is the apparent transfer coefficient denoting unsymmetrical reaction; for the fuel side α =1 and for the air side α =2. σ_0 is the interface conductivity which could be obtained experimentally (Setoguchi *et al*. 1992).

It is known that the activation polarization at the Ni-YSZ anode is generally much less than at the cathode (Virkar *et al*. 2000).

6.1.7 Ohmic overpotential

The overpotential due to ionic resistance of electrolyte and electronic/ionic resistance of electrodes can be written as:

$$\eta_{ohm} = iR_c \tag{6.20}$$

where, R_c is the total ionic and electronic resistance in the electrolyte and the electrodes. For an electrolyte-supported fuel cell, the total series resistance is mainly from the ionic resistance of the electrolyte and it depends on the temperature. An electrode-supported fuel cell can diminish electrolyte ionic resistance by reducing the thickness of the electrolyte.

6.2 Half cell SOFC FEA modeling

6.2.1 FEA model

FEA models were built up and solved with the COMSOL FEMLAB 2.3, a multiphysics PDE solver module running within the MATLAB environment (FEMLAB 2002). The convection and diffusion model from the chemical engineering module was used to describe the diffusion of the oxygen and other diffusing species in the porous electrodes. Three nonlinear stationary general PDE forms were used to create the current balances in the electrodes, the electrolyte and the current collectors. The thickness of the electrolyte was taken to be 180 μm, the thickness of the cathode was 20 μm, the width of the platinum gauze mesh was 100 μm and the diameter of the platinum was about 80 μm. On the anode side, the thickness of the Pt pasted was 5 μm. Compared to the electrodes, the conductivity of the Pt current collector was very large and its resistance could be neglected. One unit volume of the SOFC was considered and its quarter 3-D geometry was modeled as shown in Figure 6.1. The blocks on the electrodes are

gas channel and the other areas are treated as the current collectors, where the potentials are uniform. For purpose of element meshing, the thickness of the electrodes was the same in the model and the thickness of the electrolyte was scaled down. The changes of the thickness were compensated by applying scale factors in the multiphysics model. The top is the anode side and the bottom is the cathode side.

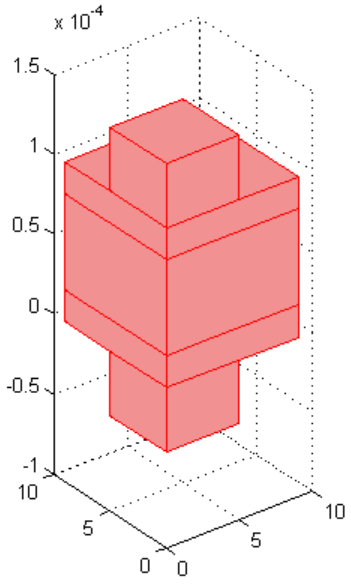

Figure 6.1. 3-D geometry of the SOFC.

6.2.2 Mass balance

In the porous electrode the diffusing species are O_2 and N_2. The mass balance for the species at steady state in the macroscopic structure is governed by the equation below neglecting the convection term,

$$\nabla \cdot \left(- D_{ieff} \cdot \nabla c_{i,c} \right) = R_{i,c} \tag{6.21}$$

where $c_{i,c}$ is the concentration, $R_{i,c}$ is the reaction rate.

The boundaries for the air in the cathode are all insulated except for the surface of the cathode/platinum mesh. At the insulated boundaries, the boundary condition is given by

$$\left(-D_{ieff}\cdot\nabla c_{i,c}\right)\cdot\mathbf{n}=0 \tag{6.22}$$

on the surface of the cathode, the boundary condition is,

$$c_{i,c}=c_{i,c0} \tag{6.23}$$

where, for the cathode $c_{i,c0}$ is the oxygen concentration in the air.

6.2.3 Current balance

The electronic current balance in the composite cathode is given by,

$$\nabla\cdot\left(-k_{el,c}\nabla\phi_{el,c}\right)-n_eFR_{i,c}=0 \tag{6.24}$$

where, $k_{el,c}$ is the electronic conductivity of the cathode, $\phi_{el,c}$ is the electronic potential, n_e is 4 for oxygen. In the current collector, the current balance is given by

$$\nabla\cdot\left(-k_{el,co}\nabla\phi_{el,co}\right)=0 \tag{6.25}$$

The ionic current sink happening in the cathode is the electronic current source and the ionic current balance in the composite cathode is given by

$$\nabla\cdot\left(-k_{ion,c}\nabla\phi_{ion,c}\right)+n_eFR_i=0 \tag{6.26}$$

and, in the electrolyte it is given by

$$\nabla \cdot \left(-k_{ion,e} \nabla \phi_{ion,e} \right) = 0 \tag{6.27}$$

Boundaries are insulated or symmetry except for the outer boundary of the current collector. The insulated/symmetry boundary conditions are given as following.

$$\left(-k_{ion,c} \nabla \phi_{ion,c} \right) \cdot \mathbf{n} = 0 \tag{6.28}$$

$$\left(-k_{ion,e} \nabla \phi_{ion,e} \right) \cdot \mathbf{n} = 0 \tag{6.29}$$

$$\left(-k_{el,c} \nabla \phi_{el,c} \right) \cdot \mathbf{n} = 0 \tag{6.30}$$

$$\left(-k_{el,co} \nabla \phi_{el,co} \right) \cdot \mathbf{n} = 0 \tag{6.31}$$

and, at the outer boundary of the current collector, the boundary condition is,

$$\phi_{el,co} = \phi_{cell} \tag{6.32}$$

Considering the anode side, all of the governing equation will be proper. One needs only change the subscript $_c$ to $_a$, except for the reaction rate equation.

6.2.4 Electrochemical charge transfer reaction

On the cathode side, the overpotential is relatively large, so the second exponent in the Butler-Volmer equation could be negligible, yielding a relation of the Tafel form (Bard and Faulkner 2001). The reaction rate in the composite cathode could be formed from the simplified charge transfer reaction combined with Faraday's law:

$$R_{i,c} = \frac{S_{a,c} i_{0,c} c_{i,c}}{n_e F c_{i,c,ref}} \exp\left[\frac{-\beta n_e F \left(\phi_{el,c} - \phi_{ion,c} - \Delta \phi_{c,ref} \right)}{RT} \right] \tag{6.33}$$

where, $c_{i,c,ref}$ is the reference concentration, which is taken as the oxygen concentration in the air, $S_{a,c}$ is the specific surface area of the cathode which to some extent reflects the TPB length per volume (Sunde 2000), and its product with the exchange current density could be taken as an effective exchange current density, $\Delta\phi_{c,ref}$ is the relative potential difference between the electronic and ionic conductors at the reference state, which is identical to the state at open cell voltage. If H_2 is fed into the anode, the OCV is close to 1 V.

On the anode side, the oxygen ions will release electrons and the product of oxygen. Since the overpotential on the anode side is small, and a linear relationship could be used as following (Bard and Faulkner 2001),

$$R_{i,a} = \frac{S_{a,a} i_{0,a} c_a}{F c_{a,ref}} \left(\phi_{el,a} - \phi_{ion,a} - \Delta\phi_{a,ref} \right) \tag{6.34}$$

Major parameters used in the modeling work are listed in Table 6.1. The effective cathodic and ionic conductivities were estimated from the references (Rim *et al*. 1998; Weber *et al*. 2000) considering the porosity and the mixture ratio of the $(Pr_{1-x}Sr_x)MnO_3$ and 8YSZ. The exchange current density of the cathode was obtained from fitting the overpotential curves of the composite cathode. The specific surface area of the cathode was estimated from the product of the B.E.T. surface specific area (m^2/g) and the density (g/m^3) of the cathode. The average radius of the pores was obtained from the B.E.T. result.

The parameters are a function of temperature, but since dimensions of the half cell SOFC are small, the temperature variation is ignored.

Table 6.1 Major parameters in the SOFCs modeling

Symbols	Names	Values	Units	Ref.
$k_{ion,e}$	Electrolyte ionic conductivity	15	S/m	(Weber *et al.* 2000)
$k_{ion,c}$	Cathode effective ionic conductivity	100-200	S/m	(Rim *et al.* 1998)
$k_{el,c}$	Cathode effective electronic conductivity	2-5	S/m	(Weber *et al.* 2000)
$i_{0,c}$	Exchange current density of cathode	1360	Am^{-2}	
$i_{0,a}$	Exchange current density of anode	>5000	Am^{-2}	(Chan *et al.* 2001)
$S_{a,c}$	Specific surface area of cathode	10^4 -10^6	m^2m^{-3}	
$c_{a,ref}$, $c_{c,ref}$	Reference concentration of oxygen (in air)	2.01	mol/m^3	
$\Delta\phi_{c,ref}$	Relative potential difference	0	V	1 if H_2 fed in anode
ε	Electrode porosity	0.3-0.4	N/A	(Dees *et al.* 1987)
τ	Electrode tortuosity	3-6	N/A	(Dees *et al.* 1987)
$\bar{r}$	Average radius of pore	0.1-0.3	μm	

6.2.5 Results

The applied voltage of the model between the anode and the cathode was from -0.1 V to -0.9 V with a step of -0.1 V, and the potential of the anode was set to zero. The simulation results for the I-V relationship of the half cell SOFC 1 before and after aging were plotted with the experimental data in the Figure 6.2. The conductivity of the electrolyte for the aged case was 8 S/m. The product term $S_{a,c}\ i_{0,a}$ was 2.3×10^7 and 1.08×10^7 m^2m^{-3} Am^{-2} before and after aging, respectively, whose effect on the SOFC will be discussed below.

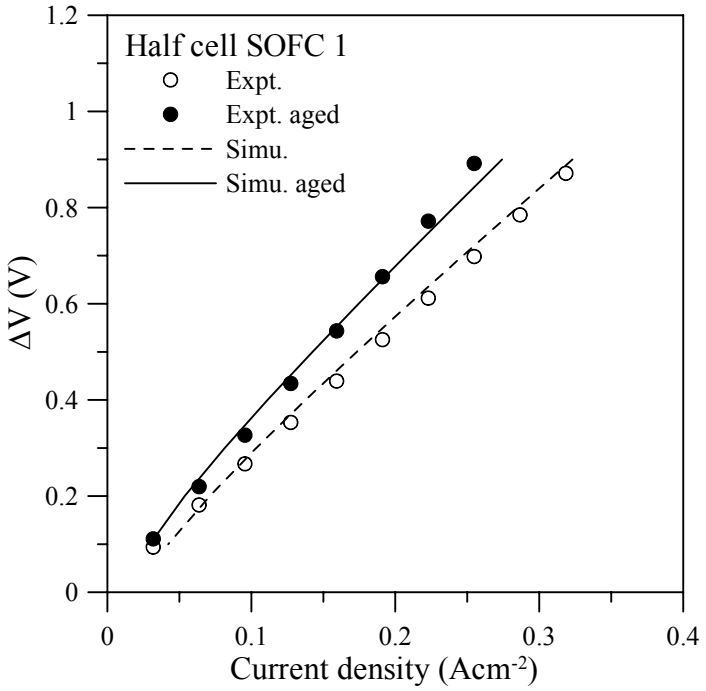

Figure 6.2. I-V curves comparison of simulation and experiment.

The simulation profiles for the case of an applied voltage of -0.3 V are presented below. The concentration of the oxygen in the cathode and the gas channel is shown in Figure 6.3. The concentration is lower under the current collector and the minimum occurs at the rear corner. Under each applied voltage, the oxygen concentrations on the symmetric line ([0 0 -4×10^{-5}] [0 0 2×10^{-5}]) of the unit cell are shown in Figure 6.4. The higher the applied voltage, the larger the gradient of the concentration in the cathode will be. The simulated voltage distribution of the cathode is shown in Figure 6.5 and Figure 6.6. Since the gas channel is located at the front corner and the current collector covers the others, the voltage drop in the region of the front corner is small due to small/no current. The thickness of the cathode is just 20 μm and at elevated temperature the diffusivity of the cathode is relatively large, so the difference of the concentration and the overpotential from the concentration and the series resistance of the cathode are small.

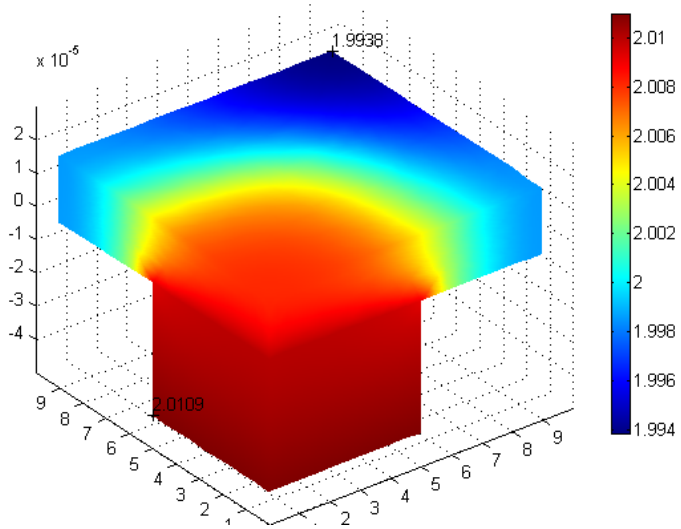

Figure 6.3. Oxygen concentration in the cathode.

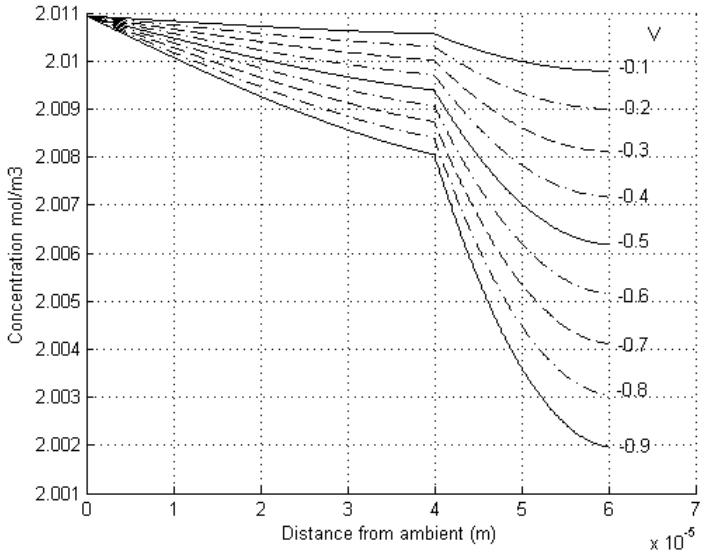

Figure 6.4. Oxygen concentration in the cathode through the symmetric line.

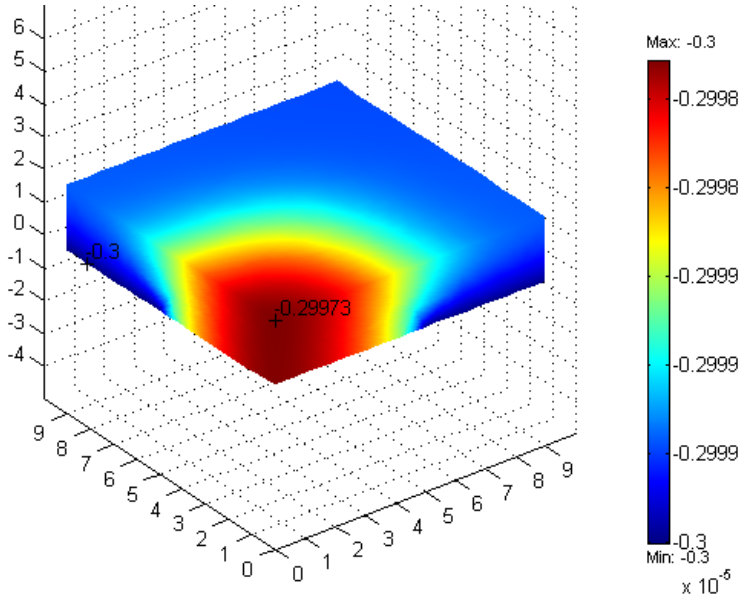

Figure 6.5. Voltage distribution of the cathode with the interface on top.

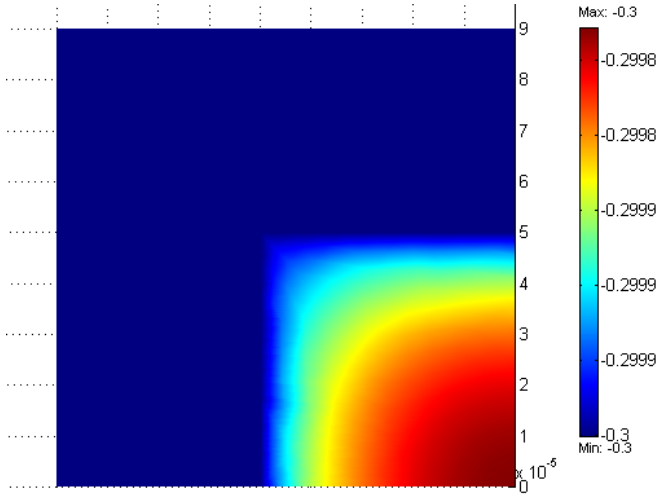

Figure 6.6. Voltage distribution of the cathode on the current collector side.

The electronic current density distribution in the cathode is shown in Figure 6.7 and Figure 6.8. From the current collector to the electrolyte, electronic current would sink into ionic current by the charge transfer electrochemical

reaction. The highest current density occurs close to the boundary between the current collector and the gas channel, where the electrons and oxygen are abundant. The sink value of the electronic current density is equal to the source value of the ionic current density as modeled before. The total current density in the cathode is shown in Figure 6.9. The total current density distribution and the electronic current density distribution are same on the current collector side. The maximum value is 4904 A/m^2, which is about 5 times of the average current density with a value of 1034 A/m^2. The total current density distribution in the cathode along line ([4 5.5 0] [4 5.5 2]) $\times 10^{-5}$ is given in Figure 6.10. A curvature in the I-V curve occurs at higher voltage, which is a result of the total balance of the gas diffusion, the electronic and the ionic overpotential.

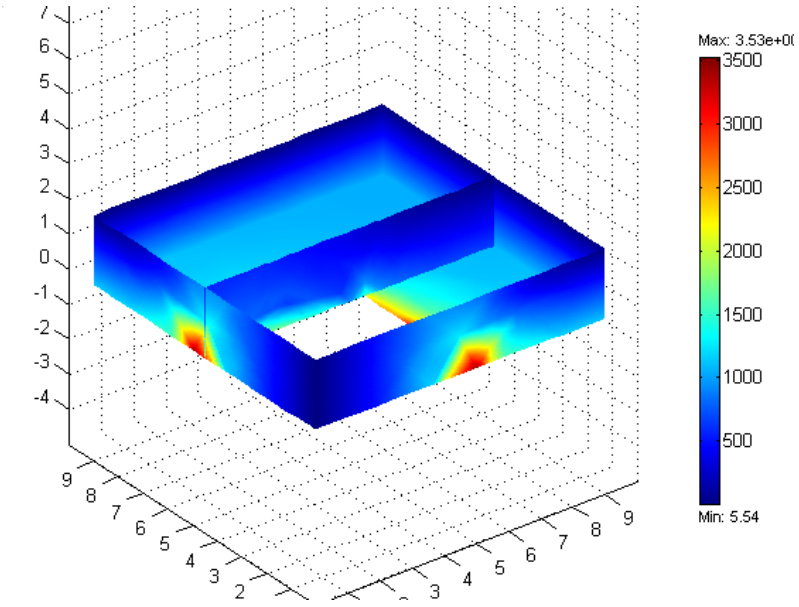

Figure 6.7. Electronic current density distribution of the cathode.

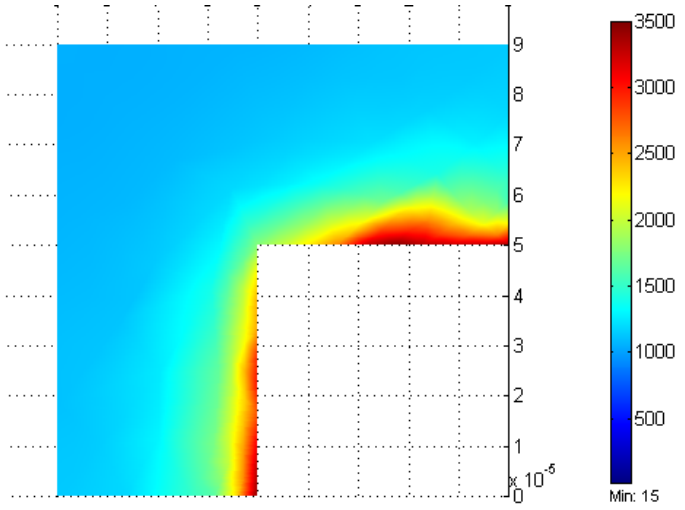

Figure 6.8. Electronic current density distribution on the current collector side.

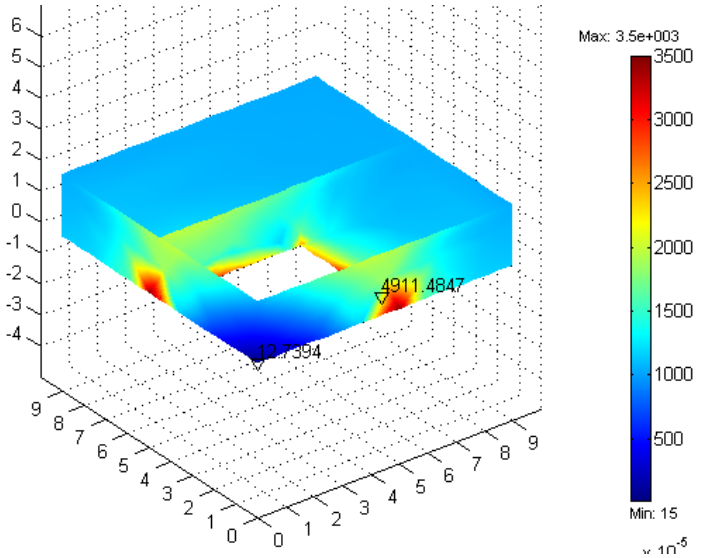

Figure 6.9. Current density distribution of the cathode.

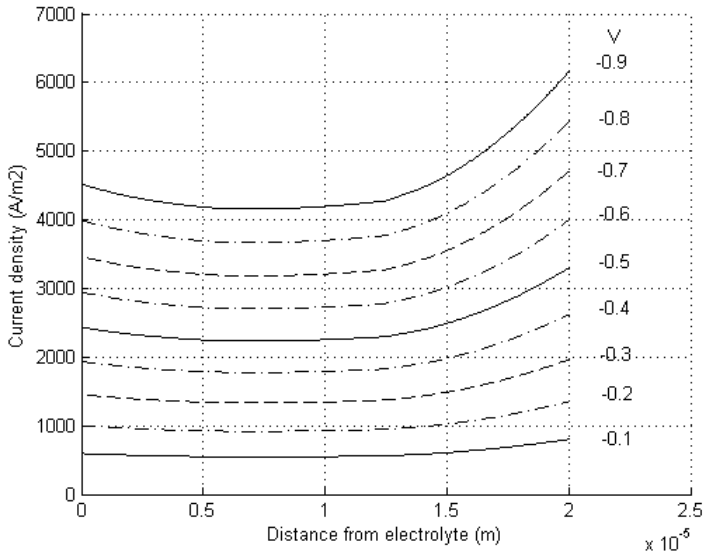

Figure 6.10. Current density in the cathode along line ([4 5.5 0] [4 5.5 2]) $\times 10^{-5}$.

The overpotential defined as $(\phi_{el,c} - \phi_{ion,c})$ in the cathode is given for a sample point in Figure 6.11 and Figure 6.12. Its absolute value increases with the increased voltage, for which the current density is a higher. Since the overpotential varies with different position, the comparison of the calculated overpotential with the experimental data is not possible.

From CHAPTER 5, during the aging, beside the conductivity change of the electrolyte, the microstructural properties, such as the pore and grain size, pore distribution, will also change. Local delamination at the interface could also occur. These combined effects would contribute to the change of the TPB and effective exchange current density, which could be reflected in the product of the exchange current density and the specific surface area (reflecting TPB length per volume) in Equation 6.33. The relationship between the average current density and the product term before aging was plotted in Figure 6.13, where the applied voltage is -0.3 V. The average current density has a linear relationship with the logarithm of the product term.

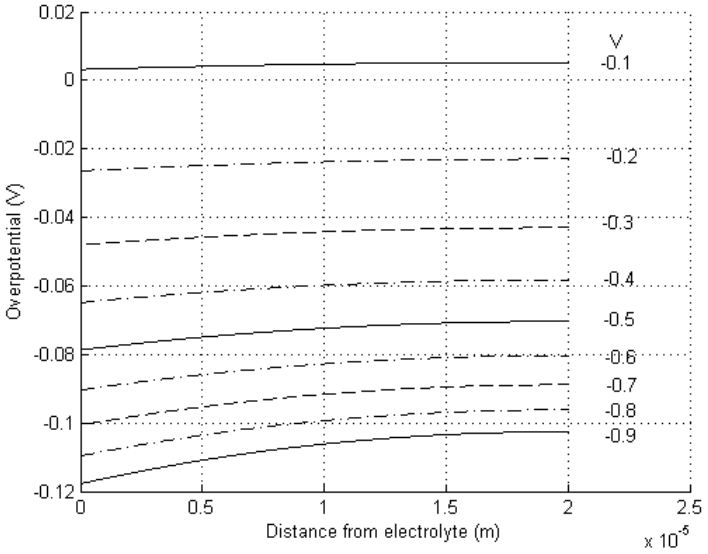

Figure 6.11. Overpotential ($\phi_{el,c} - \phi_{ion,c}$) along line ([4 5.5 0] [4 5.5 2]) $\times 10^{-5}$.

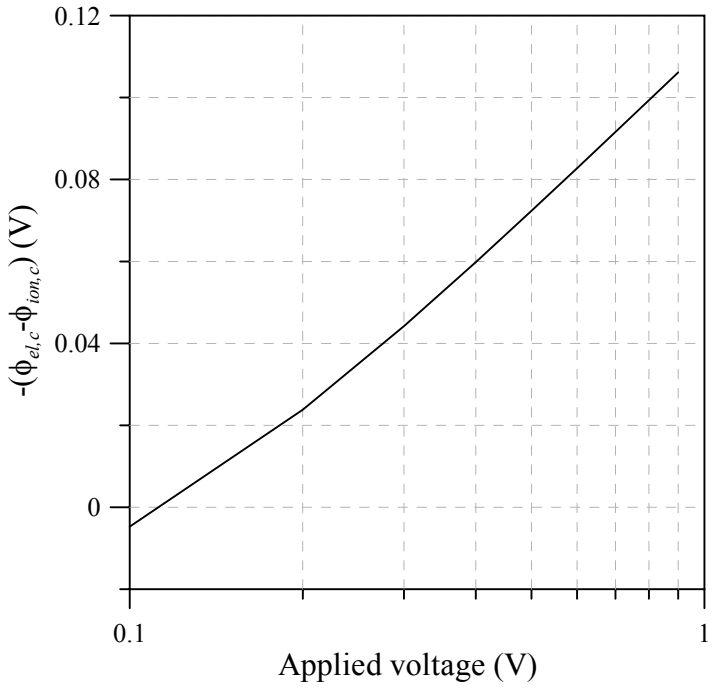

Figure 6.12. Overpotential ($\phi_{el,c} - \phi_{ion,c}$) at point [4 5.5 1] $\times 10^{-5}$.

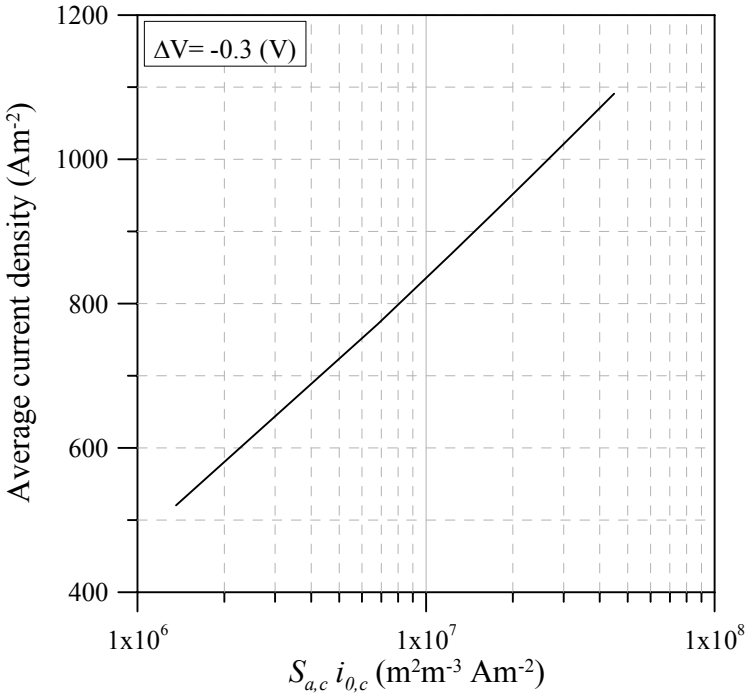

Figure 6.13. Average current density vs. the product of exchange current density and specific area surface.

The effective ionic conductivity is less than the electrolyte because of the existence of the porous $(Pr_{1-x}Sr_x)MnO_3$, which has a relationship to the volume fraction of electrode particles taken with respected to the total solid volume (Sunde 1997). Its effect on the average current density is shown in Figure 6.14. When the value of $k_{io,c}$ is increased from 1 S/m to 5 S/m (1/3 of the electrolyte), the current density increases a lot, but subsequently the effect on the average current density becomes small.

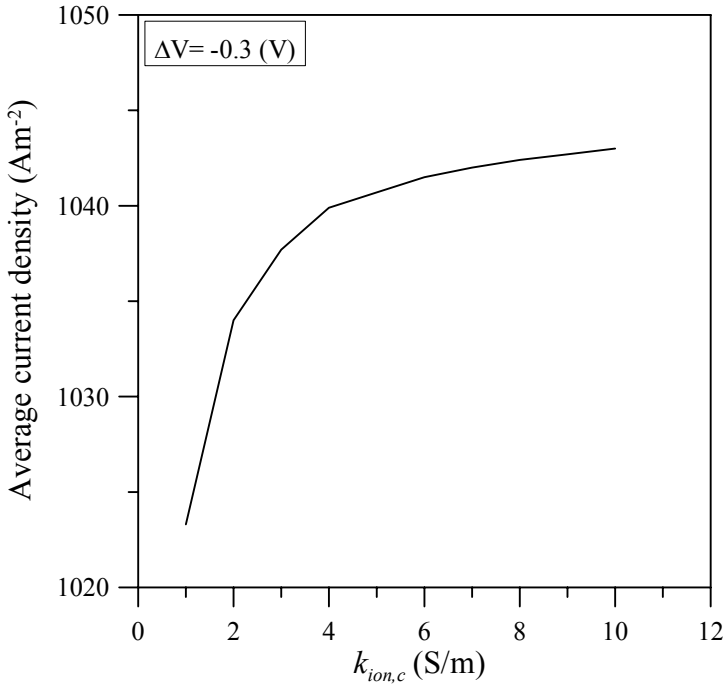

Figure 6.14. Average current density vs. the effective ionic conductivity.

6.3 Conclusions

Conclusions from the modeling work can be listed as below

- 3-D multiphysics modeling has been done on the half cell SOFC, and the predicted current and voltage curves matched the experimental data before and after aging.
- The electric potential, the electronic current density profile, the total current distribution and the gas distribution of the composite cathode are given.
- The effects of the effective exchange current density (product of the exchange current density and the specific area surface) and the

effective ionic conductivity are given. The average current density has a linear relationship to the logarithm of the effective exchange current density. The effect of the effective ionic conductivity of the composite cathode is more apparent for small total effective ionic conductivity values than for large ones.

CHAPTER 7
CONCLUSIONS AND FUTURE RECOMMENDATIONS

7.1 Conclusions from current study

7.1.1 Experimental achievements

- Professional DAQ software SOFCer 2.6 for fuel cell long-term operation was created based on Visual Basic 6.0 and NI Measurement Studio 6. In addition to the basic DAQ functions, the SOFCer 2.6 has many other advantages such as a simulating graphic, instrumental control, experiment task execution and internet remote communication *etc*.

- A pressure on ring tester for thin film material biaxial fracture strength was constructed and commissioned.

7.1.2 Mechanical properties and FEA

- It was determined that the indentation hardness measured on the agglomerations increased with aging time for the Ni-Ceria based anode materials tested in air. However, after reducing the aged anode in H_2, the indentation hardness on the agglomerations was smaller than that of the reduced anode before aging as received.

- Fracture strengths of the 3-layer and 5-layer interconnects were different statistical distributions. Aging had more effects on the

Weibull characteristic strength of the 5-layer interconnects than on that of the 3-layer ones. The initial discontinuous delamination in the interface between each layer may contribute to the increasing delamination failure of the 5-layer specimens after aging.

- FEA was performed on each kind of fracture strength test methodology used in this study. The experimental data for the pressure on ring were well predicted by the FEA model, and the stress/strain distributions were determined throughout the pressurized disk. Using the FEA model, the maximum failure stress was reported for each test. Based on the experimental or FEA predicted results, Weibull moduli, Weibull characteristic strengths and Weibull material scale parameters for tested electrolytes were found.

- The cracks created by microindentation on the electrolyte materials were found to be consistent with the median crack system. The hardness and fracture toughness for the given electrolyte materials were determined. The hardness evolution during aging did not change apparently with aging time.

- The test methodologies had significant influence on the fracture strength. It would appear that the pressure on ring test method is a preferred one for brittle thin film fracture strength tests.

7.1.3 Electrochemical findings

- As a function of aging time, the resistance of the Ni-Ceria based anode increased continually but with a decreasing rate.

- After aging in air, in the composite cathode, no reactivity was found between or in the grains and the volume of pores was

reduced due to the decrease of the nano-scale pores. Growth of granular grains was found on the $(Pr_{0.7}Sr_{0.3})MnO_{3\pm\delta}$ phases.

- Aging time with current had an effect on the damage development area in the electrolyte. Low current densities could also lead to the damage development if the aging time is long.

- An amount of impurities or contaminations was found in the interface and in the electrolyte substrate. Some cathode elements such as Pr and Mn were found in the electrolyte substrate after the SOFCs were sintered. No increasing atomic concentrations were found for them after long-term aging.

- The SOFCs degraded after long-term aging, which was mainly ascribed to the resistance increase of the 8YSZ electrolyte substrate. The decreasing activation polarization resistance was also found and could not fully compensate to bring the performance back to the initial state of the SOFCs. The current load had a significant impact on the performance by slowing down the decreasing rate of the polarization resistance of the SOFCs. Activation from cathodic current was confirmed for the composite cathode.

- The decrease of the polarization may be ascribed to the microstructural surface change thereby increasing the reaction sites of TPB through the cathode and the decrease of the amount of nano-scale pores thereby decreasing the capacitance of the cathode.

- After aging the high frequency Bode arcs/peaks shifted to a lower frequency range, and the low frequency arcs/peaks became unapparent compared to before aging.

7.1.4 Multiphysics modeling

- The 3-D multiphysics modeling has been done on the half cell SOFC, and the predicted current and voltage curves matched the experimental data before and after aging. The electric potential, the electronic current density profile, the total current distribution and the gas distribution of the composite cathode were given.

- The average current density has a linear relationship with the logarithm of the effective exchange current density. The effect of the effective ionic conductivity of the composite cathode is more apparent at small values of effective conductivity than at large ones.

7.2 Future recommendations

In this study, the aged YSZ beams indicated a drop of the Weibull strength after 1000 hours of aging at 1000 ^{o}C, while the biaxial strength study on (ring on ring) of 8YSZ showed a increase of the Weibull strength from 332 MPa to 353 MPa after 1000 hours aging at 950 ^{o}C (Lowrie and Rawlings 2000). It is useful to perform more biaxial strength tests on aged thin film electrolyte with different compositions to see how the flexural strengths change after aging.

From the modeling work, the ratio of the electrode material $(Pr_{1-x}Sr_x)MnO_3$ and the electrolyte will affect the polarization resistance by changing the effective ionic conductivity and the number of effective reaction sites, a further experiment on this kind for composite cathode of different composition ratios is recommended to find an optimum value for a lower polarization and better long-term stability.

Aging tests with a change of the oxygen partial pressure are recommended for the evaluation of the activation energy of this kind of composite cathode. Aging with different polarization loads will be useful for the determination of the exact effect on the performance from galvanization.

B.E.T. and XRD are necessary characterization for the aged SOFC with galvanization, because the polarization may have an effect on the microstructural properties and chemical compositions. In order to get accurate results for these measurements, the platinum paste should not be used.

Finally, an SOFC aging test fed with fuel is valuable for this kind of composite cathode study.

BIBLIOGRAPHY

Abraham, I., and Gritzner, G. (1993). "Mechanical-Properties of Doped Cubic Zirconia Ceramics." *Journal of Materials Science Letters*, 12(13), 995-997.

Achenbach, E. (1994). "Three-dimensional and time-dependent simulation of a planar solid oxide fuel cell stack." *Journal of Power Sources*, 49(1-3), 333-348.

Achenbach, E. (1995). "Response of a solid oxide fuel cell to load change." *Journal of Power Sources*, 57(1-2), 105-109.

Adler, S. B. (1998). "Mechanism and kinetics of oxygen reduction on porous $La_{1-x}Sr_xCoO_{3-\delta}$ electrodes." *Solid State Ionics*, 111(1-2), 125-134.

ANSYS, Inc. (2002). "ANSYS 6.0 Documentation."

Antonucci, V., Modica, E., Monforte, G., Arico, A. S., and Antonucci, P. L. (1998). "Ageing effects of electrodes in ceramic fuel cells." *Journal of the European Ceramic Society*, 18(2), 113-122.

ASTM. (2001). "Refractories; activated carbon, advanced ceramics." Annual Book of ASTM Standards, F. R. Allen, C. N. Baldini, E. L. Gutman, E. Keefe, C. M. Leinweber, V. A. Mayer, P. A. McGee, K. A. Peters, T. J. Sandler, E. A. Whealen, and R. F. Wilhelm, eds., 281-298.

Atkinson, A., and Selcuk, A. (2000). "Mechanical behaviour of ceramic oxygen ion-conducting membranes." *Solid State Ionics*, 134(1-2), 59-66.

Badwal, S. P. S. (2001). "Stability of solid oxide fuel cell components." *Solid State Ionics*, 143(1), 39-46.

Bard, A. J., and Faulkner, L. R. (2001). *Electrochemical Methods Fundamentals and Application*, John Wiley & Sons, Inc., New York.

Bhargava, P., and Patterson, B. R. (1997). "Quantitative characterization of indentation crack path in a cubic zirconia-10 vol% alumina composite." *Journal of the American Ceramic Society*, 75(7), 1863-1867.

Bieberle, A., and Gauckler, L. J. (2000). "Reaction mechanism of Ni pattern anodes for solid oxide fuel cells." *Solid State Ionics*, 135(1-4), 337-345.

Bieberle, A., and Gauckler, L. J. (2002). "State-space modeling of the anodic SOFC system Ni, H_2-H_2O|YSZ." *Solid State Ionics*, 146(1-2), 23-41.

Bird, R. B., Stewart, W. E., and Lightfoot, E. N. (2002). *Transport Phenomena*, John Wiley & Sons, Inc.

Boukamp, B. A. (1986). "A Nonlinear Least Squares Fit procedure for analysis of immittance data of electrochemical systems." *Solid State Ionics*, 20(1), 31-44.

Brant, M. C., Matencio, T., Dessemond, L., and Domingues, R. Z. (2001). "Electrical and microstructural ageing of porous lanthanum strontium manganite/yttria-doped cubic zirconia electrodes." *Chemistry Material*, 13, 3954-3961.

Chan, S. H., Khor, K. A., and Xia, Z. T. (2001). "A complete polarization model of a solid oxide fuel cell and its sensitivity to the change of cell component thickness." *Journal of Power Sources*, 93(1-2), 130-140.

Chan, S. H., Low, C. F., and Ding, O. L. (2002). "Energy and exergy analysis of simple solid-oxide fuel-cell power systems." *Journal of Power Sources*, 103(2), 188-200.

Charpentier, P., Fragnaud, P., Schleich, D. M., and Gehain, E. (2000). "Preparation of thin film SOFCs working at reduced temperature." *Solid State Ionics*, 135(1-4), 373-380.

Choi, J. H., Jang, J. H., and Oh, S. M. (2001). "Microstructure and cathodic performance of $La_{0.9}Sr_{0.1}MnO_3$/yttria-stabilized zirconia composite electrodes." *Electrochimica Acta*, 46(6), 867-874.

Choi, S. M., Lee, K. T., Kim, S., Chun, M. C., and Lee, H. L. (2000). "Oxygen ion conductivity and cell performance of $La_{0.9}Ba_{0.1}Ga_{1-x}Mg_xO_{3-\delta}$ electrolyte." *Solid State Ionics*, 131(3-4), 221-228.

Clausen, C., Bagger, C., Bilde-Sorensen, J. B., and Horsewell, A. (1994). "Microstructural and microchemical characterization of the interface between $La_{0.85}Sr_{0.15}MnO_3$ and Y_2O_3-stabilized ZrO_2." *Solid State Ionics*, 70-71(1), 59-64.

Costamagna, P., Costa, P., and antonucci, V. (1998). "Micro-modelling of solid oxide fuel cell electrodes." *Electrochimica Acta*, 43(3-4), 375-394.

de Haart, L. G. J., Mayer, K., Stimming, U., and Vinke, I. C. (1998). "Operation of anode-supported thin electrolyte film solid oxide fuel cells at 800^{o}C and below." *Journal of Power Sources*, 71(1-2), 302-305.

Dees, D. W., Claar, T. D., Easler, T. E., Fee, D. C., and Mrazek, F. C. (1987). *Journal of the Electrochemical Society*, 134, 2141.

Demin, A. K., and Gulbis, F. Y. (2000). "Zirconia-based SOFC with non-noble electrodes fed by air-methane mixture." *Solid State Ionics*, 135(1-4), 451-456.

Dewith, G., and Wagemans, H. H. M. (1989). "Ball-on-Ring Test Revisited." *Journal of the American Ceramic Society*, 72(8), 1538-1541.

Du, Y., Huang, X., Sammes, N. M., Reifsnider, K. L., and Smirnova, A. L. (2003). "Fabrication and performance evaluation of micro-tubular SOFCs using doped-lanthanum gallate electrolyte." in *Fifth Gordon Conference on Fuel Cells*, Edited by, poster.

Elangovan, S., Hartvigsen, J., Khandkar, A., Privette, R. M., Kneidel, K. E., Perna, M. A., and Rowley, D. R. (1998). "Planar solid oxide fuel cell integrated system technology development." *Journal of Power Sources*, 71(1-2), 354-360.

Endo, A., Fukunaga, H., Wen, C., and Yamada, K. (2000). "Cathodic reaction mechanism of dense $La_{0.6}Sr_{0.4}CoO_3$ and $La_{0.81}Sr_{0.09}MnO_3$ electrodes for solid oxide fuel cells." *Solid State Ionics*, 135(1-4), 353-358.

Endo, A., Ihara, M., Komiyama, H., and Yamada, K. (1996). "Cathodic reaction mechanism for dense Sr-doped lanthanum manganite electrodes." *Solid State Ionics*, 86-88(2), 1191-1195.

Endo, A., Wada, S., Wen, C.-J., Komiyama, H., and Yamada, K. (1998). "Low overvoltage mechanism of high ionic conducting cathode for solid oxide fuel cell." *Journal of the Electrochemical Society*, 145, L35-36.

Exner, H. E. (1969). *Transactions, AIME*, 245(4), 677.

FEMLAB. (2002). *User's Guide and Introduction*, COMSOL.

Fleig, J. (2002). "On the width of the electrochemically active region in mixed conducting solid oxide fuel cell cathodes." *Journal of Power Sources*, 105(2), 228-238.

Fleig, J., and Maier, J. (1996). "Finite element calculations of impedance effects at point contacts." *Electrochimica Acta*, 41(7-8), 1003-1009.

Fukunaga, H., Ihara, M., Sakaki, K., and Yamada, K. (1996). "The relationship between overpotential and the three phase boundary length." *Solid State Ionics*, 86-88(2), 1179-1185.

Gibson, I. R., Dransfield, G. P., and Irvine, J. T. S. (1998). "Influence of Yttria Concentration upon Electrical Properties and Susceptibility to Ageing of Yttria-stabilised Zirconias." *Journal of the European Ceramic Society*, 18(6), 661-667.

Hammouche, A., Siebert, E., and Hammou, A. (1989). "Crystallographic, Thermal and Electrochemical Properties of the System La1-Xsrxmno3 for High-Temperature Solid Electrolyte Fuel-Cells." *Materials Research Bulletin*, 24(3), 367-380.

Hansen, V. K., and Mogensen, M. (2003). "H_2-H_2O-Ni-YSZ electrode performance and segregation to the interface." in *Solid Oxide Fuel Cell VIII*, Edited by S. C. Singhal and M. Dokiya, 686-694.

Herbstritt, D., Weber, A., and Ivers-Tiffee, E. (2001). "Modelling and DC-polarisation of a three dimensional electrode/electrolyte interface." *Journal of the European Ceramic Society*, 21(10-11), 1813-1816.

Herschenhofer, J. H., Stauffer, D. B., Engleman, R. R., and Klett, M. G. (1998). *Fuel Cell Handbook*, Parsons Corporation.

Hilpert, K., Steinbrech, R. W., Boroomand, F., Wessel, E., Meschke, F., Zuev, A., Teller, O., Nickel, H., and Singheiser, L. (2003). "Defect formation and mechanical stability of perovskites based on $LaCrO_3$ for solid oxide fuel cells (SOFC)." *Journal of the European Ceramic Society*, In Press, Corrected Proof.

Hoogers, G. (2003). *Fuel Cell Technology Handbook*, CRC Press.

Horita, T., Yamaji, K., Sakai, N., Xiong, Y., Kato, T., Yokokawa, H., and Kawada, T. (2002). "Imaging of oxygen transport at SOFC cathode/electrolyte interfaces by a novel technique." *Journal of Power Sources*, 106(1-2), 224-230.

Horita, T., Yamaji, K., Sakai, N., Yokokawa, H., Weber, A., and Ivers-Tiffee, E. (2000). "Stability at $La_{0.6}Sr_{0.4}CoO_{3-\delta}$ cathode/$La_{0.8}Sr_{0.2}Ga_{0.8}Mg_{0.2}O_{2.8}$ electrolyte interface under current flow for solid oxide fuel cells." *Solid State Ionics*, 133(3-4), 143-152.

Horita, T., Yamaji, K., Sakai, N., Yokokawa, H., Weber, A., and Ivers-Tiffee, E. (2001). "Oxygen reduction mechanism at porous $La_{1-x}Sr_xCoO_{3-d}$ cathodes/$La_{0.8}Sr_{0.2}Ga_{0.8}Mg_{0.2}O_{2.8}$ electrolyte interface for solid oxide fuel cells." *Electrochimica Acta*, 46(12), 1837-1845.

Hsiao, Y. C., and Selman, J. R. (1997). "The degradation of SOFC electrodes." *Solid State Ionics*, 98(1-2), 33-38.

Huang, K., Tichy, R. S., and Goodenough, J. B. (1998). "Superior perovskite oxide-ion conductor; strontium- and magnesium-doped LaGaO3: I,phase

relationships and electrical properties." *Journal of the American Ceramic Society*, 81, 2581-2585.

Huang, X., Liu, J., Lu, Z., Liu, W., Pei, L., He, T., Liu, Z., and Su, W. (2000). "Properties of nonstoichiometric $Pr_{0.6-x}Sr_{0.4}MnO_3$ as the cathodes of SOFCs." *Solid State Ionics*, 130(3-4), 195-201.

Ishihara, T., Kudo, T., Matsuda, H., and Takita, Y. (1995). "Doped $PrMnO_3$ perovskite oxide as a new cathode of solid oxide fuel cells for low temperature operation." *Journal of The Electrochemical Society*, 142(5), 1519-1525.

Ishihara, T., Matsuda, H., and Takita, Y. (1994). "Doped $LaGaO_3$ perovskite type oxide as a new oxide ionic conductor." *Journal of the American Chemical Society*, 116, 3801-3803.

Ivers-Tiffee, E., Weber, A., and Herbstritt, D. (2001). "Materials and technologies for SOFC-components." *Journal of the European Ceramic Society*, 21(10-11), 1805-1811.

Iwata, M., Hikosaka, T., Morita, M., Iwanari, T., Ito, K., Onda, K., Esaki, Y., Sakaki, Y., and Nagata, S. (2000). "Performance analysis of planar-type unit SOFC considering current and temperature distributions." *Solid State Ionics*, 132(3-4), 297-308.

Jensen, K. V., Wallenberg, R., Chorkendorff, I., and Mogensen, M. (2003). "Effect of impurities on structural and electrochemical properties of the Ni-YSZ interface." *Solid State Ionics*, 160(1-2 SU -), 27-37.

Jeong, S. M., Park, S. E., and Lee, H. L. (2002). "Fracture behaviour of alumina ceramics by biaxial ball-on-3-ball test." *Journal of the European Ceramic Society*, 22(7), 1129-1135.

Jiang, S. P. (2002). "A comparison of O_2 reduction reactions on porous (La,Sr)MnO_3 and (La,Sr)(Co,Fe)O_3 electrodes." *Solid State Ionics*, 146(1-2), 1-22.

Jiang, S. P., and Badwal, S. P. S. (1997). "Hydrogen oxidation at the nickel and platinum electrodes on yttria-tetragonal zirconia electrolyte." *Journal of the Electrochemical Society*, 144, 3777-3784.

Jiang, S. P., and Badwal, S. P. S. (1999). "An electrode kinetics study of H_2 oxidation on Ni/Y_2O_3-ZrO_2 cermet electrode of the solid oxide fuel cell." *Solid State Ionics*, 123(1-4), 209-224.

Jiang, S. P., Leng, Y. J., Chan, S. H., and Khor, K. A. (2003). "Fabrication of high performance (La,Sr)MnO_3 cathodes by ion impregnation." in *Solid Oxide Fuel Cells VIII*, Edited by S. C. Singhal and M. Dokiya, Paris, France, 422-429.

Jiang, S. P., and Love, J. G. (2001). "Origin of the initial polarization behavior of Sr-doped $LaMnO_3$ for O_2 reduction in solid oxide fuel cells." *Solid State Ionics*, 138(3-4), 183-190.

Jiang, S. P., Love, J. G., and Ramprakash, Y. (2002). "Electrode behaviour at (La,Sr)MnO_3/Y_2O_3-ZrO_2 interface by electrochemical impedance spectroscopy." *Journal of Power Sources*, 110(1), 201-208.

Jiang, S. P., Love, J. G., Zhang, J. P., Hoang, M., Ramprakash, Y., Hughes, A. E., and Badwal, S. P. S. (1999). "The electrochemical performance of

LSM/zirconia-yttria interface as a function of a-site non-stoichiometry and cathodic current treatment." *Solid State Ionics*, 121(1-4), 1-10.

Jiang, S. P., and Ramprakash, Y. (1999). "H_2 oxidation on Ni/Y-TZP cermet electrodes - a comparison of electrode behaviour by GCI and EIS techniques." *Solid State Ionics*, 122(1-4), 211-222.

Jorgensen, M. J. (2001). "Lanthanum manganate based cathodes for solid oxide fuel cells," Ph.D. dissertation, Riso National Laboratory, Denmark.

Jorgensen, M. J., Holtappels, P., and Appel, C. C. (2000). "Durability test of SOFC cathodes." *Journal of Applied Electrochemistry*, 30(4), 411-418.

Jue, J. F., and Virkar, A. V. (1990). "Fabrication, microstructural characterization, and mechanical properties of polycrystalline t'-Zirconia." *Journal of the American Ceramic Society*, 73, 3650-3660.

Juhl, M., Primdahl, S., Manon, C., and Mogensen, M. (1996). "Performance/structure correlation for composite SOFC cathodes." *Journal of Power Sources*, 61(1-2), 173-181.

Kek, D., Panjan, P., Wanzenberg, E., and Jamnik, J. (2001). "Electrical and microstructural investigations of cermet anode/YSZ thin film systems." *Journal of the European Ceramic Society*, 21(10-11), 1861-1865.

Kenjo, T., and Nishiya, M. (1992). "$LaMnO_3$ air cathodes containing ZrO_2 electrolyte for high temperature solid oxide fuel cells." *Solid State Ionics*, 57(3-4), 295-302.

Kim, J.-D., Kim, G.-D., Moon, J.-W., Park, Y.-i., Lee, W.-H., Kobayashi, K., Nagai, M., and Kim, C.-E. (2001). "Characterization of LSM-YSZ

composite electrode by ac impedance spectroscopy." *Solid State Ionics*, 143(3-4), 379-389.

Koh, J.-H., Yoo, Y.-S., Park, J.-W., and Lim, H. C. (2002). "Carbon deposition and cell performance of Ni-YSZ anode support SOFC with methane fuel." *Solid State Ionics*, 149(3-4), 157-166.

Kostogloudis, G. C., Tsiniarakis, G., and Ftikos, C. (2000). "Chemical reactivity of perovskite oxide SOFC cathodes and yttria stabilized zirconia." *Solid State Ionics*, 135(1-4), 529-535.

Kostogloudis, G. C., Vasilakos, N., and Ftikos, C. (1997). "Preparation and characterization of $Pr_{1-x}Sr_xMnO_{3-\delta}$ (x = 0, 0.15, 0.3, 0.4, 0.5) as a potential SOFC cathode material operating at intermediate temperatures (500-700[deg]C)." *Journal of the European Ceramic Society*, 17(12), 1513-1521.

Kuscer, D., Holc, J., Hrovat, M., Bernik, S., Samardzija, Z., and Kolar, D. (1995). "Interactions between a thick film $LaMnO_3$ cathode and YSZ SOFC electrolyte during high temperature ageing." *Solid State Ionics*, 78(1-2), 79-85.

Kwon, N.-H., Kim, G.-H., Song, H. S., and Lee, H.-L. (2001). "Synthesis and properties of cubic zirconia-alumina composite by mechanical alloying." *Materials Science and Engineering A*, 299(1-2), 185-194.

Lankford, J. (1982). "Indentation Microfracture in the Palmqvist Crack Regime - Implications for Fracture-Toughness Evaluation by the Indentation Method." *Journal of Materials Science Letters*, 1(11), 493-495.

Lauret, H., and Hammou, A. (1996). "Localization of Oxygen Cathodic Reduction Zone at Lanthanum Manganite/Zirconia Interface." *Journal of the European Ceramic Society*, 16(4), 447-451.

Lawn, B. R., Evans, A. G., and Mashall, D. B. (1980). "Elastic/plastic indentation damage in ceramics: the median/radial crack system." *Journal of the American Ceramic Society*, 63, 574-589.

Lawn, B. R., and Fuller, E. R. (1975). "Equilibrium penney-like cracks in indentation fracture." *Journal of Materials Science*, 10((12)), 2016-2024.

Lee, H.-K. (2003). "Electrochemical characteristics of $La_{1-x}Sr_xMnO_3$ for solid oxide fuel cell." *Materials Chemistry and Physics*, 77(3), 639-646.

Lee, H. Y., Cho, W. S., Oh, S. M., Wiemhofer, H. D., and Gopel, W. (1995). "Active reaction sites for oxygen reduction in $La_{0.9}Sr_{0.1}Mno_3$/YSZ electrodes." *Journal of the Electrochemical Society*, 142(8), 2659-2664.

Lee, J.-H., Heo, J.-W., Lee, D.-S., Kim, J., Kim, G.-H., Lee, H.-W., Song, H. S., and Moon, J.-H. (2003). "The impact of anode microstructure on the power generating characteristics of SOFC." *Solid State Ionics*, 158(3-4), 225-232.

Lehnert, W., Meusinger, J., and Thom, F. (2000). "Modelling of gas transport phenomena in SOFC anodes." *Journal of Power Sources*, 87(1-2), 57-63.

Leng, Y. J., Chan, S. H., Khor, K. A., and Jiang, S. P. (2003). "Development of LSM/YSZ composite electrodes for thin film solid oxide fuel cells." in *Solid Oxide Fuel Cells VIII*, Edited by S. C. Singhal and M. Dokiya, Paris, France, 440-450.

Lessing, P. A. (2002). "Fractography of Small Pin-on Ring Tests of Zirconia Electrolytes." Idaho National Engineering & Environmental Laboratory.

Liang, K. M., Orange, G., and Fantozzi, G. (1990). "Evaluation by Indentation of Fracture-Toughness of Ceramic Materials." *Journal of Materials Science*, 25(1A), 207-214.

Lowrie, F. L., and Rawlings, R. D. (2000). "Room and high temperature failure mechanisms in solid oxide fuel cell electrolytes." *Journal of the European Ceramic Society*, 20(6), 751-760.

Matsuzaki, Y., and Yasuda, I. (2000). "The poisoning effect of sulfur-containing impurity gas on a SOFC anode: Part I. Dependence on temperature, time, and impurity concentration." *Solid State Ionics*, 132(3-4), 261-269.

Matus, Y., De Jonghe, L. C., Zhang, X.-F., Visco, S. J., and Jacobson, C. P. (2003). "Electrolytic damage in zirconia electrolytes." in *Solid Oxide Fuel Cell VIII*, Edited by S. C. Singhal and M. Dokiya, 209-213.

Meixner, D. L., and Cutler, R. A. (2002a). "Low-temperature plastic deformation of a perovskite ceramic material." *Solid State Ionics*, 146(3-4), 285-300.

Meixner, D. L., and Cutler, R. A. (2002b). "Sintering and mechanical characteristics of lanthanum strontium manganite." *Solid State Ionics*, 146(3-4), 273-284.

Mencik, J. (1992). *Strength and Fracture of Glass and Ceramics*, Elsevier, Amsterdam.

Microsoft Corp. (1998). "Miscrosoft Visual Basic 6.0."

Milliken, C., Guruswamy, S., and Khandkar, A. (1999). "Evaluation of ceria electrolytes in solid oxide fuel cells electric power generation." *Journal of The Electrochemical Society*, 146(3), 872-882.

Mitterdorfer, A., and Gauckler, L. J. (1998). "$La_2Zr_2O_7$ formation and oxygen reduction kinetics of the $La_{0.85}Sr_{0.15}Mn_yO_3$, O_2(g)|YSZ system." *Solid State Ionics*, 111(3-4), 185-218.

Mitterdorfer, A., and Gauckler, L. J. (1999a). "Identification of the reaction mechanism of the Pt, O_2(g)|yttria-stabilized zirconia system: Part I: General framework, modelling, and structural investigation." *Solid State Ionics*, 117(3-4), 187-202.

Mitterdorfer, A., and Gauckler, L. J. (1999b). "Identification of the reaction mechanism of the Pt, O_2(g)|yttria-stabilized zirconia system: Part II: Model implementation, parameter estimation, and validation." *Solid State Ionics*, 117(3-4), 203-217.

Mizusaki, J., Saito, T., and Tagawa, H. (1996). "A chemical diffusion-controlled electrode reaction at the compact $La_{1-x}Sr_xMnO_3$/stabilized zirconia interface in oxygen atmospheres." *Journal of the Electrochemical Society*, 143, 3065-3072.

Mizusaki, J., Tagawa, H., Saito, T., Yamamura, T., Kamitani, K., Hirano, K., Ehara, S., Takagi, T., Hikita, T., Ippommatsu, M., Nakagawa, S., and Hashimoto, K. (1994). "Kinetic studies of the reaction at the nickel pattern electrode on YSZ in H_2---H_2O atmospheres." *Solid State Ionics*, 70-71(1), 52-58.

Mizusaki, J., Tagawa, H., Tsuneyoshi, K., and Sawata, A. (1991). "Reaction kinetics and microstructure of the SOFC air electrode $La_{0.6}$ $Ca_{0.4}$ MnO_3/YSZ." *Journal of The Electrochemical Society*, 138, 1867-1873.

Mizutani, Y., Tamura, M., Kawai, M., and Yamamoto, O. (1994). "Development of high-performance electrolyte in SOFC." *Solid State Ionics*, 72(2), 271-275.

Mogensen, M., Jensen, K. V., Jorgensen, M. J., and Primdahl, S. (2002). "Progress in understanding SOFC electrodes." *Solid State Ionics*, 150(1-2 SU -), 123-129.

Muchtar, A., and Lim, L. C. (1998). "Indentation fracture toughness of high purity submicron alumina." *Acta Materialia*, 46(5), 1683-1690.

Muller, A. C., Weber, A., Herbstritt, D., and Ivers-Tiffee, E. (2003). "Long term stability of yttria and scandia doped zirconia electrolytes." in *Solid Oxide Fuel Cells VIII*, Edited by S. C. Singhal and M. Dokiya, Paris, France, 196-199.

Nagata, S., Momma, A., Kato, T., and Kasuga, Y. (2001). "Numerical analysis of output characteristics of tubular SOFC with internal reformer." *Journal of Power Sources*, 101(1), 60-71.

Naito, H., Sakai, N., Otake, T., Yugami, H., and Yokokawa, H. (2000). "Oxygen transport properties in ZrO_2-CeO_2-Y_2O_3 by SIMS analyses." *Solid State Ionics*, 135(1-4), 669-673.

Naoumidis, A., Ahmad-Khanlou, A., Samardzija, Z., and Kolar, D. (1999). "Chemical interaction and diffusion on interface cathode/electrolyte of SOFC." *Fresenius' Journal of Analytical Chemistry*, 365, 277-281.

National Instruments. (2001). "Measurement Studio 6.0."

Nomura, K., Mizutani, Y., Kawai, M., Nakamura, Y., and Yamamoto, O. (2000). "Aging and Raman scattering study of scandia and yttria doped zirconia." *Solid State Ionics*, 132(3-4), 235-239.

Odgaard, M., and Skou, E. (1996). "SOFC cathode kinetics investigated by the use of cone shaped electrodes: The effect of polarization and mechanical load." *Solid State Ionics*, 86-88(2), 1217-1222.

Orui, H., Watanabe, K., and Arakawa, M. (2002). "Electrochemical characteristics of tubular flat-plate-SOFCs fabricated by co-firing cathode substrate and electrolyte." *Journal of Power Sources*, 112(1), 90-97.

Ostergard, M. J. L., Clausen, C., Bagger, C., and Mogensen, M. (1995). "Manganite-zirconia composite cathodes for SOFC: influence of structure and composition." *Electrochimica Acta*, 40(12), 1971-1981.

Ostergard, M. J. L., and Mogensen, M. (1993). "AC Impedance study of the oxygen reduction mechanism on $La_{1-x}Sr_xMnO_3$ in solid oxide fuel cells." *Electrochimica Acta*, 38(14), 2015-2020.

Paulik, S. W., Baskaran, S., and Armstrong, T. R. (1998). "Mechanical properties of calcium- and strontium-substituted lanthanum chromite." *Journal of Materials Science*, 33(9), 2397-2404.

Recknagle, K. P., Williford, R. E., Chick, L. A., Rector, D. R., and Khaleel, M. A. (2003). "Three-dimensional thermo-fluid electrochemical modeling of planar SOFC stacks." *Journal of Power Sources*, 113(1), 109-114.

Reifsnider, K. L., Halverson, H. G., An, K., Huang, X., Case, S. W., Carter, R. H., Binetti, V., and Vinton, T. (2001). "Long Term Behavior of Layered Thin film Materials - Final Report Submitted to McDermott Technologies, Inc." Materials Response Group, Virginia Tech, Blacksburg, Va.

Rim, H.-R., Jeung, S.-K., Jung, E., and Lee, J.-S. (1998). "Characteristics of $Pr_{1-x}M_xMnO_3$ (M=Ca, Sr) as cathode material in solid oxide fuel cells." *Materials Chemistry and Physics*, 52, 54-59.

Rubinstein, I. (1995). *Physical Electrochemistry*, Marcel Dekker, Inc.

Sahibzada, M., Steele, B. C. H., Barth, D., Rudkin, R. A., and Metcalfe, I. S. (1999). "Operation of solid oxide fuel cells at reduced temperatures." *Fuel*, 78(6), 639-643.

Sahibzada, M., Steele, B. C. H., Zheng, K., Rudkin, R. A., and Metcalfe, I. S. (1997). "Development of solid oxide fuel cells based on a $Ce(Gd)O_{2-x}$ electrolyte film for intermediate temperature operation." *Catalysis Today*, 38(4), 459-466.

Sakaki, Y., Takeda, Y., Kato, A., Imanishi, N., Yamamoto, O., Hattori, M., Iio, M., and Esaki, Y. (1999). "$Ln_{1-x}Sr_xMnO_3$ (Ln=Pr, Nd, Sm and Gd) as the cathode material for solid oxide fuel cells." *Solid State Ionics*, 118(3-4), 187-194.

Sawata, A., Tsuneyoshi, K., Mizusaki, J., and Tagawa, H. (1990). "Oxygen chemical potential profile in a solid oxide fuel cell and simulation of electrochemical performance." *Solid State Ionics*, 40-41(1), 415-420.

Selcuk, A., and Atkinson, A. (2000). "Strength and toughness of tape-cast yttria-stabilized zirconia." *Journal of the American Ceramic Society*, 83(8), 2029-2035.

Setoguchi, T., Okamoto, K., Eguchi, K., and Arai, H. (1992). "Effects of anode material and fuel on anodic reaction of solid oxide fuel cells." *Journal of The Electrochemical Society*, 139(10), 2875-2880.

Shiratori, Y., and Yamazaki, Y. (2003). "Discharge characteristics of planar stack fuel cells." *Journal of Power Sources*, 114(1), 80-87.

Siebert, E., Hammouche, A., and Kleitz, M. (1995). "Impedance spectroscopy analysis of $La_{1-x}Sr_xMnO_3$-Yttria-stabilized zirconia electrode kinetics." *Electrochimica Acta*, 40(11), 1741-1753.

Singhal, S. C. (2000). "Advances in solid oxide fuel cell technology." *Solid State Ionics*, 135(1-4), 305-313.

Song, S., Wang, Z., and Li, W. (1993). *Physical Chemistry*, High Education Press.

Steele, B. C. H. (1997). "Behaviour of porous cathodes in high temperature fuel cells." *Solid State Ionics*, 94(1-4), 239-248.

Stevenson, J. W., Armstrong, R. W., McCready, D. E., Pederson, L. R., and Weber, W. J. (1997). "Processing and electrical properties of alkaline earth-doped lanthanum gallate." *Journal of the Electrochemical Society*, 144(10), 3613-3619.

Stevenson, J. W., Hallman, P. F., Chick, L. A., and Armstrong, R. W. (1995). "Sintering behavior of doped lanthanum and yttrium manganite." *Journal of the American Ceramic Society*, 78, 507-512.

Sunde, S. (1997). "Calculations of impedance of composite anodes for solid oxide fuel cells." *Electrochimica Acta*, 42(17), 2637-2648.

Sunde, S. (2000). "Simulations of composite electrodes in fuel cells." *Journal of Electroceramics*, 5(2), 153-182.

Svensson, A. M., Sunde, S., and Nisancioglu, K. (1996). "A mathematical model of the porous SOFC cathode." *Solid State Ionics*, 86-88(2), 1211-1216.

Tanner, C. W., and Virkar, A. V. (2003). "A simple model for interconnect design of planar solid oxide fuel cells." *Journal of Power Sources*, 113(1), 44-56.

Toshihiko Setoguchi, Takanori Inoue, Hiromichi Takebe, Koichi Eguchi, Kenji Morinaga, and Hiromichi Arai. (1990). "Fabrication and evaluation of flat thick film type solid oxide fuel cell." *Solid State Ionics*, 37(2-3), 217-221.

Tsuneyoshi, K., Mori, K., Sawata, A., Mizusaki, J., and Tagawa, H. (1989). "Kinetic studies on the reaction at the $La_{0.6}Ca_{0.4}MnO_3$/YSZ interface, as an SOFC air electrode." *Solid State Ionics*, 35(3-4), 263-268.

van Berkel, F. P. F., van Heuveln, F. H., and Huijsmans, J. P. P. (1994). "Characterization of solid oxide fuel cell electrodes by impedance spectroscopy and I-V characteristics." *Solid State Ionics*, 72(2), 240-247.

Van herle, J., Ihringer, R., Vasquez Cavieres, R., Constantin, L., and Bucheli, O. (2001). "Anode supported solid oxide fuel cells with screen-printed

cathodes." *Journal of the European Ceramic Society*, 21(10-11), 1855-1859.

van Roosmalen, J. A. M., and Cordfunke, E. H. P. (1992). "Chemical reactivity and interdiffusion of (La, Sr)MnO_3 and (Zr, Y)O_2, solid oxide fuel cell cathode and electrolyte materials." *Solid State Ionics*, 52(4), 303-312.

Virkar, A. V., Chen, J., Tanner, C. W., and Kim, J.-W. (2000). "The role of electrode microstructure on activation and concentration polarizations in solid oxide fuel cells." *Solid State Ionics*, 131(1-2), 189-198.

Wang, S., Jiang, Y., Zhang, Y., Yan, J., and Li, W. (1998). "Promoting effect of YSZ on the electrochemical performance of YSZ+LSM composite electrodes." *Solid State Ionics*, 113-115, 291-303.

Weber, A., Herbstritt, D., Muller, A., and Ivers-Tiffee, E. (2000). "Electronic, ionic and mixed conductors in SOFC." in *Materials Week*, Edited by Munich, Germany, 1-8.

Wen, T.-L., Tu, H., Xu, Z., and Yamamoto, O. (1999). "A study of (Pr, Nd, Sm)$_{1-x}Sr_xMnO_3$ cathode materials for solid oxide fuel cell." *Solid State Ionics*, 121(1-4), 25-30.

Yakabe, H., Hishinuma, M., Uratani, M., Matsuzaki, Y., and Yasuda, I. (2000). "Evaluation and modeling of performance of anode-supported solid oxide fuel cell." *Journal of Power Sources*, 86(1-2), 423-431.

Yakabe, H., Ogiwara, T., Hishinuma, M., and Yasuda, I. (2001). "3-D model calculation for planar SOFC." *Journal of Power Sources*, 102(1-2), 144-154.

Yamamoto, O. (2000). "Solid oxide fuel cells: fundamental aspects and prospects." *Electrochimica Acta*, 45(15-16), 2423-2435.

Yokokawa, H., Sakai, N., Kawada, T., and Dokiya, M. (1990). "Thermodynamic analysis on interface between perovskite electrode and YSZ electrolyte." *Solid State Ionics*, 40-41(1), 398-401.

Yoon, S. P., Han, J., Nam, S. W., Lim, T.-H., Oh, I.-H., Hong, S.-A., Yoo, Y.-S., and Lim, H. C. (2002). "Performance of anode-supported solid oxide fuel cell with $La_{0.85}Sr_{0.15}MnO_3$ cathode modified by sol-gel coating technique." *Journal of Power Sources*, 106(1-2), 160-166.

Zhu, W. Z., and Deevi, S. C. (2003). "Development of interconnect materials for solid oxide fuel cells." *Materials Science and Engineering A*, 348(1-2), 227-243.

VITA

Ke An (安柯) was born on May 21, 1976, to Shuzhai An (安书斋) and Xiuhua Geng (耿绣花) in Kaifeng, Henan Province, China. He is the third and youngest child in the family, with two brothers.

After graduating from the Kaifeng High School, the best one in Kaifeng, Ke attended Tianjin (Peiyang) University, the first university founded in China, and one of the top 3 engineering institutes, in September 1994. He earned his Bachelors degree in Chemical Engineering Machinery and Equipment in July 1998.

He earned the honor of excellent student 40 out of more than 2300 undergraduate students and got waived of the exam of graduate school admission to continue his Master program in Chemical Engineering Process Machinery. Worked with his advisor Dr. Xu Chen, Ke finished his Master of Engineering degree in December 2000 with the study on Multiaxial Low Cycle Fatigue of Welded Joint under Nonproportional Loading.

In January 2001, Ke started his PhD study in Engineering Mechanics at Virginia Polytechnic Institute and State University, Blacksburg, Virginia, USA.